Ancient mantle heterogeneities in modern intraplate lavas – insights from new analytical tools

Inaugural-Dissertation

zur

Erlangung des Doktorgrades

der Mathematisch-Naturwissenschaftlichen Fakult.t

der Universität zu Köln

vorgelegt von:

Mike Jansen

aus Simmerath

Köln, 2022

Berichterstatter: Prof. Dr. Carsten Münker
Dr. Daniel Herwartz

Tag der mündlichen Prüfung: 24.11.2022

This thesis is dedicated to my parents Meta and Hans-Peter Jansen

TABLE OF CONTENTS

I. Abstract

Since more than 4.57 billion years, several geodynamic processes are shaping the Earths ex- and interior. While several geodynamic processes occurring on the Earth's surface can be addressed using first order geological methods, geochemical studies on volcanic rocks provide important constraints on its inaccessible interior. Already since the 1950's, several studies have investigated long-lived radiogenic isotope systems (Sr, Nd, Hf, Pb) and trace-element compositions to study the composition and nature of the Earth's mantle. While it was long thought that the Earth's mantle is compositionally rather homogenous, studies on Ocean Island Basalts have indicated a rather heterogenous composition and several compositional endmembers that can be identified using geochemical evidence. Most recently, the application of short-lived isotopes, including ^{182}Hf-^{182}W, ^{146}Sm-^{142}Nd and ^{129}I-^{129}Xe in modern basalts have further indicated the survival of primordial mantle reservoirs that must have formed during the early Hadean Eon (during the first ~100 Ma in solar system history) and survived mantle convection until today. Among the previously mentioned short-lived isotope systems, the ^{182}Hf-^{182}W (half-life = 8.9 Ma, (Vockenhuber et al., 2004)) has been increasingly used to detect the participation of primordial mantle reservoirs in terrestrial rocks from the Archean as well as modern Ocean Island Basalts. The occurrence of deficient ^{182}W isotope compositions and a positive correlation with ^{3}He/^{4}He ratios found in modern plume related volcanic rocks has thereby been interpreted as evidence for the long-term survival of mantle reservoirs that record fractionation of Hf and W during Earth's primary differentiation (silicate-silicate or metal-silicate) or core-mantle interaction occurring either early – or at any time later in Earth's history. The combination of seismic- and geochemical data as well as modelling constraints have further provided evidence for Large Low Shear Velocity Provinces and Ultra Low Velocity Zones, seismically anomalous zones that are present at the roots of deep mantle plumes, as potential source reservoirs that are capable of long-term isolation.

Many young ocean island basalts show small ^{182}W deficits, in particular if they are sourced from deep-rooted mantle plumes. The origin of this anomaly is still ambiguous and proposed models focus on core-mantle interaction or the presence of reservoirs in the lower mantle that have been isolated since the Hadean. In order to evaluate the role of upper mantle reservoirs, we report the first ^{182}W data for intraplate basalts where a deep plume origin is still debated

(Ascension Island, Massif Central, Siebengebirge and Eifel) and intraplate volcanic rocks associated with either plume or subduction zone environments (Italian Magmatic Provinces). Further, we compare these data with volcanic settings where seismic investigations have indicated a deep mantle plume origin (La Réunion, Baffin Island) (**Chapter I**). Additionally, we present detailed ^{182}W data on oceanic intraplate volcanic rocks from the South Atlantic Ocean, including the three primary mantle plumes Tristan-Gough, Discovery and Shona, that are sourced by deep-mantle plume(s) and have shown to tap temporally changing magma sources (**Chapter II**). In summary, the ^{182}W composition in all intraplate volcanic provinces of questionable plume origin overlap the composition of modern upper mantle to within 3 ppm. The absence of resolvable ^{182}W anomalies in these intraplate basalts, which partially tap the lithospheric mantle, suggests that primordial components are neither present in the central and southern European lithosphere nor in the upper mantle in general. In contrast, ^{182}W compositions in samples from La Réunion and the Tristan-Gough hotspot track span a range from modern upper mantle values to deficits as low as $\mu^{182}W = -8.8$ ppm and indicate a heterogenous contribution of primordial reservoirs to these mantle plumes. Given that seismic data has shown these plumes to be rooted at the core-mantle boundary, our data provide further evidence that Large Low Shear Velocity Provinces (LLSVPs) and Ultra Low Velocity Provinces (ULVPs) play a key role as potential hosts for primordial reservoirs in the lower-mantle. Given the heterogenous distribution of primordial signatures in rising plumes, our data provide evidence for lower-mantle dynamics as the driving force for material incorporation. Further, observed co-variation of ^{182}W with Sr-Nd-Pb isotope values further confirms that the deep mantle sources of the South Atlantic volcanism comprise variable amounts of primordial material that is diluted by younger, post Hadean recycled material. Interestingly, the proto-Iceland plume basalts from Baffin Island have uniform and modern mantle-like ^{182}W of around 0 despite extremely high ($^{3}He/^{4}He$) and thus provide evidence for decoupled He-W systematics in rising plumes.

Quaternary rocks of the East and West Eifel volcanic fields in western Germany are a key suite of intraplate volcanic rocks that can provide insights into volcanism of the Central European Volcanic Province and into continental intraplate volcanism in general. Coupled trace-element and radiogenic Sr-Nd-Hf-Pb-Os isotope compositions provide detailed evidence for heterogenous mantle sources and compositionally distinct magmatic pulses (**Chapter III**). While a mantle plume origin for volcanism has been questioned, our new data and modelling constraints are in good agreement with admixtures of litospheric and asthenospheric mantle

sources. Using geochemical evidence, our data further indicate the presence residual eclogitic components present within the upper mantle underneath central Europe and also indicate a potential influence of carbonatite metasomatism. Compiling available geochemical data for Quaternary as well as Tertiary volcanic provinces in central Germany (e.g., Siebengebirge, Vogelsberg, Rhön) shows that similar spatial, temporal and compositional relationships can be traced throughout all eruptive stages of central European volcanism. Conclusively, our data argue in favor of discrete melt pulses and pooling of polybaric melts from asthenospheric (plume-like) and lithospheric mantle sources underneath central Europe.

II. Kurzzusammenfassung

Seit mehr als 4,57 Milliarden Jahren formen diverse geodynamische Prozesse die Erdkruste und den Erdmantel. Während die meisten geodynamischen Prozesse an der Erdoberfläche mit klassischen geologischen Methoden untersucht werden können, liefern geochemische Studien an Vulkaniten wichtige Erkenntnisse über den unzugänglichen Erdmantel. Bereits seit den 1950er Jahren haben Studien langlebiger, radiogener Isotopensysteme (Sr, Nd, Hf, Pb) und der Spurenelementzusammensetzungen von Vulkaniten wichtige Informationen über die Zusammensetzung und die Beschaffenheit des Erdmantels geliefert. Während man lange Zeit davon ausging, dass der Erdmantel eine eher homogene Zusammensetzung besitzt, haben Untersuchungen an Ozean-Insel Basalten auf eine eher heterogene Zusammensetzung und die Existenz mehrerer Kompositioneller Endglieder hingedeutet, welche sich anhand geochemischer Daten identifizieren lassen. In jüngster Zeit hat die Untersuchung kurzlebiger Isotopensysteme wie ^{182}Hf-^{182}W, ^{146}Sm-^{142}Nd und ^{129}I-^{129}Xe in modernen Basalten das „Überleben“ von primordialen Mantelreservoiren angedeutet, welche sich während des frühen Hadaikums (während der ersten ~100 Ma in der Geschichte des Sonnensystems) gebildet haben und von der Mantelkonvektion weitgehend isoliert geblieben sind. Von den bereits erwähnten kurzlebigen Isotopensystemen wurde ^{182}Hf-^{182}W (Halbwertszeit = 8,9 Ma, (Vockenhuber et al., 2004)) zunehmend dazu verwendet, um die Beteiligung von primordialen Mantelreservoiren in terrestrischen Gesteinen aus dem Archaikum sowie in modernen Ozean-Insel Basalten nachzuweisen. Das Auftreten defizitärer ^{182}W-Isotopenzusammensetzungen und eine positive Korrelation mit ^{3}He/^{4}He in modernen Mantel-Plumes wurde dabei als Beweis für die langfristige Isolation von Mantelreservoiren interpretiert. Diese Reservoire könnten dabei Isotopensignaturen der Fraktionierung von Hf und W während der primären Differenzierung der Erde (Silikat-Silikat oder Metall-Silikat) oder der Kern-Mantel-Wechselwirkung beinhalten. Eine Wechselwirkung von Kern und Mantel kann dabei sowohl in der Erdfrühgeschichte als auch zu einem später Zeitpunkt erfolgt sein. Die Kombination von seismischen und geochemischen Daten sowie Modellierungen haben außerdem gezeigt, dass seismisch anomale Zonen (Large Low Shear Velocity Provinces (LLSVPs) und Ultra low Velocity Zones (ULVZs)) an der Kern-Mantel Grenze vorhanden sind, welche als potenzielle Quellenreservoire dienen. Die seismischen Eigenschaften dieser Provinzen deuten dabei auf eine potentielle, langfristige Isolation hin.

Viele junge Ozean Insel Basalte weisen geringe ^{182}W-Defizite auf, insbesondere wenn sie aus tiefen Mantelplumes gespeist werden. Der Ursprung dieser Anomalien ist noch weitegehend ungegeklärt. Bisher postulierte Modelle konzentrieren sich auf eine Kern-Mantel-Wechselwirkung oder das Vorhandensein von Reservoiren im unteren Mantel, die seit dem Hadaikum isoliert geblieben sind. Um weitere Erkenntnisse über das Vorhandensein primordialer Mantelquellen, vor allem im auch im oberen Mantel weiter zu gewinnen, wurden im Rahmen dieser Studie die ersten ^{182}W Daten für Intraplatten-Basalte, deren Zusammenhang mit einem Plume noch ungeklärt ist, gesammelt. Die Lokationen umfassen dabei ozeanische- und kontinentale Intraplatten-Basalte (Ascension Island, Zentralmassiv, Siebengebirge und Eifel), sowie Vulkanite deren Ursprung entweder mit einem Mantel-Plume oder Subduktionszonen in Verbindung gebracht werden (Italienische Magmatische Provinzen). Weiterhin vergleichen wir diese Daten mit Lokationen bei denen seismische Untersuchgen eindeutig eine tiefe Mantel-Quelle angezeigt haben (La Réunion, Baffin Island) (**Kapitel I**). Darüber hinaus präsentieren wir einen detaillierten ^{182}W-Datensatz für ozeanische Intraplatten-Vulkanite aus dem Südatlantik, einschließlich der drei primären Mantel-Plumes Tristan-Gough, Discovery und Shona, welche von der Kern-Mantel Grenze gespeist werden und deren Magmen-Quellen eine räumlich/ zeitliche Variation zeigen (**Kapitel II**). Zusammenfassend lässtfeststellen, dass alle Intraplatten-Basalte, bei denen eine tiefe Mantelquelle nicht eindeutig nachweisbar ist, im Fehler von ± 3 ppm mit der ^{182}W-Zusammensetzung des modernen oberen Erdmantels übereinstimmen. Das Fehlen auflösbarer ^{182}W-Anomalien in diesen Intraplatten-Basalten, welche teilweise den lithosphärischen Mantel beproben, deutet darauf hin, dass primordiale Komponenten weder in der mittel- und südeuropäischen Lithosphäre noch im oberen Mantel im Allgemeinen vorhanden sind. Im Gegensatz dazu, zeigen die ^{182}W-Zusammensetzungen in Proben von La Réunion und des Tristan-Gough-Hotspots eine deutlich heterogene Zusammensetzung und zeigen ^{182}W Defizite von bis zu $\mu^{182}W = -8.8$ ppm, welche einen Eintrag primordialer Reservoire andeuten. Im Einklang mit seismischen Studien welche eine Quelle an der Kern-Mantel-Grenze belegen, liefern unsere Daten somit weitere Hinweise auf die seismisch anomalen „Large Low Shear Velocity Provinces (LLVPs)“ oder „Ultra Low Velocity Zones (ULVZs)“ als potentielle Mantel-Quellen primordialen Ursprungs. Angesichts der heterogenen Verteilung der primordialen Signaturen in den aufsteigenden Magmen legen unsere Daten weiterhin nahe, dass dynamische Prozesse im tiefen Mantel die treibende Kraft für die Inkorporation primordialen Materials sind. Weiterhin zeigen unsere Daten eine Korrelation von ^{182}W und Sr-Nd-Pb Isotopenzusammensetzungen, welche eine „Verdünnung“

von primordialen Signaturen durch die Beimischung von jüngerem, recyceltem Material andeutet. Interessanterweise weisen die protoisländischen Plume-Basalte von Baffin Island trotz extrem hoher ($^{3}He/^{4}He$) Werte ein einheitliches und modernes, mantelähnliches ^{182}W von etwa 0 auf und liefern damit Hinweise auf eine entkoppelte He-W-Systematik in aufsteigenden Plumes.

Die Quartären Vulkanite der Ost- und Westeifel sind ein wichtiges Vorkommen von Intraplatten-Vulkaniten, deren Untersuchung wichtige Informationen über den Vulkanismus in Mitteleuropa und Intraplatten Vulkanismus auf der ganzen Welt liefen können. Spurenelement- und radiogene Sr-Nd-Hf-Pb-Os Isotopenzusammensetzungen liefern dabei detaillierte Belege für heterogene Mantelquellen und kompositorisch unterschiedliche magmatische Pulse (**Kapitel III**). Während der Ursprung des Vulkanismus durch einen Mantel-Plume noch immer nicht abschließend geklärt wurde, deuten die hier präsentierten Daten deutlich auf eine Mischung von litosphärischen und asthenosphärischen Mantel-Quellen hin. Weiterhin finden wir deutliche Signaturen restitischer Eklogite sowie den möglichen Einfluss von Karbonat-Metasomatose in den Quellen der Eifelmagmen. Die Zusammenstellung verfügbarer geochemischer Daten für quartäre und tertiäre Vulkanprovinzen in Mitteldeutschland (z.B. Siebengebirge, Vogelsberg, Rhön) zeigt, dass ähnliche räumliche, zeitliche und kompositorische Zusammenhänge über alle eruptiven Phasen mitteleuropäischen Vulkanismus hinweg nachvollzogen werden können. Zusammenfassend sprechen unsere somit Daten für Schmelzimpulse und deine Mischung von polybarischen Schmelzen aus asthenosphärischen (plume-artigen) und lithosphärischen Mantel-Quellen unter Mitteleuropa.

III. Introduction

Modern volcanism – a window into the Earth's interior

Geochemical studies on basaltic rocks provide important constraints on the composition and evolution of the Earth because they represent melts that directly originated from the inaccessible mantle. Solid state convection transports material from the lower mantle into the shallow regions of the mantle, where it is partially molten and transported to the surface by volcanic eruptions.

Prior to the acceptance of seafloor spreading, plate tectonics and solid-state convection, it was generally believed that the Earth's mantle consists of geochemically uniform peridotites with a rather homogenous composition (e.g., Hofmann, 2003). This view served geochemist, geophysicists and petrologist as a common description of the Earth's composition and physical properties (e.g., Hofmann, 2003). However, in the last decades, several review papers on the Earth's mantle, its geochemical composition and the nature of reservoirs accessible for partial melting have demonstrated that the Earth's mantle is compositionally just as heterogenous as the crust (e.g., Hedge and Walthall, 1963; Gast et al., 1964; Tatsumoto et al., 1965; Hart, 1971; White and Hofmann, 1982; Hofmann et al., 1986; Hart et al., 1992; Hofmann, 1997; Hofmann, 2003; Stracke et al., 2005; Jackson et al., 2020a).

On modern Earth, volcanism occurs in several geodynamic environments including mid ocean ridges, subduction zones and oceanic as well as continental intraplate settings (Fig. III.1). Volcanic rocks found within intraplate settings at convergent and divergent plate margins are ultimately linked to plate tectonics and mantle convection. Depending on the geodynamic setting in which volcanic rocks are formed, they display distinct geochemical compositions that provide important constraints on their formation and source regions (Fig. III.1).

At divergent plate margins, the separation of two lithospheric plates induces upwelling of the underlying mantle. The subsequent adiabatic rise of mantle peridotite then causes partial melting due to ongoing decompression. Given that formed magmas rapidly rise towards the surface, the resulting volcanic rocks are known as Mid Ocean Ridge Basalts (MORB) (Fig. III.1). Volcanism at mid Ocean Ridges represents the most volumetric and widespread form of magmatism on Earth.

At convergent plate margins, where two lithospheric plates collide, the subduction of oceanic crust causes the release of volatiles due to the rise of pressure and temperature within the subducted slab (Fig. III.1). Volatiles that rise upwards through the overlying continental crust reduce the solidus temperature and induce partial melting within the mantle wedge. This form of volcanism is called subduction zone volcanism and occurs at convergent plate margins all around the world.

On continental as well as oceanic plates, volcanism often occurs far off divergent as well as convergent margins. Forming elongated, time progressive chains of volcanoes or islands that are aligned in the direction of plate motion, it has been inferred that magma generation is caused by stationary melt anomalies that rise from the lower mantle towards the surface (Fig. III.1). These observations have led to the concept of mantle-plumes that provide the source for so called Ocean Island Basalts (OIBs).

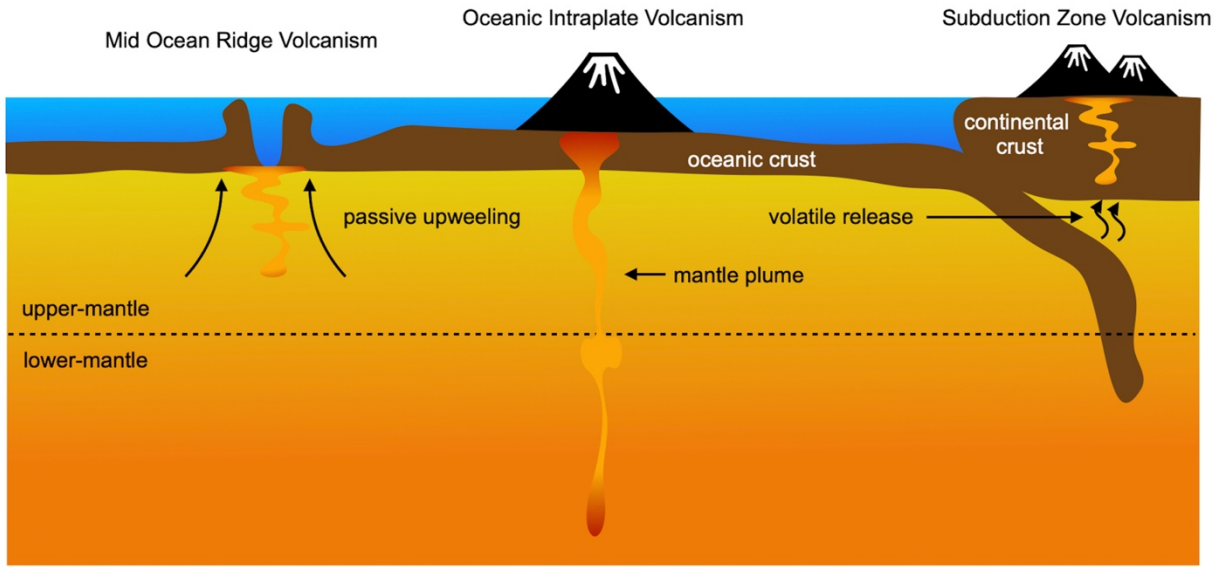

Figure III.1 Sketch illustrating the major volcanic settings in modern Earth.

Form a geochemical point of view, already since the 1960's it was shown that elemental fractionation during igneous processes, such as parent/ daughter and light-to-heavy ratios of the Rare Earth Elements (REE), can provide further constraints on the heterogenous nature of the Earth's mantle (Gast et al., 1964; Tatsumoto et al., 1965; Schilling, 1967; Schilling and Winchester, 1969; Hart, 1971). Based on geochemical data of mantle-derived volcanic rocks, fundamental compositional differences between MORBs and OIBs have led to the model of a geochemically stratified mantle that includes an incompatible (trace) element depleted upper

and an un-depleted lower mantle. The term "incompatible elements" thereby refer to trace elements that cannot easily substitute into the major element sites of igneous minerals and thus preferentially enter the melt during partial meting (e.g., Hofmann, 2003). In detail, the geochemical behavior of an element is defined by its ionic properties such as radius and charge. To relate the amount of a trace-element that preferentially enters a melt to the amount that remains within a crystal structure, each element can be assigned a specific partition coefficient "D" (e.g., Hofmann, 2003 and references therein). As partition coefficients have been determined in the laboratory for many important mineral phases, it has been shown that experimental results clearly match geochemical observations, such as the incompatible element enrichment of the continental crust (e.g., Hofmann, 2003 and references therein) (Fig. III.2). Given that Earth's continental crust has been formed throughout large-scale partial melting of the upper mantle, the depleted mantle residue is now sampled along the mid-ocean-ridge systems (e.g.,White and Hofmann, 1982; Hofmann, 1997; White, 2014). As the above mentioned observations also accounts for the of parent/daughter fractionation of radiogenic nuclides (Fig. III.3) several pioneering studies used radiogenic isotope analysis (Rb-Sr, Sm-Nd, U+Th/Pb) to decipher Earth's mantle characteristics (Hedge and Walthall, 1963; Gast et al., 1964; Tatsumoto et al., 1965; Hart, 1971). For instance, owing to the fractionation of parent/daughter nuclides and radiogenic ingrowth over time, differentiated mantle reservoirs can be distinguished by their radiogenic isotope composition. Therefore, long-lived radiogenic isotope systems such as $^{87}Sr/^{86}Sr$, $^{143}Nd/^{144}Nd$, $^{176}Hf/^{177}Hf$ and $^{206, 207, 208}Pb/^{204}Pb$ have become powerful tools in tracing mantle heterogeneity (e.g., Hofmann, 2003; Stracke et al., 2005).

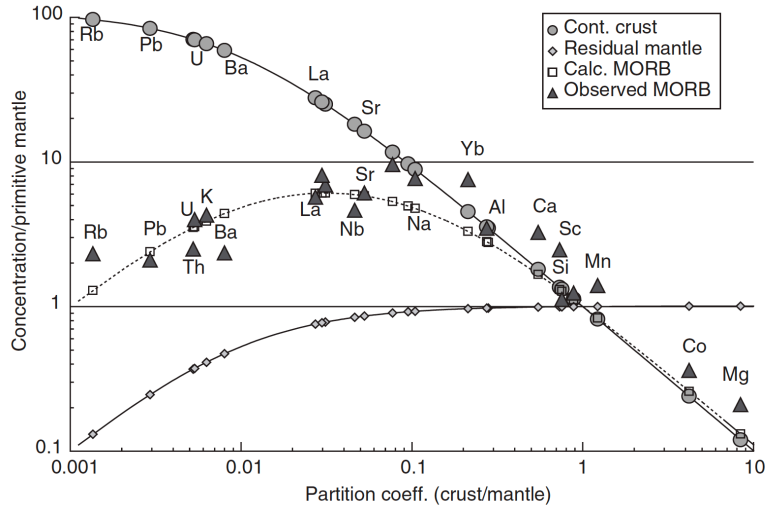

Figure III.2 Comparison oft he abbundances of major- and trace elements in average continental crust and mantle, taken from Hofmann (2003). The primitive mantle normalized concentrations versus their respective partition coefficients clearly illustrates the incompatible behavior of elements like Rb, Pb and U compared to Co and Mg.

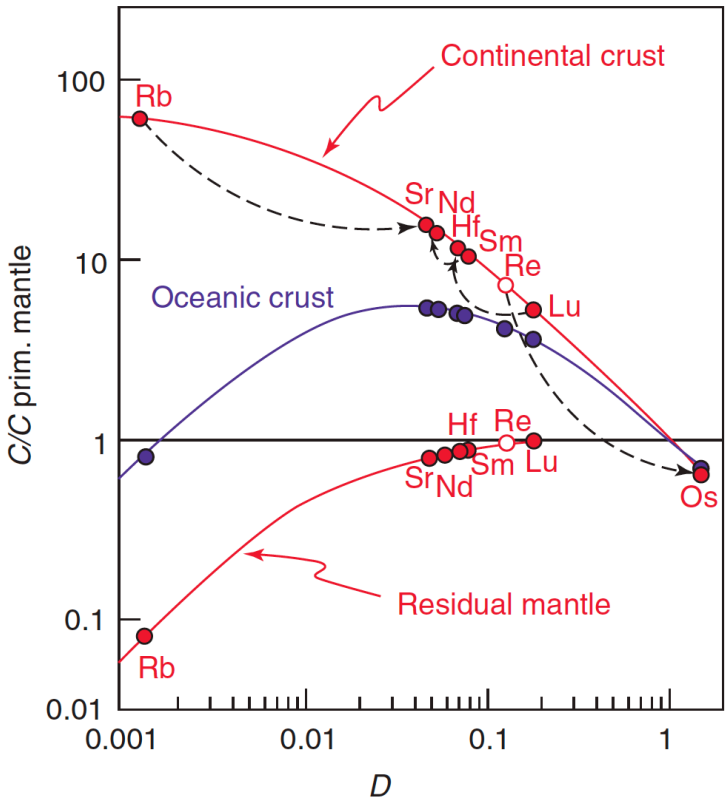

Figure III.3 Crust-mantle differentiation patterns for the long-lived Rb-Sr, Sm-Nd, Lu-Hf and Re-Os isotope systems. This diagram clearly illustrates the depletion-enrichment relationships of parent and daughter nuclides that lead to the isotopic differences as observed in MORB and crust.

In contrast to MORB that sample the Earth's upper mantle, geochemical compositions and seismic investigations have shown that the OIB sources must be rooted within lower-mantle reservoirs that are less depleted or even enriched in incompatible elements due to the deep recycling of crustal materials (e.g., Morgan, 1971; White and Hofmann, 1982; Hofmann et al., 1986; Hart et al., 1992; Hofmann, 1997; Montelli et al., 2004; Stracke et al., 2005; Montelli et al., 2006; French and Romanowicz, 2015; Jackson et al., 2020a). Besides the geochemical differences between MORBs and OIBs, geochemical studies have further shown discrete compositional differences of even individual OIB settings that can be identified and characterized throughout specific isotope compositions (Fig. III.4) (e.g., Hofmann, 2003).

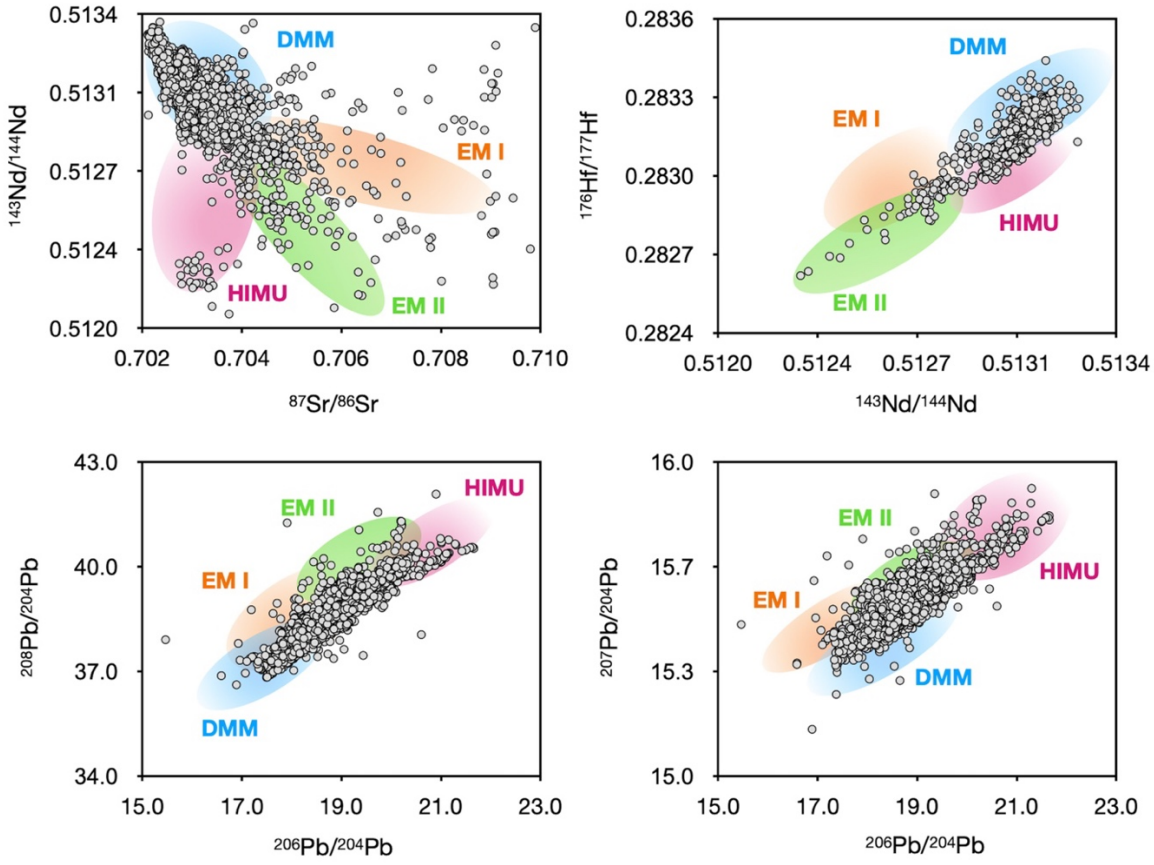

Figure III. 4: Isotope variation diagrams illustrating the mantle endmember compositions that have been inferred to contribute to modern OIB volcanism. In $^{143}Nd/^{144}Nd$ isotope space, EM I and EM II mantle endmembers are characterized throughout highly radiogenic $^{87}Sr/^{86}Sr$ ratios at un-radiogenic $^{143}Nd/^{144}Nd$ isotope compositions, reflecting the enrichment of the mantle source throughout crustal recycling. In $^{208}Pb/^{204}Pb$ vs. $^{206}Pb/^{204}Pb$ and $^{207}Pb/^{204}Pb$ vs. $^{206}Pb/^{204}Pb$ isotope space, the HIMU mantle endmember displays highly radiogenic Pb isotope compositions, reflecting the high (U-Th)/Pb ratio of the mantle source that has formed throughout long-term isolated, subducted oceanic crustal materials. The MORB endmember is characterized by radiogenic $^{143}Nd/^{144}Nd$, $^{176}Hf/^{177}Hf$ ratios and un-radiogenic Pb and Sr isotope compositions that reflect the incompatible element depletion throughout the extraction of continental crust (for reference see Hofmann, 2003). Compositional fields have been created compiling available data of various OIB settings, downloaded from the PetDB database (https://search.Earthchem.org).

Numerous geochemical studies have then led to the concept of mantle-endmember compositions, originally introduced by White (1985) and detailly defined by Zindler and Hart (1986), the generally accepted mantle-endmembers include HIMU (High-μ, $\mu = {}^{238}U/{}^{204}Pb$), EM-I and EM-I (Enriched Mantle-I and Enriched Mantle-II) and DMM (Depleted MORB Mantle). While there are still several uncertainties among the heritage and nature of the compositionally distinct geochemical reservoirs, it is clear that the rather extreme compositions found within OIBs require intensive chemical differentiation that includes depletion throughout partial melting as well as a re-enrichment of the mantle by crustal recycling within subduction zones (e.g., Hofmann, 2003).

For example, the composition of enriched mantle (EM-type) OIBs argues for a re-enrichment of a mantle source throughout the recycling of continental crustal material (Hawkesworth et al., 1979; Hofmann, 2003). While radiogenic isotope and related trace-element compositions can be explained throughout the recycling of solely continental sediments (Hawkesworth et al., 1979), alternative models also allow for admixtures of subducted oceanic crust and continental sediments to explain the observed compositional spectrum (e.g., White and Hofmann, 1982). In contrast, the radiogenic Pb- and Sr- isotope composition of the HIMU-type mantle endmember requires a source with substantially elevated U/Pb- and Th/Pb at extremely low Rb/Sr ratios (Fig. III.4). As such, the HIMU-type mantle has been inferred to represent subducted oceanic crust that has lost alkali elements and Pb during subduction modification (e.g., White and Hofmann, 1982; White, 1985; Chauvel et al., 1992).

A fifth component, originally termed PREMA (Prevalent Mantle) (Zindler and Hart, 1986), is thought to represent a rather primitive mantle component and lies within the focal zone of all mantle endmembers in isotope variation diagrams (Fig. III.4, 5). However, during the last decades, this mantle component has been subjected to ongoing discussions among its origin and composition. As such, several alternative compositional ranges and acronyms have been proposed and include FOZO (Focal Zone) (Hart et al., 1992), the C-Component (Common Component) (Hanan and Graham, 1996) and PHEM (Primitive Helium Mantle) (Farley et al., 1992). In contrast to EM-, HIMU and DMM- type mantle, the origin of this fifth component, is more complicated. Considering that the inferred composition represents the focal zone from which all other mantle endmembers radiate and form individual mixing arrays in isotope variation diagrams (Fig. III.4. 5), Hart et al. (1992) have suggested the FOZO-component to represent a source that is located within the Earths lower-mantle and that was progressively

mixed with other mantle endmembers (Fig. III.5). The unique nature of this source has been further underlined throughout high $^{3}He/^{4}He$ ratios found in OIBs with FOZO-C-PREMA-PHEM affinity (Farley et al., 1992; Hart et al., 1992). The application of primordial ^{3}He as an additional tracer of mantle heterogeneity has thus led to the identification of material that has significantly higher $^{3}He/^{4}He$ ratios compared to MORB (~8 R/R_A, where R/R_A is the ratio of the sample compared to the atmosphere), as originally introduced by Lupton and Craig (1975) and Craig and Lupton (1981). As such, it has been suggested by Farley et al. (1992) that this reservoir represents a primordial component that remained compositionally rather primitive and un-degassed for most of the 4.57 Ga duration of Earth's geological history. While it has been outlined by Hart et al. (1992) that inferred radiogenic Sr and Nd isotope compositions of FOZO are clearly not primitive but rather depleted, the presence of $^{3}He/^{4}He$ ratios is still taken as strong evidence for the participation of a less degassed and therefore potentially ancient mantle source.

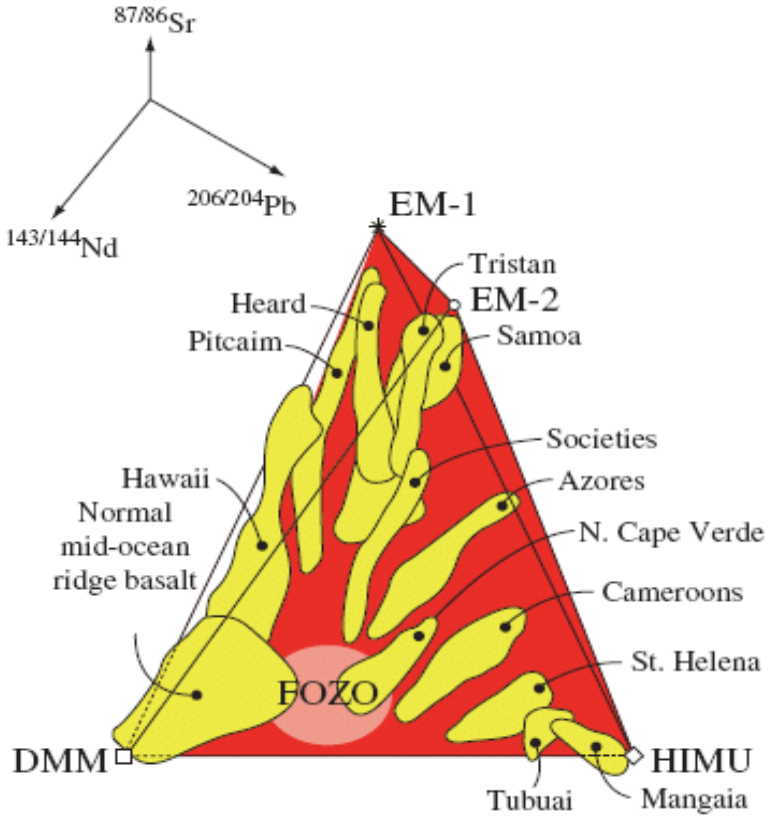

Figure III.5 Three-dimensional projection of $^{87}Sr/^{86}Sr$, $^{143}Nd/^{144}Nd$, $^{206}Pb/^{204}Pb$ isotope arrays of a large number of OIB groups (Hofmann, 2003 after Hart et al., 1992). The diagram clearly illustrates that individual OIB settings display discrete compositional ranges and can thus be grouped to distinct mantle endmember compositions. As most of the individual arrays appear to radiate from a common region labeled 'FOZO', the three-dimensional projection underlines the model of 'FOZO' representing the potential composition of the deep mantle that represents a common endmember of all OIBs.

Short-lived isotope systematics in modern Ocean Island Basalts

Considering pioneering work on the distinct mantle sources contributing to OIB volcanism (e.g., Hedge and Walthall, 1963; Gast et al., 1964; Tatsumoto et al., 1965; Hart, 1971; White and Hofmann, 1982; Hofmann et al., 1986; Hart et al., 1992; Hofmann, 1997; Stracke et al., 2005), the participation of an ancient, primordial reservoir remains enigmatic. This is mainly because traditional long-lived radiogenic isotope systems remained functionally inactive during the first million years of solar system history. Recently, scientific advances have added short-lived isotope systems such as ^{182}Hf-^{182}W (half-life = 8.9 million years) (Vockenhuber et al., 2004), ^{146}Sm-^{142}Nd (half-life = 103 million years) (Friedmann et al., 1966) and ^{129}I-^{129}Xe (half-life = 15.7 million years) (Kondev and Naimi, 2017) as tracers of Archean differentiation. The term "short-lived" thereby indicates that anomalies of those systems were generated only during the lifetime of the respective parent nuclides. In the case of the ^{182}Hf-^{182}W decay system, this implies that radiogenic ^{182}W anomalies could only be produced during the effective lifetime of ^{182}Hf, i.e. within the first 60 Ma after solar system formation (Vockenhuber et al., 2004).

^{182}W isotope compositions of mantle derived rocks – origin and implications

The ^{182}Hf-^{182}W system is a perfect tracer of metal-silicate segregation, since W is moderately siderophile and Hf is highly lithophile (Vockenhuber et al., 2004). The formation of the Earth's core has, thus led to the creation of a silicate mantle with a high Hf/W and a core with a low Hf/W ratio (Touboul et al., 2012) (Fig. III.6). Given that ^{182}W systematics have indicated core formation to be ceased >34 Ma after solar-system formation (e.g., Kleine et al., 2004; König et al., 2011) the silicate portion of the Earth has thus developed a high ^{182}W/^{184}W ratio due to the radioactive decay of ^{182}Hf to ^{182}W within the first ~60 Ma of solar system history, while the Earth's core has preserved a low ^{182}W/^{184}W ratio (Fig. III.6). Given that variations of ^{182}W/^{184}W are relatively small, tungsten isotope compositions are reported in the "μ" notation as μ^{182}W, which is the ppm deviation of a sample relative to a terrestrial standard.

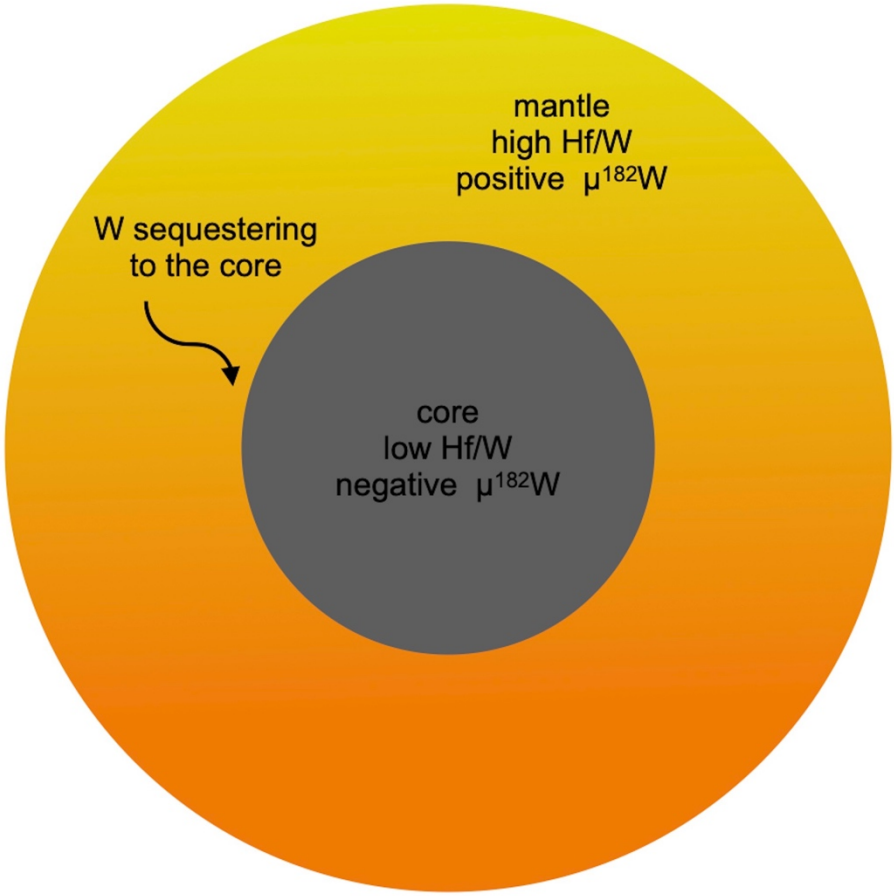

Figure III.6: Sketch illustrating the Earth after core formation. Due to the contrasting geochemical behavior of Hf being lithophile and W being highly siderophile core formation will lead to the preferential sequestration of tungsten into the core. Complementarily, the Earth's mantle has developed a high Hf/W ratio that will lead to the creation of positive ^{182}W anomalies – if core formation occurred during the lifetime of ^{182}Hf, while the Earth's core will preserve a low Hf/W ratio as well as negative ^{182}W anomalies (e.g., Touboul et a., 2012).

The first studies investigating radiogenic W isotope systematics therefore largely focused on the timing of core formation (Kleine et al., 2002; Schoenberg et al., 2002). Interestingly, small ^{182}W anomalies have been reported for Archean rock successions (e.g., Iizuka et al., 2010; Moynier et al., 2010; Willbold et al., 2011; Touboul et al., 2012; Rizo et al., 2016a; Tusch et al., 2019; Tusch et al., 2021b). High precision measurements of these rocks have indicated a +5 to +15 ppm ^{182}W excess compared to the Earths modern mantle (e.g., Willbold et al., 2011; Touboul et al., 2012; Willbold et al., 2015; Tusch et al., 2019). This is surprising, given that the earth accreted material with chondritic bulk compositions during the "late-veneer" (Chou, 1978), after core formation had ceased (e.g., Kimura et al., 1974; Walker et al., 2009). The addition of ~0.5 wt.% of this material, which has a ^{182}W/^{184}W ratio that ~200 ppm lower than the Earth's modern mantle, would have lowered the ^{182}W/^{184}W composition of the Earth by

about 10 to 20 ppm (e.g., Willbold et al., 2011; Touboul et al., 2012). While it has already been inferred from HSE abundances in Archean rocks (Maier et al., 2009) that some portions of the mantle retained a pre-late-veneer composition during the early Archean, several models thus as well suggested the ^{182}W excesses in Archean rocks to result from a mantle source that did not completely equilibrate with the material the Earth received during late accretion, i.e. the late veneer (e.g., Willbold et al., 2011; Archer et al., 2019; Tusch et al., 2019) (Fig. III.7). However, in the case of incomplete homogenization of the mantle after the late veneer or a generally sluggish late veneer addition, some portions of pre-late veneer mantle might have been preserved and were available for partial melting occurring at a later stage (e.g., Willbold et al., 2011; Archer et al., 2019; Tusch et al., 2019) (Fig. III.7). Alternatively, since W is more incompatible in most silicate minerals than Hf, variations of Hf/W ratios within the mantle might result from early crystal-liquid fractionation while ^{182}Hf was still extant (Touboul et al., 2012). A study by Touboul et al. (2012) has proposed that metal-silicate partitioning in a lower mantle magma ocean as well as silicate crystal-liquid partitioning in a whole magma ocean, taking place during the first ~30 Ma, can create isotopically enriched and depleted domains. In detail, a geochemical model by Touboul et al. (2012) demonstrated the possibility of a partially molten zone in which a silicate melt was in equilibrium with a metal phase. While this can either be a basal magma ocean interacting with the core, or alternatively accreted metal from the late-veneer that is passing through a (basal) magma ocean on the way to the core, creating reservoirs with different Hf/W ratios (Touboul et al., 2012). Alternatively, Touboul et al. (2012) have suggested crystal-liquid fractionation within a global magma ocean (Fig. III.8). Due to the distinct geochemical behaviour and compatibilities of Hf and W during these processes, extensive fractionation of Hf from W would occur, creating reservoirs with complementary ^{182}W isotope compositions (Touboul et al., 2012). As partial melting and fractional crystallization are responsible for the fractionation of Hf and W, it is important to consider the mineral phases involved during these processes. In the upper mantle, early occurring fractional crystallization is largely controlled by clinopyroxene and garnet that both preferentially incorporate Hf relative to W (Righter, 2003; Righter and Shearer, 2003). In contrast, within the lower mantle Mg- and Ca-perovskite are the major controlling mineral phases (Touboul et al., 2012). While partition coefficients have not been experimentally determined, estimated partition coefficients have indicated that Hf is more compatible than tungsten in Ca-perovskite (Corgne et al., 2003; Corgne et al., 2005 ; Puchtel et al., 2016; Rizo et al., 2016a). Early terrestrial fractionation within the perovskite stability field, could have

thus lead to the formation of an early enriched reservoir (EER) and an early depleted reservoir (EDR) (e.g. Touboul et al., 2012; Puchtel et al., 2016; Peters et al., 2018) (Fig. III.8). As such, if silicate differentiation processes occurred during the lifetime of ^{182}Hf (during the first ~60 Ma of solar system history), an EER would have preserved low Hf/W ratios, and develop an un-radiogenic ^{182}W isotope composition over time, while the complementary EDR would exhibit higher Hf/W ratio and consequently evolve to strongly radiogenic ^{182}W isotope composition. If preserved, such reservoirs might thus provide viable source reservoirs for volcanism occurring at a later stage, containing signatures of early silicate differentiation. Further evidence for this scenario has come from the finding of negative ^{182}W anomalies within Komatiites from the Schapenburg Greenstone Belt (Puchtel et al., 2016). Deficits as low as -9 ppm compared to the modern mantle were explained to trace differentiated domains that remained isolated until at least 3.55 Ga (Puchtel et al., 2016; Tusch et al., 2021a).

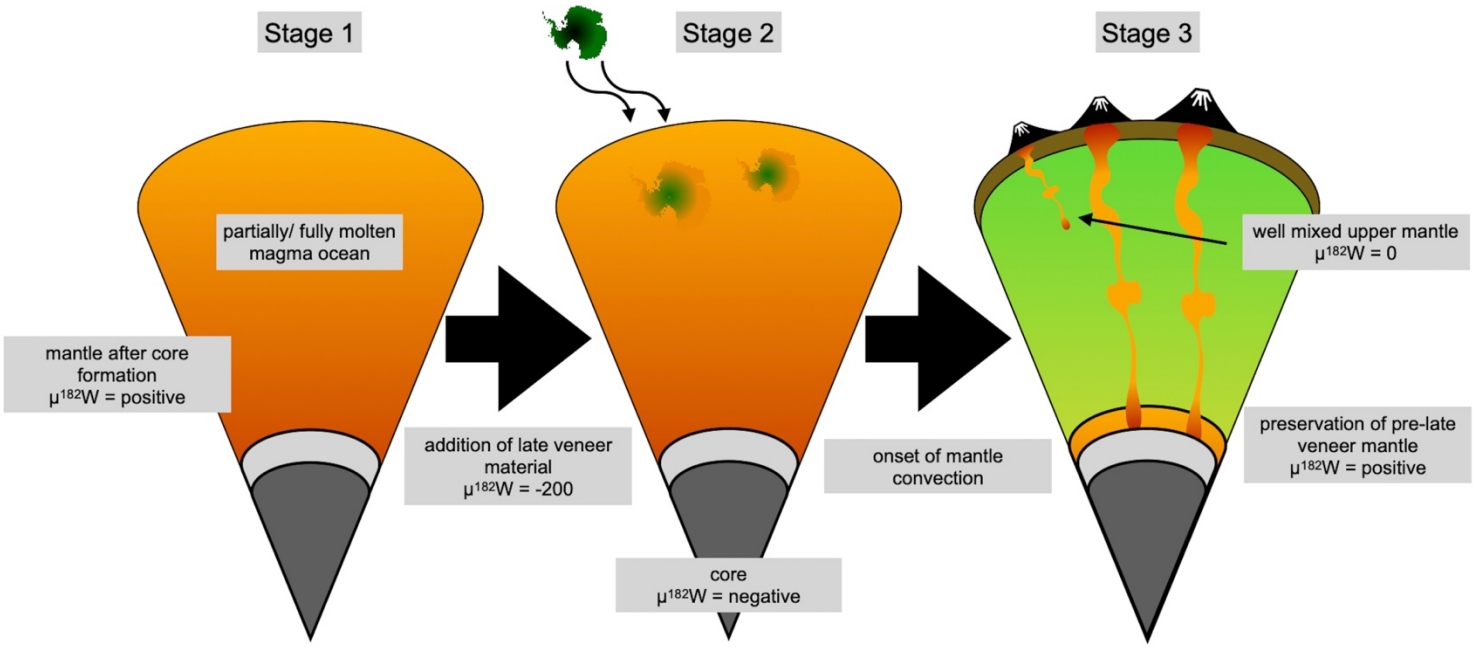

Figure III.7: Formation of ^{182}W anomalies in the mantle due to the sluggish in-mixing of late veneer material (after Willbold et al. 2011, 2015). Stage 1: After core formation the Earth's mantle exhibits a high Hf/W ratio and is therefore subjected to the radiogenic ingrowth of ^{182}W due to the radioactive decay of ^{182}Hf. Stage 2: The addition of late veneer material will subsequently lower the ^{182}W composition of the Earth's mantle. Stage 3: The onset of mantle convection leads to the homogenization of the mantle. However, if homogenization is sluggish, some portions of the pre-late-veneer mantle might be preserved and accessible for partial melting.

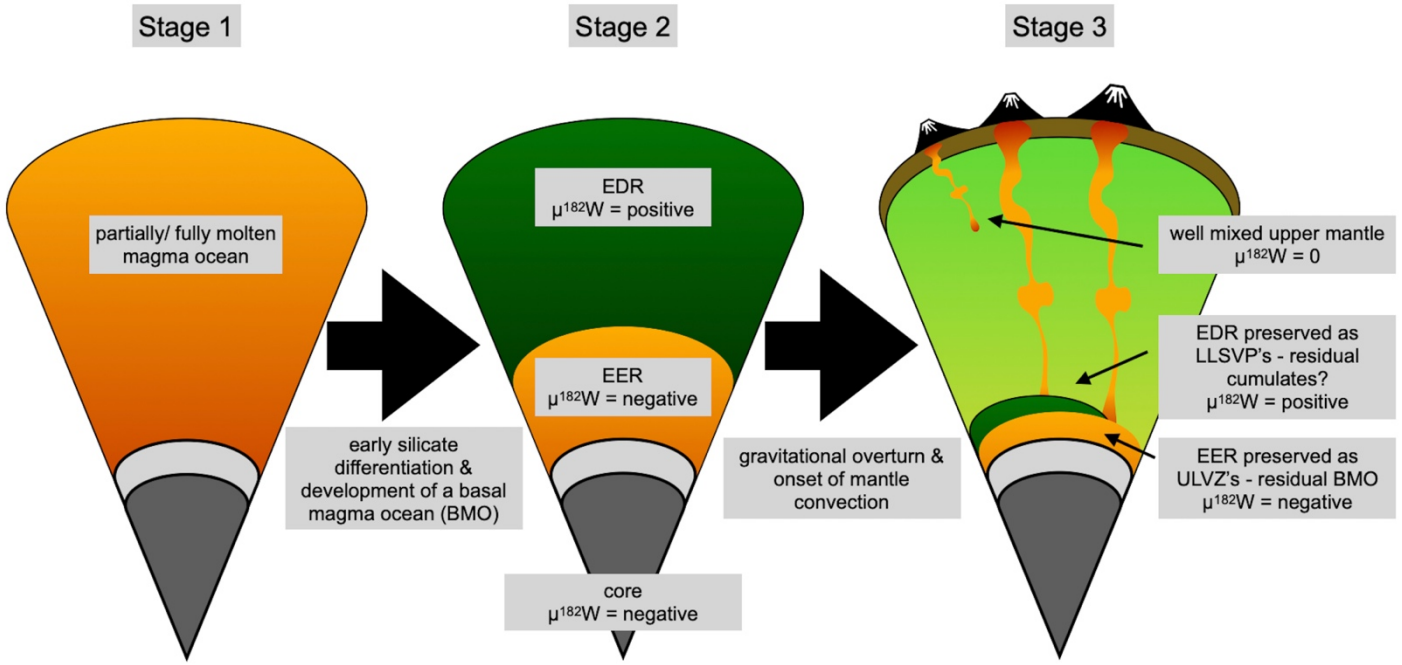

Figure III.8 The formation of ^{182}W anomalies through differentiation events, after core formation (after Touboul et al., 2012). Stage 1: After core formation, early silicate differentiation in a partially or fully molten magma formation leads to the formation of a Early Enriched Reservoir (EER) – a residual basal magma ocean that preferentially incorporated W and thus developed a negative ^{182}W isotope composition (Stage 2). In contrast, early formed cumulates preferentially incorporate Hf and form a Early Depleted Reservoir (EDR) where ^{182}Hf decay leads to positive ^{182}W anomalies (Stage 2). Stage 3: Gravitational overturn and the onset of mantle convection lead to homogenization. However, a residual Basal Magma Ocean might be preserved as ULVZs and early formed cumulates as LLVPs. Depending on how long these reservoirs survive mantle convection, later occurring partial melting and incorporation into rising mantle plumes might explain the occurrence of ^{182}W anomalies in Archean as well as modern volcanic rock

^{182}W anomalies in modern ocean island basalts – indications for long-term isolation

Most recently, ^{182}W isotope composition measurements were also applied to modern OIBs. Among the pioneering studies that investigated W isotope systematics, Willbold et al. (2011) presented the first data on plume related basalts from Iceland, La Palma and the Azores. The ^{182}W/^{184}W composition of these rocks were measured with analytical uncertainties in the range of ±10-15 ppm and were found to be undistinguishable from the modern upper mantle value (Willbold et al., 2011; Touboul et al., 2012). However, recent improvements in analytical techniques have pushed the precision of these measurements below the ±5 ppm level, thus enabling statistically resolvable, high precision measurements (Mundl et al., 2017; Mundl-Petermeier et al., 2019; Rizo et al., 2019; Tusch et al., 2019; Jackson et al., 2020b; Mundl-Petermeier et al., 2020; Peters et al., 2021; Tusch et al., 2021b; Mundl-Petermeier et al., 2022; Tusch et al., 2022). Until today, extensive measurements of modern OIBs revealed ^{182}W deficits as low as μ^{182}W = -22.7 ± 3.3 ppm (Mundl et al., 2017; Mundl-Petermeier et al., 2019; Rizo et al., 2019; Mundl-Petermeier et al., 2020; Peters et al., 2021). Since the ^{182}H-^{182}W system became functionally extinct after the first million years of solar system history, the presence of ^{182}W anomalies imply that early formed mantle reservoirs were able to survive mantle convection for as long as 4.57 Ga (Rizo et al., 2016b; Mundl et al., 2017; Mundl-Petermeier et al., 2019; Rizo et al., 2019; Mundl-Petermeier et al., 2020; Peters et al., 2021; Jansen et al., 2022). Interestingly, for Archean Cratons, positive as well as negative ^{182}W anomalies were reported (Iizuka et al., 2010; Willbold et al., 2011; Touboul et al., 2012; Willbold et al., 2015; Puchtel et al., 2016; Rizo et al., 2016a; Reimink et al., 2018; Archer et al., 2019; Tusch et al., 2019; Reimink et al., 2020; Tusch et al., 2021a; Tusch et al., 2021b; Mundl-Petermeier et al., 2022), whereas modern OIB are characterized by ^{182}W deficits (Mundl et al., 2017; Peters et al., 2018; Mundl-Petermeier et al., 2019; Rizo et al., 2019; Mundl-Petermeier et al., 2020; Peters et al., 2021). Positive μ^{182}W anomalies up to +50 ppm were only reported for the Ontong-Java-Plateau and the North Atlantic Igneous Province (Rizo et al., 2016b). However, more recent studies in which stratigraphically related rocks were re-investigated did not find such elevated ^{182}W signatures (Kruijer and Kleine, 2018; Mundl-Petermeier et al., 2019). While, occurrence of ^{182}W excesses in modern volcanic rocks remains ambiguous, these studies have clearly shown the importance of carefully monitoring the elemental W budget of samples prior to ^{182}W isotope analysis. In silicate system, W is one of the most incompatible elements, similar to U and Th. Thus, due to the siderophile and fluid mobile behavior of W, elemental ratios of

W and lithophile elements like U and Th provide important insights on the behavior of W in modern igneous reservoirs (e.g., König et al., 2008; König et al., 2011). Detailed investigations by König et al., (2008, 2011) and Reifenröther et al., (2020, 2021) have shown that W/Th and U/W ratios in MORB and OIB are solely controlled by crystal-liquid fractionation in silicate systems, whereas Arc lavas and altered samples display substantially elevated ratios due to the secondary re-distribution of W in fluid mediated environments. While it has already been shown by Tusch et al., (2019, 2021) that ^{182}W in Archean rocks can been obscured by a metasomatic overprint, Mundl-Petermeier et al., (2019) suggested a similar origin for the positive ^{182}W anomalies reported by Rizo et al., (2016a) for modern volcanic rocks.

However, the finding of negative ^{182}W anomalies in modern OIB are consistent with long-lived isotope systems, and therefore raise the question among the survival of reservoirs formed by early silicate differentiation (e.g., Mundl et al., 2017; Peters et al., 2018; Peters et al., 2021). Alternatively, given that modern OIB solely display deficient ^{182}W isotope compositions, several models have as well suggested the preservation of a basal magma ocean that equilibrated with the W-rich core or formed by continuous core-mantle interaction at any time in Earth's history (Mundl-Petermeier et al., 2019; Rizo et al., 2019; Mundl-Petermeier et al., 2020) (Fig. III.9). Further, detailed investigations have shown ^{182}W compositions to be negatively correlated with $^{3}He/^{4}He$ ratios that suggest the potentially primordial reservoir to be less degassed compared to the ambient mantle (e.g., Mundl et al., 2017; Mundl-Petermeier et al., 2019; Mundl-Petermeier et al., 2020; Jackson et al., 2020). While these findings provide strong indications for the survival of early-formed mantle domains, a recent study by Jackson et al., (2020) has shown that primordial signatures are subsequently overprinted throughout the addition of recycled, younger crustal materials. Introducing the $D^{Sr\text{-}Nd\text{-}Pb}$ value, that integrates Sr-Nd-Pb isotope signatures and describes the compositional range of OIB samples, Jackson et al., (2020) have shown primordial signatures to be limited to mantle domains least affected by crustal contamination.

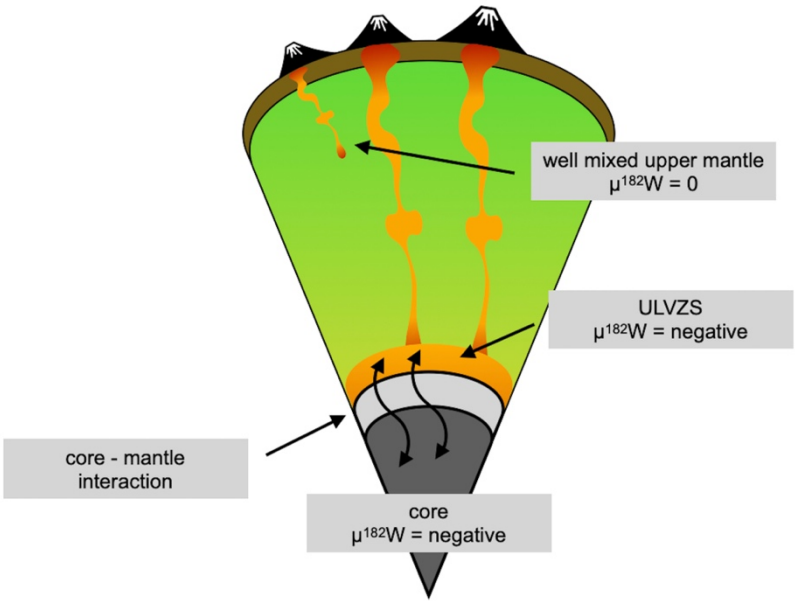

Figure III.9 Sketch illustrating the potential of core mantle interaction (after Rizo et al., 2019 and Mundl-Petermeier et al., 2020). As the Earth's core preserves a negative ^{182}W isotope composition, any interaction between the core and the lower mantle provide a viable explanation of the finding of negative ^{182}W anomalies in modern OIB. Core-mantle interaction can thereby occur early- or at any time in Earth's history. Given the unique seismic properties of Ultra Low Velocity Zones (ULVZs) that have been reported to be present at the core-mantle boundary (e.g., French and Romanowizc, 2015), these zones provide a viable reservoir to contain material that has interacted with the core (e.g., Mundl et al.,2017).

Further insights on the potential preservation of ancient, long-term isolated mantle reservoirs came from seismic investigations (Montelli et al., 2004; Montelli et al., 2006; French and Romanowicz, 2015). Earth's modern hotspots have shown to be sourced by broad, quasi-vertical conduits that extend throughout the whole-mantle and are rooted at the core-mantle boundary (Montelli et al., 2004; Montelli et al., 2006; French and Romanowicz, 2015). Furthermore, in the lowermost mantle, these conduits are rooted in zones of reduced shear-wave velocity (French and Romanowizc, 2015). Detailed seismic investigations have mapped out two low-seismic velocity patches underneath Africa and Pacific that exhibit spatial scales of 100-1000km in width and height (French and Romanowizc, 2015; McNamara, 2019) and have been termed large-low-shear-velocity provinces (LLSVPs) (Fig. III.10, 11). Furthermore, at the core–mantle boundary, LLSVPs are underlain by smaller patches that display seismic evidence of even greater reduced shear-wave velocity, termed ultra-low-velocity zones (ULVZs) (French and Romanowizc, 2015; McNamara, 2019). While only little is known about the nature and heritage of the zones, their seismic properties have important implications on the nature of global mantle dynamics and the understanding of mantle evolution through time (McNamara, 2019) (Fig. III.11). Based on their seismic properties Trampert et al. (2004) have

converted tomographic data into probability density functions for temperature, perovskite and iron variations that are indicative of chemical heterogeneity within the lower 1000 km of the mantle. Given that several billions of years of isolation require an excess density and a more viscous rheology than the surrounding mantle (Christensen and Hofmann, 1994; Kellogg et al., 1999; Tackley, 2002; Davies et al., 2012), several studies reporting ^{182}W deficits and $^{3}He/^{4}He$ ratios, have as such favoured LLSVPs and ULZVs as potential hosts of primordial material (e.g., Mundl et al., 2017 and references therein). However, while the exact geochemical composition and heritage of these zones remains largely unconstrained, it was suggested that LLSVPs could represent: 1) potential remnants of a basal magma ocean (Labrosse et al., 2007; Brown et al., 2013), 2) accumulated subducted crust (Christensen and Hofmann, 1994), 3) dense silicate melts (Lee et al., 2010), or 4) mantle lithosphere (Coltice and Ricard, 1999). In contrast, ULVZs have even sharper seismic boundaries that were attributed to the presence of dense, iron-rich silicate melts (Rost et al., 2006; Wicks et al., 2010). Conclusively, the combination of geochemical, seismic data and modelling constraints provide several lines of evidence for these zones to play a key role in search of a host for primordial mantle reservoirs that remained isolated throughout most of Earth's history.

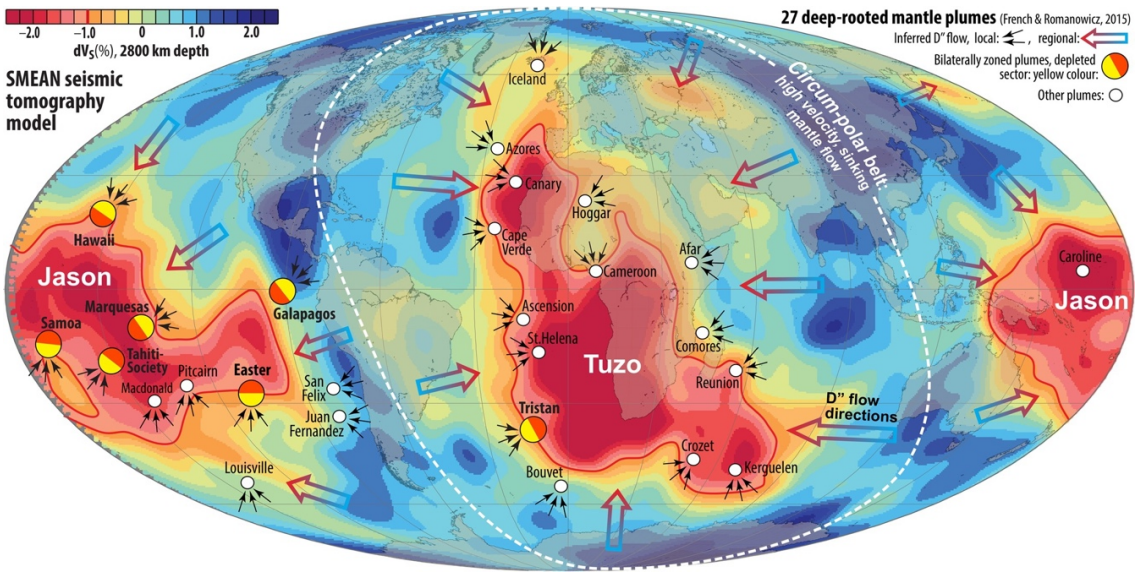

Figure III.10 Tomographic model map of Torsvik et al., (2016), showing the SMEAN seismic tomography model at 2800 km depth, and the two Large Low Shear Velocity Provinces (LLSVPs). The white line refers to high velocity circumpolar belt that is presumably the location of descending flow of cold mantle (e.g., subducted slabs). Circles refer to the deep mantle plumes as suggested in French and Romanowicz (2015).

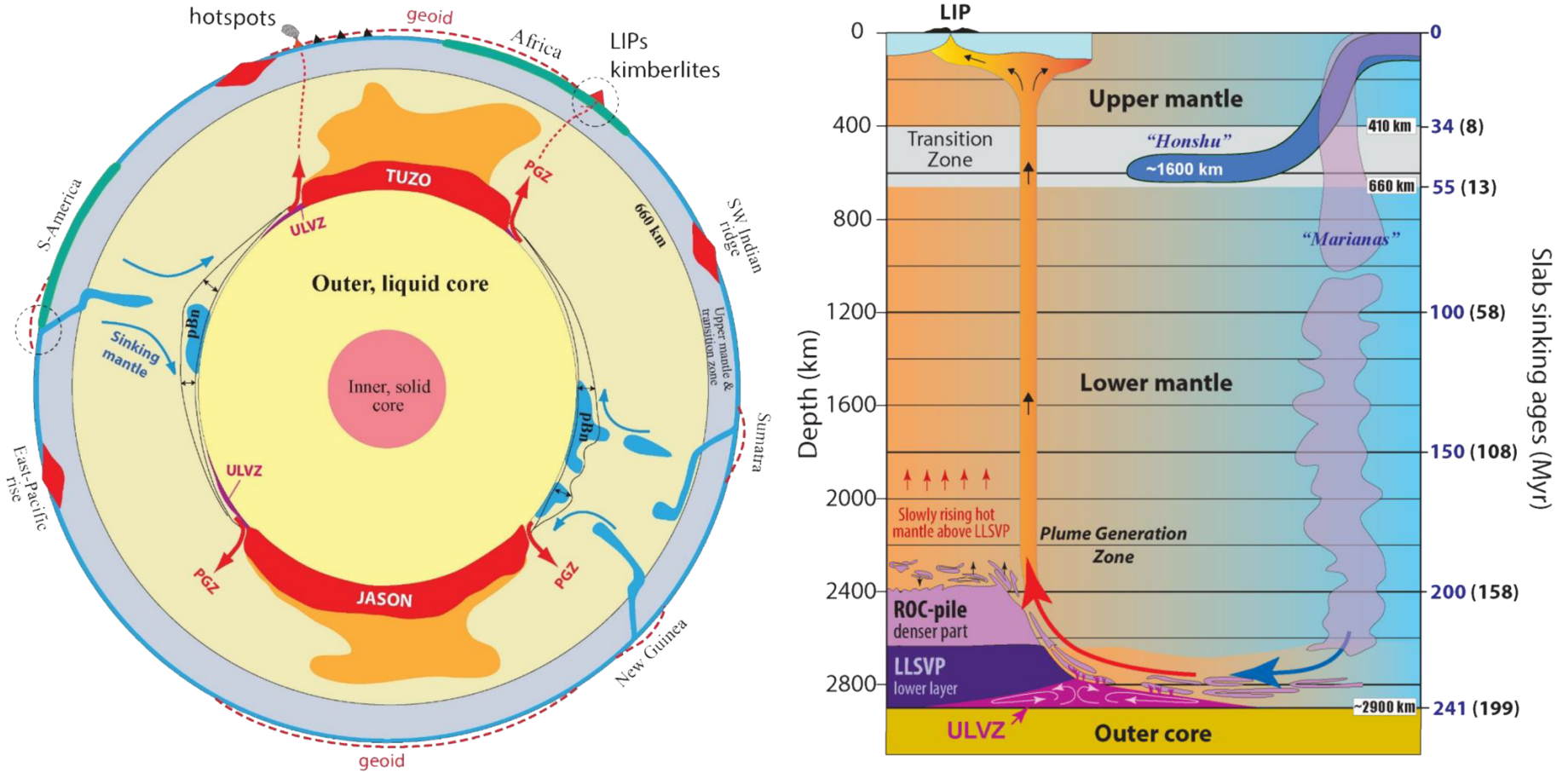

Figure III.11 Lower mantle dynamics as inferred by Kevin C. A. Burke. The Earth is thereby degree-2 planet with two stable antipodal thermo-chemical piles in the lowermost mantle (large low-shear velocity provinces: LLSVPs) that are underlain by ultra-low-velocity zones (ULVZs). Earths modern hotspots are sourced in "plume-generation-zones" (PGZ) and lower-mantle dynamics are governed by sinking slabs and rising mantle plumes. (Picture taken from https://commons.wikimedia.org/wiki/File:Burkian_Earth.png).

IV. Overview

This Thesis provides new insights into the heterogenous nature of Earth's modern mantle. In three Chapters, we report high-precision ^{182}W, $^{87}Sr/^{86}Sr$, $^{143}Nd/^{144}Nd$, $^{176}Hf/^{177}Hf$, $^{206, 207, 208}Pb/^{204}Pb$ and $^{187}Os/^{188}Os$ isotope composition data on volcanic rocks sourced that originate from various tectono-magmatic settings.

The first chapter (**chapter I**) provides further constraints on the potential contribution of long-term isolated mantle reservoirs to modern volcanic settings. While previous studies have largely focused on oceanic intraplate settings where seismic data has indicated a clearly resolvable plume structure rooted at the core mantle boundary (e.g., Mundl et a., 2017; Mundl-Petermeier et ., 2019; Rizo et al., 2019; Mundl-Petermeier et al., 2020; Jackson et al., 2020), we have analyzed samples from intraplate volcanic settings that are compositionally similar to OIBs but lack a seismically resolvable plume source (Ascension Island, Massif Central, Siebengebirge and Eifel) and intraplate volcanic rocks associated with either plume or subduction zone environments (Italian Magmatic Provinces). Further, these data are compared to settings where seismic data have indicated a deep mantle plume origin (La Réunion and Baffin Island). Analyzing volcanic rocks of a questionable lower-mantle origin, our data provide important constraints on the potential participation of primordial mantle reservoirs to upper-mantle sourced volcanism.

In **Chapter II**, a comprehensive ^{182}W dataset on the Tristan-Gough-, Discovery- and Shona-hotspot tracks is presented. Although these settings are located within hundreds of kilometers in distance to each other, geochemical, seismic and modelling constraints revealed that these settings derive from/share a common mantle source (e.g., Geldmacher et al., 2011; Rohde et al., 2013; Hoernle et al., 2015; Hoernle et al., 2016; Schwindrofska et al., 2016; Homrighausen et al., 2018; Homrighausen et al., 2019; Homrighausen et al., 2020; Zhou et al., 2020). A previous study by Mundl-Petermeier et al. (2020) has already published ^{182}W data on Tristan da Cunha and the Discovery Ridge, indicating that primordial reservoirs contribute to South Atlantic Volcanism. However, while previous studies have investigated the ^{182}W isotope composition of numerous modern ocean island- as well as continental intraplate basalts (e.g., Mundl et al., 2017; Rizo et al., 2019; Mundl-Petermeier et al., 2020; Peters et al., 2021), detailed investigations on single hot-spot tracks with temporally changing magma sources are

scarce and thus far have only been conducted for the Iceland plume (Mundl-Petermeier et al., 2019). As such, this study provides temporal and spatial information on the variability of primordial reservoir contribution within a single hot-spot track.

In **chapter III**, the first comprehensive long-lived radiogenic isotope dataset on quaternary Eifel volcanism is presented. The Eifel Volcanic Field belongs to the Central European Volcanic Provinces, where volcanism has initiated in the Tertiary and which has been extensively studied during the last decades (e.g., Wörner et al., 1986; Fekiacova et al., 2007; Schmincke, 2007; Schneider et al., 2016; Mayer et al., 2018). However, high precision geochemical data on Quaternary rocks is still scarce. While volcanism is located on the European continental lithosphere, available trace-element and long-lived radiogenic isotope compositions resemble those of classical OIBs (e.g., Wörner et al., 1986; Fekiacova et al., 2007). Therefore, it has been suggested that Central European volcanism might be sourced by a deep-rooted mantle plume (e.g., Goes et al., 1999). However, seismic data that has been collected for the European realm rather indicates the presence of several small-scale "plumelets" rooted in the upper mantle (Ritter et al., 2001). The new radiogenic isotope and trace-element data obtained in this study thus provides further important constraints on the nature and heritage of mantle sources involved in magma generation within the Cenozoic European Province

Chapter I: Upper mantle control on the W isotope record of shallow level plume and intraplate volcanic settings

Introduction

Tungsten isotope measurements of Archean rocks (e.g., Willbold et al., 2011; Puchtel et al., 2016; Rizo et al., 2016; Tusch et al., 2019, 2021a, 2021b) and modern plume-derived basalts (e.g., Willbold et al., 2011; Rizo et al., 2016; Mundl et al., 2017; Mundl-Petermeier et al., 2019, 2020) have revealed heterogeneities in the relative abundance of ^{182}W, the radiogenic nuclide of short-lived ^{182}Hf with a half-life of ~9 Ma (Vockenhuber et al., 2004). The presence of ^{182}W anomalies in modern basalts requires the preservation of old mantle domains that either formed by early crystal-liquid fractionation within the silicate Earth (Touboul et al., 2012; Tusch et al., 2021a) or did not fully equilibrate with material the Earth received during its late accretion (e.g., Willbold et al., 2011; Tusch et al., 2021b). Both theories are consistent with observations from other short-lived decay series, such as ^{146}Sm-^{142}Nd or ^{129}I-^{129}Xe that indicate early crystal-liquid fractionation within the silicate Earth (Carlson and Boyet, 2008; Peters et al., 2018) and the survival of primordial, relatively undegassed domains deep in the mantle (e.g., Mukhopadhyay, 2012).

In contrast to most Archean rocks, modern intraplate basalt provinces display deficits in ^{182}W (e.g., Mundl et al., 2017; Mundl-Petermeier et al., 2019, 2020). Positive ^{182}W isotope compositions in modern rocks have so far only been reported for basalts from the proto-Iceland plume and the Ontong-Java-Plateau (Rizo et al., 2016). ^{182}W deficits in modern ocean island basalts (OIBs) are consistent with the preservation of a residual basal magma ocean domain that equilibrated with the core (e.g., Mundl-Petermeier et al., 2019, 2020), or the presence of mantle reservoirs formed by continuous core-mantle interaction (e.g., Rizo et al., 2019 and references therein). Seismic constraints reveal a spatial association between mantle plumes and zones of reduced shear-velocity, termed Large Low Shear Velocity Provinces (LLSVPs) and Ultra Low Velocity Zones (ULVZs) (French and Romanowicz, 2015). These zones are possibly home to long-term isolated, primordial domains at the core-mantle boundary

(e.g., French and Romanowicz, 2015; Rizo et al., 2016; Mundl et al., 2017; Mundl-Petermeier et al., 2020, 2019).

Previous W isotope studies have primarily focused on OIBs that likely originated from deep-rooted mantle plumes, as revealed by shear-wave velocity models (e.g., French and Romanowicz, 2015). These groups of "continuous plumes", which extend throughout the whole mantle, are the most promising source of deep mantle that would record interaction with the core. Notably, only two samples of mid ocean ridge basalts (MORB) have been analyzed thus far (e.g., Mundl et al., 2017; Rizo et al., 2019). Therefore, the composition of the convecting upper mantle remains largely unknown.

Despite the assumption of whole mantle convection and mantle depletion as a consequence of crust formation, numerous studies on long-lived radiogenic isotope compositions have demonstrated that the upper mantle contains innumerable geochemical heterogeneities formed by crustal recycling (e.g., Hart et al., 1992; Regelous et al., 2009; Paulick et al., 2010). Early geochemical models suggested that the composition of some OIBs can be best explained by the presence of recycled enriched material in the lower mantle (Hart et al., 1992). However, this view was recently questioned by seismic evidence that found no detectable upwelling of lower mantle material at plume-related settings that are characterized by OIBs with an enriched composition (e.g., French and Romanowicz, 2015; Jackson et al., 2020). To resolve this ambiguity, upper mantle material, such as refertilized subcontinental lithospheric mantle (SCLM) (e.g., Lustrino and Wilson, 2007), recycled plume material (e.g., Hoernle et al., 1995) or delaminated, ancient crustal components were suggested as alternative sources for the enriched geochemical composition of some intraplate basalts (e.g., Regelous et al., 2009). However, the contributions of these different upper-mantle sources to the ^{182}W inventory of intraplate basalts are still poorly constrained. Currently, there are only ^{182}W data for two MORBs (Mundl et al., 2017; Rizo et al., 2019) and two contrasting datasets for kimberlites (Tappe et al., 2020; Nakanishi et al., 2021). Kimberlites may either record the composition of the upper mantle (Tappe et al., 2020) or of lower mantle reservoirs (Nakanishi et al., 2021). Thus, it is presently unknown if ^{182}W heterogeneities are also preserved in upper mantle domains or if they are exclusively present in lower mantle domains.

To better constrain the W isotope compositions of upper-mantle domains we have analyzed a comprehensive suite of continental- and oceanic intraplate basalts from a variety of tectono-magmatic settings. This group of samples comprises oceanic intraplate basalts from Ascension

Island as well as continental intraplate settings, including the European Cenozoic Volcanic Province (CEVP) (Eifel, Massif Central, Siebengebirge) and intraplate basalts from the Italian Magmatic Province (IMP) (Mt. Etna, Hyblean Plateau, Pantelleria). The intraplate basalts from the IMP are compared to volcanic rocks linked to a nearby subduction-zone environment (Stromboli, Vulture, Vesuvio). Our sample set is complemented by deep mantle plume-derived basalts that originate from the Piton des Neiges (PDN) and Piton de la Fournaise (PDF) volcanic edifices at La Réunion (Kurzweil et al., 2019) and high $^{3}He/^{4}He$ basalts from the proto-Iceland plume (PIP) from Baffin Island (Stuart et al., 2003; Starkey et al., 2009). To reconstruct the mantle sources involved and to explore the long-term preservation potential of upper mantle reservoirs, we combine new high precision W-Hf-Nd isotope-data and W-U-Th concentration data with previously published Sr-Nd-Pb-He and some new Hf-Nd isotope data.

Sample Material

For this study we have selected 46 samples, including basalts, basanites and melilitites (SiO_2 = 38.9 – 52.63 wt.%; MgO = 4.47 – 20.0 wt.%, Table A-1) from different geodynamic settings (Fig. 1.1). With the exception of samples from the Eifel, Massif Central, and the Hyblean Plateau, all samples have been subject to detailed geochemical investigation. For sources of additional data see Appendix I. If not already published, existing Hf-Nd isotope-data and W-U-Th concentration data have been complemented herein.

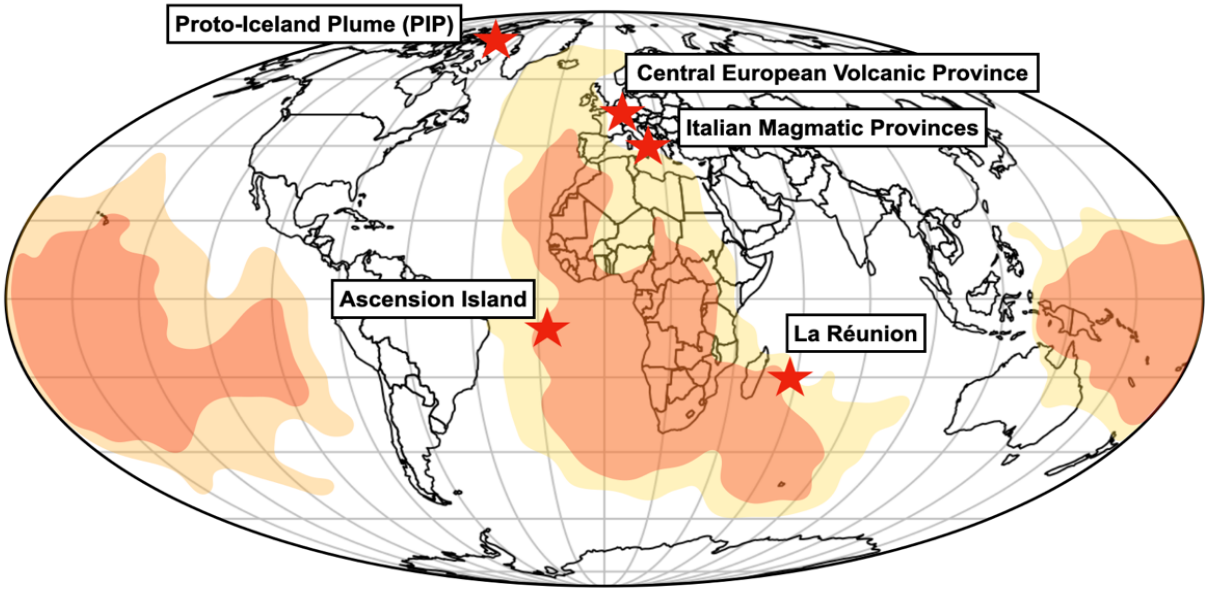

Figure 1.1 Location of the volcanic settings investigated. The background map is modified after French and Romanowicz (2015) and includes the inferred location of LLSVPs and ULVZs based on the whole-mantle-shear-wave volicity model SEMUCB-WM1. LLSVP boundaries are markred by yellow color shadings, center regions are marked in red.

Analytical methods

Isotope dilution and long-lived radiogenic isotope measurements

High-precision determinations of W, U, Th and Ta concentrations were performed by isotope dilution, together with $^{176}Hf/^{177}Hf$ and $^{143}Nd/^{144}Nd$ isotope measurements. While ^{182}W was analyzed for all samples, $^{176}Hf/^{177}Hf$ and $^{143}Nd/^{144}Nd$ have only been determined on samples where data were not available. Isotope dilution measurements for W, U, Th and Ta have only been conducted for samples where trace element measurements yielded concentrations ≤600 ng/g. For higher concentrations conventional quadrupole ICPMS data were used. A detailed description of the analytical procedure for the measurements of long-lived radiogenic isotopes as well as major and trace element concentrations can be found in Appendix I.

Tungsten isotope measurements

Tungsten was separated from bulk rock samples following the protocols described in Tusch et al. (2019, 2021a, 2021b), applying a four-column procedure employing cation, anion, TEVA and TODGA resins. Depending on the W concentration, up to 30 sample splits (1-1.2 g) were individually passed through the chemical separation procedure and recombined prior to the measurement. The approximate amount of sample material used to generate the measurements is reported in Table 2. Procedural yields for W were generally ≥70%. Total procedural W blanks were determined by isotope dilution (i.e. Kurzweil et al., 2018) and were usually below 300 pg, contributing less than 1% to the total analyte. High-precision W isotope composition measurements were performed using the Thermo-Fisher® Neptune Plus MC-ICP-MS at the University of Cologne, following the protocols given by Tusch et al. (2019, 2021a, 2021b). To assess the long-term reproducibility we always included one of our three in-house reference materials during each analytical session (historical La Palma Basalt "LP 1", Kurzweil et al. (2019) and a 3455 Ma old grey gneiss "AGC 351" from southwest Swaziland Kröner et al. (2014)). During the analytical campaign we also analyzed a 3.27 Ga old komatiite from the Pilbara Craton (sample 160245, Ruth Well Formation), Western Australia, that was shown to exhibit an excess in W of +6.8 ± 2.3 ppm (Tusch et al., 2021a, Tusch et al., 2021b). Final results are reported in the μ notation (ppm deviation relative to NIST SRM 3163). The intermediate precision of our in-house reference materials, given by the mean value of multiple session averages, is μ182W = −0.2 ± 1.0 ppm (AGC 351), −0.7 ± 1.2 ppm (LP 1) and 8.1 ± 1.3 ppm (160245), respectively (Fig. 1.2). It must be noted that some samples were measured during the early campaign of the Tusch et al. (2019) study and bear small nuclear field shift effects on ^{183}W (marked in Table 5). These effects were shown to became negligible after applying a modified dry-down protocol (cHNO_3 – 30% H_2O_2) (Tusch et al., 2019). However, nuclear field shift effects do not affect ^{182}W compositions that are mass bias corrected relative to ^{186}W/^{184}W (^{182}W (6/4)) and do not involve ^{183}W. This is demonstrated by our data for sample Ei 27, that involve both dry-down protocols and yield ^{182}W (6/4) isotope compositions that overlap within error (Appendix I, Table. 5). A more detailed description of analytical methods can be found in the supplementary material

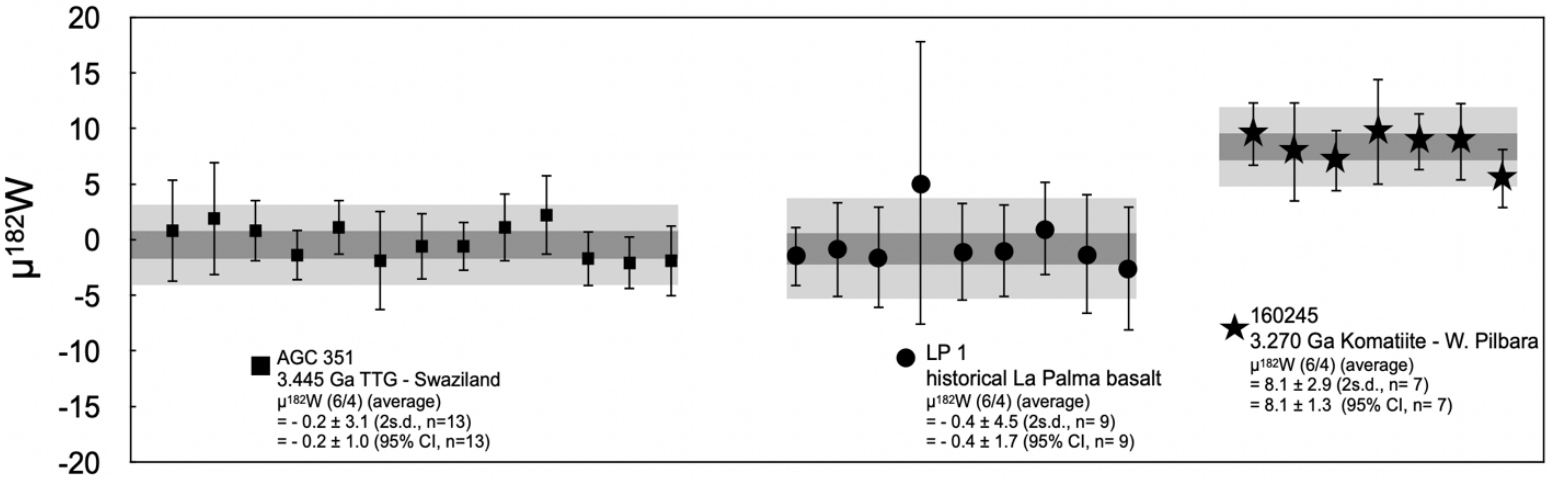

Figure 1.2 Intermediate precision for $\mu^{182}W$ (6/4). Values are inferred from the repeated analysis of multiple digestions for our in-house reference materials granite AGC 351, basalt LP 1 and komatiite 160245 that are reported relative to NIST SRM 3163. Each symbol refers to the average value of multiple measurements (up to n = 13) conducted during an analytical session. The uncertainties for the session mean values are given by the corresponding 95% c.i. The long-term intermediate precision (2 standard deviations) for our in-house reference materials are given by the 2 SD of the session mean values

Results

All data of this study are listed in Appendix I, Tables 1-5. Major and trace element compositions are reported in Appendix I, Table 2 and 3, $^{143}Nd/^{144}Nd$ and $^{176}Hf/^{177}Hf$ compositions are presented in Table 3. Values of εNd (−3.0 to +9.1) and εHf (−3.7 to +17.5, Table 4, Fig. 1.3) show a broad range of different mantle-reservoir compositions (Fig. 1.3) (e.g., Hofmann, 2003). Concentrations of W, U and Th are reported in Table 5. Tungsten concentrations range from 50 ng/g (DUR 7) to 6770 ng/g (VES 95). Most samples compositionally overlap the inferred W/Th and W/U of modern MORBs and OIBs (e.g., König et al., 2008, 2011) (Fig. 1.4) However, extremely elevated W/Th ratios were found in ASD 16 from Ascension Island (W/Th = 5.86) and DUR 1 from Baffin Island (W/Th = 16.5), which are further discussed below. The session averages for high-precision W isotope analysis together with their corresponding 95% CI are reported in Appendix I, Table 5. Our samples exhibit W values between −8.8 ± 4.1 ppm and +3.9 ± 4.0 ppm, within the range of previously reported ^{182}W compositions of MORBs and OIBs (Fig 1.6, e.g., Rizo et al., 2019; Mundl-Petermeier et al., 2019, 2020). Clearly resolvable negative W values are only found for the PDF volcanic edifice at La Réunion.

Discussion

Characterization of mantle domains using $^{143}Nd/^{144}Nd$ and $^{176}Hf/^{177}Hf$ compositions

Based on long-lived (e.g., Sr-Nd-Hf-Os), short-lived (e.g., ^{142}Nd, ^{182}W) radiogenic isotope and noble gas compositions (e.g., $^{3}He/^{4}He$), it has been suggested that intraplate volcanism taps an array of chemically distinct reservoirs in the mantle (e.g., Hofmann, 2003). This array is commonly characterized by different mantle endmembers displaying moderately radiogenic (PREMA, FOZO) or un-radiogenic $^{143}Nd/^{144}Nd$ and $^{177}Hf/^{176}Hf$ (EM I, EM II) as well as highly radiogenic Pb-isotope compositions (HIMU) (e.g., Hofmann, 2003 and references therein). The convecting upper mantle tapped by MORB has highly radiogenic $^{143}Nd/^{144}Nd$ and $^{177}Hf/^{176}Hf$ that likely represents the depleted residue after crust formation (e.g., Hofmann, 2003; Hart et al., 1992). Another component has been identified that shows distinctly higher $^{3}He/^{4}He$ ratios than average upper mantle components ($^{3}He/^{4}He$ = ∼8 R/R_A) (e.g., Hart

et al., 1992; Hofmann, 2003 and references therein). While earlier studies defined a common deep mantle endmember composition that resembles a less-degassed, primordial reservoir (FOZO) (e.g., Hart et al., 1992), the compositional spread of associated Sr-Nd-Hf-Pb isotope data questions the presence of such a distinct endmember (e.g., Starkey et al., 2009). This is further strengthened by recent studies of Mundl-Petermeier et al. (2020) and Jackson et al. (2020) who have identified different co-variations between $^{3}He/^{4}He$ ratios and ^{182}W isotope compositions in modern OIBs that indicate a variety of undegassed mantle endmember compositions. While it was long believed that recycled materials only contribute to deep-rooted plumes from the lower-mantle, recently published studies on intraplate volcanic rocks by Belay et al. (2019) and Guimarães et al. (2020) have invoked delaminated and refertilized SCLM materials as sources for OIB-like volcanism in places where a plume is difficult to resolve. This is broadly similar to models for the origin of the DUPAL-anomaly (Dupré and Allègre, 1983) found in volcanic rocks from the southern hemisphere (Hart et al., 1992). It is identified by distinct $^{207,208}Pb/^{204}Pb$ and $^{87}Sr/^{86}Sr$ patterns, and is thought to originate from disrupted continental crust and SCLM material recycled into the upper-mantle (e.g., Regelous et al., 2009).

Considering the geodynamic settings covered by this study, the large range of εNd (−3.0 to +9.1) and εHf compositions (−3.7 to +17.5, Table 4, Fig. 1.3) of the samples investigated resemble a broad range of mantle endmember compositions, classically displayed by plume-sourced OIBs. Plume-related basalts from La Réunion and the PIP display a limited compositional range, overlapping with FOZO (La Réunion: εNd = +4.1 to +4.5; εHf = +8.9 to +9.7) and enriched MORB (PIP: εNd = +5.6 to +9.4; εHf = +14.9 to +17.5). In contrast, a plume origin for settings like the CEVP, the IMP and Ascension Island has been proposed, but is still under debate (e.g., Granet et al., 1995; French and Romanowicz, 2015). The samples analyzed here resemble EM I/EM II to HIMU compositions (EVF: εNd = +0.8 to +3.6 and εHf = −1.3 to +4.0), FOZO (Massif Central, Siebengebirge, Pantelleria, Mt. Etna, Hyblean Plateau: εNd = +3.4 to +7.0; εHf = +6.5 to +10.1) and enriched MORB (Ascension Island: εNd = +7.6 to +9.1; εHf = +11.0 to +13.0) (Fig. 1.3). As expected, the subduction related samples from the IMP display evidence for the contribution of recycled crustal materials to their sources (εNd = −3.0 to +0.8; εHf = −1.0 to +2.8) (Table 3, Fig. 1.3).

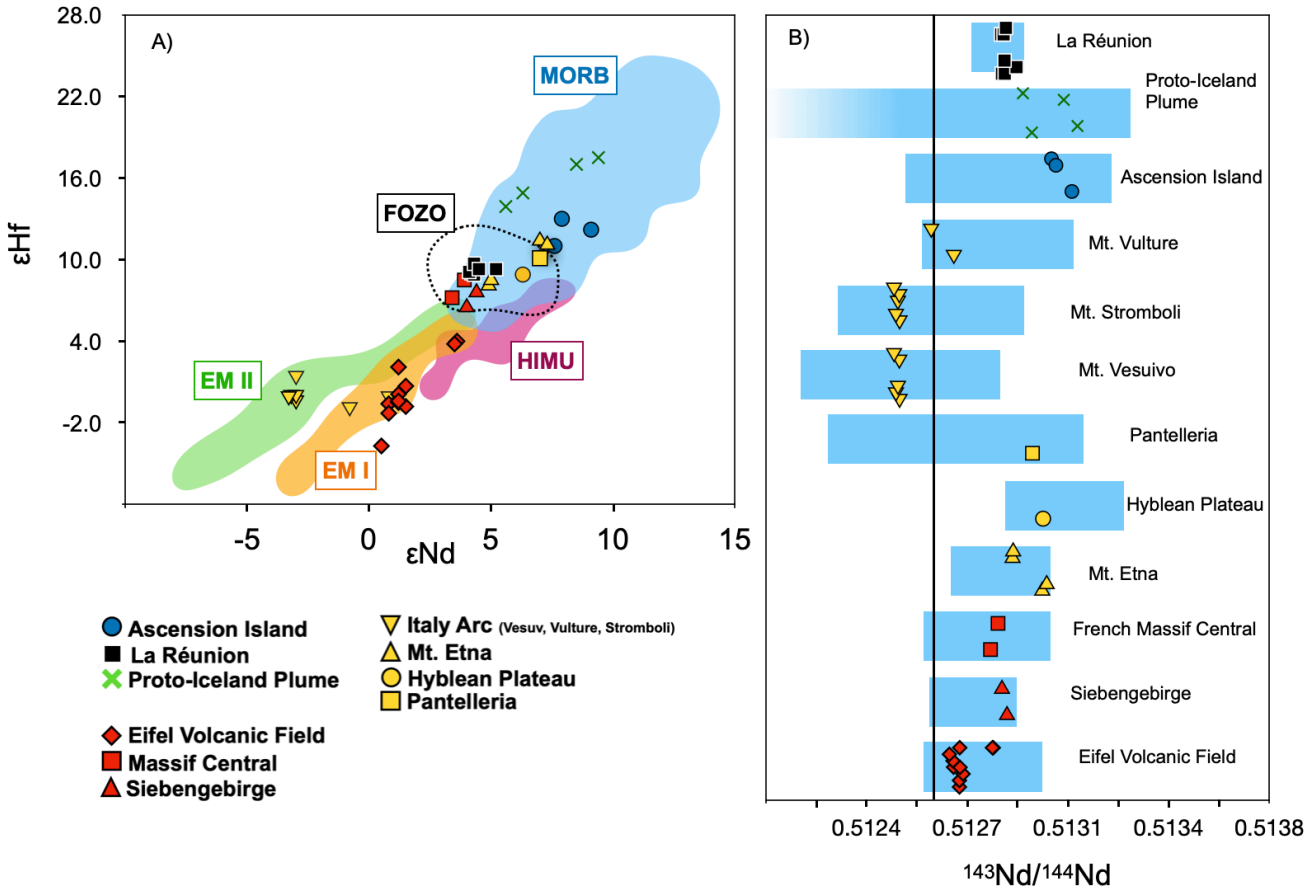

Figure 1.3 εHf vs. εNd compositions of all analyzed basalts relative to compositional fields for classical mantle domains (A) and comparison of $^{143}Nd/^{144}Nd$ with literature data (B). In Figure 3A, the sample selection covers most traditional mantle endmembers and our data are in good agreement with previously reported data in the literature. Color shaded fields indicate compositional variations of MORBs, OIBs and intraplate volcanic rocks. In Figure 3B, $^{143}Nd/^{144}Nd$ data of our samples are compared to previously published data. The blue shaded areas thereby indicate the total range of published data. The average composition as well as the 2SD of the data is further displayed by the error bars. For further references see the supplementary information. CHUR values from Bouvier et al. (2008). Compositional fields were generated using data from the GeoRoc Database (http://georoc.mpch-mainz.gwdg.de/georoc/)

Elemental W-Th-U systematics and sources of W

In silicate systems, W is one of the most incompatible elements, similar to U and Th. Due to the moderately siderophile and fluid mobile behavior of W, elemental ratios of W and lithophile elements like U and Th can provide valuable insights on the behavior of W in modern igneous reservoirs (e.g., König et al., 2008, 2011; Kurzweil et al., 2019; Newsom et al., 1996; Noll et al., 1996). Detailed investigation of MORBs and OIBs by König et al. (2008, 2011) showed a discrete range of "canonical" elemental W/Th ratios (MORB: W/Th = 0.090 – 0.24 / OIB: W/Th = 0.040 – 0.23), implying that this element ratio is solely controlled by crystal-liquid fractionation in silicate systems, where W-Th-U are so incompatible that partial melting does not significantly fractionate W/Th and W/U ratios. In contrast, W concentrations and related W/Th and W/U ratios in arc lavas and altered samples can be substantially elevated due to the selective re-distribution of W in fluid-mediated environments (e.g., König et al., 2008, 2011; Reifenröther et al., 2021, 2022). As secondary W re-distribution can overprint primary ^{182}W isotope signatures, it is essential to carefully monitor the elemental W budget of samples prior to ^{182}W isotope analysis (e.g., Tusch et al., 2021a, Tusch et al., 2021b).

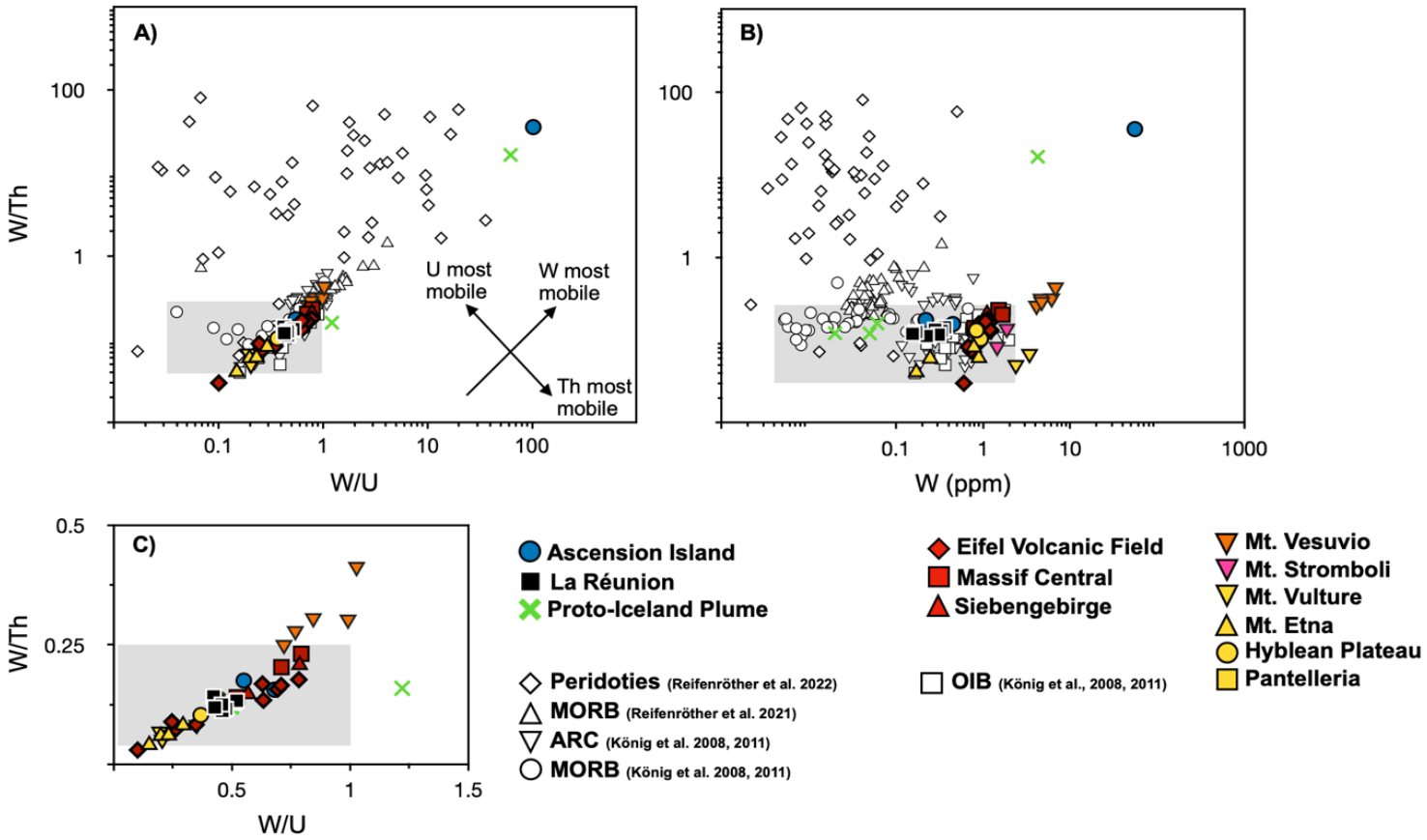

Figure 1.4 Evaluation of elemental W behavior based on W/Th vs. W/U (A, C) and W/Th vs. W (B) patterns. Most samples analyzed throughout this study overlap with the inferred canonical field as defined by MORB and OIB, indicating a control of igneous processes on elemental W systematics. Many arc-related samples from Italy (Mt Stromboli and Mt. Vulture) do not display significantly elevated elemental W/Th and W/U ratios. Only samples from Mt. Vesuvio are displaced towards higher W/Th ratios. Some samples from the Italian Magmatic Provinces, Ascension Island and the Proto-Iceland plume display selective W enrichments and elevated W/Th ratios. This is in good agreement with secondary re-distribution of W during alteration and within aqueous subduction zone environments. Grey shaded areas define canonical compositions of MORB, OIB previously analyzed by König et al. (2008, 2011). Data from König et al. (2008, 2011) and Reifenröther et al. (2020, 2022) are plotted for comparison.

Considering that most samples analyzed here have W/Th and W/U ratios similar to the canonical range defined by MORB and OIB (Fig. 1.4), we regard their W budget as undisturbed by metasomatic processes. However, samples from Ascension Island (ASD 16) and the proto-Iceland plume (DUR 1) exhibit significantly elevated W concentrations of 55.2 ppm (ASD 16) and 4.24 ppm (DUR 1) at high W/Th ratios (16.5, DUR 1; 35.6, ASD 16). While such extreme enrichments could be caused by contamination during sample preparation (e.g., saw blade/jaw-crusher), both samples lack significant enrichments of other siderophile elements such as Ni, Cr or Fe. Despite the lack of alteration signatures in other sensitive isotope (e.g., $^{87}Sr/^{86}Sr$ (Stuart et al., 2003; Starkey et al., 2009; Paulick et al., 2010) and trace element markers (e.g., Ba), this extreme enrichment of W might therefore be caused by fluid-controlled alteration processes that selectively mobilized W. This is consistent with previous studies by Kurzweil et al. (2020) reporting substantially elevated W concentrations and related W/Th, W/U ratios in Eoarchean rocks from Isua, suggesting the preferential mobilization of W within CO_2 rich fluids. Among the samples analyzed here, sample ASD 16 has been collected from the submarine ASI #3 drillcore, which was likely disturbed by hydrothermal alteration (e.g., Nielson and Sibbett, 1996). High W/Th of sample DUR 1 may reflect surface alteration, with fluids likely being released from the underlying basement (e.g., Mundl-Petermeier et al., 2019).

The intraplate volcanic samples from the CEVP mostly display similar W/Th ratios in the canonical range (Fig. 1.4, Table 5). Only one melilititefrom the Eifel exhibits a sub-canonical W/Th ratio (Ei 10b; W/Th = 0.03). The origin of melilitites is debated, but trace element modeling and P-T estimates suggest an origin in the lowermost lithospheric mantle (e.g., Jung et al., 2011; Pfänder et al., 2018). A study by Pfänder et al. (2018) has further proposed 3-5% partial melting of a highly enriched, metasomatized carbonated phlogopite bearing garnet–lherzolite. Therefore, it is likely that some minerals such as rutile, phyllosilicates or amphibole that are stable in the lithospheric mantle may have retained some of the W during low-degree partial melting (e.g., Liu et al., 2018).

The elemental W systematics of the Italian basalts needs to be discussed in the context of a complex subduction zone setting. Whereas some subduction-related lavas from Vesuvio exhibit slightly elevated W/Th ratios, Italian arc and intraplate samples fall within the canonical range defined by MORB and OIB with same samples pointing towards subcanonical values

(Mt Etna and Vulture). The origin of these low W/Th was suggested as being related to the interaction with the carbon-rich SCLM (Bragagni et al., 2022). A closer look at the W-Th-U concentrations of the subduction-related samples from Vesuvio, Vulture and Stromboli (W = 1.45 – 6.77 ppm; Th = 14.5 – 40.9 ppm; U = 3.89 – 17.9 ppm) reveals W-U-Th abundances that by far exceed previously reported concentration ranges from arc settings (König et al., 2008, 2011, Fig. 4). Avanzinelli et al. (2018) suggested the presence of a complex mantle source beneath Vesuvio, characterized by a first episode of subduction-related metasomatism due to silica-rich components (similar to those affecting Stromboli), capable of enriching the mantle in Th and other incompatible trace elements. The recent addition of carbonate-rich fluids/melts was inferred to account for ^{238}U-excesses measured in Vesuvio's magmas. In this context, CO_2-rich fluids and melt-like slab components display a great potential of mobilizing W as well as U to similar extents (e.g., König et al., 2008, 2011). This is clearly illustrated in Fig. 1.4, where samples from Vesuvio are displaced towards higher W/Th and W/U ratios compared to our samples from Stromboli that display canonical W/Th ratios and carry no ^{238}U-excess (Bragagni et al., 2014, 2022; Tommasini et al., 2007). With the exception that Stromboli basalts lack any evidence of the involvement of CO_2 rich components, basalts from Stromboli and Vesuvio are geochemically similar, suggesting related mantle sources (Peccerillo, 2017).

Origin of W isotope compositions in the samples from deep-rooted mantle plumes

Despite a deep mantle origin (e.g., French and Romanowicz, 2015), volcanic rocks from La Réunion have previously been shown to plot within a restricted compositional range of long-lived radiogenic isotope compositions, similar to the PREMA/FOZO component with a clear DUPAL-flavor (Dupré and Allègre, 1983; Bosch et al., 2008). This composition is present in the samples analyzed within this study (Table 4, Fig 1.3). The negative W found for the PDF basalts from La Réunion (as low as −8.8 ± 4.4 ppm, Table 5.) are consistent with previous investigations (Rizo et al., 2019; Peters et al., 2021). Notably, samples from the older PDN edifice reveal no significant W isotope anomalies, scattering around the inferred modern upper-mantle value (W = −2.2 ± 4.1 to +0.0 ± 6.3; Fig. 1.6). While such compositions might reflect heterogenous source compositions of both volcanoes, deficits as low as −9.6 (Peters et al., 2021) argue for a sampling bias of volcanic edifices, PDN (N = 5) and PDF (N = 14) respectively. Rizo et al. (2019) and Peters et al. (2021) have suggested that La Réunion basalts

preserve a contribution from a lower mantle reservoir that has previously interacted with the core. This is broadly similar to the model developed by Mundl-Petermeier et al. (2019, 2020) and Jackson et al. (2020) who have ascribed a negative correlation of He and W isotope compositions to the presence of primordial reservoirs that remained isolated for most of Earth history (see also Graham, 2002 for He). These authors have also proposed that these primordial reservoirs originate from LLSVPs, because such domains presumably formed during early silicate differentiation (high $^{3}He/^{4}He$ ratios and W = ~0), and from ULVZs that may have inherited their W inventory via chemical and isotopic equilibration from the core (Mundl-Petermeier et al., 2019, 2020; Rizo et al., 2019). Assuming $^{3}He/^{4}He$ of 13 R_A (e.g. Füri et al., 2011) and W = 0.0 to −16.5 (Rizo et al., 2019; Peters et al., 2021; this study), La Réunion lavas plot on the W-He trends that are defined by Hawaii and Samoa (e.g., Mundl-Petermeier et al., 2020). Unlike for ^{182}W, ^{142}Nd heterogeneities in La Réunion lavas clearly suggest the involvement of early differentiated silicate reservoirs (Peters et al., 2018, 2021) that must have remained isolated since the late Hadean. This is in good agreement with long-lived radiogenic isotope compositions that indicate a major contribution of the relatively unprocessed FOZO/PREMA mantle reservoir (e.g., Bosch et al., 2008). However, small-scale variations in $^{206, 207, 208}Pb$ and ^{143}Nd-^{176}Hf have revealed discrete mixing relationships, suggesting that the edifices originate from compositionally distinct small-scale mantle-blobs that interacted with recycled domains and depleted mantle materials (e.g., Bosch et al., 2008).

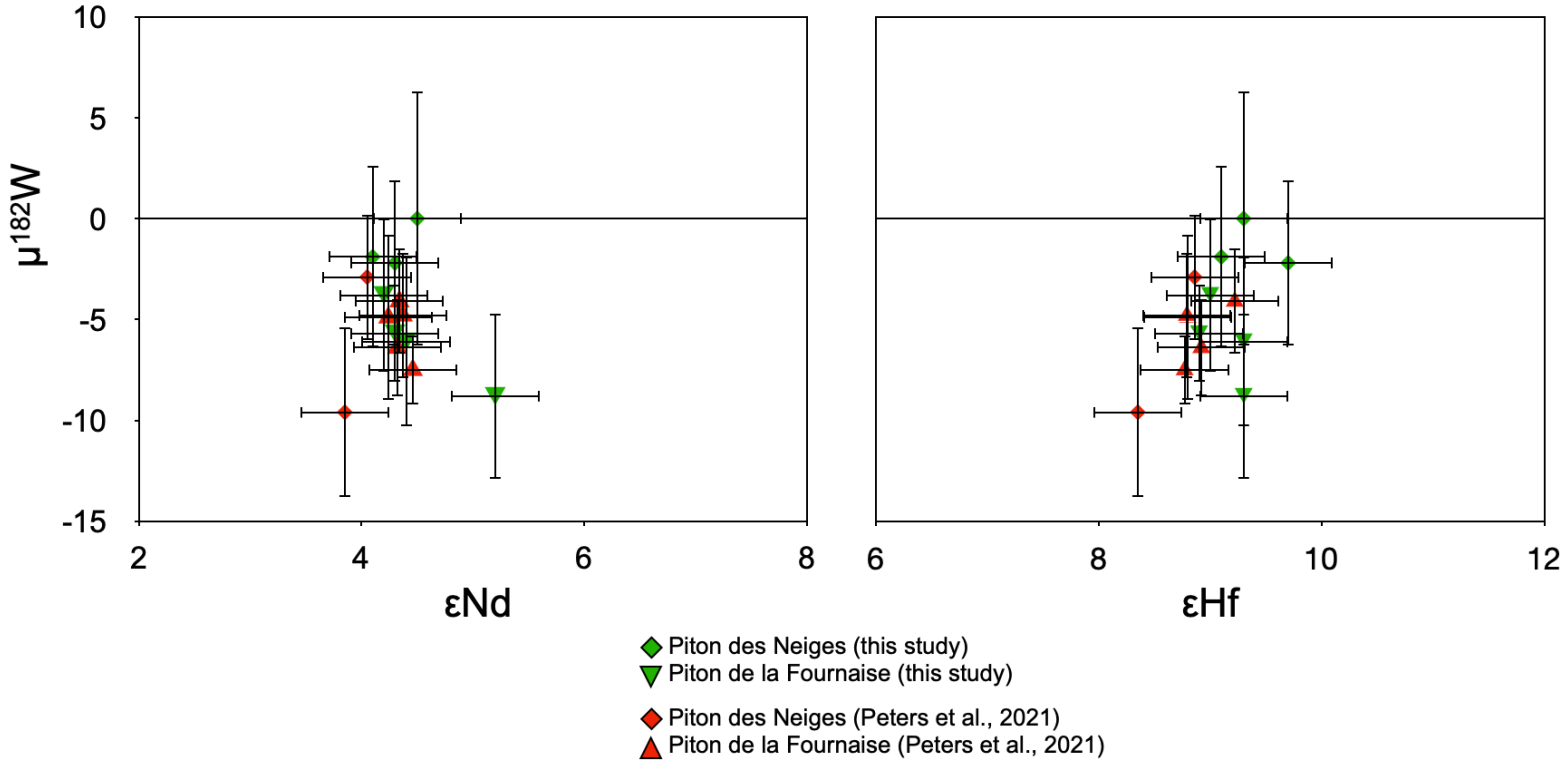

Figure 1.5 ^{182}W vs. $^{143}Nd/^{144}Nd$ and ^{182}W vs. $^{176}Hf/^{177}Hf$ compositions of La Réunion samples from this study and Peters et al. (2021). Samples of both studies largely overlap within their $^{143}Nd/^{144}Nd$ and $^{176}Hf/^{177}Hf$ isotope compositions but display heterogenous ^{182}W isotope compositions.

Compiling available ^{182}W, $^{143}Nd/^{144}Nd$ and $^{176}Hf/^{177}Hf$ data for the La Réunion hotspot (Fig. 1.5), our data are in good agreement with previously published data by Peters et al. (2021) and confirm a rather heterogenous contribution of variable mantle domains displaying heterogenous ^{182}W ($\mu^{182}W = -9.6 \pm 4.6$ to 0.0 ± 6.3) at given ^{143}Nd-^{176}Hf isotope compositions, respectively. To explain the observed heterogeneity of ^{182}W, ^{142}Nd and $^{3}He/^{4}He$ isotope systematics, Peters et al. (2021) have proposed a complex model that involves mixing of a core equilibrated, enriched Hadean magma ocean remnant, depleted magma ocean relics and small amounts of recycled Hadean mafic crust. While our samples from PDF with clear ^{182}W deficits might indeed indicate contributions of a W-rich, primordial component having interacted with the Earth's core, the concurrent DUPAL-flavor in Sr-Pb isotope space also suggests contributions of shallower crustal reservoirs (Bosch et al., 2008; Regelous et al., 2009). Investigating fresh volcanic glass samples from the Mid-Atlantic Ridge at 26°S and off-axis seamounts, Regelous et al. (2009) linked the DUPAL anomaly to shallow level incorporation of disrupted lower-continental crust and lithospheric mantle fragments. In the case of the La Réunion hotspot, these models are also supported by the presence of Archean zircons found in Mauritius lavas (Ashwal et al., 2017) and a recent study by Nauret et al. (2019), identifying the presence of ancient crustal fragments at shallower depths. We note that our suggestions are also in line with recent models claiming the presence of disrupted and metasomatized SCLM domains beneath several intraplate volcanoes, a viable alternative source for geochemical signatures that were previously ascribed to lower mantle reservoirs (e.g., Belay et al., 2019; Guimarães et al., 2020). By analogy to the nearby Kaapvaal Craton (e.g., Puchtel et al., 2016; Tusch et al., 2021a), the presence of ^{182}W deficits in La Réunion basalts may thus also call for the recycling of lower-crustal Hadean to early Archean restites from prolonged TTG formation that significantly contributed to magmatism in the Indian ocean. Following the model of Tusch et al. (2021a), mixing of such material with classical mantle end-members can readily account for the observed heterogenous ^{182}W, ^{142}Nd and long-lived radiogenic isotope systematics in OIBs like those from La Réunion. However, as moderately high and exceptionally uniform $^{3}He/^{4}He$ ratios of ~13 R_A (Füri et al., 2011) are apparently inconsistent with a contribution of crustal material it has been previously suggested that the source has been recently enriched by unradiogenic helium through diffusion (e.g., Regelous et al., 2009 and references therein).

In contrast to La Réunion, the picrites from the proto-Iceland plume (PIP) display a large range of trace element and radiogenic isotope compositions (Stuart et al., 2003; Starkey et al., 2009; Willhite et al., 2019). Although lavas from the PIP display overall depleted long-lived radiogenic isotope compositions similar to MORB, recent studies have imaged a plume structure underneath Iceland that tilts to the NNW at 350-400 km depth, reaching beneath eastern Greenland (Celli et al., 2021). Most importantly, samples from the PIP display the highest $^{3}He/^{4}He$ ratios measured so far (as high as 50 R/R_A (Stuart et al., 2003; Starkey et al., 2009; Willhite et al., 2019). This likely reflects the pollution of plume-entrained mantle by volatiles from He-rich high $^{3}He/^{4}He$ deep mantle domains (e.g., Starkey et al., 2009; Dale et al., 2009). Alternatively, the PIP samples a unique, deep mantle reservoir that has remained isolated throughout most of Earth's history (Willhite et al., 2019). Previous ^{182}W analyses of PIP basalts have yielded contrasting results (e.g., Rizo et al., 2016; Mundl-Petermeier et al., 2019, 2020). A study by Rizo et al. (2016) has reported exceptionally high ^{182}W excesses in samples from Padloping Island (up to $W = +48.4 \pm 4.6$ ppm) and attributed this to the preservation of a depleted reservoir that formed through Hadean silicate differentiation. The same study reported ^{182}W excesses of similar magnitude in modern volcanic rocks from the Ontong-Java Plateau (OJP) that, however, were inconsistent with previous measurements by Willbold et al. (2011) and more recent measurements of stratigraphically similar rocks from the OJP (Kruijer and Kleine, 2018). This follow-up study postulated that the excesses reported by Rizo et al. (2016) might be analytical artifacts induced by nuclear field shift effects (Kruijer and Kleine, 2018).

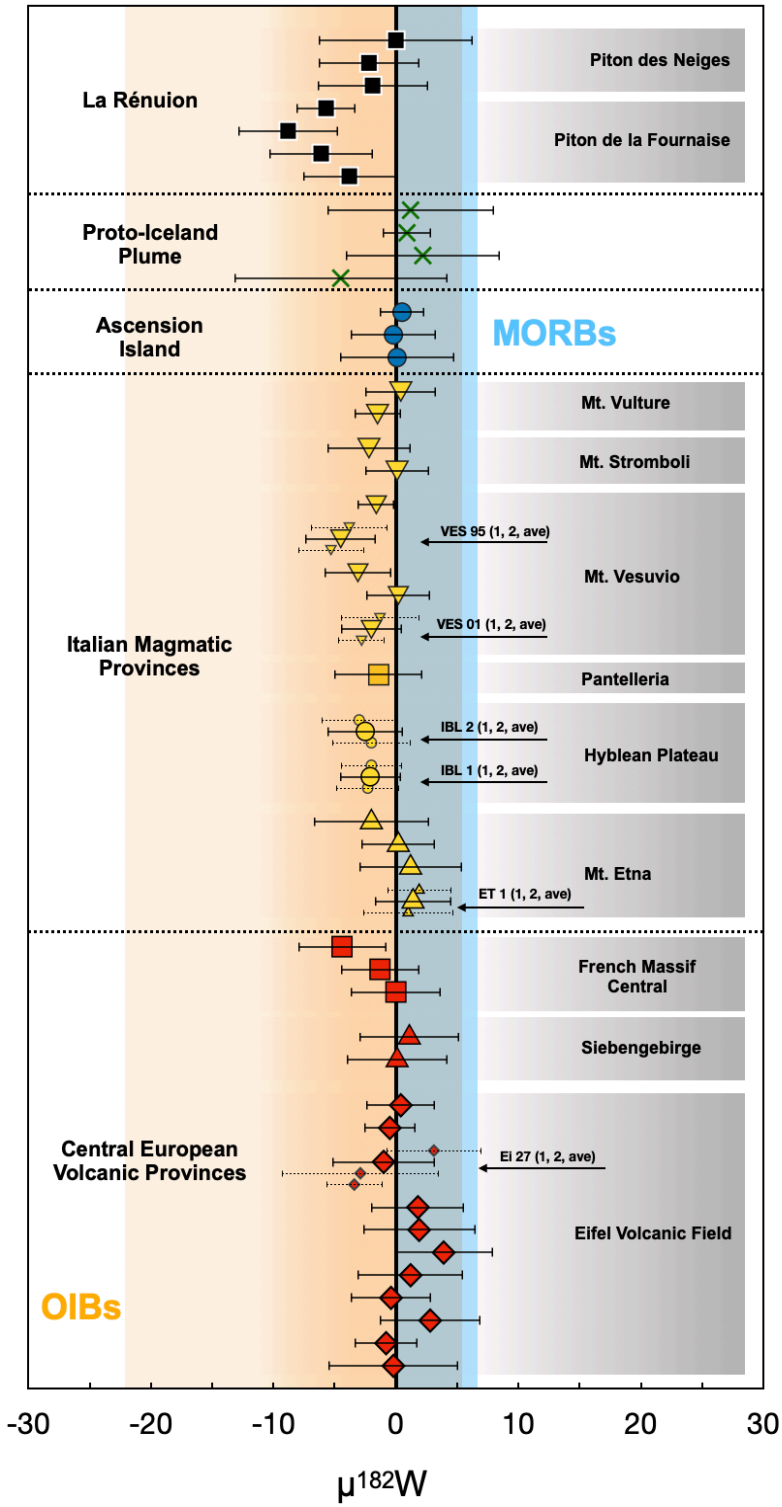

Figure 1.6 Measured $\mu^{182}W$ of samples investigated throughout this study. Samples from the CEVP, Ascension Island, Pantelleria and the NAIP display no anomalous ^{182}W isotope compositions. In comparison, data from La Réunion indicate a heterogenous plume source composition. The light brown colored field indicates the total range of ^{182}W compositions in modern OIB (Willbold et al. 2011; Mundl et al. 2017; Rizo et al. 2019; Mundl-Petermeier et al. 2019; 2020). The light blue colored field indicates the total range of 182W compositions of MORBs (Mundl et al. 2017; Rizo et al. 2019).

The same study reported ^{182}W excesses of similar magnitude in modern volcanic rocks from the Ontong-Java Plateau (OJP) that, however, were inconsistent with previous measurements by Willbold et al. (2011) and more recent measurements of stratigraphically similar rocks from the OJP (Kruijer and Kleine, 2018). This follow-up study postulated that the excesses reported by Rizo et al. (2016) might be analytical artifacts induced by nuclear field shift effects (Kruijer and Kleine, 2018). Alternatively, Mundl-Petermeier et al. (2020) suggested that the elevated ^{182}W isotope compositions could be inherited from the Archean basement by metasomatic fluids. To clarify this controversy, we have analyzed four high $^{3}He/^{4}He$ PIP picrites from Durban Island and Padloping Island. The W values for our PIP samples with undisturbed elemental W budgets (canonical W/Th) display a narrow range from −4.5 ± 8.7 to +2.2 ± 6.3 ppm (Table 5, Fig. 1.6), clearly demonstrating that the W isotope compositions of the parental sources are indistinguishable from the inferred composition of modern upper mantle. Metasomatic agents that carry ^{182}W excesses appear not to account for the extreme anomalies found by Rizo et al. (2016), because sample DUR 1 with elevated W/Th also shows modern upper mantle-like W (Fig. 1.5). The absence of a W isotope anomaly in the highest $^{3}He/^{4}He$ basalts available provide no clear support for previous claims for a unique high $^{3}He/^{4}He$ reservoir in the deep mantle that has remained isolated from convective mixing since the first few 10s Myr (e.g., Graham, 2002; Jackson et al., 2020). Instead, the data are more consistent with models where He isotopes are decoupled from other isotope systems either by mixing of He-rich deep mantle with depleted and enriched mantle components entrained by the plume, or by long-term diffusion of He from a primordial volatile-rich reservoir (Starkey et al., 2009).

Origin of W isotope compositions in intraplate lavas derived from shallow mantle plumes

In contrast to classical plume settings discussed above, the origin of Ascension Island volcanism is still highly debated. While geochemical studies have indicated highly heterogeneous mantle sources (e.g., Paulick et al., 2010; Zhang et al., 2020), seismic studies have yielded contrasting results in that both deep- as well as shallow-plume origins have been suggested (French and Romanowicz, 2015 and references therein). Basalts from Ascension Island and the surrounding MAR segments (e.g., Paulick et al., 2010) can be explained by binary mixing between depleted mantle and HIMU reservoirs (Zhang et al., 2020 and references therein). The $^{143}Nd/^{144}Nd$ and $^{176}Hf/^{177}Hf$ compositions of the samples analyzed here

represent the enriched endmember that contributed to nearly all eruptive stages of Ascension volcanism (Paulick et al., 2010) (Fig. 1.2). Irrespective of fluid alteration (which affected sample ASD 16), the ^{182}W composition of our samples is homogenous with values ranging from $\mu^{182}W = -0.2 \pm 3.5$ to $+0.1 \pm 4.7$ ppm (Table 2, Fig. 1.6). We can not fully exclude that magmatism on Ascension Island, that is located on the edge of the African LLSVP (Fig. 1.1), may tap a deep plume-related magma source or interacts with non-anomalous ^{182}W plumes such as the nearby plumes of St. Helena and Tristan (Zhang et al., 2020; Mundl-Petermeier et al., 2020; Jackson et al., 2020). However, the combination of our data with published $^{3}He/^{4}He$ data (6.3 to 7.3 R_A; Ammon et al., 2009) indicates a major control of upper mantle reservoirs on the compositions of Ascension Island lavas (Paulick et al., 2010; Fig. 1.7). This is also in good agreement with recent seismic dataindicating a shallow-plume origin (French and Romanowicz, 2015).

Seismic studies of the CEVP have revealed shallow plume structures rooted at the mantle transition zone (Ritter et al., 2001). However, the presence of deep rooted plume structures still remains debated (e.g., Granet et al., 1995; French and Romanowicz, 2015). Based on a similar long-lived radiogenic isotope compositions of lavas sampled across all eruptive centers of the CEVP, several studies have suggested a common mantle reservoir that is accessible for partial melting beneath Europe (Common Mantle or European Asthenospheric Reservoir (CMR or EAR); e.g., Hoernle et al., 1995; Lustrino and Wilson, 2007). Considering the Sr-Hf-Nd-Pb isotope compositions of CEVP lavas, the CMR comprises a range of very different mantle endmembers, covering EM I, EM II and HIMU-like compositions (Lustrino and Wilson, 2007). While EM I- and EM II-like endmembers may reflect contributions from younger crustal material that has been mixed into the mantle during orogenic events (e.g. the Variscian orogeny), the HIMU-like endmember may have interacted with CMR-like asthenospheric melts that tapped metasomatized SCLM (Jung et al., 2011; Lustrino and Wilson, 2007; Pfänder et al., 2018). However, the origin of the HIMU-like component in CEVP lavas is still debated and an asthenospheric as well as an SCLM origin have been suggested (e.g., Lustrino and Wilson, 2007). Rather low $^{3}He/^{4}He$ ($\sim$6 R_A) ratios measured in mantle xenoliths and gas from Eifel springs (Dunai and Baur, 1995; Bekaert et al., 2019 and references therein) further suggest an upper- rather than a lower mantle origin.

The continental intraplate volcanic rocks of the CEVP analyzed here display no resolvable ^{182}W deficits (Eifel Volcanic Field: W = −0.8 ± 2.6 ppm to W = +3.9 ± 4.0 ppm; Massif Central: W = −4.4 ± 3.6 ppm to W = 0.0 ± 3.7 ppm; Siebengebirge: W = +0.1 ± 4.1 ppm to W = +1.1 ± 4.1 ppm). Therefore, our ^{182}W isotope perspective provides no evidence for the contribution of long-term isolated mantle material (Table 5, Fig. 1.6). Notably, assimilation of continental crust during slow magma ascent may modify the original geochemical composition of continental intraplate melts. However, the presence of mantle nodules in volcanic rocks of the CEPV, their high MgO contents and their radiogenic isotope compositions argue for rapid magma ascent and little interaction with continental crust (e.g., Wörner et al., 1986; Schmicke et al., 2007; Lustrino and Wilson, 2007 and references therein). Considering radiogenic isotope compositions of the samples analyzed here (Table 3, Fig. 1.3) and the review of CEVP volcanism by Lustrino and Wilson (2007), our data are in good agreement with models that propose contributions from shallow-plumes (Ritter et al., 2001 and references therein) and a dominant litospheric control on the incompatible element budget of magmatic rocks from the CEVP, including that of W (Lustrino and Wilson, 2007; Pfänder et al., 2018) (Fig. 1.7C).

Collectively, the volcanic settings discussed above demonstrate that combined geochemical and seismic constraints can not always provide unambiguous evidence for a deep plume structure. Ascension Island and the CEVP are exemplary sites, where different seismic models permit different depths of mantle domains involved in magma generation (e.g., Montelli et al., 2006; French and Romanowicz, 2015; Granet et al., 1995; Ritter et al., 2001), despite resembling long-lived radiogenic isotope compositions similar to classical plume settings (e.g., Lustrino and Wilson, 2007; Paulick et al., 2010). This calls for the careful combination of multiple proxies such as W isotopes, seismic studies, long-lived radiogenic isotope- and noble gas compositions. We argue that this multi-proxy approach, now complemented by our new ^{182}W data, provides strong evidence for a shallow plume origin of Ascension Island and CEVP volcanism that is broadly similar to the previously published models of Belay et al. (2019) and Guimarães et al. (2020).

Tungsten isotope compositions in intraplate lavas from the Italian Magmatic Province associated with subduction

Compositionally, volcanic rocks from the Tyrrhenian Sea region nearly cover the complete spectrum of mantle endmembers known to date (e.g., Lustrino and Wilson, 2007; Peccerillo, 2017). Throughout this study, we have investigated a variety of settings that include intraplate volcanic rocks (Mt Etna, Hyblean Plateau, Pantelleria) with Hf-Nd isotope compositions similar to the CMR (Fig. 1.3) as well as samples indicative of subduction-related crustal contributions (Stromboli, Vesuvio, Vulture) (Table 4, Fig. 1.3). Previous studies have suggested the influence of a mantle plume (Hoernle et al., 1995) as well as inflow of African asthenospheric material (Trua et al., 2003). However, with ^{182}W compositions in a range from W = −4.5 ± 2.9 ppm to +2.8 ± 4.3 ppm (Table 5, Fig. 1.6) we do not find evidence for a significant contribution of anomalous lower mantle material to the magma source of Mt. Etna and Pantelleria. Considering the subduction-controlled settings of Mt. Vesuvio and Stromboli, and to a lesser extent of Mt. Vulture, our samples generally reveal similar results with ^{182}W compositions in a range from W = −2.2 ± 3.4 to −0.4 ± 2.9 ppm (Table 5, Fig. 1.6). Our results are further in line with the absence of elevated $^{3}He/^{4}He$ ratios (2.2 to 6 R_A, e.g., Martelli et al., 2008). However, slightly deficient ^{182}W compositions in one sample from Vesuvio (W = −4.5 ± 2.9 ppm) might indicate the influence of ancient material, but this needs further investigation. Our samples from Etna, Pantelleria and the Hyblean Plateau, that are the most likely candidates for contributions of deep plume material, also display modern upper mantle-like ^{182}W compositions.

The magmas of the Hyblean Plateau (Trua et al., 1998) show evidence for a SCLM component enriched by carbonatite metasomatism. Such a contribution was recently discovered also at Mt. Etna on the basis of HFS elements (Bragagni et al., 2022). The lithospheric mantle below Sicily, which influences magmatism of the Hyblean plateau and Etna, shows model ages attesting melt depletion events that occurred in the Archean or earlier (Sapienza et al., 2007), while carbonatite metasomatism was likely much more recent (Trua et al., 1998). The lack of any anomalous ^{182}W compositions at Etna and the Hyblean argues against an ancient origin of the ambient SCLM. Pantelleria shows no sign of SCLM contribution indicating a purely asthenospheric mantle source (Avanzinelli et al., 2014; Bragagni et al., 2022). The absence of anomalous ^{182}W composition is consistent with an origin of the magmas from Pantelleria from

the upper mantle due to passive upwelling resulting from lithospheric stretching with no evidence for the presence of a deep-seated mantle plume (see also Avanzinelli et al., 2014) as a whole, our data indicate that the local upper mantle and the SCLM beneath southern Italy do not carry anomalous ^{182}W, similar to what observed in other volcanoes of the CMR. In absence of a deep plume source at Vesuvio, we rather suggest, that CO_2-rich fluids/melt released during subduction of ancient material lead to secondary redistribution of W in the source region of Mt. Vesuvio lavas.

Conclusions

This study presents the first comprehensive ^{182}W dataset for intraplate volcanic rocks involving shallow plume, continental intraplate and subduction-related settings as well as new data for deep-rooted mantle plumes. In Fig. 1.7 we illustrate the geodynamic implications and conclusions based on the data gained throughout this study. In summary, the following key findings that emerge from our study are:

1)

Data for deep plume-related La Réunion lavas indicate ^{182}W heterogeneities that are in good agreement with previously reported data by Peters et al. (2021). While the heterogeneous distribution of lower-mantle material within the rising plume would certainly provide a viable explanation, the combination of our ^{182}W data and previously published $^{3}He/^{4}He$ compositions only slightly overlap with previously proposed correlation trends (Mundl-Petermeier et al., 2020; Jackson et al., 2020). By analogy to a recent study on ^{182}W compositions in Archean rocks from the Kaapvaal Craton (Tusch et al., 2021a), we alternatively suggest that the ^{182}W-poor mantle tapped by the PDF volcanism may result from the incorporation of recycled restites from Hadean protocrust within the upper mantle. This model is in line with the strong DUPAL signature in the Pb isotope record of the PDF lavas (Fig. 1.7A) but conflicts with seismic studies that image a clear plume structure anchored in the lower mantle (French and Romanowicz, 2015).

2)

The high temperature picritic basalts erupted by the early Iceland plume do not display resolvable ^{182}W anomalies. The absence of ^{182}W anomalies provide no clear support for suggestions of a long-isolated primordial reservoir present at the core-mantle boundary but are consistent with He pollution of entrained mantle (e.g., Starkey et al., 2009) (Fig. 1.7B), as ^{182}W and $^{3}He/^{4}He$ are decoupled.

3)

The absence of ^{182}W anomalies in shallow plume-sourced Ascension Island samples indicates an upper mantle control on the ^{182}W composition and no contributions from anomalous lower mantle reservoirs (Fig. 1.7A) even though Ascension Island is located on the margin of the African LLSVP (Fig. 1.1).

4)

A largely homogenous ^{182}W composition of our samples from the CEVP is in good agreement with noble gas data suggesting an upper mantle origin (Fig. 1.7C), and a strong influence of lithospheric components. These data also suggest the absence of anomalous ^{182}W domains in the mantle beneath Central Europe.

5)

The ^{182}W budget of intraplate volcanism within the IMP is largely controlled by shallow upper mantle components such as the CMR (Fig. 1.7D), with contributions from relatively recent SCLM at the Hyblean Plateu and Mt. Etna, and variable (carbonate-rich vs. carbonate-poor) subduction-related components in Vesuvio and Stromboli, and to a lesser extent in Mt. Vulture.

6)

Our data support models claiming that anomalous ^{182}W compositions are confined to lower mantle reservoirs and do not occur in shallow mantle plumes. However, the combination of our ^{182}W data and previously published Sr-Nd-Hf-Pb-He isotope data might indicate recycled Hadean crustal fragments as a potential source of deficient W isotope compositions in La Réunion lavas.

7)

The widespread absence of ^{182}W anomalies in basalts from the European portion of the northern hemisphere can also be explained by the absence of isotopically anomalous and isolated domains in the deep mantle beneath the European hemisphere, as also suggested by geophysical evidence (e.g., French and Romanowicz, 2015).

8)

In combination with previously published data on OIBs, our newly gained data on highly variable geodynamic settings provide strong evidence for a geochemically stratified mantle. Although further investigations are necessary, combined He–W systematics suggest the lower-mantle to be the host region of primordial reservoirs within the earths modern mantle (e.g., Graham et al., 2002).

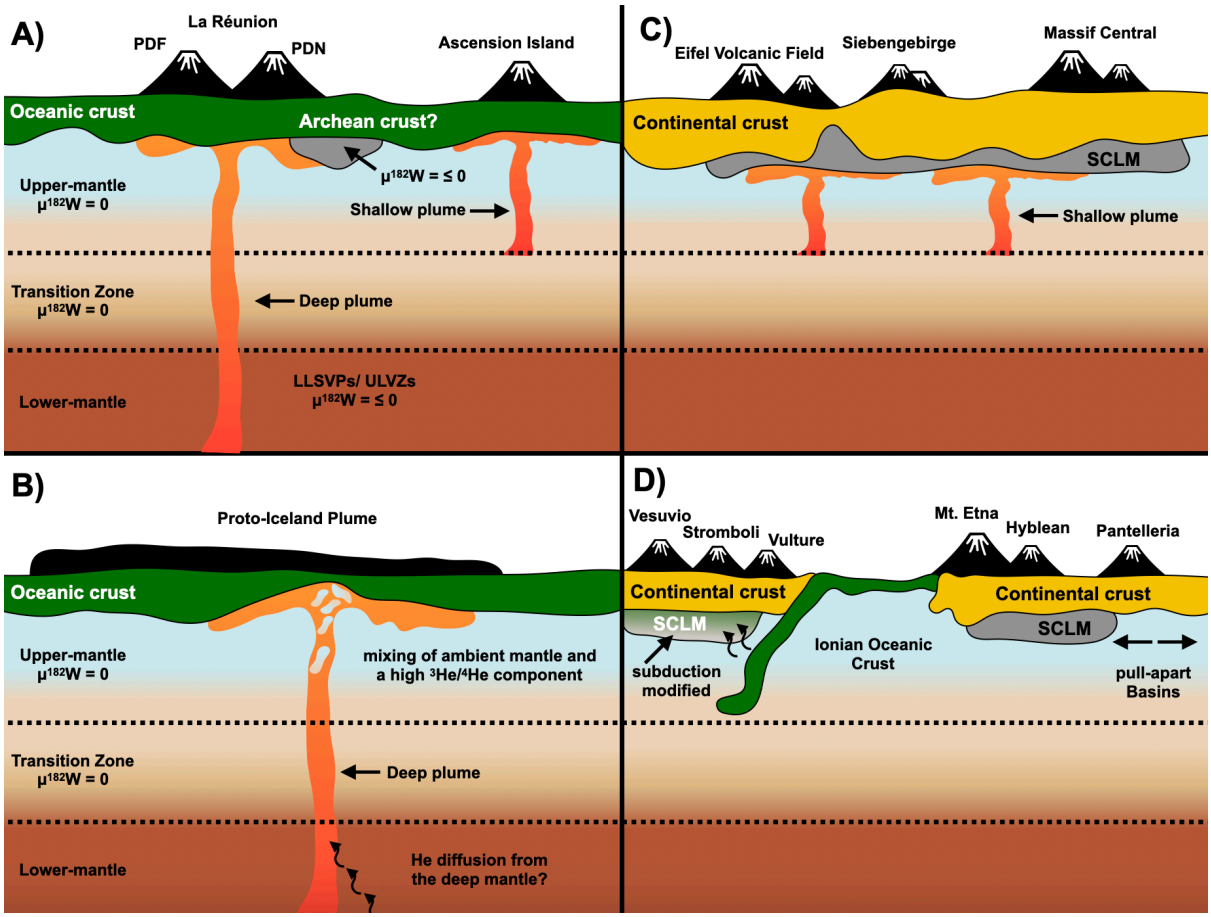

Figure 1.7: Schematic sketch illustrating the geodynamic implications gained by ^{182}W isotope data from this study and the literature. A) Deep plumes as a carrier of negative ^{182}W anomalies; a heterogenous distribution of LLSVP and ULVZ material within the plume is responsible for the heterogenous ^{182}W compositions of both volcanic edifices (e.g., Mundl-Petermeier et al. 2019, 2020); Alternatively, recycled Archean crustal materials that account for the Pb-DUPAL flavor of PDF volcanic samples (Bosch et al. 2008) also carry anomalous ^{182}W signatures. The compositions of shallow-plume related Ascension Island lavas are controlled by the upper-mantle or potentially reflect primordial signatures, present as relicts from the interacting St. Helena and Tristan plumes (e.g., Zhang et al. 2020). B) Data for samples from Baffin Bay and Padloping Island indicate a dominant influence of upper mantle material (e.g., Stuart et al. 2003; Starkey et al. 2009); the absence of deficient ^{182}W compositions despite high $^{3}He/^{4}He$ ratios (Starkey et al. 2009) further indicates that the W and He budgets are apparently decoupled (Mundl-Petermeier et al. 2019; 2020; Jackson et al. 2020). C) For the CEVP, our data are in good agreement with noble-gas compositions (e.g., Moreira et al. 2018; Bekaert et al. 2019) and detailed evaluations of long-lived radiogenic isotope compositions that suggest a common mantle reservoir (CMR), located within the upper mantle underneath the CEVP. D) Similar to the CEVP, seismic studies have provided evidence for a shallow-plume origin of Etna volcanism (e.g., Montelli et al. 2006) and radiogenic isotope compositions are similar to the CMR (Lustrino and Wilson, 2007). The largely homogenous ^{182}W composition of all settings analyzed here, overlapping with the modern upper-mantle value, does not indicate contributions of primordial material from the lower-mantle.

Supplementary Information

Major element concentrations (Appendix I, Table II) were analyzed using a Panalytical Zetium spectrometer at the University of Cologne For trace element concentration measurements ca. 100 mg of sample were dissolved in 6 ml of a 1:1 $cHNO_3$/cHF mixture. Following a repeated drydown in concentrated HNO_3, the samples were re-dissolved in diluted HNO_3 media for measurements. Trace elements (Table 1) were measured with a quadrupole ICP-MS using an Agilent 7500cs mass spectrometer at the University of Kiel following the analytical protocol given in Garbe-Schönberg (1993) or with a Thermo Fischer iCap-Q at the University of Cologne. Repeated analyses of the basaltic reference materials yielded an accuracy of better than 10 % (Garbe-Schönberg, 1993).

For samples with W, Th, U concentrations lower than 600 ng/g we additionally performed isotope dilution measurements. Additionally, we have performed isotope composition measurements for Hf and Nd. For isotope dilution and concentration measurements, approximately 100mg splits of samples were spiked with mixed $^{233\text{-}236}U$ – ^{229}Th and ^{183}W – ^{180}Ta – ^{180}Hf – ^{176}Lu – ^{94}Zr tracers (Weyer et al. 2002; Münker, 2010) and dissolved in 6 ml of a 1:1 $cHNO_3$/cHF mixture on a hotplate at 130 °C for ~24h. After a repeated drydown in concentrated HNO_3, the samples were re-dissolved in 6 ml of a 6N HCl – 0.06N HF solution for 5-6h at 120 °C to achieve full sample-spike equilibrium. In case of full HSFE separation, a 20% aliquot of the equilibrated sample solution was used for W separation, following a shortened procedure described in Kleine et al. (2004). For Hf separation we have applied the three-step ion exchange chromatography by Münker et al. (2001), during which a U-Th cut can be taken during the loading step of the second ion exchange column. The elements U, Th and a REE cut were separated following the method of Luo et al. (1997). To achieve full Nd separation, we have applied the separation protocol described in Pin and Zalduegui (1997). For a more detailed description, see Tusch et al. (2019, 2021). All isotope dilution measurements were conducted at the University of Cologne, using a Thermo-Fisher® Neptune MC-ICP-MS and following the protocols of Thiemens et al. (2019), Kleine et al. (2004) and Weyer et al. (2002). The external precision and accuracy for isotope dilution measurements is typically better than ± 1%.

Tungsten was separated from bulk rock samples following the protocols described in Tusch et al. (2019, 2021). Up to 30 g of sample powder were digested in a 1:1 $cHNO_3$/cHF mixture in closed Savillex® PFA vials on a hotplate at 130°C for at least 24 h. The approximate amount of sample material used for measurements is reported in Table 2. After evaporation to near dryness, the samples were dried down three times using 5 ml concentrated HNO_3 to avoid the formation of insoluble fluorides. Following complete evaporation at moderate temperatures (~100°C) the samples were converted to chloride form using 30 ml 6 N HCl and fully digested at 130°C. In case of incomplete dissolution, the HCl digestion step was repeated. When the solution was visibly clear, the samples were dried down and 1.2 g sample aliquots were re-dissolved in up to 20 ml of 1 M HCl. Tungsten was separated in a four-column procedure employing cation, anion, TEVA and TODGA resins (Tusch et al. 2019, 2021). Depending on the W concentration, up to 30 sample splits were individually passed through the chemical separation procedure and recombined prior to the measurement. Procedural yields for W were generally ≥70%. Total procedural W blanks were determined by isotope dilution (i.e. Kurzweil et al., 2018) and were usually below 300 pg, contributing less than 1% to the total analyte. High-precision W isotope composition measurements were performed using the Thermo-Fisher® Neptune Plus MC-ICP-MS at the University of Cologne, following the protocols given by Tusch et al. (2019, 2021). The low-abundance isotope ^{180}W and the interference monitor ^{177}Hf were measured in Faraday collectors connected to 10^{13} Ω amplifiers, , while all other isotopes were measured using 10^{11} Ω amplifiers. Analyses were performed in static and low-resolution mode, using a standard sample and an X-type skimmer cone. Interferences at masses 184 and 186 were monitored by simultaneously measuring ^{188}Os, while Hf and Ta interferences on mass 180 were monitored by measuring ^{177}Hf, ^{178}Hf and ^{181}Ta. For mass bias corrections we used the exponential law, normalizing either to $^{186}W/^{184}W = 0.92767$ (denoted '6/4') or $^{186}W/^{183}W = 1.9859$ (denoted '6/3'). For a 50 ng/g solution, a signal intensity of 4.5 V was typically achieved for ^{182}W (corresponding to 90 V per ppm W). Samples analyzed in this study were run at ^{182}W intensities between 1.3 and 27.4 V. To achieve sufficient precision, we performed multiple measurements of sample solutions that were combined from 1-1.2 g aliquots, each of which were individually processed through the separation procedure. In each measurement session samples were bracketed by the reference material NIST SRM 3163. To assess the long-term reproducibility we always included one of our three in-house reference materials during each analytical session (historical La Palma Basalt "LP 1", Kurzweil et al.

(2019) and a 3455 Ma old grey gneiss "AGC 351" from southwest Swaziland (Kroener et al. 2014)). During the analytical campaign we also analyzed a 3.27 Ga old komatiite from the Pilbara Craton (sample 160245, Ruth Well Formation), Western Australia, that was shown to exhibit an excess in μ^{182}W of +6.8 ± 2.3 ppm (Tusch et al. 2021). Final results are reported in the μ notation (ppm deviation relative to NIST SRM 3163). The intermediate precision of our in-house reference materials, given by the mean value of multiple session averages, is μ182W = -0.2 ± 1.0 ppm (AGC 351), -0.7 ± 1.2 ppm (LP 1) and 8.1 ± 1.3 ppm (160245), respectively.

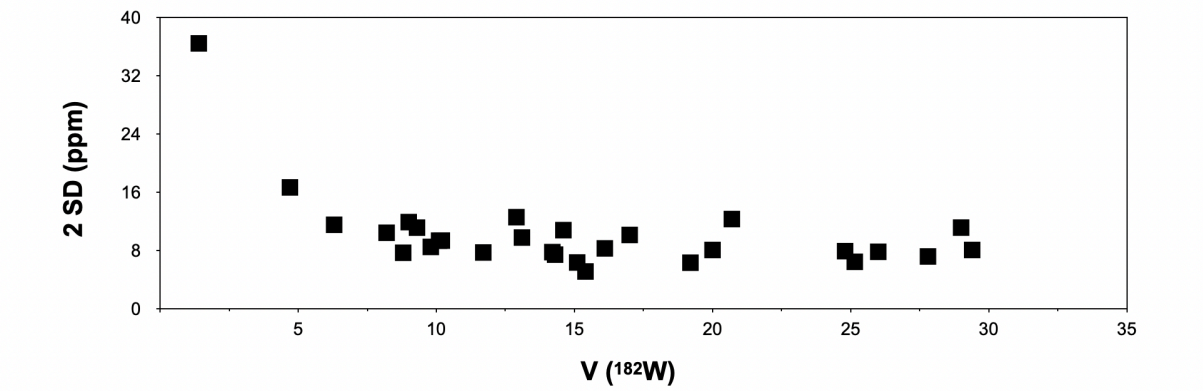

Figure SI 1. V(^{182}W) vs. 2SD of in-house reference materials.

Chapter II: Temporal, spatial and compositional variability within the Tristan-Gough hot-spot track – new insights from ^{182}W systematics

Introduction

During the last decades, the combined application of short-lived isotope systematics, such as ^{142}Nd and ^{182}W, and noble gas systematics (^{129}Xe, $^{3}He/^{4}He$) have provided valuable insights into geodynamic processes, such as the formation and preservation of compositionally distinct domains present within the modern terrestrial mantle (e.g., Carlson and Boyet, 2008; Parai et al., 2012; Rizo et al., 2016; Mundl et al., 2017; Peters et al., 2018; Mundl-Petermeier et al., 2019; Rizo et al., 2019; Jackson et al., 2020b and references therein; Peters et al., 2021). Detailed studies (e.g., Mundl et al., 2017; Mundl-Petermeier et al., 2019; Mundl-Petermeier et al., 2020; Jansen et al., 2022) that investigated the ^{182}W isotope composition of modern Ocean Island Basalts (OIB) have revealed small heterogeneities in the relative abundance of ^{182}W, the daughter nuclide of short-lived ^{182}Hf ($t_{1/2}$ = ~9 Ma Vockenhuber et al. (2004)). The presence of ^{182}W deficits (as low as $\mu^{182}W$ = -22) in modern OIBs has been interpreted to result from contributions of mantle domains that either experienced core-mantle interaction (e.g., Mundl et al., 2017; Rizo et al., 2019; Jackson et al., 2020b and references therein; Mundl-Petermeier et al., 2020) or incorporated delaminated restites of a differentiated Hadean protocrust (Tusch et al., 2022) or that experienced core-mantle interaction (e.g., Mundl et al., 2017; Rizo et al., 2019; Jackson et al., 2020b and references therein; Mundl-Petermeier et al., 2020). A compilation by Jackson et al. (2020b) has shown that only geochemically depleted OIB with high $^{143}Nd/^{144}Nd$, low $^{206}Pb/^{204}Pb$ as well as high $^{3}He/^{4}He$ (≥ 8 R/R_A, typical MORB value relative to atmosphere) exhibit anomalous ^{182}W signatures. Thus, it has been inferred that primordial signatures are confined to mantle domains least modified by crustal recycling processes (Jackson et al., 2020b). Further, a recent study by Jansen et al., (2022) has shown that shallow-plume/ upper-mantle sourced continental- and oceanic-intraplate volcanic rocks are largely devoid of anomalous ^{182}W signatures. These combined constraints indicate the high $^{3}He/^{4}He$–low ^{182}W domains to be located within the Earths lower mantle, and likely along the core-mantle boundary (e.g., Mundl et al., 2017; Mundl-Petermeier et al., 2020; Jackson et al., 2020b; Jansen et al., 2022).

In this study, we present high precision ^{182}W isotope composition data for a comprehensive set of samples from the spatially associated Tristan-Gough hot-spot track (Walvis Ridge, Etendeka), the Discovery seamounts (Northern and Southern Seamounts) and the Shona hot-spot track, located within the South Atlantic (Fig. 2.1). Based on high $^{3}He/^{4}He$ ratios and slightly deficient $\mu^{182}W$ compositions found within lavas from Gough-type EM I lavas, it has recently been suggested that a primordial domain contributes to South Atlantic volcanism (Mundl et al., 2017). Our new data complement and significantly expand these initial data on South Atlantic volcanism. We also provide high-precision concentration data for W-U-Th (isotope dilution technique) to confirm that ^{182}W isotope systematics were not modified by late-stage alteration (e.g., König et al., 2011; Tusch et al., 2021). Finally, we combine our results with previously published Sr-Nd-Hf-Pb isotope data to constrain the contribution of primordial domains in the mantle to the sources of South Atlantic volcanism, to estimate the influence of recycled crustal materials and to constrain the geodynamic processes active in the mantle beneath the South Atlantic.

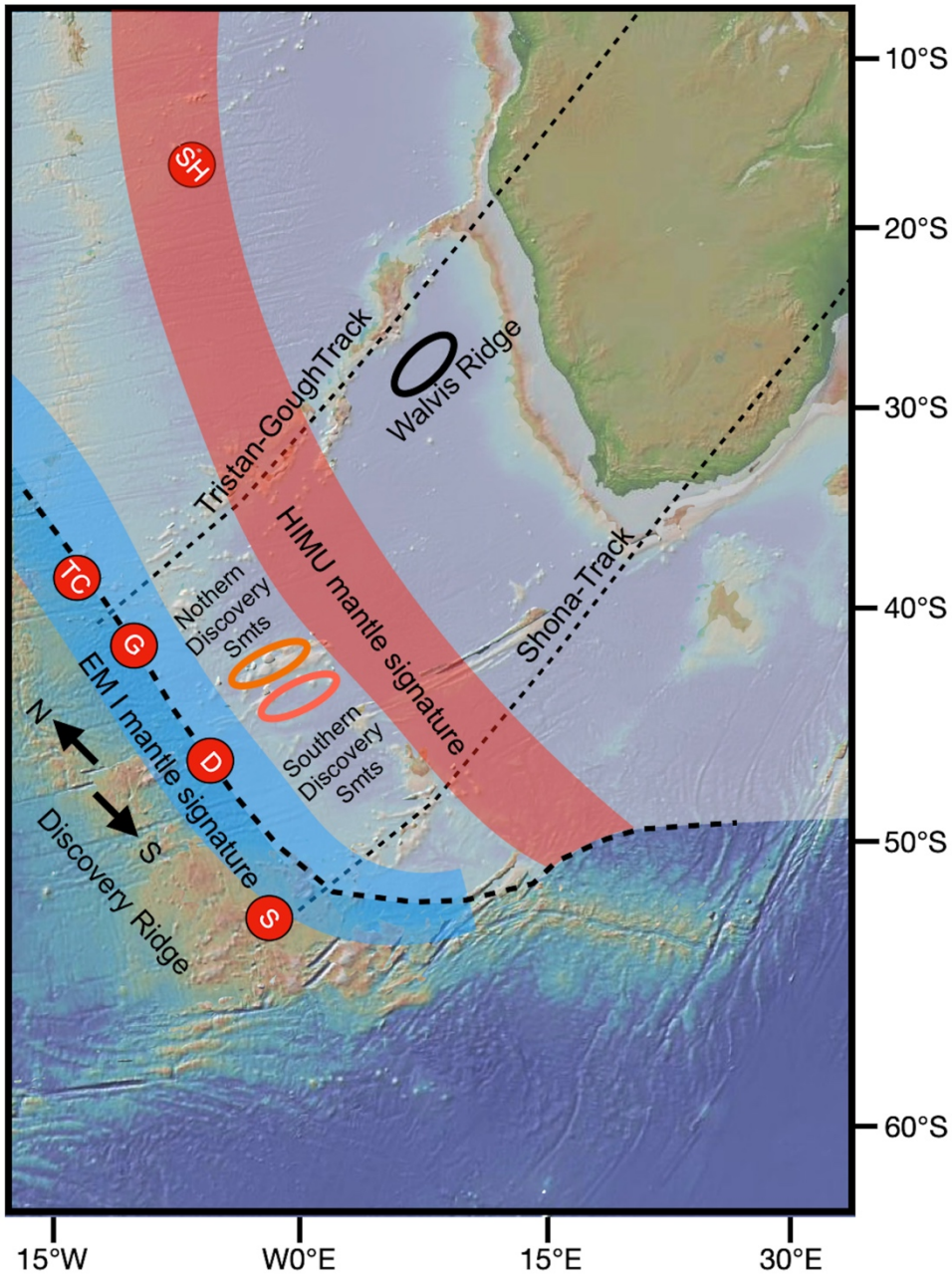

Figure 2.1 Bathymetric map of the South Atlantic, modified after Homrighausen et al. (2020). The map shows South Atlantic hotspot locations at present day including (red circle): SH, St. Helena; TC, Tristan da Cunha; G, Gough; D, Discovery; and S, Shona. Related hotspot tracks are indicated by dashed lines, the thick dotted line represents the 1% ∂Vs contour of the African LLSVP margin. The blue and red bands define the source regions that have been inferred for HIMU and EM I-type mantle sources in the lower-mantle. The Figure has been prepared using the Mac version of GeoMapApp (www.geomapapp.org).

Geological background

In the South Atlantic, three primary hotspots (Tristan-Gough, Discovery and Sona) occur in close proximity and are aligned along the outer margin of the African Large Low-Shear Velocity Province (LLSVP) (Fig. 2.1). Based on geochemical data, numerical simulations, geographical reconstructions and seismic data, it has been shown that Tristan-Gough, Discovery and Shona hotspots form age-progressive tracks and they are sourced from plume material originating from the lower-mantle (e.g., Homrighausen et al., 2020 and references therein). Notably, a deep source for the Tristan da Cunha hotspot series has been detected within several seismic tomography catalogues (e.g., Courtillot er al., 2003; French and Romanowicz, 2015; Doucet et al., 2020). In more detail, the currently active volcanic islands Tristan da Cunha and Gough are connected with the Etendeka/ Parana flood basalt provinces via a submarine track comprising the Walvis Ridge, the Rio Grande Rise and the Guyot Province (Fig. 2.1). Located approximately 500 km south of Tristan da Cunha and Gough, the Discovery hotspot is relatively short and comprises two separate seamount chains, the southern- and the northern- Discovery seamounts respectively (e.g., Schwindrofska et al., 2016 and references therein). Additionally, previous studies have shown the adjacent Mid Atlantic Ridge (MAR) segment and the (adjacent) Discovery seamounts to share geochemical similarities, suggesting discrete interactions of the rising plume and the MAR (Sarda et al., 2000; Schwindrofska et al., 2016). With regard to the Shona hotspot track, complex tectonic displacement has aggravated the reconstruction of a hotspot track (e.g., Hoernle et al., 2016 and references therein). However, current reconstructions and geochemical data suggest a zigzag pattern that connects volcanism from Africa across the Cape Rise seamounts, the Richardson seamount, the Agulhas Ridge, the Meteor Seamounts and the Shona Ridge (Fig. 2.1) (e.g., Hoernle et al., 2016 and references therein). Based on high $^{3}He/^{4}He$, deficient $\mu^{182}W$ and overall heterogenous Sr-Nd-Hf-Pb isotope compositions, it has been inferred that volcanism in the South Atlantic is sourced by multiple reservoirs that carry signals from recycled as well as primordial mantle materials (Homrighausen et al., 2020; Jackson et al., 2020b; Mundl-Petermeier et al., 2020). Notably, the three hot-spots investigated in this study lie above the outer margin of the African LLSVP and form paired, partially overlapping hot-spot tracks (Homrighausen et al., 2020 and references therein). For the Tristan-Gough hot-spot track, a systematic temporal offset of ~30 to ~40 Ma between EM I- and HIMU-like volcanism has been suggested to reflect the alignment of melt anomalies within the mantle in the direction

of plate motion (Homrighausen et al., 2020 and references therein). In this regard, the sharp geochemical and temporal zonation of the Tristan-Gough hot-spot track and its orientation roughly perpendicular to the margin of the African LLSVP led a recent study to suggest that active volcanism and the convective removal of material causes internal instabilities within the LLSVPs that result in secondary plume formation, tapping a HIMU-like reservoir (Homrighausen et al., 2020).

Results

The analytical protocols for HFSE concentration and W isotope measurements are summarized in the SI, protocols followed those of Tusch et al. (2019). All data can be found in Appendix II, Tables 1-5. Although concentrations of U (0.446–1.92 µg/g), Th (0.592–6.16 µg/g) and W (0.280–1.10 µg/g) display a wide range, the elemental ratios of W/Th (0.03 to 0.21) and W/U (0.14 to 0.58) are in the canonical range as confined by unaltered MORB glasses and OIBs (König et al., 2008; König et al., 2011) (Table 5, Fig. 2.2). Results of high precision ^{182}W isotope measurements are reported in the µ notation (ppm deviation relative to NIST SRM 3163) and represent averages of 4 to 13 single measurements conducted during one analytical session (Table 5, Fig. 2.3). Our samples exhibit $\mu^{182}W$ (6/4) values between -5.6 ± 6.5 and +4.6 ± 7.6 (+/- 95% c.i.) and overlap with ^{182}W isotope compositions that have been previously reported for MORBs, OIBs and continental intraplate volcanic rocks (Rizo et al., 2016; Rizo et al., 2019; Jackson et al., 2020b and references therein; Jansen et al. 2022). Further, ^{182}W compositions in samples from the Etendeka Plateau (NAM 61; $\mu^{182}W$ = -4.3 ± 4.0) and the Walvis Ridge (DR 90-6; $\mu^{182}W$ = -5.6 ± 6.5/ DR 89-7; $\mu^{182}W$ = -4.8 ± 3.7) that belong to the Walvis-Mocamedes subtrack of the Tristan-Gough hot-spot and represent the late-stage HIMU endmember composition, are in good agreement with the data presented by (Mundl-Petermeier et al., 2020). While measurements have often been performed on the edge of analytical resolvability, resulting in large uncertainties, calculated mean ^{182}W values of $\mu^{182}W$ = -4.9 ± 2.2 (HIMU) and $\mu^{182}W$ = +0.6 ± 1.2 (EM I) of both mantle endmembers are clearly resolvable. In the case of a low number of single measurements, the 2 s.d. of our inhouse reference materials measured at similar signal intensities was used throughout the discussion and related figures. This effects measurements of samples DSDP Leg 74 525 A57, MSM 19/3 DR53-1A and MSM 19/3 DR 49-2 that are now discussed with the 2 s.d. of two LP1 measurements of ± 3.4 and ± 4.3 respectively. Interestingly, those samples with more radiogenic Sr and Pb and

un-radiogenic Nd isotope composition that sample the EM I endmember (for data see Appendix II, Table 2-4, for references see Table 1) tend to less anomalous $\mu^{182}W$ values.

Discussion

Elemental ratios of W/Th and W/U can provide valuable insights into the origin and behavior of W within silicate systems (e.g., König et al. 2011, Jansen et al., 2022 and references therein). Given that fluid-mediated re-distribution of W during late-stage alteration can effectively overprint primary ^{182}W isotope signatures (e.g., Tusch et al., 2021), it is essential to carefully evaluate elemental concentrations. With the exception of sample MSM 19/3 DR 53-1A that exhibits slightly sub-canonical W/Th, the volcanic rocks analyzed here overlap with the defined canonical range (Fig. 2.2, Table. 5). Hence, measured W concentrations and isotope compositions can be regarded as being unaffected by secondary processes (Fig. 2.2).

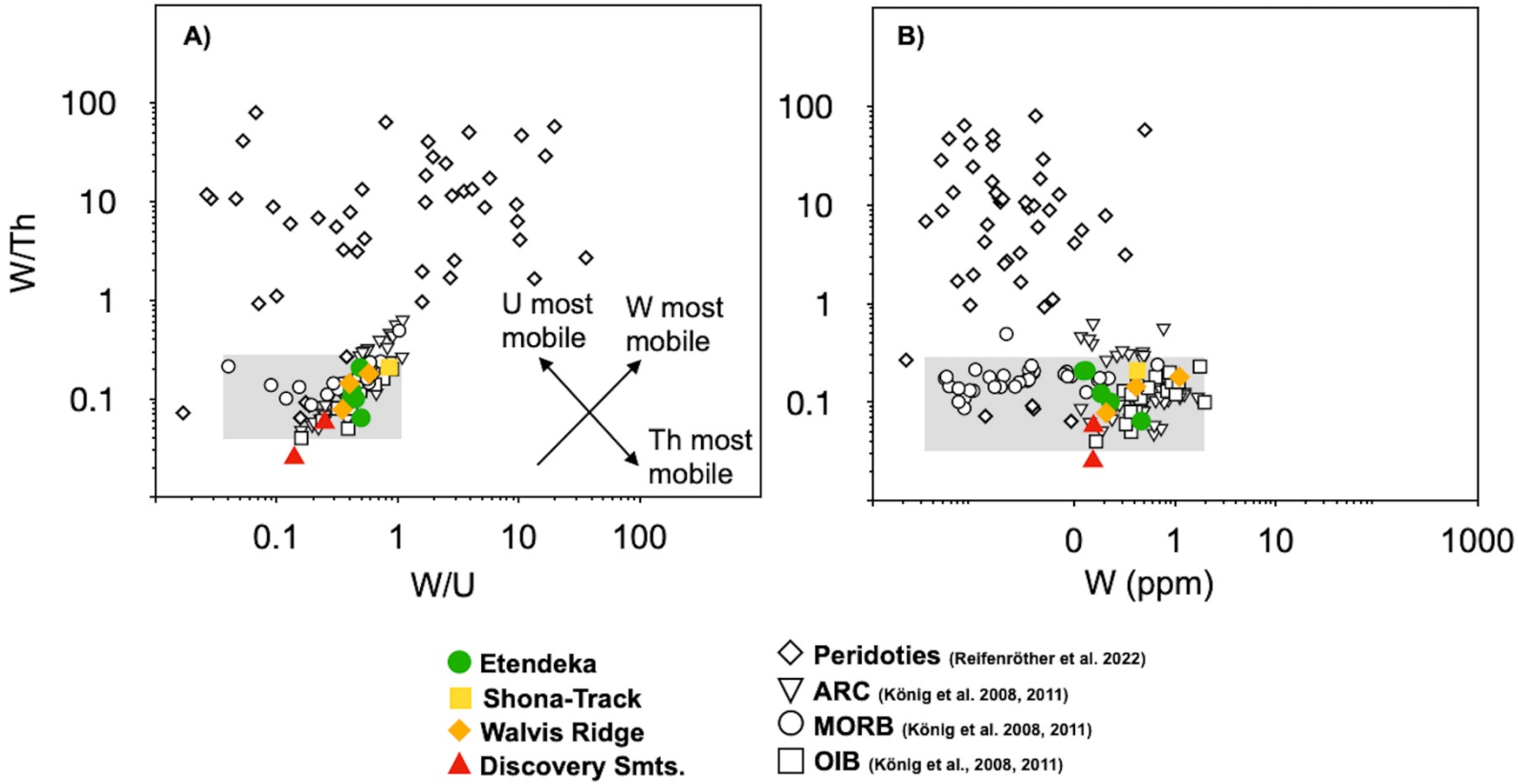

Figure 2.2 Evaluation of elemental W systematics using W/Th and W/U ratios**.** Grey shaded areas define canonical compositions defined by unaltered MORB glasses and OIB from König et al. (2008, 2011). Samples of peridotites and subduction settings are taken from Reifenröther et al. (2021, 2022) and König et al. (2008, 2011). With the exception of one sample that is displaced towards sub-canonical W/Th ratios, all samples analyzed within this study overlap with the canonical compositions that have been inferred for MORB and OIB. As such, we do not find evidence for a secondary re-distribution of tungsten.

Considering volcanism in the south Atlantic, several seismic and geochemical investigations have shown related hotspots to be derived from the African LLSVP (e.g., Courtillot er al., 2003; French and Romanowicz, 2015; Doucet et al., 2020; Homrighausen et al., 2020). Additionally, previous literature data for samples from the Tristan-Gough hot-spot-track and the Discovery Ridge revealed $\mu^{182}W$ values as low as -9.0 ± 2.7 ppm that are correlated with high $^{3}He/^{4}He$ ratios up to 15 R/R_A (Mundl-Petermeier et al. (2020). A recent, global compilation by Jackson et al. (2020b) has shown that the Sr-Nd-Pb isotope compositions of OIBs are coupled with $^{3}He/^{4}He$ and ^{182}W systematics. The authors introduced the $D^{Sr\text{-}Nd\text{-}Pb}$ value, that integrates Sr-Nd-Pb isotope signatures and describes the compositional range of OIB samples. This approach can reveal that primordial anomalies are mostly found in OIBs that tap mantle domains least affected by recycling or interaction with the DM. Indeed, our more comprehensive suite of OIB samples from the Tristan-Gough, Discovery and Shona hot-spot-tracks ($D^{Sr\text{-}Nd\text{-}Pb}$ from 0.74 to 2.9) confirm the coupling between $D^{Sr\text{-}Nd\text{-}Pb}$ values and ^{182}W isotope compositions and reveal that the global trend even appears at the scale of small-scale plume systems (Fig. 2.4). Similar to Mundl-Petermeier et al. (2020) some of our samples exhibit slightly deficient $\mu^{182}W$ isotope compositions (-5.6 ± 6.5 to -4.3 ± 4.0 ppm) that are on the edge of analytical resolvability but confirm the contribution of a primordial reservoir within the Tristan-Gough hot-spot-track. Samples with slightly negative $\mu^{182}W$ values belong to the secondary Walvis-Mocamedes HIMU-lineage, a sub-track of the Tristan-Gough hot-spot (Homrighausen et al., 2020). In contrast, older volcanic rocks from the Tristan-Gough hot-spot-track, samples from the Discovery Seamounts and the Shona-Track that display radiogenic isotope compositions of EM I affinity do not display anomalous ^{182}W isotope compositions ($\mu^{182}W$ = -1.3 ± 3.1 to +4.6 ± 3.4). While anomalous compositions of single samples are barely resolvable in some cases, the calculated mean ^{182}W values of $\mu^{182}W$ = -4.9 ± 2.2 (HIMU) and $\mu^{182}W$ = +0.6 ± 1.2 (EM I) in our sample collection suggest the contribution of primordial material to be limited to late-stage Walvis-Mocamedes volcanism of the Tristan-Gough hotspot track with HIMU affinity.

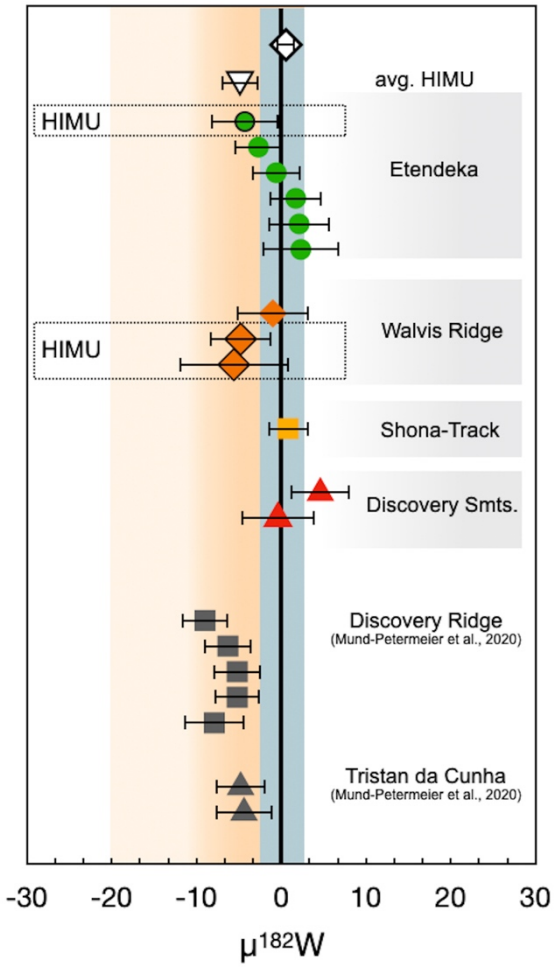

Figure 2.3 Measured $\mu^{182}W$ compositions of OIB samples from this study. Additional data from the Discovery Ridge and Tristan da Cunha are taken from (Mundl et al., 2017; Mundl-Petermeier et al., 2020). Analytical uncertainties are given by the 95% c.i. of multiple single measurements. In the case of a low number of single measurements, the 2 s.d. of our inhouse reference materials measured at similar signal intensities was used. This effects measurements of samples DSDP Leg 74 525 A57, MSM 19/3 DR53-1A and MSM 19/3 DR 49-2.While single measurements are on the edge of resolvability, calculated mean values for EM-I and HIMU-like samples clearly suggest deficient ^{182}W compositions to be restricted to samples of HIMU-affinity.

Given that primordial ^{182}W signatures at low $D^{Sr\text{-}Nd\text{-}Pb}$ values are still found within Gough-Type EM lavas (Mundl-Petermeier et al., 2020) as well as now in HIMU-type lavas of the South Atlantic region (this study), it appears likely that entrained primordial signatures were not completely overprinted by the addition of recycled material. However, at increasing amounts of recycled material and higher $D^{Sr\text{-}Nd\text{-}Pb}$ of the anomalous $\mu^{182}W$ disappear, which is again in line with the model by Jackson et al. (2020b) (Fig. 2.4).

Considering the global dataset, ^{182}W anomalies and high $^{3}He/^{4}He$ ratios have been reported for OIBs sourced by the African- as well as the Pacific-LLSVP. Recent geodynamic models have indicated a deep-mantle geochemical dichotomy, that can be best explained by the African LLSVP as being contaminated by continental crustal materials whereas the Pacific LLSVP has been largely protected of such additions for least the past 600 Ma (Doucet et al., 2020). In detail, this has been explained by the changing subduction polarity that is associated with the supercontinent cycle and an enhanced enrichment of the African LLSVP during the assembly and breakup of Gondwana (Doucet et al., 2020). Further, this compositional heterogeneity has lead to different densities of both LLSVPs, resulting in different long-term interactions and material exchange with the surrounding mantle (Yuan et al., 2022). Combining new and existing ^{182}W and long-lived radiogenic isotope data, the heterogenous distribution of primordial material with south Atlantic plume volcanism thus provides further evidence for a general instability of the African LLSVP (e.g., Homrighausen et al., 2020; Yuan et al., 2022). Given that the oldest reported HIMU volcanism of the Tristan-Gough hotspot track is ~30 to 40 Ma younger than the EM I-type volcanism at the same location, Homrighausen et al., (2020) has proposed that the sudden removal of EM material at the outer LLSVP margin has generated internal instabilities that have triggered smaller, transient secondary plumes from the interior of the LLSVP. Conclusively, our data thus indicates that lower-mantle dynamics, such as cold downwellings and the constant removal of LLSVP material throughout plume related upwellings, lead to a heterogenous entrainment of primordial material. Combining the data of Mundl-Petermeier et al., (2020) and this study, measured ^{182}W composition thus tentatively suggest that the entrainment of primordial material within South Atlantic mantle plumes has been triggered by secondary plume formation.

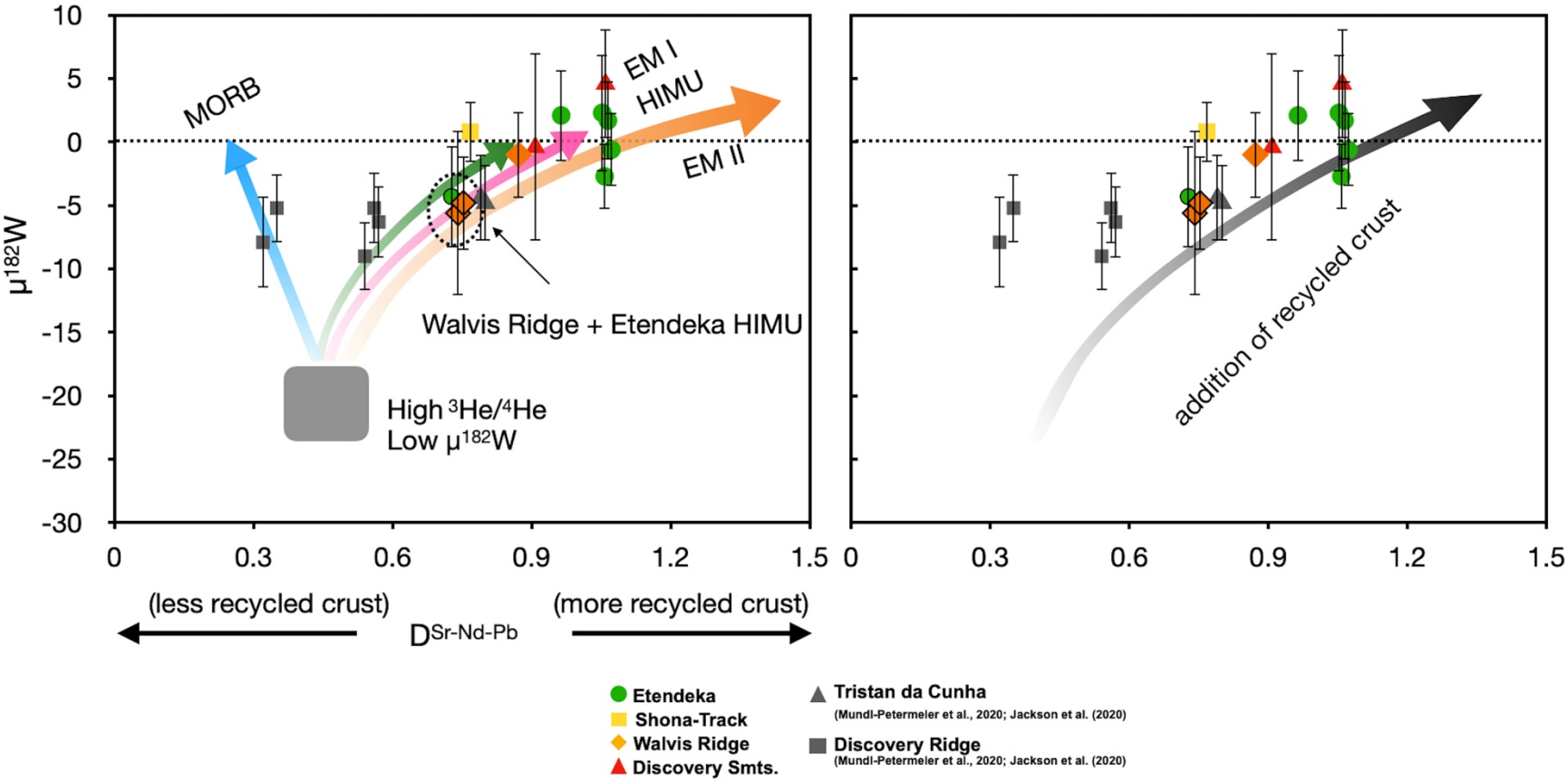

Figure 2.4 Plot of $\mu^{182}W$ versus the $D^{Sr\text{-}Nd\text{-}Pb}$ value defining the amount of recycle components(Jackson et al. (020b) . $D^{Sr\text{-}Nd\text{-}Pb}$ values were calculated using previously published data (for references see Table 1). Note that $D^{Sr\text{-}Nd\text{-}Pb}$ values for literature data from Discovery Ridge are not shown by Jackson et al. (2020b) but have been calculated using Sr-Nd-Pb isotope compositions of the samples published in Sarda et al. (2000). We observe a positive correlation between $D^{Sr\text{-}Nd\text{-}Pb}$ and $\mu^{182}W$ for our dataset, indicating that primordial signatures are obscured by the addition of recycled material. Excluding modelled curves of Jackson et a., (2020), the trend displayed by south-Atlantic volcanism is clearly illustrated in the right panel.

Supplementary Information

For W, U, Th isotope dilution measurements, approximately 100mg splits of samples were spiked with mixed $^{233\text{-}236}U$ – ^{229}Th and ^{183}W – ^{180}Ta – ^{180}Hf – ^{176}Lu – ^{94}Zr tracers (Weyer et al. 2002; Münker, 2010) and dissolved in 6 ml of a 1:1 $cHNO_3$/cHF mixture on a hotplate at 130 °C for ~24h. After a repeated drydown in concentrated HNO_3, the samples were re-dissolved in 6 ml of a 6N HCl – 0.06N HF solution for 5-6h at 120 °C to achieve full sample-spike equilibrium. Tungsten separation was then achieved following a shortened procedure described in Kleine et al. (2004). Further, the elements U and Th were separated following the method of Luo et al. (1997). All isotope dilution measurements were conducted at the University of Cologne, using a Thermo-Fisher® Neptune MC-ICP-MS. For a more detailed description, see Tusch et al. (2019, 2021). The external precision and accuracy for isotope dilution measurements is typically better than ± 1%.

Tungsten was separated from bulk rock samples following the protocols described in Tusch et al. (2019, 2021). Up to 26 g of sample powder were digested in a 1:1 $cHNO_3$/cHF mixture in closed Savillex® PFA vials on a hotplate at 130°C for at least 24 h. The approximate amount of sample material used for measurements is reported in Table 1 of the main manuscript. After evaporation to near dryness, the samples were dried down three times using 5 ml concentrated HNO_3 to avoid the formation of insoluble fluorides. Following complete evaporation at moderate temperatures (~100°C) the samples were converted to chloride form using 30 ml 6 N HCl and fully digested at 130°C. In case of incomplete dissolution, the HCl digestion step was repeated. When the solution was visibly clear, the samples were dried down and sample aliquots were re-dissolved in up to 20 ml of 1 M HCl. Tungsten was separated in a four-column procedure employing cation, anion, TEVA and TODGA resins (Tusch et al. 2019, 2021). Depending on the W concentration, up to 30 sample splits were individually passed through the chemical separation procedure and recombined prior to the measurement. Procedural yields for W were generally ≥ 60%. Total procedural W blanks were determined by isotope dilution (i.e. Kurzweil et al., 2018) and were usually below 500pg, contributing less than 1% to the total analyte. High-precision W isotope composition measurements were performed using the Thermo-Fisher® Neptune Plus MC-ICP-MS at the University of Cologne, following the protocols given by Tusch et al. (2019, 2021). The low-abundance isotope ^{180}W and the

interference monitor ^{177}Hf were measured in Faraday collectors connected to 10^{13} Ω amplifiers, while all other isotopes were measured using 10^{11} Ω amplifiers. Analyses were performed in static and low-resolution mode, using a standard sample and an X-type skimmer cone. Interferences at masses 184 and 186 were monitored by simultaneously measuring ^{188}Os, while Hf and Ta interferences on mass 180 were monitored by measuring ^{177}Hf, ^{178}Hf and ^{181}Ta. For mass bias corrections we used the exponential law, normalizing either to ^{186}W/^{184}W = 0.92767 (denoted '6/4') or ^{186}W/^{183}W = 1.9859 (denoted '6/3'). For a 50 ng/g solution, a signal intensity of 4.5V was typically achieved for ^{182}W (corresponding to 90 V per ppm W). Samples analyzed in this study were run at ^{182}W intensities between 1.1 and 25 V. To achieve sufficient precision, we performed multiple measurements of sample solutions that were combined from 1-1.2 g aliquots, each of which were individually processed through the separation procedure. In each measurement session samples were bracketed by the reference material NIST SRM 3163. To assess the long-term reproducibility we always included one of our three in-house reference materials during each analytical session (historical La Palma Basalt "LP 1", Kurzweil et al. (2019) and a 3455 Ma old grey gneiss "AGC 351" from southwest Swaziland (Kroener et al. 2014)). During the analytical campaign we also analyzed a 3.27 Ga old komatiite from the Pilbara Craton (sample 160245, Ruth Well Formation), Western Australia, that was shown to exhibit an excess in μ^{182}W of +6.8 ± 2.3 ppm (Tusch et al. 2021). Final results are reported in the μ notation (ppm deviation relative to NIST SRM 3163). The intermediate precision of our in-house reference materials, given by the mean value of multiple session averages, is μ182W = -0.2 ± 0.8 ppm (AGC 351), -0.6 ± 1.5 ppm (LP 1) and 8.3 ± 1.1 ppm (160245). These data include as well measurements that have been conducted during the analytical campaign of Jansen et al. (2022) (Fig. SI 1).

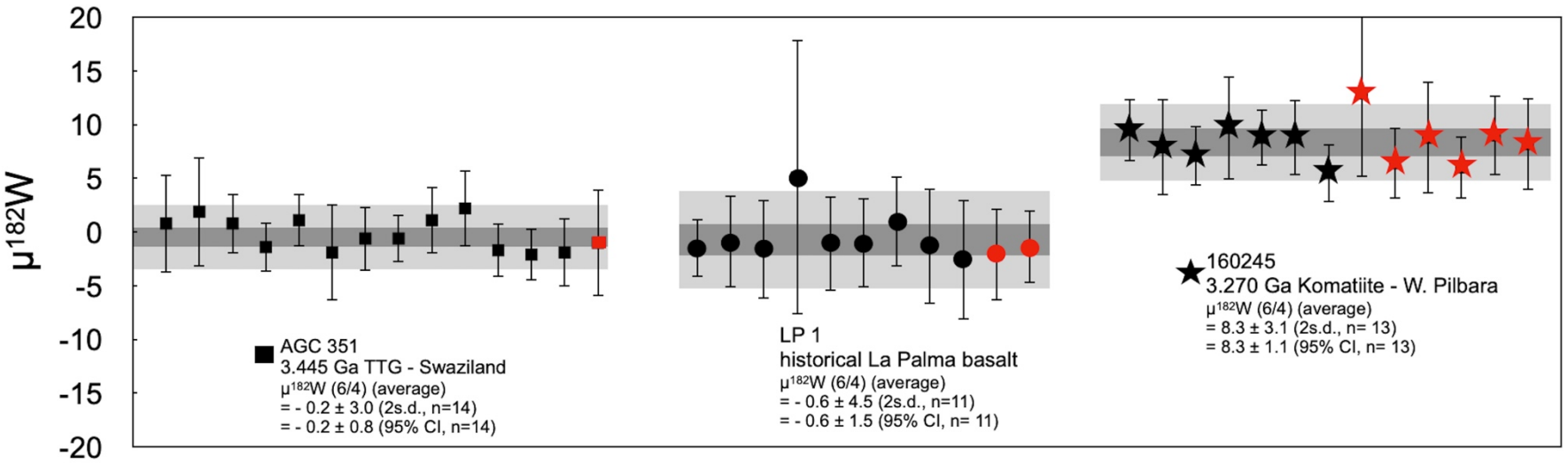

Figure SI 1. Intermediate precision for $\mu^{182}W$ (6/4). Values are inferred from the repeated analysis of multiple digestions for our in-house reference materials granite AGC 351, basalt LP 1 and komatiite 160245 that are reported relative to NIST SRM 3163. Each symbol refers to the average value of multiple measurements (up to n = 14) conducted during an analytical session. The uncertainties for the session mean values are given by the corresponding 95% c.i. The long-term intermediate precision (2 standard deviations) for our in-house reference materials are given by the 2 SD of the session mean value. This Figure also includes measurements that have been conducted during the analytical campaign of Jansen et al., (2022).

Chapter III: Petrogenesis of magmatic rocks from the Quaternary Eifel Volcanic Fields, Germany- insights from combined high precision trace-element and Sr-Nd-Hf-Pb-Os isotope data

Introduction

Volcanism within the Central European Volcanic Province (CEVP) commenced in the late Cretaceous (< 65 Ma, (Wilson and Downes, 1991)) and continued throughout the Tertiary until today (Wilson and Downes, 1991). The CEVP forms a 750 km-long volcanic belt that extends across continental Europe from France to Poland and Hungary. Eruptive volcanism has been dominated by lavas that occur in spatially distinct, individual volcanic fields and comprise monogenetic centers, scattered necks and plugs (Wörner et al., 1986; Wilson and Downes, 1991; Cohen and Waters, 1996; Lustrino and Wilson, 2007). Focusing on northern central Europe, several studies have investigated the geochronological, geochemical and petrological characteristics of pre-Pleistocene volcanism within the Siebengebirge (e.g.,Todt and Lippolt, 1980; Kolb et al., 2012; Schneider et al., 2016; Jung et al., 2012), Vogelsberg (Jung and Masberg, 1998; Haase et al., 2004; Jung et al., 2011), Rhön (Jung and Hoernes, 2000; Jung et al., 2005), Westerwald (Haase et al., 2004), Urach-Hegau (e.g., Hegner et al., 1995), Heldburg (Abratis et al., 2015, Pfänder et al., 2018) and the Hocheifel (Jung et al., 2006; Fekiacova et al., 2007). One of the major questions driving ongoing research on CEVP volcanism is, as to whether the mantle sources of the primary magmas are dominated by the convecting asthenosphere or the overlying lithospheric mantle. Based on geochemical compositions that are broadly similar to Ocean Island Basalts (OIB) (Hofmann, 2003; Stracke et al., 2005) and on geophysical evidence (e.g., Granet et al., 1995; Hoernle et al., 1995; Goes et al., 1999), it has been argued that CEVP volcanism is linked to mantle plume activity. However, although several seismic studies reported anomalous mantle temperatures and low-velocity anomalies in the mantle underneath the CEVP (e.g., Ritter et al., 2001; Ritter and Christensen, 2007), it yet remains ambiguous if one or multiple mantle plumes exist underneath central Europe and from which mantle depth upwelling material is sourced (e.g., Granet et al., 1995; Goes et al., 1999; Goes et al., 2000; Ritter et al., 2001; Ritter and Christensen, 2007). As an alternative to plume models, OIB-like compositions found in continental intraplate volcanic rocks have been

explained by the entrainment of mantle lithosphere and crustal materials en route to the surface, given that continental intraplate basalts erupt through a variably thick lithosphere (e.g., Wilson and Downes, 1991). As most of the volcanic fields within the CEVP are pertaining to a NNE-trending rift system that includes the Rhone, Limagne, Bresse, Rhine, Ruhr and Leine Graben structures (e.g., Wilson and Downes, 1991) volcanism has been suggested to originate from passive upwelling and extension-induced adiabatic decompression melting (e.g., Bogaard and Wörner, 2003; Fekiacova et al., 2007; Kolb et al., 2012). Notably, state of the art geochemical data for volcanic rocks from the quaternary Eifel Volcanic Field in western Germany, one of the key volcanic suites to better understand magmatism of the CEVP, were missing so far. In this study, we aim to fill this gap by presenting a comprehensive trace element and Sr-Nd-Pb-Hf-Os isotope dataset for representative volcanic rocks of the Quaternary Eifel volcanic field that helps to evaluate the different petrogenetic models being proposed.

Regional Geological Setting and sample selection

The Eifel Volcanic Field (EVF) is located within the Rhenish Massif, an uplifted lithological block that is confined by the Upper- and Lower Rhine Graben in Western Germany. The continental lithosphere beneath Europe has experienced a complex history of collisional- and extensional events, causing volcanism in both subduction- and extension related settings (Wilson and Downes, 1991). Major structural domains of central Europe (e.g., Rhenish Massif) have been emplaced during the Hercynian orogeny (360 to ~300 Ma (Wilson and Downes, 1991)) in the Upper Devonian and Lower Carboniferous (Wilson and Downes, 1991). As a result, several microcontinents have been accreted during the collision of Laurasia and Gondwana, juxtaposing various tectonic terranes with different tectono-magmatic histories (Wilson and Downes, 1991). Continuous subsidence during the Cenozoic and Quaternary as well as during the Alpine orogeny have facilitated the formation of numerous horst and graben systems, potentially generating pathways for melts. These pathways were generated by (1) lithospheric flexure and passive decompression melting of the upper-mantle, (2) lithospheric mantle sources or (3) upwelling material from one or multiple mantle plumes (e.g.,Wilson and Downes, 1991; Ritter et al., 2001; Ritter and Christensen, 2007). Conclusively, it has been proposed that the primary magmas of the CEVP result from a complex mixture involving overall heterogenous asthenospheric- and lithospheric mantle sources (e.g.,Wörner et al., 1986; Wilson and Downes, 1991; Jung et al., 2006; Kolb et al., 2012; Pfänder et al., 2012; Schneider

et al., 2016; Pfänder et al., 2018). Stratigraphically, the basement of the EVF is built up by upper-crustal Devonian and Triassic sediments, a mid-crustal metamorphic basement (e.g., mica-schists) and lower crustal mafic rocks in granulite facies (Stosch and Lugmair, 1984; Wörner et al., 1985; Stosch and Lugmair, 1986; Wörner et al., 1986). Based on spatial, temporal and compositional patterns, the EVF can be further subdivided into a Tertiary Hocheifel Volcanic Field (HEVF) (~44-35 Ma (Fekiacova et al., 2007)) and two Quaternary subfields, the West Eifel Volcanic Field (WEVF, ~700-10.8 ka) and the East Eifel Volcanic Field (EVF, 500 – 12.9 ka) (Schmincke, 2007 and references therein). The older WEVF is dominated by scoria cones and maars, has an aerial extent of ~600 km^2 and extends form Ormond in the northwest to Bad Bertrich in the southeast. In contrast, the EEVF (areal extent of ~400 km^2) comprises four phonolitic centers that can be distinguished in space and time: Kempenich (450 to 500 ka (Schmincke, 2007)), Rieden (430 to 360 ka (Viereck, 1984)), Wehr (215 to 190 ka (van den Bogaard et al., 1989)) and Laacher See (12.9 ka (Van den Bogaard, 1995)).

The eruptive products of the WEVF differ from those of the EEVF by displaying more mafic and silica-undersaturated magmatic compositions and a greater abundance of mantle xenoliths (e.g., Schmincke, 2007 and references therein). The EEFV contains rare maars but numerous scoria cones and large-scale lava flows (e.g., Schmincke, 2007 and references therein) that are often more differentiated in composition. Primitive volcanic rocks of the WEVF and EEVF are all SiO_2 undersaturated, mafic and alkaline and the WEVF rocks can be subdivided into distinct petrogenetic suites, (1) a suite mainly composed of nephelinites and melilitites (F-suite) and an olivine-nephelinite-basanite-Suite (ONB-Suite) (Mertes and Schmincke, 1985).
The occurrence and distribution of both petrogenetic suites in the WEVF appears to be time sensitive (Mertes and Schmincke, 1985; Mertz et al., 2015). Magmas of F-Suite affinity are found in lavas older than 480 ka, whereas ONB-Suite magmas are restricted to the younger magmatic episode between 81 and 11 ka (Mertz et al., 2015). Within the EEVF, mafic magmas generally resemble the compositional spectrum reported for the F-Suite in the WEVF and are thus referred to here as the eastern F-Suite (FE-Suite). From a Sr-Nd-Pb isotope perspective, samples of the Quaternary EVF span a range from compositions similar to enriched Mid-Ocean-Ridge Basalt (E-MORB) to Bulk Silicate Earth (BSE) compositions, and some lavas even display compositional similarities to the classical Enriched Mantle- (EM-I, EM-II) and HIMU endmembers found in plume-related OIBs (Wörner et al., 1986). Detailed evaluations by Wörner et al. (1986) have demonstrated that crustal assimilation has only played a minor

role within EVF volcanism, as the variability of isotope compositions rather records a heterogenous composition of mantle underneath the EEVF. However, compared to other volcanic provinces within central Europe, only limited high precision trace-element and radiogenic isotope data are available for Quaternary EVF volcanism. In addition, most previous studies focused on Tertiary volcanic rocks (e.g., Wörner et al., 1986; Jung et al., 2006; Fekiacova et al., 2007). Thus, the relationships between Tertiary and Quaternary volcanism and the difference in mantle sources involved in magma genesis remain poorly constrained.

Extensive studies on mantle xenoliths have shown that minerals found within clinopyroxenite and hornblendite veins share nearly the same diversity in trace-element and radiogenic isotope compositions as all of the Quaternary Eifel lavas (e.g., Witt-Eickschen and Kramm, 1998; Witt-Eickschen et al., 2003). As the mantle xenoliths display Sr-Nd-Pb isotope compositions of HIMU-EM I affinity, but lack a DMM signature, it has been inferred that a metasomatic overprint of the lithospheric mantle underneath the Eifel has occurred at earliest in the Tertiary (Witt-Eickschen and Kramm, 1998; Witt-Eickschen et al., 2003). Witt-Eickschen et al. (2003) have suggested that the compositional diversity of xenoliths in Eifel lavas has resulted from the interaction of primary (DMM-like) asthenospheric melts and a highly enriched litospheric mantle. This is broadly similar to the model of Mertz et al. (2015) who envisioned mixtures of asthenospheric and litospheric melts to account for the varying geochemical compositions of west Eifel ONB- and F-Suites. Moreover, based on detailed age constraints and seismological data, Mertz et al. (2015) have mapped out a spatial boundary separating > 480 ka F-Suite and < 80 ka ONB-Suite volcanism. While the ONB-Suite overlaps with a surface-projected low-velocity anomaly, indicative of a plume-like source within the asthenosphere, seismic data suggests that the areal extent of F-Suite volcanism is rather linked to an intensive thermal erosion of the lithosphere. As such, the geochemical compositions of ONB-Suite volcanic rocks are therefore thought to mirror the asthenospheric source reservoir, whereas F-Suite rocks are compositionally similar to the metasomatized litospheric mantle (Mertz et al., 2015).

For this study we have selected 59 samples that cover both Quaternary volcanic subfields, the WEVF and the EEVF, respectively. Moreover, we have sampled volcanic edifices (e.g., scoria cones, lava flows, dikes) that have been previously characterized (Mertes, 1983; Mertes and Schmincke, 1985) and were used to define the F-, FE- and ONB-Suite petrogenetic groups (Mertes and Schmincke, 1985). Furthermore, we have sampled selected highly differentiated

phonolitic domes from the EEVF, including the Rieden and Wehr volcanic complexes. The sampling sites are shown in a simplified geological map in Figure 3.1. More details on the sampling sites, including coordinates can be found in Appendix III. In the field, sampling has been focused on fresh, large scale blocks from which hand specimens were also collected. Following further alteration control throughout thin sections, we analyzed all samples for their major- and trace element compositions as well as their $^{87}Sr/^{86}Sr$, $^{143}Nd/^{144}Nd$, $^{176}Hf/^{177}Hf$, $^{206,207,208}Pb/^{204}Pb$ isotope compositions. Selected samples were also analyzed for their $^{187}Os/^{188}Os$ isotope compositions and HSE content.

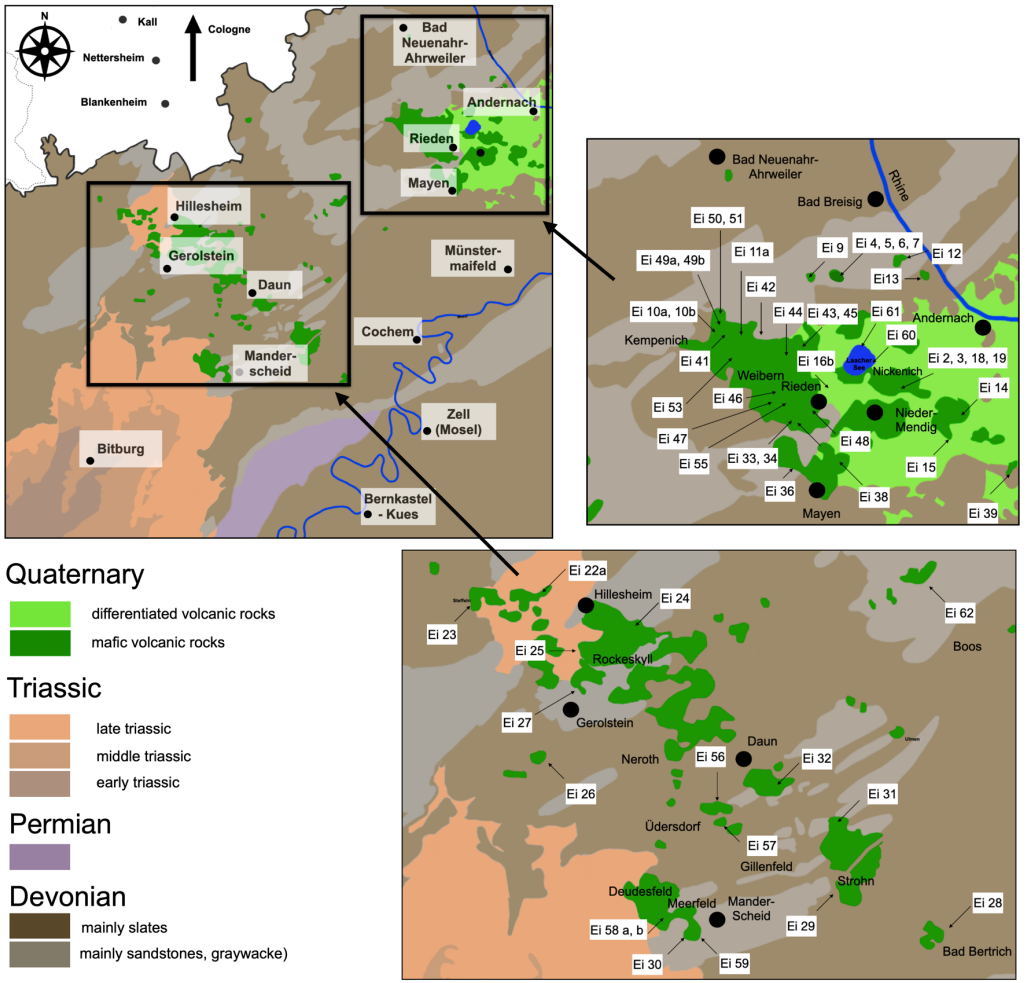

Figure 3.1 Simplified geological map showing the regional extent of the Quaternary Eifel Volcanic Fields (EVF) and the sample sites investigated.

Methods

Major elements were analyzed by XRF on fused disks using a Phillips PW 2400 spectrometer at the University of Cologne (see Appendix III, Table 1). Trace elements were measured with a quadrupole ICP-MS using an Agilent 7500cs mass spectrometer at the University of Kiel following the analytical protocol by Garbe-Schönberg (1993) or with a Thermo Fischer iCap-Q at the University of Cologne. For trace element analysis, a representative sample split of ~100 mg was dissolved through the following digestion steps. In the first step, the samples were dissolved in a 1:1 $cHNO_3$/cHF mixture (6ml) in closed Savillex® PFA Beakers on a hot plate at 130-150 °C for at least two days (Tabletop digestion). To ensure the complete digestion of more differentiated, felsic samples, the samples were dried down and re-digested in Parr® bombs for 24h at 180°C using the same acid mixture as for the Tabletop digestion (e.g., Hoffmann et al., 2011). Next, the samples were evaporated to near dryness and ~10 ml $cHNO_3$ were added. This step was repeated three times to remove any residual HF. To ensure complete sample digestion, samples were re-dissolved in ~5 ml 2.8 N HNO_3 and checked for residual precipitates. Fully dissolved samples were dried down at ~100 °C, before they were dissolved again in 10 ml 2.8 N HNO_3 and diluted for final measurements.

For Sr-Nd-Hf isotope analysis ~100 mg of sample powder was leached in cold 6N HCl for 15 min. After repeated washing steps, the samples were digested following the same digestion technique as for trace elements by tabletop digestion. To avoid the formation of insoluble fluorides, the samples were dried down to incipient dryness and treated three times with ~10 ml $cHNO_3$. Following a complete drydown, the samples were re-dissolved in ~5 ml 3N HCl. Following the procedure of Münker et al. (2001) a clean Hf and a matrix cut were obtained using Eichrom Ln-Spec ion exchange resin. Further separation of Sr and Nd from the matrix cut followed the methods given in, using AG 50W-X8 and Eichrom Ln-Spec ion exchange resins (Pin and Zalduegui, 1997).

For Pb isotope measurements, ~250 mg, hand-picked 3-4 mm sized, whole rock chips were chosen and subsequently leached in 3N and 6N HCl for 1h, respectively (Schuth et al., 2011). Following a digestion step in a 3:1 cHF-$cHNO_3$ mixture, Pb was purified following the methods outlined in Korkisch and Hazan (1965) using AG 1-X8 anion resin.

For HSE (highly siderophile elements) and ^{187}Re-^{187}Os analysis, ~0.5 to 2 g of sample powder was spiked with a mixed ^{185}Re–^{190}Os–^{192}Ir–^{194}Pt tracer, digested in 7 ml of a 5:1 $cHNO_3$-cHCl

mixture and treated at 270°C between 100 and 130 bar in an Anton Paar high-pressure asher (HPA) for 12 h. Osmium was then extracted from the liquidus phase using the liquid extraction procedure described by Cohen and Waters (1996) and further purified using a H_2SO_4/ H_2CrO_4 micro-destillation technique (Birck et al., 1997). Following the Os extraction, the aqua regia fraction which contains all other HSEs and undissolved components was dried down and re-dissolved in cHF at 120°C. After the samples were dried down the HSEs were separated on AG 1-X8 resin, following published protocols by Rehkämper and Halliday (1997) and Coggon et al. (2013).

Strontium-Nd-Hf-Pb Isotope measurements were performed on a Thermo Fisher Neptune MC ICP-MS at the University of Cologne. The measured Sr-Nd isotope data were mass bias corrected using the exponential law and normalized to $^{86}Sr/^{88}Sr = 0.1194$ and $^{146}Nd/^{144}Nd = 0.7219$, respectively. The measured values are reported relative to the accepted values for NBS 987 and La Jolla ($^{87}Sr/^{86}Sr = 0.710240$ for NBS 987 and $^{143}Nd/^{144}Nd = 0.511859$ for La Jolla). Hafnium isotope data are reported relative to the Münster AMES standard which has a $^{176}Hf/^{177}Hf$ of 0.282160 and is indistinguishable from the JMC 475 Hf standard (Blichert-Toft and Albarède, 1997). The external long-term reproducibility is ±0.5 ε-units for Sr and ±0.4 ε-units for Nd and Hf respectively. Procedural blanks were typically <100 pg for Hf and <300 pg for Nd and Sr.

For Pb isotope analysis, doped NBS 991 Tl was used for mass bias correction, assuming a $^{205}Tl/^{203}Tl$ ratio of 1.0083 (Hirata, 1996; Albarede et al., 2004; Kirchenbauer et al., 2011). Procedural blanks of Pb isotope measurements were typically better than 40 pg.

Osmium isotope compositions were measured using a Thermo Finnigan Triton Thermal Ionization Mass Spectrometer at the Department of Lithospheric Research at the University of Vienna. Osmium was measured as OsO^{3-} ions, applying a peak hopping sequence using the Triton SEM detector. Oxygen corrections have been performed using $^{17}O/^{16}O = 0.0003866$ and $^{17}O/^{16}O = 0.00203406$ (Van Acken et al., 2011). Isobaric interferences of ^{187}Re on ^{187}Os and mass fractionation were conducted offline, using $^{192}Os/^{188}Os = 3.083$.

Rhenium, Os, Pt and Ir concentrations were measured by isotope dilution on a Thermo Element ICP-MS at the Steinmann Institute at the University of Bonn. Instrumental drift was monitored and corrected using a 1 ppb in-house multi-element HSE standard solution with ratios of $^{185}Re/^{187}Re = 0.5986$, $^{191}Ir/^{193}Ir = 0.5957$ and $^{198}Pt/^{195}Pt = 0.2117$. Additional isobaric Hf-oxide interferences on Ir and Pt were monitored and corrected offline. Analytical blanks were in a range of 0.5–0.5 pg (Os), 3–4 pg (Re), 0.5–2 pg (Ir) and 10-30 pg for Pt.

Results

Major- and Trace-element compositions

All data of this study are listed in Appendix III, Tables 1-5. Major and trace element compositions are listed in Appendix III, Table 1 and 2 and shown in Figs. 3.2-3.4. The samples analyzed in this study were classified using the TAS (total alkali vs. silica) classification (Le Bas et al., 1986). Based on this classification, the samples are characterized as silica undersaturated and alkaline (SiO_2 = 39.4 wt.% to 54.7 wt.%; Na_2O+K_2O = 4.22 to 19.2 wt. %) (Fig. 3.2). Using the CIPW nomenclature (see Appendix III, Table 4), most samples that plot within the basanite/ tephrite field and contain ≥ 10 wt.% olivine (Fig. 3.3). With the exception of few samples from the F-Suite, foiditic and more differentiated compositions are only found within samples from the EEVF. Foiditic rocks from the EEVF define a differentiation trend that can be identified by decreasing amounts of normative larnite (15.0 wt.% to 0.0 wt.%) at increasing amounts of normative nepheline (16.9 wt.% to 31.8 wt.%) and orthoclase (0.0 wt.% to 45.7 wt.%). Following the previous classification-scheme for foiditic rocks from Le Bas (1989), some of the EEVF foidites can be further subdivided into melilitites (Ei 4, 5, 6, 7) and nephelinites (Ei 10a/b, 36). However, for simplicity, we will simply refer to these rocks as foidites throughout this study. In Na_2O vs. K_2O space (Fig. 3.2B), the samples define two magmatic groups. Samples from the EEVF are more potassium enriched compared to WEVF samples that show a bimodal distribution. While samples from the F-Suite are potassic and overlap with the compositions of the EEVF, the samples from the ONB-Suite are more sodic. In major element variation diagrams (Fig. 3.3), samples of both fields reveal negative co-variations of SiO_2, Al_2O_3, K_2O and Na_2O- and positive co-variations of CaO, TiO_2 and FeO vs. MgO (wt.%). Volcanic rocks of both fields can be clearly distinguished based on MgO compositions, where WEFV samples are characterized by generally higher MgO concentrations (MgO = 10.8 – 14.6 %; Mg# = 64 – 74), compared to EEVF samples (MgO = 6.57 – 10.6 Mg# = 57– 68). This is further underlined by positive co-variations of MgO with Ni and Cr (Fig. 3.3), where WEVF magmas mark near-primitive compositions with higher MgO and generally elevated Ni (68.0 – 383 ppm) and Cr (98.0 – 580 ppm) concentrations compared to EEVF lavas (Ni = 32.7 – 142 ppm; Cr = 21.4 – 317 ppm). With the exception of two samples (Ei 27, Sarresdorfer Lavastrom and Ei 57, Emmelberg), ONB-Suite samples tend towards even higher MgO concentrations (MgO = 10.9 – 14.5; Mg# = 70 – 74), in accord with

previous observations (Mertes and Schmincke, 1985; Mertz et al., 2015). In primitive mantle normalized trace element diagrams (Fig. 3.4), mafic samples display positive anomalies of Ba and Nb, negative Pb and K anomalies and also small throughs for U-Th and Zr-Hf. Detailed comparisons of both Eifel volcanic fields indicate that the K and Pb anomalies are more pronounced in samples from the EEVF compared to the WEVF, in foidites compared to basanites within the EEVF, and in the ONB-Suite compared to the F-Suite within the WEVF (Fig. 3.4A-C). In contrast, trace element patterns of more differentiated rocks (phono-tephrites and phonolites) display features indicative of fractional crystallization with clear negative Ba and Ta and positive Nb, Pb and Zr anomalies relative to REE (Fig. 3.4D). However, negative Eu anomalies are absent within all differentiated samples. ONB-Suite samples display stronger negative anomalies for K ($K/K^* = 0.287–0.454$) compared to F-Suite and EEVF samples. Furthermore, mafic samples display high Zr/Hf (39.6 – 62.2) and Nb/Ta (15.9 - 23.5) that exceed ratios of primitive OIB (Zr/Hf up to 45, Nb/Ta ~15-16) (Pfänder et al., 2007), but overlap with ratios previously reported for CEVP intraplate basalts (Kolb et al., 2012; Pfänder et al., 2012; Pfänder et al., 2018). Similarly, Ce/Pb (19.3–75.4) and Nb/U (27.7–46.5) ratios of mafic samples generally agree with previously reported ratios of OIB and the CEVP (e.g., Jung et al., 2006; Fekiacova et al., 2007; Mayer et al., 2018), but exceed the canonical ratios of Ce/Pb ~25 and Nb/U ~47 that have been inferred for OIBs (Hofmann et al., 1986). However, differentiated samples (phono-tephrites, nephelinites and phonolites) trend towards lower Ce/Pb (3.95–17.3) at variable Nb/U ratios (26.3–70.4), and partially overlap with the compositional fields that have been inferred for the lower continental crust. Additionally, REE ratios such as primitive mantle normalized $(Dy/Yb)_N$ (1.61 – 1.98) and $(La/Yb)_N$ (21.7 – 31.3) only display minor variations within mafic and differentiated samples and are in good agreement with previously reported values for CEVP volcanic rocks (Haase et al., 2004; Jung et al., 2006; Mayer et al., 2018).

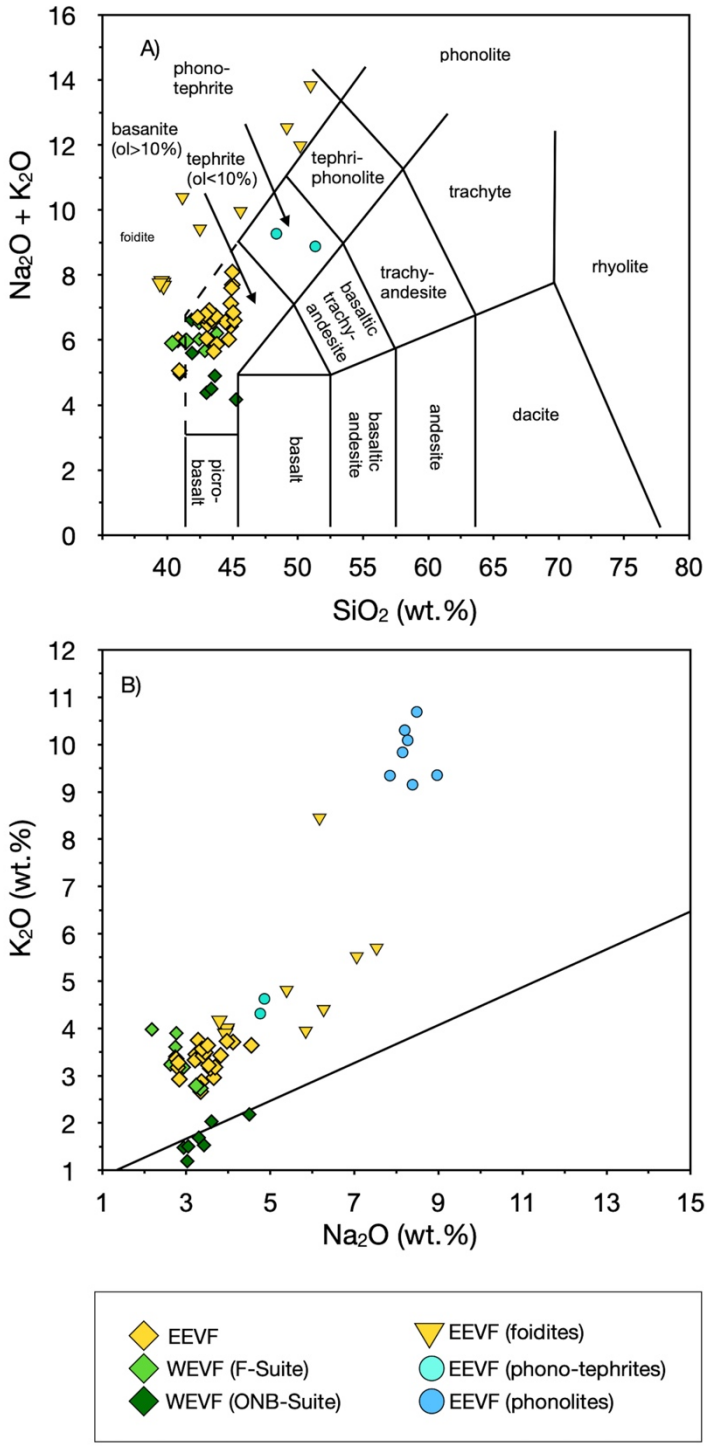

Figure 3.2 (A) Total Alkali ($Na_2O + K_2O$ versus Silica (SiO_2) (TAS) diagram of the samples investigated within this study. The samples are characterized as silica undersaturated and alkaline (SiO_2 = 39.4 wt.% to 54.7 wt.%; Na_2O+K_2O = 4.22 to 19.2) with most samples plotting in the basanite/ tephrite field. Foiditic and phonolitic volcanic rocks are only found within samples from the EEVF. (B) Plot of Na_2O (wt.%) versus K_2O (wt.%), defining clear compositional groups. The samples of this study follow different magmatic trends. Samples from the EEVF are potassium enriched while WEVF volcanic rocks display a bimodal distribution. Samples from the F-Suite are potassic and compositionally overlap with the EEVF. In contrast, ONB-Suite samples are more sodic.

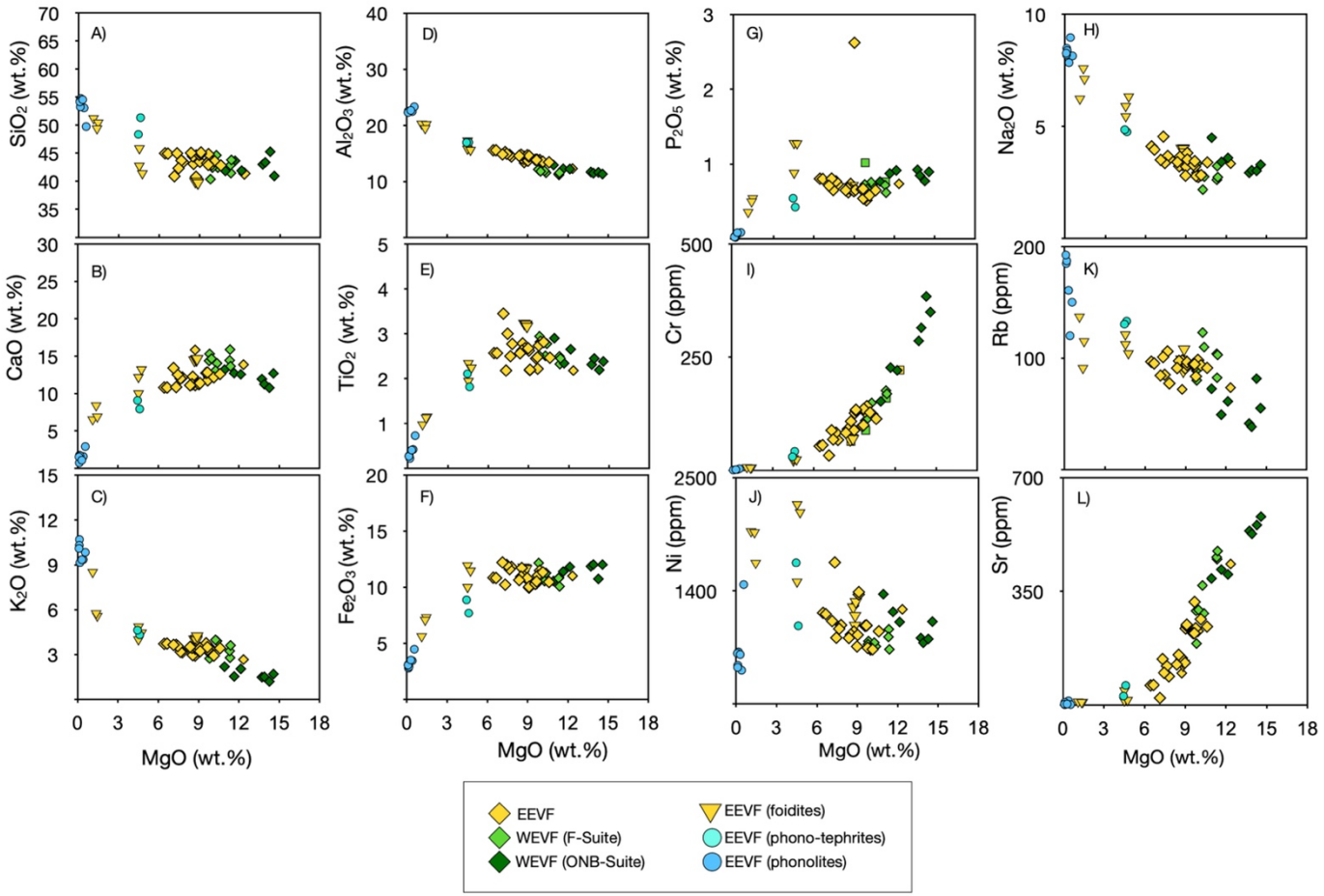

Figure 3.3 MgO (wt. %) vs. selected major element oxide (A-H) variation diagrams clearly illustrate magmatic differentiation trends. Samples of both fields show negative co-variations of SiO_2, Al_2O_3, K_2O, and Na_2O and positive co-variations of CaO, TiO_2 and FeO vs. MgO (wt.%). In MgO (wt. %) vs. selected trace-element variation diagrams (I-L), MgO concentrations are positively correlated with Cr (I) and Sr (L) and display a negative co-variation with Ni (J) and Rb (K). Samples of the WEVF characterized by generally higher MgO (wt. %), Ni and Cr concentrations, illustrating the more mafic and rather primitive character of especially ONB-Suite volcanic rocks.

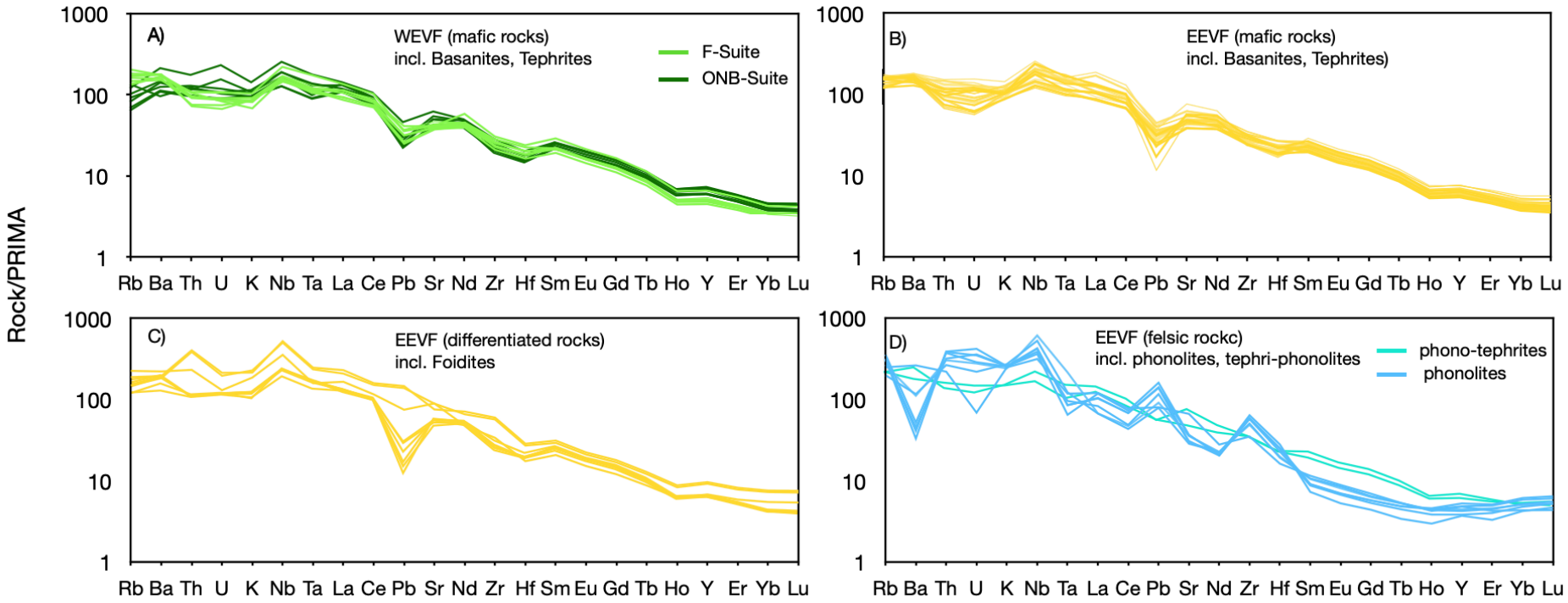

Figure 3.4 Primitive mantle normalized trace element diagrams of samples from the Eifel volcanic field**.** Illustrated in figures A) and B), mafic samples of the WEVF and the EEVF display strong depletions/enrichments for Ba, Nb and Pb and negative Zr-Hf anomalies. Detailed comparisons of both volcanic fields indicate K and Pb anomalies are more pronounced in samples from the EEVF (B) compared to the WEVF (A), in foidites compared to basanites within the EEVF (B, C) and the ONB-Suite compared to the F-Suite within the WEVF (A). In contrast, trace element patterns of differentiated rocks (phono-tephrites and phonolites) (D) display patterns indicative for fractional crystallization with negative Ba and Ta and positive Nb, Pb and Zr anomalies. A negative Eu anomaly is not recognized and absent within all differentiated samples (D). Trace element compositions have been normalized after Palme et al. (2004).

Radiogenic isotope compositions

Radiogenic Sr, Nd, Hf and Pb isotope compositions are listed in Appendix III, Table 4 and are plotted in Fig. 3.6-3.8. Samples of the Eifel Volcanic Field cover a broad range of radiogenic isotope compositions with $^{86}Sr/^{87}Sr$ = 0.703855– 0.705408, $^{143}Nd/^{144}Nd$ = 0.512666–0.512825; (εNd =-0.2 to +3.6), $^{176}Hf/^{177}Hf$ = 0.282681 – 0.282935 (εHf = -3.1 to +5.8), $^{206}Pb/^{204}Pb$ = 18.61 – 19.70, $^{207}Pb/^{204}Pb$ = 15.62 – 15.67 and $^{208}Pb/^{204}Pb$ = 38.89 – 39.76, respectively (Fig. 3.6-3.9). With the exception of the phono-tephritic sample Ei 38, all differentiated samples largely overlap with the compositional spread defined by mafic basanites and foidites. In isotope variation diagrams (Fig. 3.6-3.8) samples from the quarternary EVF plot between compositions of E-MORB and BSE, suggesting the influence of multiple endmembers similar to HIMU, EM-I and MORB. In addition, while F-Suite and EEVF samples compositionally overlap, ONB-Suite samples can be clearly distinguished in $^{143}Nd/^{144}Nd$ vs. $^{86}Sr/^{87}$ and $^{143}Nd/^{144}Nd$ vs. $^{176}Hf/^{177}Hf$ isotope spaces (Fig. 3.6-3.9). The ONB samples trend towards more radiogenic $^{143}Nd/^{144}Nd$ (0.512739–0.512822) and $^{176}Hf/^{177}Hf$ isotope compositions (0.282935–0.282796) at lower $^{86}Sr/^{87}Sr$ ratios (0.703855–0.703950). However, two ONB-Suite samples (Ei 58, Ei 28) are shifted towards higher $^{86}Sr/^{87}Sr$ and less radiogenic $^{143}Nd/^{144}Nd$ and $^{176}Hf/^{177}Hf$ isotope compositions, suggestive of crustal contamination or mixing with F-suite compositions. In $^{206,207,208}Pb/^{204}Pb$ isotope spaces, samples of both volcanic fields plot above the North Hemispheric Reference Line (NHRL) and display discrete compositional ranges for ONB-, F-Suite and EEVF samples (Fig. 3.8). Volcanic rocks of the F-Suite tend towards generally elevated $^{206}Pb/^{204}Pb$ and $^{208}Pb/^{204}Pb$ ratios and suggest a predominant influence of E-MORB/ HIMU-like mantle endmembers, whereas EEVF samples display less radiogenic Pb isotope compositions similar to an EM I-like mantle reservoir. In accord with Sr-Nd-Hf isotopes, ONB-Suite samples also show distinct Pb isotope compositions, by having higher $^{206}Pb/^{204}Pb$ and lower $^{208}Pb/^{204}Pb$ and $^{207}Pb/^{204}Pb$ compositions (Fig. 3.8). Interestingly, the foiditic rocks of the EEVF analyzed within this study are indistiguishable from the basanite and tephrites, showing overall similar Sr-Nd-Hf isotope compositions (Fig. 3.6, 3.8). However, in $^{206,207,208}Pb/^{204}Pb$ isotope spaces, foiditic rocks compositionally link the EEVF and WEVF petrogenetic suites by displaying intermediate Pb isotope compositions compared to both volcanic fields and petrogenetic suites (Fig. 3.8). For ^{187}Re-^{187}Os and HSE analysis we have selected 13 samples of the EEVF, the F-Suite and the ONB-Suite, respectively. In a primitive mantle normalized PGE diagram (Fig. 3.5) the samples analyzed within this study display

enrichments of the PPGE's compared to the IPGE's, which is typical for primitive mantle melts and reflects the incompatible behavior of Pt and Re during partial melting (e.g., Mondal, 2011). Measured Re/Os ratios reveal a large range from 4.22 to 72.1, which is equivalent to $^{187}Re/^{188}Os$ ratios ranging from 21.1 to 356 (Table 4.). Similarly variable patterns are found for Os concentrations (2 to 148 ppt) and $^{187}Os/^{188}Os$ ratios that vary from near primitive upper mantle values (primitive upper mantle = 0.129 (Meisel et al., 1996)), such as $^{187}Os/^{188}Os = 0.139$, to ratios as high as $^{187}Os/^{188}Os = 0.697$. Further, the samples analyzed in this study display an inverse correlation of $^{187}Os/^{188}Os$-and Re/Os ratios (Fig. 3.15).

In general, measured trace-element and Sr-Nd-Hf-Pb compositions of our samples from the quaternary EVF are in good agreement with previously published data for the Quaternary and Tertiary Eifel volcanic fields (e.g., Wörner et al., 1986; Jung et al., 2006; Fekiacova et al., 2007) as well as for the CEVP (e.g., Jung and Masberg, 1998; Jung and Hoernes, 2000; Jung et al., 2006; Fekiacova et al., 2007; Lustrino and Wilson, 2007; Jung et al., 2011; Lustrino, 2011; Pfänder et al., 2012; Pfänder et al., 2018). Additionally, measured Os isotope compositions of the quaternary Eifel samples are similar to published age corrected data on Tertiary volcanic rocks from the CEVP (e.g., Jung et al., 2005; Jung et al., 2011; Mayer et al., 2013; Mayer et al., 2018) that also revealed radiogenic Os isotope compositions above the mantle value.

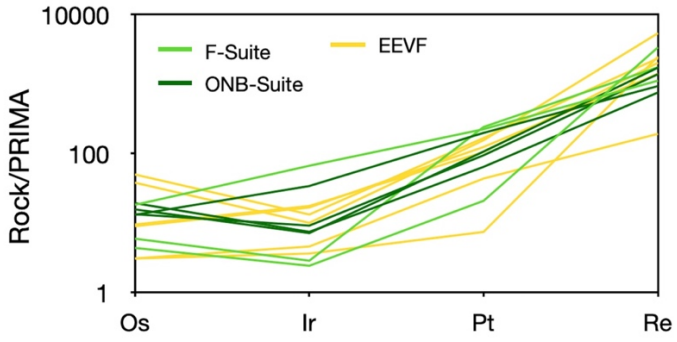

Figure 3.5 Primitive mantle normalized highly siderophile element (HSE) patterns. The samples analyzed within this study display enrichments of the PPGE's compared to the IPGE's, which is typical for primitive mantle melts and reflects the incompatible behavior of Pt and Re during partial melting (e.g., Mondal, 2011).

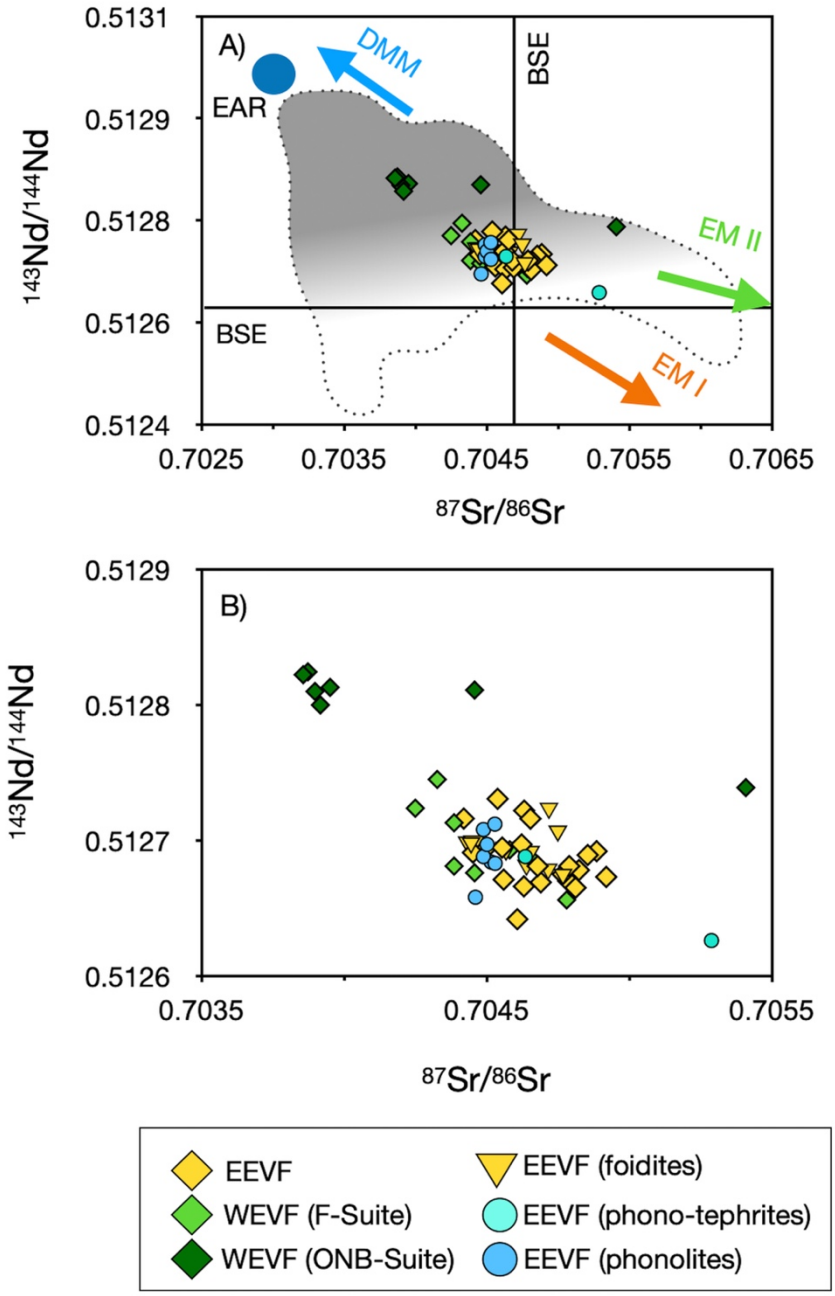

Figure 3.6 In $^{143}Nd/^{144}Nd$ vs. $^{86}Sr/^{87}Sr$ isotope space (A, B), the samples display a compositional spread suggesting the influence of depleted mantle endmembers that are compositionally similar to DMM as well as enriched reservoirs of EM I/ EM II affinity. While Sr-Nd compositions of mafic as well as differentiated samples of both volcanic fields generally overlap, ONB-Suite samples can be clearly distinguished forming a high $^{143}Nd/^{144}Nd$–low$^{86}Sr/^{87}Sr$ group. This is further illustrated by reducing the scale of Sr and Nd isotope compositions on the axes (B). Additionally, two samples from the ONB-Suite and one phonolite trend towards more radiogenic $^{86}Sr/^{87}Sr$ and lower $^{143}Nd/^{144}Nd$ isotope compositions that are indicative of crustal contamination. Grey shaded areas indicate the compositional spread of CEVP volcanism, colored areas indicate compositions of classical mantle endmembers. Compositional fields have been generated using data from the GeoRoc Database (https://georoc.eu/georoc/new-start.asp).

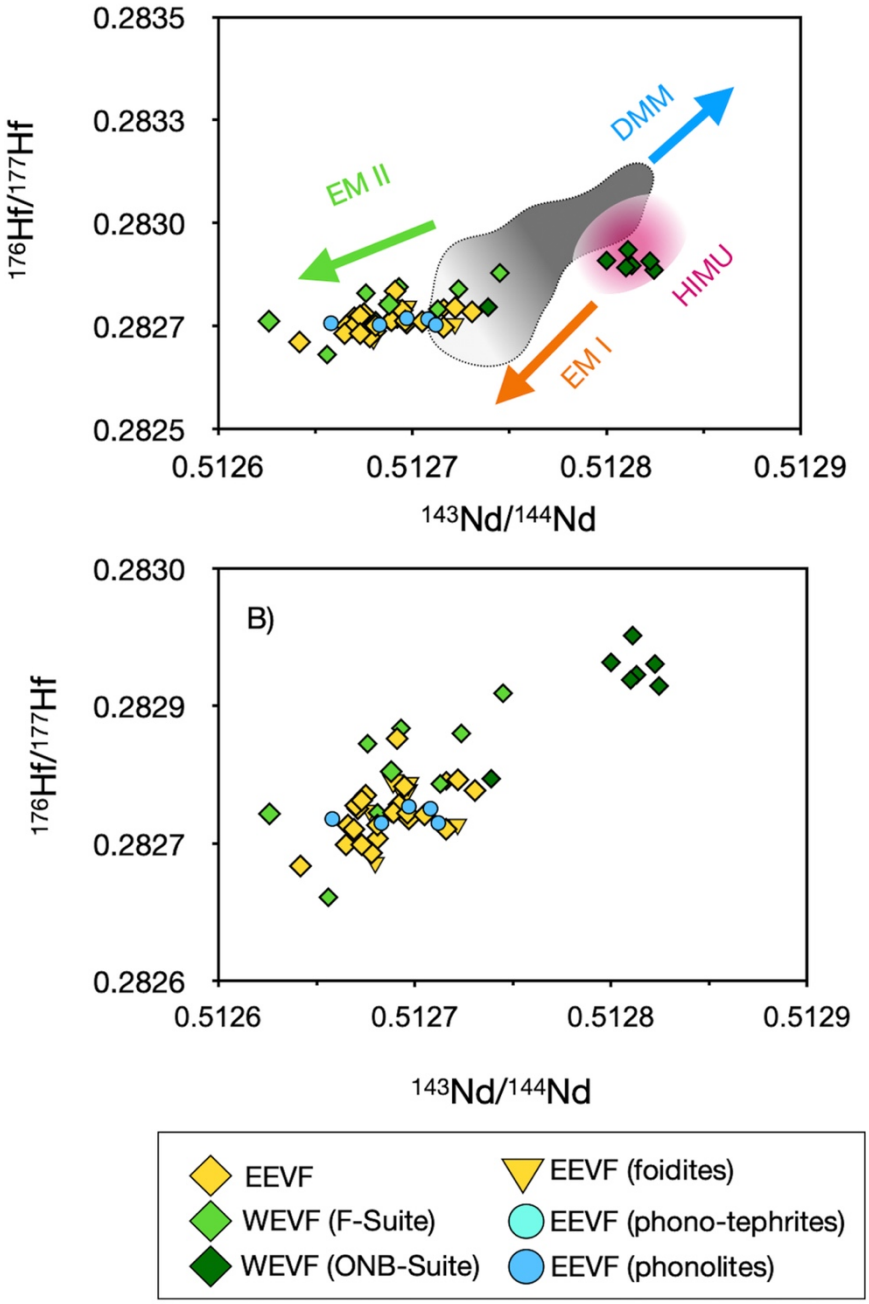

Figure 3.7 In $^{143}Nd/^{144}Nd$ vs. $^{176}Hf/^{177}Hf$ isotope space (A, B) Samples display a compositional spread that is broadly similar to their respective Sr-Nd-Pb isotope compositions, suggesting the influence of a DMM/ HIMU-type mantle source for the ONB-Suite and an EM I-like mantle endmember for F-Suite and EEVF volcanism. ONB-Suite rocks can be clearly distinguished, forming a high $^{143}Nd/^{144}Nd$– high $^{176}Hf/^{177}Hf$ group. The compositional spread is further underlined by reducing the scale of Hf and Nd isotope compositions on the axes in B). Grey shaded areas indicate the compositional spread of CEVP volcanism, colored areas indicate compositions of classic mantle endmembers. Compositional fields have been generated using data from the GeoRoc Database (https://georoc.eu/georoc/new-start.asp).

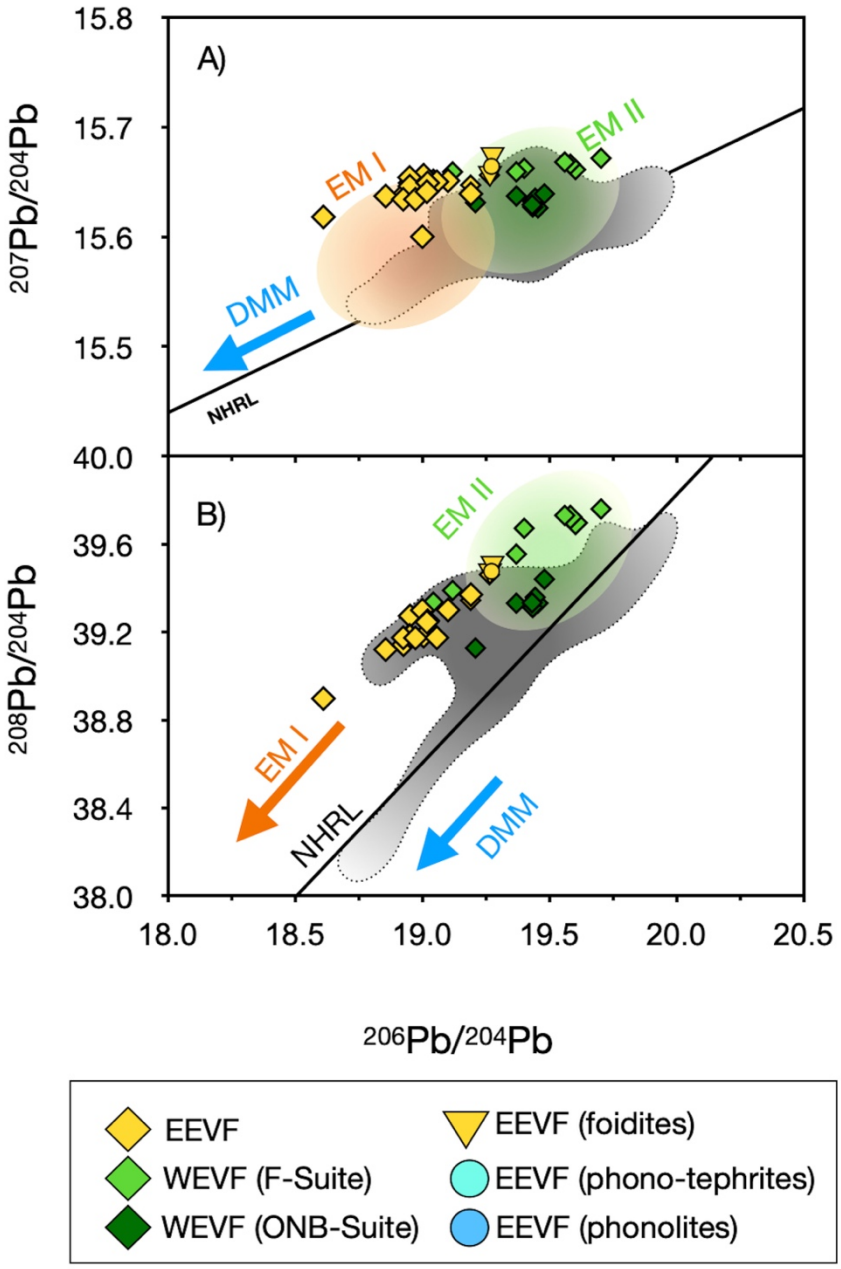

Figure 3.8 In $^{207}Pb/^{204}Pb$ $^{208}Pb/^{204}Pb$ vs. $^{206}Pb/^{204}Pb$ isotope spaces (A, B) samples of both volcanic fields plot above the North Hemispheric Reference Line (NHRL) (Zindler et al., 1982) and form a linear array. The samples display discrete compositional ranges for ONB-, F-Suite and EEVF samples. F-Suite volcanic rocks trend towards generally elevated $^{206}Pb/^{204}Pb$, $^{207}Pb/^{204}Pb$ and $^{208}Pb/^{204}Pb$ ratios and suggest a predominant influence of a HIMU-type mantle endmember, while EEVF samples display less radiogenic Pb isotope compositions similar to an EM I/ DMM-like mantle reservoir. ONB-Suite samples show distinctly lower $^{207}Pb/^{204}Pb$ and $^{208}Pb/^{204}Pb$ isotope compositions at given $^{206}Pb/^{204}Pb$ ratios. Grey shaded areas indicate the compositional spread of CEVP volcanism, colored areas indicate compositions of classical mantle endmembers. Compositional fields have been generated using data from the GeoRoc Database (https://georoc.eu/georoc/new-start.asp).

Discussion

Effects of fractional crystallization

Positive co-variations of CaO, Fe_2O_3, Ni and Cr and a negative correlation of Al_2O_3 contents with MgO (Fig. 3.3) are in good agreement with typical magmatic differentiation trends, caused by predominant fractionation of olivine and clinopyroxene. More differentiated samples (including foidites, phono-tephrites and phonolites) also show trends towards generally lower Ce/Pb at variable Nb/U ratios (Fig. 3.9) and thus overlap with compositions indicative of crustal contamination. Further, the lack of negative Eu anomalies (Fig. 3.4) in more differentiated samples could provide evidence for the absence of large-scale plagioclase fractionation as suggested by plagioclase bearing cumulate xenoliths that have been reported from the area (Loock et al., 1990; Viereck, 1984). However, more detailed investigations of differentiated rocks from the quaternary EVF that have been sampled at the Laacher See, Rieden- and Wehr- volcanic complexes have provided evidence for plagioclase fractionation taking place at upper-crustal depth (Schmincke et al., 1983; Viereck, 1984; Wörner et al., 1986; Schmincke, 2007) and in particular the presence of green-core clinopyroxene has suggested polybaric differentiation of magmas during their ascent (Duda and Schmincke, 1985). Considering the samples analyzed within this study, the trace element patterns of our more differentiated samples are in good agreement with enhanced fractional crystallization of olivine, pyroxene, titanite, nepheline, K-felspar and leucite (Viereck, 1984) and a rather limited influence of crustal contamination. In detail, titanite is responsible for the fractionation of Nb and Ta (Bea et al., 1994), garnet for Zr and Hf and K-felspar for Ba and Pb (Viereck, 1984; Green et al., 2000; Klemme et al., 2002). The effects of crustal contamination are further assessed below using Sr isotopes.

Effects of crustal assimilation

While it is generally accepted that geochemical compositions of OIBs can be used to constrain the composition and nature of their respective mantle sources, data for continental intraplate basalts require a more careful interpretation due to the potential influence of crustal assimilation and metasomatism of the lithospheric mantle. Given that continental intraplate volcanic rocks erupt through variably thick, compositionally heterogenous lithosphere, diverse crustal materials might be entrained throughout assimilation-fractional-crystallization

processes (AFC) (DePaolo, 1981). With a focus on the CEVP, previous studies have already largely precluded a significant role of crustal contamination by examining the geochemical composition of mafic and felsic lavas (e.g., Wörner et al., 1986; Jung et al., 2006; Fekiacova et al., 2007; Kolb et al., 2012; Jung et al., 2012; Schneider et al., 2016; Mayer et al., 2018). Despite these results, other, more sophisticated approaches that focused on energy-constrained AFC-modelling (Bohrson and Spera, 2001; Spera and Bohrson, 2001) have revealed that the assimilation of lower-crustal granulites might have played a significant role for more differentiated samples (e.g., Jung et al., 2006; Kolb et al., 2012; Schneider et al., 2016). This was also postulated for tholeiites based on Os isotopes (Jung et al. 2011).

Considering the samples analyzed within this study, the low SiO_2 (< 50 wt.%), high MgO (> 6.5 wt.%) and high Ni and Cr concentrations within mafic lavas from the EVF generally argue for their near-primitive nature. This is also in good agreement with the presence of ultramafic mantle xenoliths that occur in many mafic lavas of both Tertiary and Quaternary volcanic fields within the Eifel (Witt-Eickschen et al., 2003; Schmincke, 2007). Although positive Pb and negative Ta anomalies are present in some differentiated ONB/ EEVF rocks that can be regarded as indicators for contamination with continental crust, negative Pb and positive Nb anomalies prevail and these are a characteristic feature of asthenospheric upper mantle melts and rule out large effects of crustal contamination (Hofmann et al., 1986; Hofmann, 1997). Among the samples analyzed within study, only phonolitic samples display positive Pb anomalies but no negative anomalies for Nb, while mafic samples generally resemble typical trace element patters of enriched OIBs (Fig. 3.4). Further, given the similar compatibilities of Pb-Ce and Nb-U, respectively, elemental ratios of Ce/Pb and Nb/U can be used to detect the influence of crustal contamination (Hofmann et al., 1986). While mantle derived melts typically exhibit ratios of Ce/Pb ~25 and Nb/U ~47 (Hofmann et al., 1986; Hofmann, 2003), typical continental crust displays much lower ratios of Ce/Pb ~4 and Nb/U ~10 In Ce/Pb vs. Nb/U space (Fig. 3.9) the majority of our samples plot within the compositional field defined by OIBs and, therefore, do not show any evidence for significant crustal contamination.

Given the limited occurrence of differentiated volcanic rocks within the WEVF (Schmincke et al., 1983; Mertes and Schmincke, 1985) and the apparent age difference between F-Suite, EEVF and ONB-Suite volcanism, we have focused our model on differentiated samples from the EEVF that erupted during a similar period of volcanic activity. To estimate the potential influence of crustal contamination on the composition of EEVF samples more quantitatively,

we have carried out a simple energy-constrained assimilation-fractional-crystallization (EC-AFC) model by Bohrson and Spera (2001) and Spera and Bohrson (2001), with a particular focus on Sr-Nd isotopes. As initial composition, we have used the MgO-rich sample Ei 55 (Bräuning volcano) that represents a mafic eruptive center, located within the Rieden volcanic complex which also contains abundant phonolites. For the EC-AFC model at various depths we have used modelling parameters that were previously used for the nearby Siebengebirge volcanic field (Schneider et al. 2016). As representative for the lower crustal contaminant, we used granulite sample S32 from Stosch and Lungmair (1984), as representative for a upper crustal contaminant a Devonian slate (S200) as well as a mica-schist (S144) from Wörner et al. (1985). All these rocks have been previously investigated for their Sr-Nd isotope compositions and can be regarded as compositionally representative of the various crustal levels underneath the EVF (Wörner et al., 1985). The results of the modelling calculations are illustrated in Fig. 3.10.

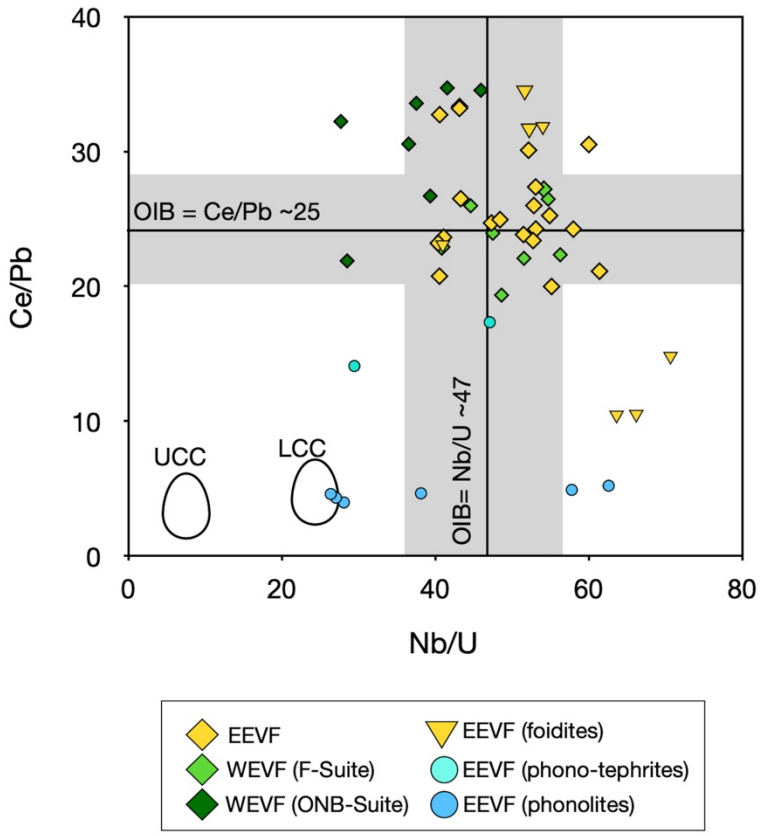

Figure 3.9 Ce/Pb and Nb/U ratios of mafic samples generally agree with published ratios of OIBs but exceed the canonical ratios of ~25 Ce/Pb and ~47 Nb/U, that have been inferred for OIBs (Hofmann et al., 1986). Differentiated samples (phono-tephrites, nephelinites and phonolites) trend towards Ce/Pb at variable Nb/U ratios, and partly overlap with the compositional fields that have been inferred for the lower continental crust (Hofmann et al., 1986)

Applying the EC-AFC model to the samples analyzed within this study that display a considerable spread of Sr-Nd isotope compositions shows that their Sr-Nd compositions overlap with the modelled assimilation curves for all crustal endmembers (Fig. 3.10). However, given that all of the potential assimilants are characterized by substantially more radiogenic $^{87}Sr/^{86}Sr$ and un-radiogenic $^{143}Nd^{144}Nd$ isotope compositions than in our samples from the EEVF, potential crustal assimilation must have been rather insignificant, even for the phonolites. Further, regardless of which assimilant is assumed, the Sr-Nd isotope composition of the mafic as well as of the differentiated rocks only permit a maximum of 5-6% assimilated material at 40-60% fractional crystallization. However, one phono-tephrite (Ei 38) exhibits significantly more radiogenic Sr isotope compositions ($^{87}Sr/^{86}Sr$ = 0.705288) that could be consistent with up to 10% assimilated material (Fig. 3.10). While some potential crustal assimilation within the differentiated phonolites has been suggested above based on lower Ce/Pb ratios, Sr-Nd isotope compositions seem to be rather unaffected by AFC processes (Figs. 3.5-3.7). This might reflect that the Sr and Nd inventories of the lavas are much more buffered than that of Pb. In agreement with such a model, Sr isotope compositions in phonolites from the Laacher See eruption are much more radiogenic in their Sr isotope compositions than all phonolites analysed here (Wörner et al. 1985), because these phonolites underwent plagioclase fractionation which lowered their Sr contents.

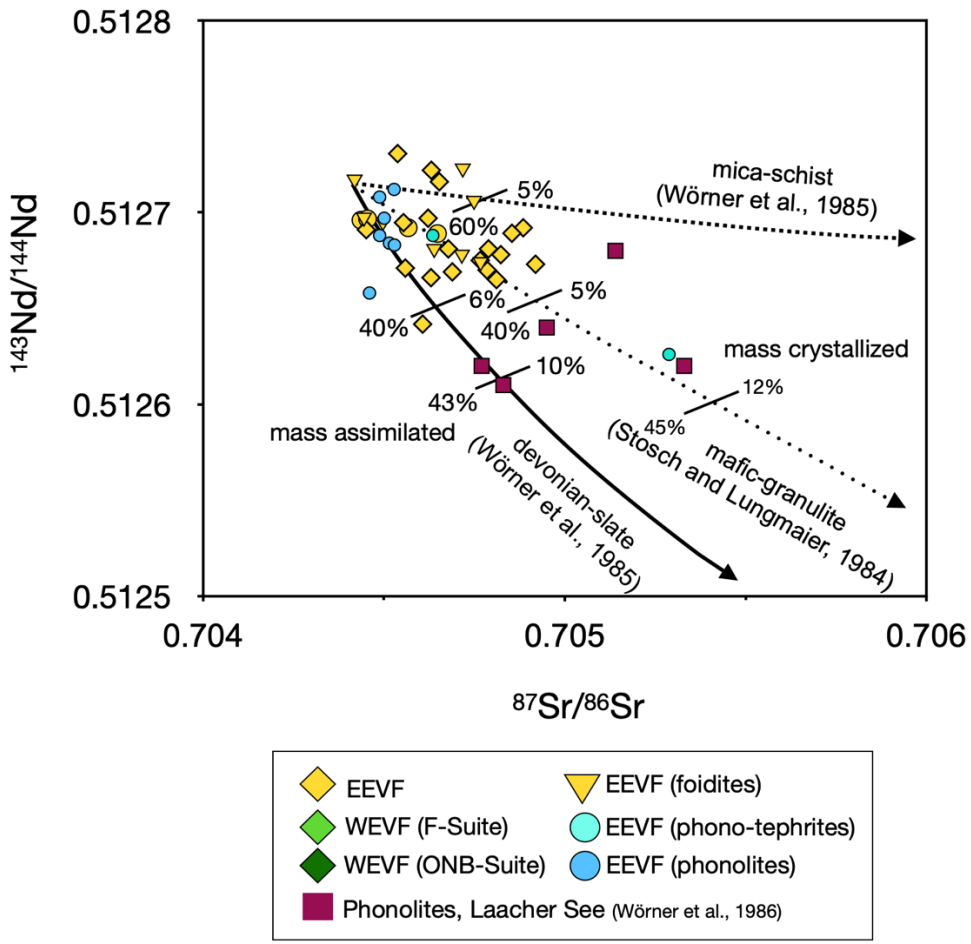

Figure 3.10 Energy-constrained assimilation-fractional-crystallization (EC-AFC) model by Bohrson and Spera, (2001) and Spera and Bohrson, (2001), using modelling parameters given in (Schneider et al., 2016). Sr-Nd isotope modelling of mafic as well as differentiated rocks reveals that the amounts of assimilated material cannot have exceeded 5-6% at 40-60% fractional crystallization. However, one phono-tephrite sample displays radiogenic Sr isotope compositions that are consistent with up to 10% assimilated material.

Mantle source characteristics

Melting conditions

Given the limited influence of crustal assimilation on the compositions of mafic and more differentiated volcanic rocks from the EVF analyzed here, it can be inferred that their radiogenic isotope compositions reflect the composition of their mantle source reservoirs. Based on the overall heterogenous compositions of volcanic rocks from the CEVP that resemble OIB-like compositions, several studies have suggested the presence of one or several mantle plumes underneath the CEVP (e.g., Granet et al., 1995; Goes et al., 1999; Goes et al., 2000; Ritter et al., 2001; Ritter and Christensen, 2007). However, it has been argued that the expected diameter (~2000 km) of a single mantle-plume rising upwards from the core-mantle boundary is inconsistent with the dimensions of the individual CEVP eruptive centers (Wilson and Downes, 1991; Fekiacova et al., 2007). Moreover, seismic investigations have indicated P-wave anomalies that more are consistent with the presence of small-scale "plumelets" rooted in the mantle-transition zone rather than in the lower-mantle (Ritter et al., 2001; Ritter and Christensen, 2007). With respect to the ongoing debate of mantle plume involvement (Ritter et al., 2001; Ritter and Christensen, 2007), several studies have therefore suggested that CEVP volcanic rocks are rather sourced from the upper-asthenospheric and lithospheric mantle of which the latter has been refertilized as a consequence of enhanced subduction recycling during the Variscan orogeny (e.g., Wilson and Downes, 1991; Witt-Eickschen et al., 2003). While previous studies on mantle xenoliths, found within eruptive products of the EVF, have indicated that the upper-mantle underneath the CEVP consists mostly of metasomatized spinel peridotite (e.g., Witt-Eickschen and Kramm, 1998; Witt-Eickschen et al., 2003), several studies have provided evidence for the involvement of residual garnet in the source of CEVP volcanism and mixtures of partial melts generated in the spinel- as well as the garnet stability field (e.g., Haase et al., 2004; Jung et al., 2006; Fekiacova et al., 2007; Mayer et al., 2018).

Considering the samples analyzed in this study, plots of Ce/Pb vs. Pb and KN*/KN/ vs. SiO_2 (Fig. 3.11) provide evidence for residual mineral phases such as amphibole and phlogopite in the source of EVF volcanism. Given that ONB-, F-Suite (WEVF) and EEVF samples display distinctly negative K and Pb anomalies in primitive mantle normalized trace-element diagrams, negative correlations of Ce/Pb vs. Pb and a positive correlation of KN*/KN/ vs. SiO^2 (Fig

3.11), indicates that these trace element ratios are fractionated during partial melting (Mayer et al., 2018). This feature was also observed previously in other volcanic rocks of the CEVP (Jung and Hoernes, 2000; Kolb et al., 2012; Mayer et al., 2018) and is best explained by variable degrees of partial melting in the presence of residual amphibole or phlogopite. High Ce/Pb and low KN*/KN therefore might indicate small degrees of partial melting whereas low Ce/Pb and high KN*/KN together with higher SiO_2 contents might result from the release of Pb and K during amphibole or phlogopite breakdown at higher degrees of partial melting and shallower depths (Jung and Hoernes, 2000). In good agreement with previous studies, our data thus indicate that ONB- as well as F- and EVF are sourced from mantle sources that have been affected by mantle metasomatism that resulted in the formation of secondary phlogopite and amphibole (e.g., Witt-Eickschen and Kramm, 1998; Witt-Eickschen et al., 2003).

To further evaluate the depth and melting conditions, several models carried out for CEVP volcanism have been focused on REE systematics, such as plots of Dy/Yb vs. La/Yb (e.g., Haase et al., 2004; Jung et al., 2006; Mayer et al., 2018; Jung et al., 2006), as well as silica content and major element ratios such as CaO/Al_2O_3 (e.g., Fekiacova et al., 2007). Given that the HREE are strongly fractionated by garnet, a plot of primitive mantle normalized $(Dy/Yb)_N$ vs. $(La/Yb)_N$ can be used to distinguish between partial melting within the garnet peridotite and the spinel-peridotite stability field (e.g., Thirlwall et al., 1994; Jung et al., 2006). Additionally, if mixing of melts sourced from spinel- and garnet peridotite occurs, the investigated samples should plot along linear mixing arrays of both sources (e.g., Jung et al., 2006). In Fig. 3.12 we show non-modal, batch-melting curves of a garnet- amphibolite peridotite and a spinel-amphibolite peridotite that have been calculated using using the PetroGram workbook program of Gündüz et al., (2021) and the parameters, source compositions and mineral proportions given in Jung et al. (2006 and references therein). The calculated model curves shown in Fig. 3.12 imply that Quaternary Eifel magmas, plotting in a range from $(Dy/Yb)_N = 1.61 – 1.98$ and $(La/Yb)_N = 21.7 – 31.3$, could result from 1-5% partial melting. Additionally, our samples overlap with calculated mixing lines, indicating that small degree-partial melts from a garnet-bearing source were mixed with melts, produced at similar degrees of partial melting within a spinel-bearing source (Fig. 3.12). Given that analyzed samples from the WEVF (ONB- and F-Suite) trend towards elevated $(Dy/Yb)_N$ ratios in a range from 1.86 to 1.98, this suggests a greater contribution from a garnet-bearing sources compared to samples from the EEVF (Fig. 3.12). Further, foiditic samples from the EEVF display elevated $(La/Yb)_N$ and suggest

generally lower degrees of partial melting compared to the basanites (Fig. 3.11). This is in good agreement with generally elevated CaO/Al_2O_3 ratios and decreasing CaO/Al_2O_3 at increasing SiO_2 that suggest increasing degrees of partial melting in the series foidite-basanite as well as the influence of residual garnet in the source of the WEVF volcanic rocks (Fig. 3.10) (e.g., Jung et al., 2006; Kolb et al., 2012).

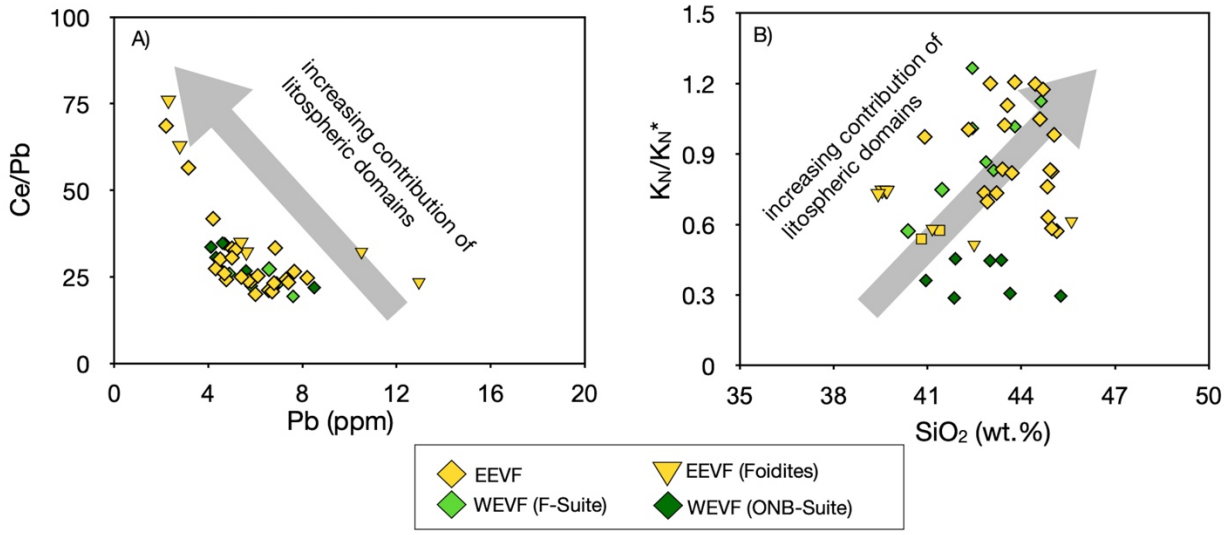

Figure 3.11 In Ce/Pb vs. Pb (A) and K_N*/K_N vs. SiO_2 (B) space, samples of both volcanic fields display a negative correlation of Ce/Pb vs. Pb (A) and a positive correlation of KN*/KN/ vs. SiO_2 (B). This indicates that these trace element ratios are fractionated during partial melting (Mayer et al., 2018). Furhter, these features are best explained by variable degrees of partial melting in the presence amphibole or phlogopite (Mayer et al., 2018)

Hence, our data provide strong evidence for a greater influence of a deeper, garnet-bearing mantle source for West Eifel ONB- and F-Suite volcanism whereas samples from the EEVF might be sourced from shallower depth and partial melting within the spinel-peridotite field. Collectively, our data is thus in good agreement with experimental results that have indicated basanites to be generated from peridotite sources by melting degrees in excess of 1% (Kushiro, 1996). Following the modelling approaches that have been carried out for tertiary CEVP volcanism, a temperature and pressure range of 1250–1300°C and 25–30 kbar, respectively, can be deduced, corresponding to depths of ca. 75–90 km, along the garnet-spinel stability transition zone (Kushiro, 1996; Fekiacova et al., 2007).

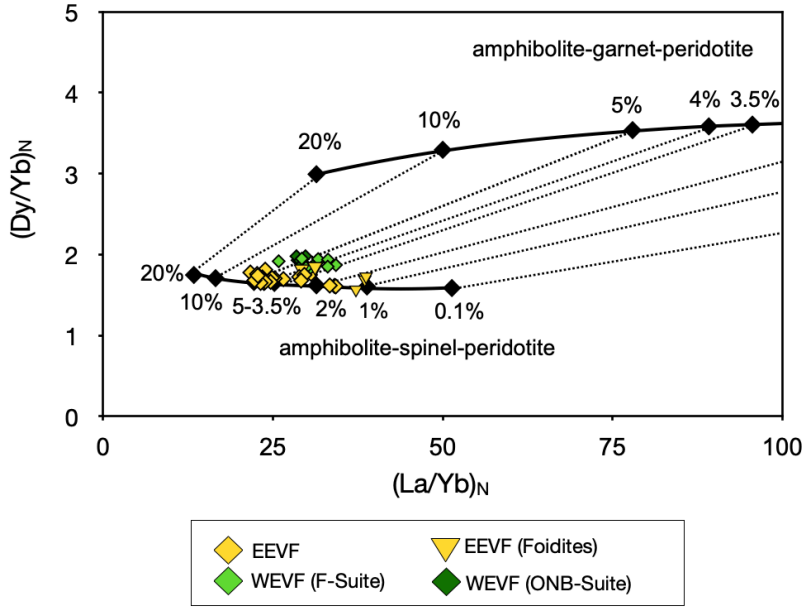

Figure 3.12 In a plot of $(Dy/Yb)_N$ vs. $(La/Yb)_N$, our data are in good agreement with mixing of partial melts originating within the spinel- as well as the garnet stability field .Further, our data provide strong evidence for mixing of melts originating from variable depths within the mantle (e.g., Haase et al., 2004; Jung et al., 2006; Fekiacova et al., 2007; Lustrino and Wilson, 2007; Mayer et al., 2018). The model has been created using the PetroGram workbook program of Gündüz et al., (2021) and the parameters, source compositions and mineral proportions given in Jung et al. (2006 and references therein)

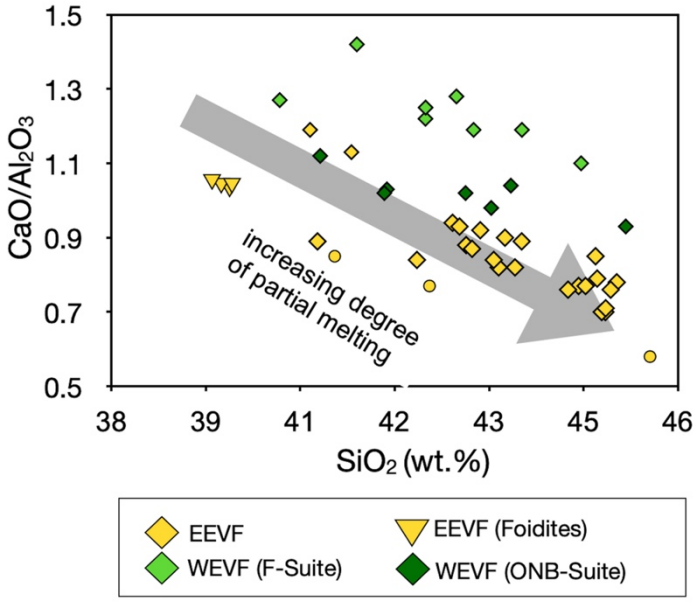

Figure 3.13 In CaO/Al_2O_3 vs SiO_2 space, the samples form a linear array, indicating variable depth and degrees of partial melting (Kushiro, 1996). Melting depth and degrees of partial melting are thereby lower for foiditic rocks and increase towards basanites and tephrites.

Nature of the mantle sources involved in Quaternary volcanism

As indicated throughout the results of our melting model, Quaternary volcanic rocks are sourced from variable depth within the mantle. Hence, analyzed geochemical compositions of the respective magmatic suites could thus provide further evidence for the nature and potential heritage of distinct mantle sources tapped by CEVP volcanism. Previously analyzed radiogenic Sr-Nd-Hf-Pb isotope compositions of EVF lavas have indicated a contribution of mantle sources with characteristics similar to HIMU/ FOZO– and EM-I-type OIB to the Quaternary and Tertiary Eifel volcanic fields (e.g., (Wörner et al., 1986; Jung et al., 2006; Fekiacova et al., 2007) as well as to the CEVP in general (e.g., Jung and Masberg, 1998; Jung and Hoernes, 2000; Jung et al., 2006; Fekiacova et al., 2007; Lustrino and Wilson, 2007; Jung et al., 2011; Lustrino, 2011; Pfänder et al., 2012; Pfänder et al., 2018). From a geochemical point of view, several studies have further suggested a common, asthenospheric mantle reservoir underneath central Europe that has been termed European Asthenospheric Reservoir (EAR) (Cebria and Wilson, 1995), Low Velocity Component (LVC) (Hoernle et al., 1995), Common Mantle Reservoir (CMR) (Lustrino and Wilson, 2007), or Prevalent Mantle (PREMA) (Wörner et al., 1986) and is thought to provide the HIMU-FOZO flavour. Although the proposed compositions for this component vary in detail, it is believed to exhibit a rather geochemically depleted composition and represents a common mantle endmember located within the asthenosphere (e.g., Lustrino and Wilson, 2007). Given that the inferred compositions of this reservoir are broadly similar to the defined composition of FOZO (Hart et al., 1992), we will refer to this acronym throughout this study. In contrast, the more enriched EM-I signatures found in CEVP volcanic rocks have been inferred to result from contributions of the metasomatically overprinted litospheric mantle (e.g., Wilson and Downes, 1991; Witt-Eickschen and Kramm, 1998; Witt-Eickschen et al., 2003.

In general, radiogenic isotope data of the samples investigated within this study are in broad agreement with previous studies but now enable to discriminate more compositional groups. In Sr-Nd-Hf-Pb isotope spaces (Fig. 3.6-3.8) the samples exhibit a large variation that implies a substantial heterogeneity of the mantle sources involved in magma generation. In Sr-Nd-Hf isotope spaces Fig. 3.6-3.8), Samples of the ONB-Suite form a discrete compositional low $^{87}Sr/^{86}Sr$–high $^{143}Nd/^{144}Nd$–high $^{176}Hf/^{177}Hf$ group. ONB-suite samples thus display DMM/FOZO-like compositions and also overlap compositions of lavas from many Tertiary

volcanic fields, suggesting a major-influence of a FOZO-type reservoir on young volcanism in the WEVF (Fig. 3.6-3.8). In contrast, samples from the F-Suite and the EEVF plot close to the bulk silicate earth (BSE) values in Hf-Sr-Nd isotope spaces, suggesting the influence of an EM-I-type mantle endmember Fig. 3.6-3.8). In Pb-Pb isotope spaces, samples of the F-Suite and the EEVF form a linear trend that is consistent with mixing of source reservoirs having variable (U+Th/Pb) ratios. While samples from the F-Suite display highly radiogenic $^{206}Pb/^{204}Pb$ isotope compositions (19.1 – 19.6) that are in good agreement with an enhanced contribution of a HIMU-like endmember, samples from the EEVF appear to be sourced from a lower (U+Th/Pb) reservoir that is compositionally similar to the EM-I-type mantle endmember. In contrast, ONB-Suite samples display generally lower $^{207}Pb/^{204}Pb$ and $^{208}Pb/^{204}Pb$ at given $^{206}Pb/^{204}Pb$ ratios and thus form a second trend, roughly paralleling the trend formed by F-Suite and EEVF volcanism (Fig. 3.8). Moreover, ONB-suite samples are again compositionally very similar to previously analyzed samples from the Tertiary HEVF (e.g., Jung et al., 2006; Fekiakova et al., 2007) in Pb-Pb isotope space. In contrast to analyzed samples from the EVF and the F-Suite, that resemble a EM-I–HIMU mixing line, the sub-parallel arrangement of these samples suites provides further evidence for a unique source of ONB-type volcanism that is best resembled by a FOZO-type mantle source.

Considering the samples analyzed in this study, the overall heterogenous isotope composition thus indicates the participation of at least two different mantle endmembers. As such, Quaternary volcanism in the EVF cannot be explained by simple partial melting of a single plume source alone. Instead, our data is in good agreement with previous models that have been carried out, suggesting that CEVP volcanism is sourced from a FOZO-type component that is located within the asthenosphere (e.g., Jung et al., 2006; Fekiacova et al., 2007) and provide a source for Na_2O-rich basalts (ONB-Suite) as well as a more enriched source of EM-I affinity that might be located close to the thermal boundary layer and sources K_2O-rich (F-Suite and EEVF) basalts (Wilson et al., 1995; Jung et al., 2006).

Thus, given the unique character of ONB-suite volcanic rocks, several lines of evidence (high Mg#, Ni and Cr) suggest that volcanism younger than 80 ka represent the most mafic endmember with a potential asthenospheric origin of the primary melt, as also suggested throughout the results of our melting model. Given the overall geochemical similarity of Quaternary ONB-Suite and Tertiary HEVF rocks with compositions reported from a FOZO-

type source, we have therefore adapted previous isotope and trace-element modelling constraints for the Hocheifel volcanic field (Fekiacova et al. 2007). Using a batch melting approach (Shaw, 1970) we have calculated mixing of a FOZO-type- (represented here by Raivavae lava RVV 360A by Lassiter et al. (2003)) and a DMM-melt (Salters and Stracke, 2004) to create an enriched hybrid melt. Presented in Fig. 3.13, our data indicate that mixing of 10-14% of a FOZO-type melt and up to 90% of a DMM melt, generated at 6-8% partial melting in the garnet-stability field respectively, produces melt with trace element patterns that broadly resemble those of the ONB-Suite as well as the HEVF, including the negative K and Pb anomalies (Fekiacoca et al., 2007). However, as already noted in the previous section, all eruptive suites analyzed within this study display multi-proxy evidence for the involvement of residual amphibolite or phlogopite. As these minerals are only stable within the litosphere or the at thermal boundary layer (TBL), ONB-suite rocks cannot represent direct partial melts of a mantle plume source. Hence, our results are rather in good agreement with previous models that have suggested mafic CEVP melts to be generated by partial melting of the TBL that has been overprinted by the impingement of one or multiple mantle plumes at the base of the base of the European litosphere (e.g., Wilson et al., 1995).

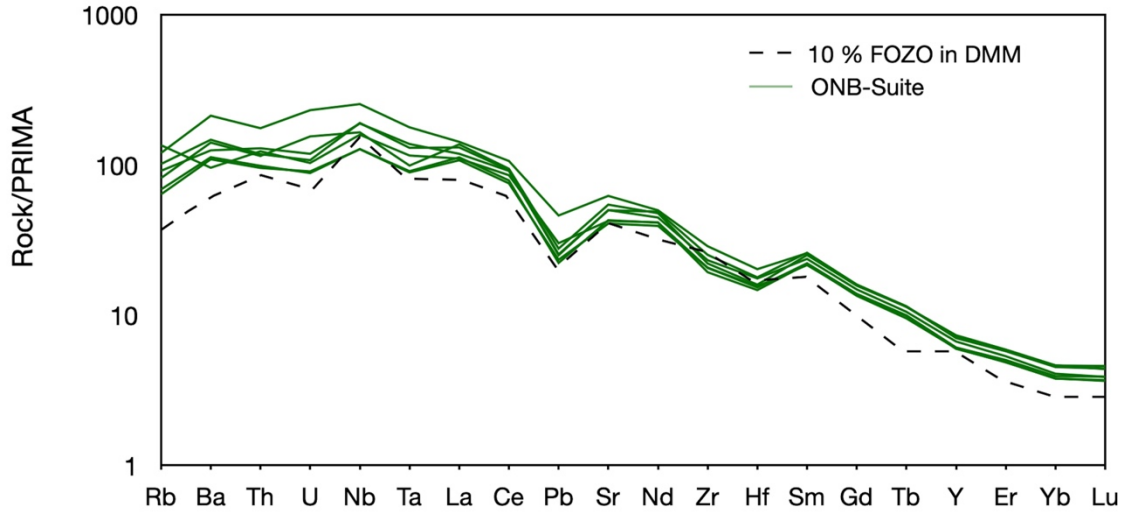

Figure 3.14 Adopting the batch melting approach of Shaw (1970) and using modelling paramters from Fekiacova et al. (2007), we have modelled mixing of a FOZO- and a DMM-like melt to create an enriched hybrid melt. Using the simple modal batch melting approach our results indicate that an enriched hybrid melt, created by mixing of 10-14% of FOZO-type melt (Raivavae lavas; RVV 360A; Lassiter et al. (2003)) and 86-90% of a DMM melt perfectly resembles the trace-element patters as found within our ONB-type lavas. Including the characteristic, negative K and Pb anomalies.

Given the distinct compositional differences of Quaternary volcanic rocks from the EVF further insights on the mantle sources of CEVP lavas can be retrieved from ^{187}Re-^{187}Os isotope

systematics. Samples from the EVF analyzed within this study are the first Quaternary ones and display generally elevated $^{187}Os/^{188}Os$ ratios in a range from 0.140 – 0.699 (Table 4). This range is in good agreement with previously reported, age corrected compositions of Tertiary intraplate volcanic rocks from the CEVP that yielded $^{187}Os/^{188}Os$ ratios up to 0.750. (Blusztajn and Hegner, 2002; Jung et al., 2005; Jung et al., 2011). The elevated $^{187}Os/^{188}Os$ compositions (0.140-0.699) as observed in Eifel volcanic rocks from this study generally argue against pure asthenospheric and (non-metasomatized) lithospheric mantle sources that should both have slightly sub- to near-chondritic $^{187}Os/^{188}Os$ ratios of ≤ 0.127 (Shirey and Walker, 1998). As this effects ONB- as well as F-suite and EEVF samples, Os isotope compositions further underline that none of the Quaternary volcanic suites are direct derivatives of a rising mantle plume and that both mantle sources have been affected by mantle metasomatism. Given that Re behaves highly incompatible during partial melting (Shirey and Walker, 1998; Hauri, 2002), the continental crust is characterized by high Re/Os that evolves towards strongly radiogenic $^{187}Os/^{188}Os$ compositions over time (>1.5) (Asmerom and Walker, 1998). Hence, crustal contamination may also affect $^{187}Os/^{188}Os$, but Os contents in continental crust are generally very low. Indeed, substantially elevated $^{187}Os/^{188}Os$ compositions in volcanic rocks from the CEVP have previously been inferred to reflect crustal contamination (Blusztajn and Hegner, 2002; Jung et al., 2005; Jung et al., 2011). However, while we have already excluded a substantial influence of crustal contamination, a negative correlation between $^{187}Os/^{188}Os$ and Re/Os in the EVF samples analyzed (Fig. 3.15A) further argues that the influence of a Re-enriched crust must have been insignificant (Hauri, 2002) and suggests a more complex, multi-stage history of the HSE inventory in Eifel volcanic rocks. With respect to lithospheric mantle components underneath the CEVP, previous studies on mantle xenoliths from the EVF have reported $^{187}Os/^{188}Os$ ratios ranging from 0.114 to 0.142, indicating that the Os isotope composition of some of these xenoliths have been as well been overprinted by mantle metasomatism (Schmidt and Snow, 2002; Fischer-Gödde et al., 2011). Additionally, a previous study by Kolb et al. (2012) has proposed the influence of residual eclogites in the source of CEVP volcanism. Given that residual eclogites tend to evolve towards highly radiogenic $^{187}Os/^{188}Os$ ratios due to elevated Re/Os ratios of their precursor rocks, we therefore argue that the observed Re-Os isotope features in EVF rock are rather in accord with residual recycled crustal materials. Additionally, as later occurring, partial re-melting of these components will result in the release of Os, but not Re that is strongly sequestered into garnets (Righter and Hauri, 1998; Hauri, 2002), residual eclogites could thus explain the anti-correlation between

$^{187}Os/^{188}Os$ and Re/Os and the observed positive correlations between $^{187}Os/^{188}Os$ and Mg# ratios that further provide evidence for an important role of eclogites within the source of EVF volcanism (Fig. 3.15). Given that the positive correlation of $^{187}Os/^{188}Os$ and Mg# is best resembled by ONB-suite volcanic rocks, our data does thus tentatively suggest a major influence of residual eclogites within the source of younger, WEVF volcanism. However, a weakness of this model is that direct melting eclogite produces melts with generally lower MgO concentrations (Dasgupta et al., 2005; Dasgupta et al., 2006) that do not agree with the high MgO compositions found within our samples from the ONB-Suite. The latter is further demonstrated by the decoupling of Zr/Hf and Mg# (Fig. 3.15). Hence, ONB-Suite rocks cannot represent direct melts of an eclogitic source and rather represent mixed partial melts of eclogitic sources and litospheric-mantle melts, where there is some overprint of the low, mantle-like Re/Os signature by the eclogitic components with high Re/Os.

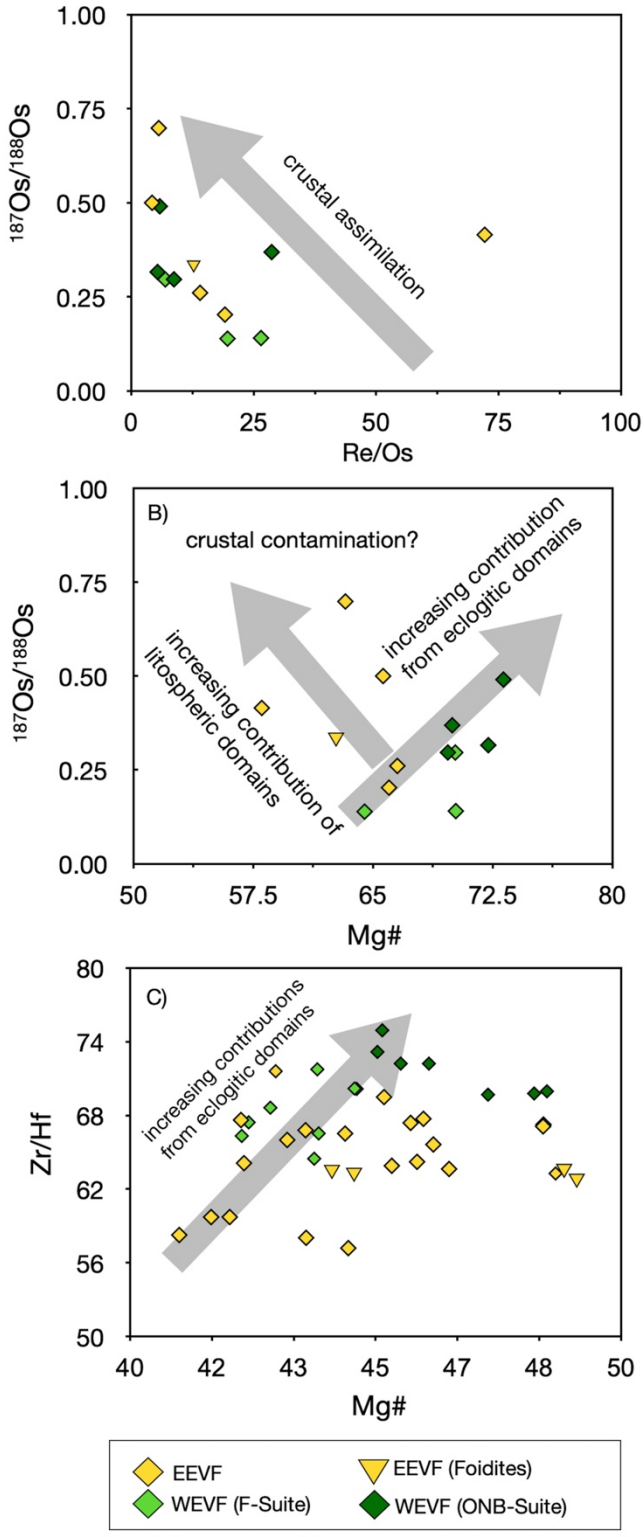

Figure 3.15 In $^{187}Os/^{188}Os$ vs. Re/Os (A) and $^{187}Os/^{188}Os$ vs. Mg# (B) space, samples display negative co-variations. Generally lower Re/Os ratios at increasing $^{187}Os/^{188}Os$ isotope compositions (A) and a positive correlation of Zr/Hf and Mg# are in good agreement with the influence of residual eclogites within the source of EVF volcanism. However, direct melting of eclogite produces melts with generally lower MgO concentrations that do not agree with the positive correlation found in $^{187}Os/^{188}Os$ vs. Mg# space (B). As such, ONB-Suite rocks cannot represent direct melts of an eclogitic source and rather represent mixed partial melts of an eclogitic source and litospheric-mantle melts.

Evidence for residual, carbonated eclogites in the source of the Eifel volcanic fields

Several experimental studies have provided strong evidence for the influence of carbonated eclogites on modern oceanic- as well as continental intraplate volcanism (e.g., Dasgupta et al., 2004; Dasgupta et al., 2005; Dasgupta et al., 2006). In detail, it has been inferred that carbonated eclogite bodies that enter the convecting upper mantle will release carbonate melts that may account for observed seismic anomalies at 280-400 km depth (Dasgupta et al., 2004), which is similar to what has been observed for the EVF (Ritter et al., 2007). Considering the influence of residual eclogites on CEVP volcanism, a previous model of Kolb et al. (2012) has proposed high Zr/Hf ratios and a positive correlation of Zr/Hf with La/Yb ratios in volcanic rocks from the Siebengebirge to result from the presence of residual eclogites. This eclogite pattern reflects the diagnostic fractionation of Zr from Hf in residual Ca-rich almandine, a typical mineral phase within mantle eclogites (see experimental data by Klemme et al., 2002). While the influence of a garnet-bearing mantle source has already been indicated throughout out melting model, samples from the EVF from this study also display a positive correlation in Zr/Hf vs. La/Yb space, with samples from the ONB-Suite and EEVF foidites yielding the highest Zr/Hf and La/Yb ratios (Fig. 3.16D). This observation further illustrates a distinct nature of ONB-Suite rocks compared to the EEVF and F-Suite and tentatively suggest the involvement of recycled oceanic crustal materials, predominantly within ONB-Suite volcanism. Further, the involvement of distinct, metasomatically overprinted lithospheric mantle sources is indicated by substantially elevated Nb/Ta ratios (15.9 to 23.5) in mafic samples that exceed compositions reported of OIBs (Nb/Ta = ~15-16 (Pfänder et al., 2012). Further to this, Nb/Ta in EVF lavas show positive co-variations with Lu/Hf and Zr/Hf ratios, and negative co-variations with Zr/Nb ratios (Fig. 3.16A-D). Our data reveal that most samples from the EEVF and the F-Suite have Nb/Ta ratios broadly similar to those observed in OIBs, whereas ONB-Suite samples and some foidites from the EEVF trend towards substantially elevated Nb/Ta and Zr/Hf ratios. A similar correlation has been found for volcanic rocks from the Vogelsberg, where Pfänder et al. (2012) proposed the involvement of carbonatitic material or remelting of carbonatized peridotite which are both characterized by elevated Nb/Ta and Lu/Hf ratios of ≥20 and ≥0.1, respectively. These features are explained by extreme depletions of Zr and Hf relative to the Heavy Rare Earth Elements (HREE) and only moderate depletions of Nb and Ta relative to the Light Rare Earth Elements (LREE) in carbonatites (e.g., Pfänder et al., 2012 and references therein). Additionally, it has been previously shown (e.g., by

Aulbach et al. 2011) that carbonatite metasomatism can substantially influence the HFSE inventory of (sub-) lithospheric mantle domains as mirrored by Nb/Ta and Zr/Hf ratios in kimberlites. This is in accordance with previously published modelling constraints that indicate European melilitites to originate from the interaction of CO_2-H_2O-enriched partial melts that form carbonated peridotite layers at the base of the litosphere (e.g., Wilson et al, 1995). While this provides a viable explanation on the compositions found within foiditic rocks analyzed in this study, carbonatite metasomatism has as well been shown to occur within the asthenosphere, which could explain as well explain the ratios found within ONB-Suite rocks, that display indications for a greater contribution of garnet-bearing, eclogitic mantle sources.

Conclusively, our results are in good agreement with a polybaric melting model where EVF melts are derived from both asthenospheric and lithospheric sources. The proportion of lithospheric components varies, with ONB suite rocks marking greater contributions of the asthenospheric endmember. While higher average depths of partial melting and radiogenic isotope compositions identify a major contribution of a FOZO-type mantle source to ONB-Suite volcanism, F-Suite and EEVF trace-element and radiogenic isotope compositions are in good agreement with an enhanced contribution of lithospheric sources and shallower melting depths. Based on high Nb/Ta, Zr/Hf, La/Yb and radiogenic $^{187}Os/^{188}Os$ compositions, our data provide evidence for the presence of residual and potentially carbonated eclogitic components present within the upper mantle underneath the CEVP and a potential influence of carbonatite metasomatism (Fekiacova et al., 2007; Kolb et al., 2012; Pfänder et al., 2012). While eclogitic components have shown to be stable on rising mantle plumes (e.g., Shi et al., 2022), our results indicate that ONB-Suite represent partial melts generated from a metasomatically overprinted TBL at the base of the European litosphere, rather direct melts of a mantle plume (Wilson et al., 1995).

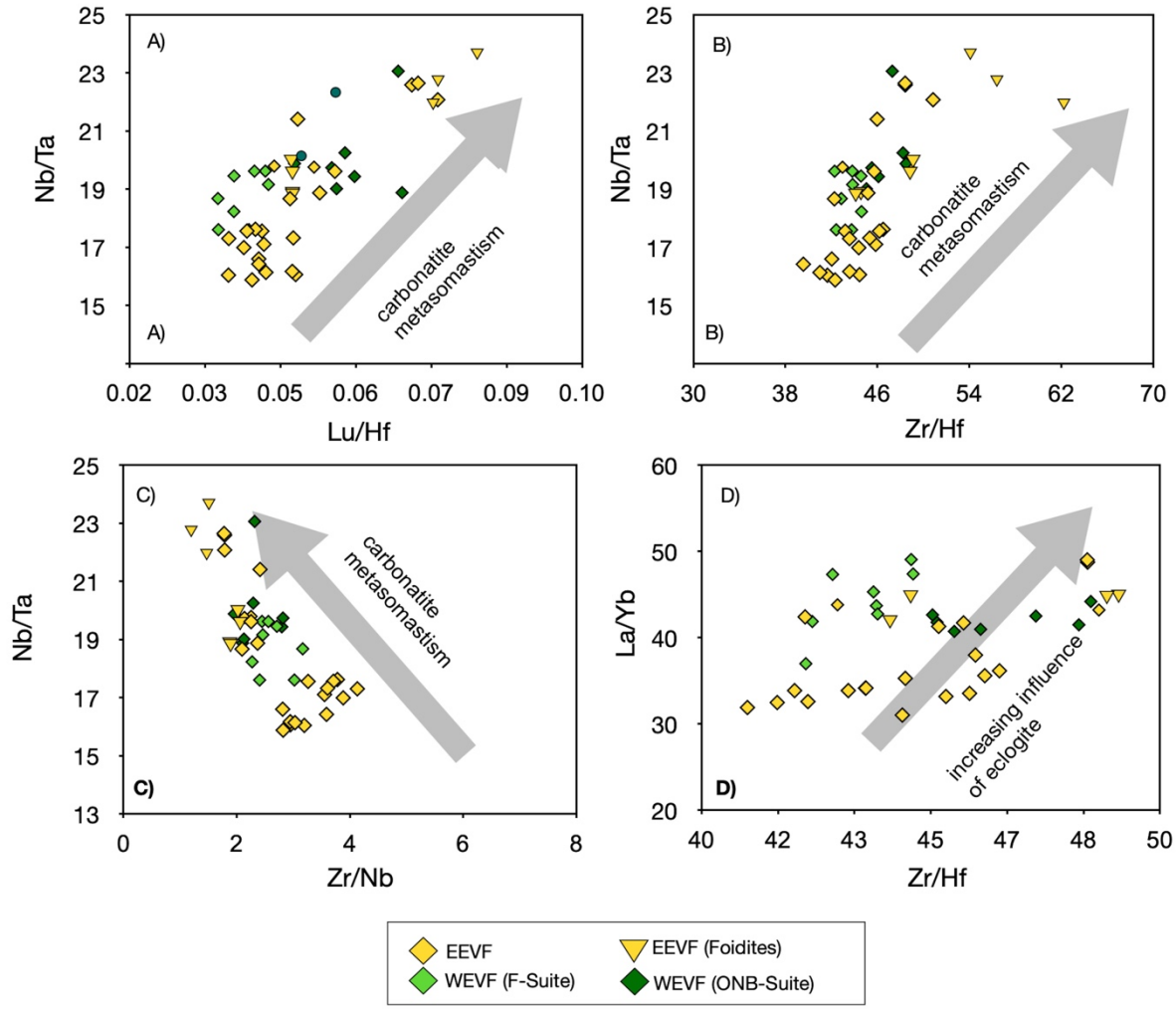

Figure 3.16 In Nb/Ta vs. Lu/Hf- (A), Nb/Ta vs. Zr/Hf- (B), Nb/Ta vs. Zr/Nb- (C) and La/Yb vs. Zr/Hf (C): Nb/Ta ratios exceed compositions reported of OIBs (Nb/Ta = ~15-16 (Pfänder et al., 2012) and are positively correlated with Lu/Hf (A) and Zr/Hf (B) and negatively correlated with Zr/Nb (C) ratios. Similar to a previous study on volcanic rocks from the Vogelsberg volcano, our data thus suggest the influence of a reservoir that has been subjected to carbonatite metasomatism (Pfänder et al., 2012). Further, the samples display a positive correlation of Zr/Hf vs. La/Yb ratios (D). This is similar to what has been observed for volcanic rocks from the Siebengebirge and indicates element fractionation through Ca-rich almandine-bearing residual eclogites (Kolb et al., 2012).

Spatial and temporal constraints on EVF volcanism

The prevailing SiO_2–undersaturated volcanism within the EVF has emerged during distinct periods that were initiated during the Tertiary (HEVF at ~44-35 Ma (Fekiacova et al., 2007)) and had intermittently occurred until the Holocene (WEVF, ~700 Ma – 10.8 ka; EVF, 500 Ma – 12.9 ka (Schmincke, 2007)). Previous studies have suggested that the bimodal time-space-composition distribution of the EVF patterns reflect the seismological contrast of the asthenosphere (Ritter and Christensen, 2007; Mertz et al., 2015). In detail, a study by Mertz et al. (2015) has combined seismological and geochemical data on Quaternary Eifel volcanism,

reporting that the areal extent of ONB-suite volcanism, younger <80 ka, is in good agreement with a surface projected P-wave anomaly that is thought to reflect a mantle plume underneath the EVF (Ritter and Christensen, 2007). In contrast, volcanic edifices that compositionally resemble F-suite volcanism are located outside the boarders of surface projected P-wave anomaly (Mertz et al., 2015). From these seismic patterns, it has been inferred that ONB-Suite volcanic rocks have incorporated more plume-derived asthenospheric components compared to F-Suite rocks that are rather dominated by refractory lithospheric sources (Mertz et al., 2015). In general, our newly obtained high precision radiogenic isotope and trace element data confirm the previously reported temporal, spatial and compositional differences between EEVF, F- and ONB-Suite magmatism. However, Mertz et al. (2015) suggested that volcanism within the WEVF prior to 80 ka must have interacted with lithospheric mantle domains that were no longer available for younger, ONB-Suite volcanism. While this may hold true for the WEVF, temporal and compositional overlap of FE-Suite and WEVF magmatism and the distinct isotopic nature of ONB-Suite lavas rather suggest that both mantle domains are still present underneath the EVF. Likewise, the trace-element and radiogenic isotope composition of ONB samples analyzed within this study require at least some minor addition of metasomatized lithospheric domains, possibly in a longer melting column that preferentially taps asthenospheric mantle. This is also illustrated by the highly radiogenic $^{187}Os/^{188}Os$ compositions (0.297-0.491) observed in ONB-Suite samples that are still more radiogenic compared to pure asthenospheric and (non-metasomatized) lithospheric mantle melts (e.g., Shirey and Walker, 1998).

The new data presented here allows some new constraints on the temporal evolution of magmatism within the CEVP. Broadly similar to the model of Mertz et al. (2015), previous studies by Haase et al. (2004) and Jung et al. (2006) have suggested spatial, temporal and compositional heterogeneities to result from discrete magmatic pulses. In detail, combining temporal constraints from Haase et al. (2004) and geochemical compositions of newly measured HEVF samples, the study by Jung et al. (2006) showed that the variability of $^{206}Pb/^{204}Pb$ ratios within tertiary volcanic can be tied to distinct eruptive periods: 39 Ma (Hocheifel) with $^{206}Pb/^{204}Pb$ = ~19, 37 Ma to 20 Ma (Hocheifel, Siebengebirge and Westerwald) with $^{206}Pb/^{204}Pb$ = 19.3 to 19.7 and 20 Ma to 10 Ma (Vogelsberg, Hessian Depression) with $^{206}Pb/^{204}Pb$ = 18.8 to 19.3. As a potential explanation, Haase et al. (2004) and Jung et al. (2006) suggested the elevated $^{206}Pb/^{204}Pb$ to result from enhanced contributions of asthenospheric melts, likely reflecting plume-derived material, whereas lower $^{206}Pb/^{204}Pb$ are

attributed to result from an EM I-like reservoir, most likely the lithosperic mantle (Jung et al., 2006).

While it has already been noted by Jung et al. (2006) that the low $^{206}Pb/^{204}Pb$ samples from the youngest Quaternary Eifel volcanism, previously measured by Wörner et al. (1986) rather resemble an asthenospheric endmember, our data combined with previous age data (Nowell et al., 2006 and references therein) now indicate that the overall compositional–temporal trends continue throughout the Quaternary (Fig. 3.17). In fact, the temporal evolution of radiogenic Sr-Nd-Pb isotope compositions reveal wave-like that indicate discrete magmatic pulses and variable participation of asthenospheric and lithospheric reservoirs with time (Fig.17). In detail, distinct pulses of asthenospheric, plume-like material can be identified based on radiogenic Pb and Nd and unradiogenic Sr isotope compositions (Fig. 17) and seem to occur around ~35 Ma (Hocheifel), ~25 Ma (Siebengebirge, Westerwald), 500 ka (some samples of the F-Suite, EEVF) and <80 ka (ONB-Suite, EEVF). In contrast, enhanced contributions of litospheric sources are indicated by radiogenic Sr and unradiogenic Nd and Pb isotope compositions (Fig. 3.17) and are found within volcanism older than 35 Ma (Hocheifel), around ~15 Ma (Vogelsberg) and around ~250 ka (EEVF, F-Suite). Focussing on the samples analyzed within this study, our data suggest the enhanced influence of thermal boundary layer/ lithospheric source input for F-Suite and EEVF volcanism, whereas ≤ 80 ka ONB-Suite volcanism with $^{206}Pb/^{204}Pb$ ratios between 19.3 -19.5 resemble an asthenospheric or plume-like source. Figure 3.17C displays that some samples from the F-Suite plot at slightly higher $^{206}Pb/^{204}Pb$ at about 500 ka, potentially indicating a small-scale pulse by plume-like material. Collectively, our data are in good agreement with models inferring discrete melt pulses to account for the compositional, temporal and spatial variability of CEVP volcanism. Collectively, by providing as one of the first studies detailed high precision radiogenic isotope and trace-element data for Quaternary volcanic rocks of the CEVP, our study provides further evidence for discrete asthenospheric and lithospheric melt sources underneath the CEVP that are tapped at variable proportions through time.

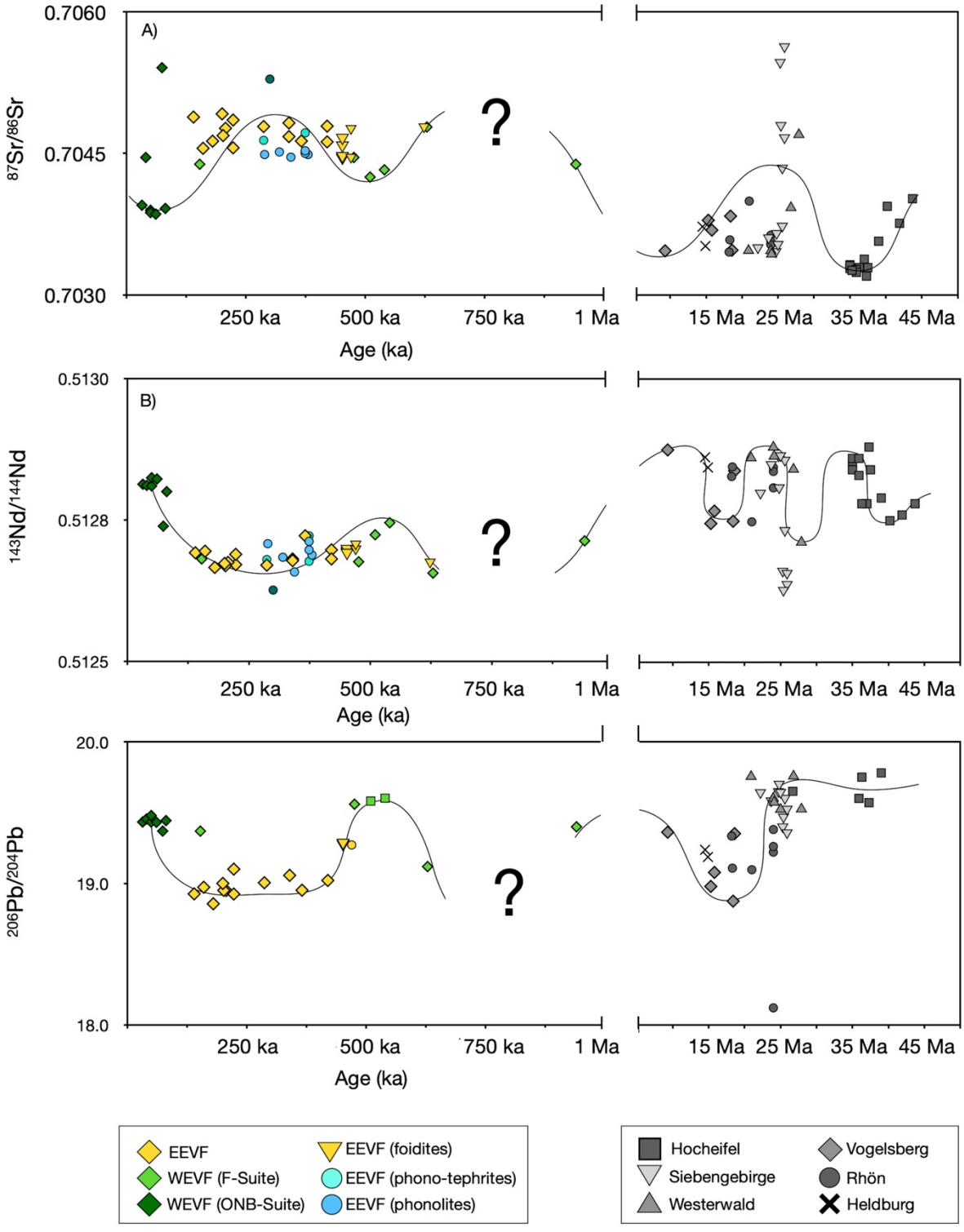

Figure 3.17 In $^{87}Sr/^{86}Sr$-, $^{143}Nd/^{144}Nd$ and $^{206}Pb/^{204}Pb$ vs. Age diagrams combined isotope–age constraints display wave-like patterns, indicating that available mantle sources change with time. (ages and isotope compositions of tertiary volcanic rocks: Haase et al., 2004; Jung et al., 2006; Nowell et al., 2006; Fekiacova et al., 2007; Kolb et al., 2012; Mayer et al., 2013; Schneider et al., 2016). For age references on volcanic edifices investigated in this study see Nowell et al., 2006).

Conclusions

Our study provides a new comprehensive trace element and radiogenic isotope dataset for volcanic rocks from the Quaternary Eifel volcanic field, providing the following new constraints on the origin and source composition of magmatism beneath western Germany and the Cenozoic European Volcanic Province in general:

The majority of samples investigated are mafic, primitive volcanic rocks (Mg# ≥ 57) that have undergone only limited fractional crystallization of olivine, clinopyroxene and amphibole. Plagioclase fractionation is mostly insignificant. Volcanic rocks in the WEVF are more mafic than in the EEVF.

1) Our newly obtained radiogenic isotope compositions are in good agreement with previous Sr-Nd-Pb isotope studies (Wörner et al. (1986) and mirror the previous, petrogenetic subdivision of Mertes and Schmincke (1985) that was based on major elements. While samples from both volcanic fields display a general compositional overlap within their Sr-Nd-Hf isotope compositions, ONB- and F-Suite volcanic rocks and samples from the EEVF can be clearly distinguished based on their distinct Pb isotope compositions. Samples from the EEVF and the F-Suite display a linear mixing array, with F-Suite samples defining the most radiogenic- and samples from the EEVF defining the unradiogenic end of the array.

2) Samples from the ONB-Suite can be clearly distinguished from the other suites by unradiogenic Sr and radiogenic Hf-Nd isotope compositions. Additionally, ONB samples are shifted towards lower $^{207}Pb/^{204}Pb$ and $^{208}Pb/^{204}Pb$ at given $^{206}Pb/^{204}Pb$ isotope compositions.

3) EC-AFC modelling of Sr-Nd isotope compositions for mafic and more differentiated samples rules our any significant contribution of assimilated lower- or upper-crustal material. Therefore, we conclude that their radiogenic isotope compositions reflect the composition of their parental magmatic sources.

4) Combined trace-element and radiogenic isotope compositions of ONB-Suite samples are in good agreement with results from batch melting models that indicate a hybrid composition formed through mixing 10% of a FOZO-like melt with 90% of a DMM-like melt, similar to melts from the Tertiary HEVF.
5) Partial melting of an enriched, FOZO-EAR-like asthenospheric mantle endmember cannot account for the range of elevated Nb/Ta, Zr/Hf and La/Yb and Ce/Pb, K*/K ratios observed in this study. As evidenced by radiogenic Sr-Nd-Pb isotope compositions of F-Suite and EEVF and ONB lavas, the admixture of melts from lithospheric mantle sources is required.
6) Elevated Nb/Ta and Lu/Hf ratios at variable $^{187}Os/^{188}Os$ ratios are in good agreement with partial melting of a lithospheric mantle that has been overprinted by carbonatite metasomatism (Pfänder et al., 2012). In contrast, a positive correlation of Zr/Hf and La/Yb and the elevated Nb/Ta also indicate the presence of residual carbonated eclogites (Pfänder et al., 2007; Kolb et al., 2012), which can also account for the radiogenic $^{187}Os/^{188}Os$ and the anti-correlation between $^{187}Os/^{188}Os$ and Re/Os.
7) Combined geochemical and temporal constraints suggest that CEVP volcanism in central and western Germany has resulted from compositionally distinct magmatic pulses. While a lithospheric component must have contributed to variable extent to all eruptive periods, an influence of an asthenospheric, FOZO-like mantle source is predominantly found within the ONB-Suite of our sample set and distinct eruptive periods of Siebengebirge-, Weseterwald and Hocheifel volcanism.
8) Although we can neither fully exclude nor confirm the presence of a mantle plume, our data rather argue in favor of plume-like melt pulses that might provide a viable explanation for the temporal and compositional cyclicity of CEVP volcanism (Haase et al., 2004; Jung et al., 2006).
9) Our results are similar to a petrogenetic models that suggested pooling of polybaric melts from asthenospheric and lithospheric sources to be responsible for the geochemical composition of Quaternary intraplate volcanic rocks elsewhere (Haase et al., 2004; Jung et al., 2006; Sprung et al., 2007). Asthenospheric source are increasingly tapped by deeper melting columns.

References

Abratis, M., Viereck, L., Pfänder, J.A., Hentschel, R., 2015. Geochemical composition, petrography and 40Ar/39Ar age of the Heldburg phonolite: implications on magma mixing and mingling. International Journal of Earth Sciences 104, 2033-2055.

Albarede, F., Telouk, P., Blichert-Toft, J., Boyet, M., Agranier, A., Nelson, B., 2004. Precise and accurate isotopic measurements using multiple-collector ICPMS. Geochimica et Cosmochimica Acta 68, 2725-2744.

Ammon K., Dunai T.J., Stuart F. M., Meriaux A-S., & Gayer E., (2009). Cosmogenic ^{3}He exposure ages and geochemistry of basalts from Ascension Island, Atlantic Ocean. Quaternary Geochronology 4, 423-430.

Archer, G.J., Brennecka, G.A., Gleißner, P., Stracke, A., Becker, H., Kleine, T., 2019. Lack of late-accreted material as the origin of 182W excesses in the Archean mantle: Evidence from the Pilbara craton, western Australia. Earth and Planetary Science Letters 528, 115841.

Ashwal, L.D., Wiedenbeack M., Torsvik T. H., 2017. Archean zircons in Miocene oceanic hotspot rocks establish ancient continental crust beneath Mauritius. Nature Communications, 14089

Asmerom, Y., Walker, R.J., 1998. Pb and Os isotopic constraints on the composition and rheology of the lower crust. Geology 26, 359-362.

Aulbach, S., O'Reilly, S.Y., Pearson, N.J., 2011. Constraints from eclogite and MARID xenoliths on origins of mantle Zr/Hf–Nb/Ta variability. Contributions to Mineralogy and Petrology 162, 1047-1062.

Avanzinelli, R., Braschi, E., Marchionni, S., Bindi, L. (2014). Mantle melting in within-plate continental settings: Sr–Nd–Pb and U-series isotope constraints in alkali basalts from the Sicily Channel (Pantelleria and Linosa Islands, Southern Italy). Lithos, 188, 113-129.

Avanzinelli, R., Casalini, M., Elliott, T., & Conticelli, S. (2018). Carbon fluxes form subducted carbonates revealed by uranium excess at Mount Vesuvius, Italy. Geology, 46(3), 259–262. https://doi.org/10.1130/G39766.1.

Bea, F., Pereira, M., Stroh, A., 1994. Mineral/leucosome trace-element partitioning in a peraluminous migmatite (a laser ablation-ICP-MS study). Chemical Geology 117, 291-312.

Bekaert, D. V., Broadley, M.W., Caracausi, A., Marty, B., 2019. Novel insights into the degassing history of Earth's mantle from high precision noble gas analysis of magmatic gas. Earth Planet. Sci. Lett. 525, 115766. https://doi.org/10.1016/j.epsl.2019.115766

Belay, I. G., Tanaka, R., Kitagawa, H., Kobayashi, K., & Nakamura, E. (2019). Origin of ocean island basalts in the West African passive margin without mantle plume involvement. Nature communications, 10(1), 1-12.

Birck, J.L., Barman, M.R., Capmas, F., 1997. Re-Os isotopic measurements at the femtomole level in natural samples. Geostandards newsletter 21, 19-27.

Blichert-Toft, J., Albarède, F., 1997. The Lu-Hf isotope geochemistry of chondrites and the evolution of the mantle-crust system. Earth and Planetary Science Letters 148, 243-258.

Blusztajn, J., Hegner, E., 2002. Osmium isotopic systematics of melilitites from the Tertiary Central European Volcanic Province in SW Germany. Chemical Geology 189, 91-103.

Bogaard, P., Wörner, G., 2003. Petrogenesis of basanitic to tholeiitic volcanic rocks from the Miocene Vogelsberg, Central Germany. Journal of Petrology 44, 569-602.

Bohrson, W.A., Spera, F.J., 2001. Energy-constrained open-system magmatic processes II: application of energy-constrained assimilation–fractional crystallization (EC-AFC) model to magmatic systems. Journal of Petrology 42, 1019-1041.

Bosch, D., Blichert-Toft, J., Moynier, F., Nelson, B.K., Telouk, P., Gillot, P.Y., Albarède, F., 2008. Pb, Hf and Nd isotope compositions of the two Réunion volcanoes (Indian Ocean): A tale of two small-scale mantle "blobs"? Earth Planet. Sci. Lett. 265, 748–765. https://doi.org/10.1016/j.epsl.2007.11.018

Bouvier, A., Vervoort, J.D., Patchett, P.J., 2008. The Lu-Hf and Sm-Nd isotopic composition of CHUR: Constraints from unequilibrated chondrites and implications for the bulk composition of terrestrial plantes. Earth Planet. Sci. Lett. 237, 48–57.

Bragagni, A., Avanzinelli, R., Freymuth, H., Francalanci, L., 2014. Recycling of crystal mush-derived melts and short magma residence times revealed by U-series disequilibria at Stromboli volcano. Earth Planet. Sci. Lett. 404, 206–219.

Bragagni, A., Mastroianni, F., Münker, C., Conticelli, S. and Avanzinelli, R., 2022. A carbon-rich lithospheric mantle as a source for the large CO2 emissions of Etna volcano (Italy). Geology.

Brandl, P.A., Genske, F.S., Beier, C., Haase, K.M., Sprung, P., Krumm, S.H., 2015. Magmatic evidence for carbonate metasomatism in the lithospheric mantle underneath the Ohře (Eger) Rift. Journal of Petrology 56, 1743-1774.

Brown, S., Elkins-Tanton, L., Walker, R., 2013. Linking early Earth magma ocean crystallization and overturn with observed large low-shear-velocity provinces (LLSVPs) and short-lived radioisotopic measurements in Archean rocks, AGU Fall Meeting Abstracts, pp. V33D-2782.

Caracausi, A., Avice, G., Burnard, P.G., Füri, E., Marty, B., 2016. Chondritic xenon in the Earth's mantle. Nature 533, 82–85. https://doi.org/10.1038/nature17434

Carlson, R.W., Boyet, M., 2008. Composition of the Earth's interior: The importance of early events. Philos. Trans. R. Soc. A Math. Phys. Eng. Sci. 366, 4077–4103. https://doi.org/10.1098/rsta.2008.0166

Cebria, J., Wilson, M., 1995. Cenozoic mafic magmatism in Western/Central Europe: a common European asthenospheric reservoir. Terra Nova 7, 162.

Celli, N. L., Lebedev, S., Schaeffer, A. J., & Gaina, C. (2021). The tilted Iceland Plume and its effect on the North Atlantic evolution and magmatism. Earth and Planetary Science Letters, 569, 117048.

Chauvel, C., Hofmann, A.W., Vidal, P., 1992. HIMU-EM: the French Polynesian connection. Earth and Planetary Science Letters 110, 99-119.

Chou C.-L. (1978) Fractionation of siderophile elements in the earth´s upper mantle. Proc. Lunar Planet. Sci. Conf. 9th, 219–230.

Christensen, U.R., Hofmann, A.W., 1994. Segregation of subducted oceanic crust in the convecting mantle. Journal of Geophysical Research: Solid Earth 99, 19867-19884.

Coggon, J.A., Luguet, A., Nowell, G.M., Appel, P.W., 2013. Hadean mantle melting recorded by southwest Greenland chromitite 186Os signatures. Nature Geoscience 6, 871-874.

Cohen, A.S., Waters, F.G., 1996. Separation of osmium from geological materials by solvent extraction for analysis by thermal ionisation mass spectrometry. Analytica Chimica Acta 332, 269-275.

Coltice, N., Ricard, Y., 1999. Geochemical observations and one layer mantle convection. Earth and Planetary Science Letters 174, 125-137.

Corgne, A., Allan, N.L., Wood, B.J., 2003. Atomistic simulations of trace element incorporation into the large site of MgSiO3 and CaSiO3 perovskites. Physics of the Earth and Planetary Interiors 139, 113-127.

Corgne, A., Liebske, C., Wood, B.J., Rubie, D.C., Frost, D.J., 2005. Silicate perovskite-melt partitioning of trace elements and geochemical signature of a deep perovskitic reservoir. Geochimica et Cosmochimica Acta 69, 485-496.

Courtillot, V., Davaille, A., Besse, J. and Stock, J., 2003. Three distinct types of hotspots in the Earth's mantle. *Earth and Planetary Science Letters*, *205*(3-4), pp.295-308.
Craig, H., Lupton, J.E., 1981. 11. HELIUM-3 AND MANTLE VOLATILES IN. The oceanic lithosphere 7, 391.

Dale, C. W., Pearson, D. G., Starkey, N. A., Stuart, F. M., Ellam, R. M., Larsen, L. M., Fitton, J.G., Macpherson, C. G. (2009). Osmium isotopes in Baffin Island and West Greenland picrites: Implications for the 187Os/188Os composition of the convecting mantle and the nature of high 3He/4He mantle. Earth and Planetary Science Letters, 278(3-4), 267-277.

Dasgupta, R., Hirschmann, M.M., Dellas, N., 2005. The effect of bulk composition on the solidus of carbonated eclogite from partial melting experiments at 3 GPa. Contributions to Mineralogy and Petrology 149, 288-305.

Dasgupta, R., Hirschmann, M.M., Stalker, K., 2006. Immiscible transition from carbonate-rich to silicate-rich melts in the 3 GPa melting interval of eclogite+ CO2 and genesis of silica-undersaturated ocean island lavas. Journal of Petrology 47, 647-671.

Dasgupta, R., Hirschmann, M.M. and Withers, A.C., 2004. Deep global cycling of carbon constrained by the solidus of anhydrous, carbonated eclogite under upper mantle conditions. *Earth and Planetary Science Letters*, *227*(1-2), pp.73-85.

Davies, D.R., Goes, S., Davies, J.H., Schuberth, B.S.A., Bunge, H.P., Ritsema, J., 2012. Reconciling dynamic and seismic models of Earth's lower mantle: The dominant role of thermal heterogeneity. Earth and Planetary Science Letters 353, 253-269.

DePaolo, D.J., 1981. Trace element and isotopic effects of combined wallrock assimilation and fractional crystallization. Earth and planetary science letters 53, 189-202.

Doucet, L.S., Li, Z.X., Gamal El Dien, H., Pourteau, A., Murphy, J.B., Collins, W.J., Mattielli, N., Olierook, H.K., Spencer, C.J. and Mitchell, R.N., 2020. Distinct formation history for deep-mantle domains reflected in geochemical differences. Nature Geoscience, 13(7), pp.511-515.

Duda, A., Schmincke, H.-U., 1985. Polybaric differentiation of alkali basaltic magmas: evidence from green-core clinopyroxenes (Eifel, FRG). Contributions to Mineralogy and Petrology 91, 340-353.

Doubrovine, P.V., Steinberger, B. and Torsvik, T.H., 2016. A failure to reject: Testing the correlation between large igneous provinces and deep mantle structures with EDF statistics. Geochemistry, Geophysics, Geosystems, 17(3), pp.1130-1163.

Dunai, T. J., & Baur, H. (1995). Helium, neon, and argon systematics of the European subcontinental mantle: Implications for its geochemical evolution. Geochimica et Cosmochimica Acta, 59(13), 2767-2783.

Dupré, B., Allègre, C.J., 1983. Pb–Sr isotope variation in Indian Ocean basalts and mixing phenomena. Nature 303, 142–146.

Farley, K., Natland, J., Craig, H., 1992. Binary mixing of enriched and undegassed (primitive?) mantle components (He, Sr, Nd, Pb) in Samoan lavas. Earth and Planetary Science Letters 111, 183-199.

Fekiacova, Z., Mertz, D.F., Renne, P.R., 2007. Geodynamic setting of the tertiary Hocheifel volcanism (Germany), Part I: 40 Ar/39 Ar geochronology, Mantle Plumes. Springer, pp. 185-206.

Fischer-Gödde, M., Becker, H., Wombacher, F., 2011. Rhodium, gold and other highly siderophile elements in orogenic peridotites and peridotite xenoliths. Chemical Geology 280, 365-383.

Friedman, A.M., Milsted, J., Metta, D., Henderson, D., Lerner, J., Harkness, A.L. and Op, D.R., 1966. Alpha decay half lives of 148Gd 150Gd and 146Sm. Radiochimica Acta, 5(4), pp.192-194.

Füri, E., Hilton, D.R., Murton, B.J., Hémond, C., Dyment, J., Day, J.M.D., 2011. Helium isotope variations between Réunion Island and the Central Indian Ridge (17°–21°S): New evidence for ridge–hot spot interaction. Journal of Geophysical Research 116. https://doi.org/10.1029/2010JB007609

Garbe-Schönberg, C.D., 1993. Simultaneous determination of thirty-seven trace elements in twenty-eight international rock standards by ICP-MS. Geostandards Newsletter 17, 81-97.

Gast, P.W., Tilton, G., Hedge, C., 1964. Isotopic composition of lead and strontium from Ascension and Gough Islands. Science 145, 1181-1185.

Geldmacher, J., Hoernle, K., Hanan, B.B., Blichert-Toft, J., Hauff, F., Gill, J.B., Schmincke, H.-U., 2011. Hafnium isotopic variations in East Atlantic intraplate volcanism. Contributions to Mineralogy and Petrology 162, 21-36.

Goes, S., Govers, R., Vacher, 2000. Shallow mantle temperatures under Europe from P and S wave tomography. Journal of Geophysical Research: Solid Earth 105, 11153-11169.

Goes, S., Spakman, W., Bijwaard, H., 1999. A lower mantle source for central European volcanism. Science 286, 1928-1931.

Graham, D.W., 2002. Noble Gas Isotope Geochemistry of Mid-Ocean Ridge and Ocean Island Basalts: Characterization of Mantle Source Reservoirs. Reviews in Mineralogy and Geochemistry, 47 (1), 247–317. doi: https://doi.org/10.2138/rmg.2002.47.8

Granet, M., Wilson, M., Achauer, U., 1995. Imaging a mantle plume beneath the French Massif Central. Earth Planet. Sci. Lett. 136, 281–296.

Green, T., Blundy, J., Adam, J., Yaxley, G., 2000. SIMS determination of trace element partition coefficients between garnet, clinopyroxene and hydrous basaltic liquids at 2–7.5 GPa and 1080–1200 C. Lithos 53, 165-187.

Guimarães, A.R., Fitton, J.G., Kirstein, L.A., Barfod, D.N., 2020. Contemporaneous intraplate magmatism on conjugate South Atlantic margins: A hotspot conundrum. Earth Planet. Sci. Lett. 536, 116147.

Gündüz, M. and Asan, K., 2021. PetroGram: An excel-based petrology program for modeling of magmatic processes. Geoscience Frontiers, 12(1), pp.81-92

Haase, K.M., GOLDSCHMIDT, B., GARBE-SCHÖNBERG, C.-D., 2004. Petrogenesis of Tertiary continental intra-plate lavas from the Westerwald region, Germany. Journal of petrology 45, 883-905.

Hanan, B., Graham, D., 1996. Lead and helium isotope evidence from oceanic basalts for a common deep source of mantle plumes. Science 272, 991-995.

Hart, S., 1971. K, Rb, Cs, Sr and Ba contents and Sr isotope ratios of ocean floor basalts. Philosophical Transactions of the Royal Society of London. Series A, Mathematical and Physical Sciences 268, 573-587.

Hart, S., Hauri, E., Oschmann, L., Whitehead, J., 1992. Mantle plumes and entrainment: isotopic evidence. Science 256, 517-520.

Hauri, E.H., 2002. Osmium isotopes and mantle convection. Philosophical Transactions of the Royal Society of London. Series A: Mathematical, Physical and Engineering Sciences 360, 2371-2382.

Hawkesworth, C., Norry, M., Roddick, J., Vollmer, R., 1979. 143Nd/144Nd and 87Sr/86Sr ratios from the Azores and their significance in LIL-element enriched mantle. Nature 280, 28-31.

Hedge, C., Walthall, F., 1963. Radiogenic strontium-87 as an index of geologic processes. Science 140, 1214-1217.

Hegner, E., Walter, H., Satir, M., 1995. Pb-Sr-Nd isotopic compositions and trace element geochemistry of megacrysts and melilitites from the Tertiary Urach volcanic field: source composition of small volume melts under SW Germany. Contributions to Mineralogy and Petrology 122, 322-335.

Heyn, B.H., Conrad, C.P., Trønnes, R.G., 2020. Core-mantle boundary topography and its relation to the viscosity structure of the lowermost mantle. Earth and Planetary Science Letters 543, 116358.

Hirata, T., 1996. Lead isotopic analyses of NIST standard reference materials using multiple collector inductively coupled plasma mass spectrometry coupled with a modified external correction method for mass discrimination effect. Analyst 121, 1407-1411.

Hoernle, K., Rohde, J., Hauff, F., Garbe-Schönberg, D., Homrighausen, S., Werner, R., Morgan, J.P., 2015. How and when plume zonation appeared during the 132 Myr evolution of the Tristan Hotspot. Nature communications 6, 1-10.

Hoernle, K., Schwindrofska, A., Werner, R., van den Bogaard, P., Hauff, F., Uenzelmann-Neben, G., Garbe-Schönberg, D., 2016. Tectonic dissection and displacement of parts of Shona hotspot volcano 3500 km along the Agulhas-Falkland Fracture Zone. Geology 44, 263-266.

Hoernle, K., Zhang, Y.-S., Graham, D., 1995. Seismic and geochemical evidence for large-scale mantle upwelling beneath the eastern Atlantic and western and central Europe. Nature 374, 34-39.

Hoffmann, J.E., Münker, C., Polat, A., König, S., Mezger, K., Rosing, M.T., 2010. Highly depleted Hadean mantle reservoirs in the sources of early Archean arc-like rocks, Isua supracrustal belt, southern West Greenland. Geochimica et Cosmochimica Acta 74, 7236-7260.

Hoffmann, J.E., Münker, C., Næraa, T., Rosing, M.T., Herwartz, D., Garbe-Schönberg, D. and Svahnberg, H., 2011. Mechanisms of Archean crust formation inferred from high-precision HFSE systematics in TTGs. *Geochimica et Cosmochimica Acta*, *75*(15), pp.4157-4178.

Hofmann, A., 2003. Sampling mantle heterogeneity through oceanic basalts: isotopes and trace elements. Treatise on geochemistry 2, 568.

Hofmann, A.W., 1997. Mantle geochemistry: the message from oceanic volcanism. Nature 385, 219-229.

Hofmann, A.W., Jochum, K.P., Seufert, M., White, W.M., 1986. Nb and Pb in oceanic basalts: new constraints on mantle evolution. Earth and Planetary science letters 79, 33-45.

Homrighausen, S., Hoernle, K., Hauff, F., Geldmacher, J., Wartho, J.-A., van den Bogaard, P., Garbe-Schönberg, D., 2018. Global distribution of the HIMU end member: Formation through Archean plume-lid tectonics. Earth-science reviews 182, 85-101.

Homrighausen, S., Hoernle, K., Hauff, F., Wartho, J.-A., van den Bogaard, P., Garbe-Schönberg, D., 2019. New age and geochemical data from the Walvis Ridge: The temporal and spatial diversity of South Atlantic intraplate volcanism and its possible origin. Geochimica et Cosmochimica Acta 245, 16-34.

Homrighausen, S., Hoernle, K., Zhou, H., Geldmacher, J., Wartho, J.-A., Hauff, F., Werner, R., Jung, S., Morgan, J.P., 2020. Paired EMI-HIMU hotspots in the South Atlantic—Starting plume heads trigger compositionally distinct secondary plumes? Science advances 6, eaba0282.

Iizuka, T., Nakai, S.i., Sahoo, Y.V., Takamasa, A., Hirata, T., Maruyama, S., 2010. The tungsten isotopic composition of Eoarchean rocks: implications for early silicate differentiation and core–mantle interaction on Earth. Earth and Planetary Science Letters 291, 189-200.

Jackson, M.G., Blichert-Toft, J., Halldórsson, S.A., Mundl-Petermeier, A., Bizimis, M., Kurz, M.D., Price, A.A., Harðardóttir, S., Willhite, L.N., Breddam, K., 2020a. Ancient helium and tungsten isotopic signatures preserved in mantle domains least modified by crustal recycling. Proceedings of the National Academy of Sciences 117, 30993-31001.

Jansen, M.W., Tusch, J., Münker, C., Bragagni, A., Avanzinelli, R., Mastroianni, F., Stuart, F.M., Kurzweil, F., 2022. Upper mantle control on the W isotope record of shallow level plume and intraplate volcanic settings. Earth and Planetary Science Letters 585, 117507.

Jung, C., Jung, S., Hoffer, E., Berndt, J., 2006. Petrogenesis of Tertiary mafic alkaline magmas in the Hocheifel, Germany. Journal of Petrology 47, 1637-1671.

Jung, S., Hoernes, S., 2000. The major and trace element and isotope (Sr, Nd, O) geochemistry of Cenozoic mafic volcanic rocks from the Rhön area (central Germany); constraints on the origin of continental alkaline and tholeiitic basalts and their mantle source. J Petrol 86, 151-177.

Jung, S., Vieten, K., Romer, R.L., Mezger, K., Hoernes, S. and Satir, M., 2012. Petrogenesis of Tertiary alkaline magmas in the Siebengebirge, Germany. *Journal of Petrology*, *53*(11), pp.2381-2409.

Jung, S., Masberg, P., 1998. Major-and trace-element systematics and isotope geochemistry of Cenozoic mafic volcanic rocks from the Vogelsberg (central Germany): constraints on the origin of continental alkaline and tholeiitic basalts and their mantle sources. Journal of volcanology and geothermal research 86, 151-177.

Jung, S., Pfänder, J., Brauns, M., Maas, R., 2011. Crustal contamination and mantle source characteristics in continental intra-plate volcanic rocks: Pb, Hf and Os isotopes from central European volcanic province basalts. Geochimica et Cosmochimica Acta 75, 2664-2683.

Jung, S., Pfänder, J., Brügmann, G., Stracke, A., 2005. Sources of primitive alkaline volcanic rocks from the Central European Volcanic Province (Rhön, Germany) inferred from Hf, Os and Pb isotopes. Contributions to Mineralogy and Petrology 150, 546-559.

Kellogg, L.H., Hager, B.H., van der Hilst, R.D., 1999. Compositional stratification in the deep mantle. Science 283, 1881-1884.

Kimura K., Lewis R. S. and Anders E. (1974) Distribution of gold and rhenium between nickel-iron and silicate melts: implications for the abundance of siderophile elements on the Earth and Moon. *Geochim. Cosmochim. Acta* **38**, 683–701

Kirchenbaur, M., Münker, C., Schuth, S., Garbe-Schönberg, D., Marchev, P., 2011. Tectonomagmatic Constraints on the Sources of Eastern Mediterranean K-rich Lavas. Journal of Petrology 53, 27-65.

Kleine, T., Mezger, K., Münker, C., Palme, H., Bischoff, A., 2004. 182Hf-182W isotope systematics of chondrites, eucrites, and martian meteorites: Chronology of core formation and early mantle differentiation in Vesta and Mars. Geochim. Cosmochim. Acta 68, 2935–2946.

Kleine, T., Münker, C., Mezger, K., Palme, H., 2002. Rapid accretion and early core formation on asteroids and the terrestrial planets from Hf–W chronometry. Nature 418, 952-955.

Klemme, S., Blundy, J.D., Wood, B.J., 2002. Experimental constraints on major and trace element partitioning during partial melting of eclogite. Geochimica et Cosmochimica Acta 66, 3109-3123.

Kolb, M., Paulick, H., Kirchenbaur, M., Münker, C., 2012. Petrogenesis of mafic to felsic lavas from the Oligocene Siebengebirge volcanic field (Germany): implications for the origin of intracontinental volcanism in Central Europe. Journal of Petrology 53, 2349-2379.

Kondev, F., Naimi, S., 2017. The NUBASE2016 evaluation of nuclear properties. Chinese physics C 41, 030001.

König, S., Münker, C., Hohl, S., Paulick, H., Barth, A.R., Lagos, M., Pfänder, J., Büchl, A., 2011. The Earth's tungsten budget during mantle melting and crust formation. Geochim. Cosmochim. Acta 75, 2119–2136.

König, S., Münker, C., Schuth, S., Garbe-Schönberg, D., 2008. Mobility of tungsten in subduction zones. Earth Planet. Sci. Lett. 274, 82–92.

Korkisch, J., Hazan, I., 1965. Anion exchange separations in hydrobromic acid-organic solvent media. Analytical Chemistry 37, 707-710.

Kröner, A., Hoffmann, J.E., Hangqiang X., Münker, C., Hegner, E., Yusheng, W., Hofmann, A., Liu, D., Jinhui, Y., 2014. Generation of early Archean grey gneisses through melting of older crust in the eastern Kaapvaal craton, southern Africa. Precambrian Research 255, 823-

Kruijer, T.S., Kleine, T., 2018. No 182W excess in the Ontong Java Plateau source. Chemical Geology 485, 24-31.

Kurzweil, F., Münker, C., Grupp, M., Braukmüller, N., Fechtner, L., Christian, M., Hohl, S. V, Schoenberg, R., 2019. The stable tungsten isotope composition of modern igneous reservoirs. Geochim. Cosmochim. Acta 251, 176–191.

Kurzweil, F., Münker, C., Grupp, M., Braukmüller, N., Fechtner, L., Christian, M., Hohl, S. V, Schoenberg, R., 2019. The stable tungsten isotope composition of modern igneous reservoirs. Geochim. Cosmochim. Acta 251, 176–191.

Kurzweil, F., Münker, C., Hoffmann, J. E., Tusch, J., & Schoenberg, R. (2020). Stable W isotope evidence for redistribution of homogeneous W-182 anomalies in SW Greenland. Geochem. Perspect. Lett., 14, 53-58.

Kurzweil, F., Münker, C., Tusch, J., & Schoenberg, R., 2018. Accurate stable tungsten isotope measurements of natural samples using a 180W-183W double-spike. Chemical Geology, 476, 407-417.

Kushiro, I., 1996. Partial melting of fertile mantle peridotite at high pressures: an experimental study using aggregates of diamond. Geophysical Monograph-American Geophysical Union 95, 109-122.

Labrosse, S., Hernlund, J., Coltice, N., 2007. A crystallizing dense magma ocean at the base of the Earth's mantle. Nature 450, 866-869.

Lassiter, J.C., Blichert-Toft, J., Hauri, E.H., Barsczus, H.G., 2003. Isotope and trace element variations in lavas from Raivavae and Rapa, Cook–Austral islands: constraints on the nature of HIMU- and EM-mantle and the origin of mid-plate volcanism in French Polynesia. Chemical Geology 202, 115-138.

Le Bas, M., 1989. Nephelinitic and basanitic rocks. Journal of Petrology 30, 1299-1312.

Le Bas, M., Maitre, R.L., Streckeisen, A., Zanettin, B., Rocks, I.S.o.t.S.o.I., 1986. A chemical classification of volcanic rocks based on the total alkali-silica diagram. Journal of petrology 27, 745-750.

Lee, C.-T.A., Luffi, P., Höink, T., Li, J., Dasgupta, R., Hernlund, J., 2010. Upside-down differentiation and generation of a 'primordial'lower mantle. Nature 463, 930-933.

Liu, J., Pearson, D.G., Chacko, T., Luo, Y., 2018. A reconnaissance view of tungsten reservoirs in some crustal and mantle rocks: Implications for interpreting W isotopic compositions and crust-mantle W cycling. Geochimica et Cosmochimica Acta 223, 300–

Loock, G., Stosch, H.G. and Seck, H.A., 1990. Granulite facies lower crustal xenoliths from the Eifel, West Germany: petrological and geochemical aspects. *Contributions to Mineralogy and Petrology*, *105*(1), pp.25-41.

Luo, X., Rehkämper, M., Lee, D.-C., Halliday, A.N., 1997. High precision 230Th/232Th and 234U/238U measurements using energyfiltered ICP magnetic sector multiple collector mass spectrometry. Int. J. Mass Spectrom. Ion Process. 171, 105–117.

Lupton, J., Craig, H., 1975. Excess 3He in oceanic basalts: evidence for terrestrial primordial helium. Earth and Planetary Science Letters 26, 133-139.

Lustrino, M., 2011. What 'anorogenic'igneous rocks can tell us about the chemical composition of the upper mantle: case studies from the circum-Mediterranean area. Geological Magazine 148, 304-316.

Lustrino, M., Wilson, M., 2007. The circum-Mediterranean anorogenic Cenozoic igneous province. Earth-Science Reviews 81, 1-65

Maier, W.D., Barnes, S.J., Campbell, I.H., Fiorentini, M.L., Peltonen, P., Barnes, S.-J., Smithies, R.H., 2009. Progressive mixing of meteoritic veneer into the early Earth's deep mantle. Nature 460, 620-623.

Martelli, M., Nuccio, P.M. Stuart, F.M., Di Liberto, V., Ellam, R.M. (2008) Constraints on mantle source and interactions from He-Sr isotope variation in Italian Plio-Quaternary volcanism Geochemistry Geophysics Geosystems Q02001, doi: 10.1029/2007GC001730

Mayer, B., Jung, S., Brauns, M., Münker, C., 2018. The role of mantle-hybridization and crustal contamination in the petrogenesis of lithospheric mantle-derived alkaline rocks: constraints from Os and Hf isotopes. Contributions to Mineralogy and Petrology 173, 1-15.

Mayer, B., Jung, S., Brauns, M., Pfänder, J., 2013. Os isotopes in hornblende-bearing intra-plate alkaline lavas (Central European Volcanic Province; CEVP), AGU Fall Meeting Abstracts, pp. V33A-2725.

McNamara, A.K., 2019. A review of large low shear velocity provinces and ultra low velocity zones. Tectonophysics, 760, pp.199-220.

Meisel, T., Walker, R., Morgan, J., 1996. The osmium isotopic composition of the Earth's primitive upper mantle. Nature 383, 517-520.

Mertes, H., 1983. Aufbau und Genese des Westeifeler Vulkanfeldes. Bochumer Geologische und Geotechnische Arbeiten 9.

Mertes, H., Schmincke, H.-U., 1985. Mafic potassic lavas of the Quaternary West Eifel volcanic field. Contributions to Mineralogy and Petrology 89, 330-345.

Mertz, D.F., Löhnertz, W., Nomade, S., Pereira, A., Prelević, D., Renne, P.R., 2015. Temporal–spatial evolution of low-SiO2 volcanism in the Pleistocene West Eifel volcanic field (West Germany) and relationship to upwelling asthenosphere. Journal of Geodynamics 88, 59-79.

Mondal, S.K., 2011. Platinum group element (PGE) geochemistry to understand the chemical evolution of the Earth's mantle. Journal of the Geological Society of India, 77(4), pp.295-302.

Montelli, R., Nolet, G., Dahlen, F., Masters, G., 2006. A catalogue of deep mantle plumes: New results from finite-frequency tomography. Geochemistry, Geophysics, Geosystems 7.

Montelli, R., Nolet, G., Dahlen, F., Masters, G., Engdahl, E.R., Hung, S.-H., 2004. Finite-frequency tomography reveals a variety of plumes in the mantle. Science 303, 338-343.

Morgan, W.J., 1971. Convection plumes in the lower mantle. Nature 230, 42-43.

Moynier, F., Yin, Q.-Z., Irisawa, K., Boyet, M., Jacobsen, B., Rosing, M.T., 2010. Coupled 182W-142Nd constraint for early Earth differentiation. Proceedings of the National Academy of Sciences 107, 10810-10814.

Mukhopadhyay, S., 2012. Early differentiation and volatile accretion recorded in deep-mantle neon and xenon. Nature 486, 101–104. https://doi.org/10.1038/nature11141

Mundl-Petermeier, A., Viehmann, S., Tusch, J., Bau, M., Kurzweil, F., Münker, C., 2022. Earth's geodynamic evolution constrained by 182W in Archean seawater. Nature communications 13, 1-8.

Mundl-Petermeier, A., Walker, R., Fischer, R., Lekic, V., Jackson, M., Kurz, M., 2020. Anomalous 182W in high 3He/4He ocean island basalts: Fingerprints of Earth's core? Geochimica et Cosmochimica Acta 271, 194-211.

Mundl-Petermeier, A., Walker, R., Jackson, M., Blichert-Toft, J., Kurz, M., Halldórsson, S.A., 2019. Temporal evolution of primordial tungsten-182 and 3He/4He signatures in the Iceland mantle plume. Chemical Geology 525, 245-259.

Mundl, A., Touboul, M., Jackson, M.G., Day, J.M., Kurz, M.D., Lekic, V., Helz, R.T., Walker, R.J., 2017. Tungsten-182 heterogeneity in modern ocean island basalts. Science 356, 66-69.

Münker, C., 2010. A high field strength element perspective on early lunar differentiation. Geochim. Cosmochim. Acta 74, 7340–7361.

Münker, C., Weyer, S., Scherer, E., Mezger, K., 2001. Separation of high field strength elements (Nb, Ta, Zr, Hf) and Lu from rock samples for MC-ICPMS measurements. Geochemistry, Geophysics, Geosystems 2.

Nakanishi, N., Giuliani, A., Carlson, R. W., Horan, M. F., Woodhead, J., Pearson, D. G., & Walker, R. J. (2021). Tungsten-182 evidence for an ancient kimberlite source. Proceedings of the National Academy of Sciences, 118(23).

Nauret, F., Famin, V., Vlastélic, I., Gannoun, A., 2019. A trace of recycled continental crust in the Réunion hotspot. Chem. Geol. 524, 67–76.

Newsom, H. E., Sims, K. W., Noll Jr, P. D., Jaeger, W. L., Maehr, S. A., & Beserra, T. B. (1996). The depletion of tungsten in the bulk silicate earth: constraints on core formation. Geochimica et Cosmochimica Acta, 60(7), 1155-1169.

Nielson, D.L., Sibbett, B.S., 1996. Geology of Ascension Island, South Atlantic Ocean. Geothermics 25, 427–448

Noll Jr, P. D., Newsom, H. E., Leeman, W. P., & Ryan, J. G. (1996). The role of hydrothermal fluids in the production of subduction zone magmas: evidence from siderophile and chalcophile trace elements and boron. Geochimica et Cosmochimica Acta, 60(4), 587-611.

Nowell, D.A.G., Jones, M.C., Pyle, D.M., 2006. Episodic quaternary volcanism in France and Germany. Journal of Quaternary Science: Published for the Quaternary Research Association 21, 645-675.

Palme, H., O'Neill, H., St, C., 2004. Cosmochemical estimates of mantle composition in the mantle and core. Treatise on Geochemistry (2). Amsterdam: Elsevier.

Paulick, H., Münker, C., Schuth, S., 2010. The influence of small-scale mantle heterogeneities on Mid-Ocean Ridge volcanism: Evidence from the southern Mid-Atlantic Ridge (7°30'S to 11°30'S) and Ascension Island. Earth Planet. Sci. Lett. 296, 299–310. https://doi.org/10.1016/j.epsl.2010.05.009

Peccerillo, A., 2017. Cenozoic volcanism in the Tyrrhenian Sea region. Springer.

Peters, B. J., Mundl-Petermeier, A., Carlson, R. W., Walker, R. J., & Day, J. (2021). Combined lithophile-siderophile isotopic constraints on Hadean processes preserved in ocean island basalt sources. Geochemistry, Geophysics, Geosystems, e2020GC009479.

Peters, B.J., Carlson, R.W., Day, J., Horan, M.F., 2018. Hadean silicate differentiation preserved by anomalous 142Nd/144Nd ratios in the Réunion hotspot source. Nature 555, 89-93.

Peters, B.J., Mundl-Petermeier, A., Carlson, R.W., Walker, R.J., Day, J.M., 2021. Combined Lithophile-Siderophile Isotopic Constraints on Hadean Processes Preserved in Ocean Island Basalt Sources. Geochemistry, Geophysics, Geosystems 22, e2020GC009479.

Pfänder, J.A., Jung, S., Klügel, A., Münker, C., Romer, R.L., Sperner, B., Rohrmüller, J., 2018. Recurrent local melting of metasomatised lithospheric mantle in response to continental rifting: Constraints from basanites and nephelinites/melilitites from SE Germany. Journal of Petrology 59, 667-694.

Pfänder, J.A., Jung, S., Münker, C., Stracke, A., Mezger, K., 2012. A possible high Nb/Ta reservoir in the continental lithospheric mantle and consequences on the global Nb budget–Evidence from continental basalts from Central Germany. Geochimica et Cosmochimica Acta 77, 232-251.

Pfänder, J.A., Münker, C., Stracke, A., Mezger, K., 2007. Nb/Ta and Zr/Hf in ocean island basalts—implications for crust–mantle differentiation and the fate of Niobium. Earth and Planetary Science Letters 254, 158-172. Pin, C., Zalduegui, J.S., 1997. Sequential separation of light rare-earth elements, thorium and uranium by miniaturized extraction chromatography: application to isotopic analyses of silicate rocks. Analytica Chimica Acta 339, 79-89.

Price, R., Chappell, B., 1975. Fractional crystallisation and the petrology of Dunedin volcano. Contributions to mineralogy and petrology 53, 157-182.

Puchtel, I.S., Blichert-Toft, J., Touboul, M., Horan, M.F., Walker, R.J., 2016. The coupled 182W-142Nd record of early terrestrial mantle differentiation. Geochemistry, Geophysics, Geosystems 17, 2168-2193.

Regelous, M., Niu, Y., Abouchami, W., Castillo, P.R., 2009. Shallow origin for South Atlantic Dupal Anomaly from lower continental crust: Geochemical evidence from the Mid-Atlantic Ridge at 26 S. Lithos 112, 57–72.

Rehkämper, M., Halliday, A., 1997. Development and application of new iondashexchange techniques for the separation of the platinum group and other siderophile elements from geological samples. Talanta 44, 663-672.

Reifenröther, R., Münker, C. and Scheibner, B., 2021. Evidence for tungsten mobility during oceanic crust alteration. Chemical Geology, 584, p.120504.

Reifenröther, R., Münker, C., Paulick, H. and Scheibner, B., 2022. Alteration of abyssal peridotites is a major sink in the W geochemical cycle. Geochimica et Cosmochimica Acta.

Reimink, J.R., Chacko, T., Carlson, R.W., Shirey, S.B., Liu, J., Stern, R.A., Bauer, A.M., Pearson, D.G., Heaman, L.M., 2018. Petrogenesis and tectonics of the Acasta Gneiss Complex derived from integrated petrology and 142Nd and 182W extinct nuclide-geochemistry. Earth and Planetary Science Letters 494, 12-22.

Reimink, J.R., Mundl-Petermeier, A., Carlson, R.W., Shirey, S.B., Walker, R.J., Pearson, D.G., 2020. Tungsten isotope composition of Archean crustal reservoirs and implications for terrestrial μ182W evolution. Geochemistry, Geophysics, Geosystems 21, e2020GC009155.

Righter, K., 2003. Metal-silicate partitioning of siderophile elements and care formation in the early earth. Annual Review of Earth and Planetary Sciences 31, 135.

Righter, K., Hauri, E.H., 1998. Compatibility of rhenium in garnet during mantle melting and magma genesis. Science 280, 1737-1741.

Righter, K., Shearer, C., 2003. Magmatic fractionation of Hf and W: constraints on the timing of core formation and differentiation in the Moon and Mars. Geochimica et Cosmochimica Acta 67, 2497-2507.

Ritter, J.R., Christensen, U.R., 2007. Mantle Plumes. Springer.

Ritter, J.R., Jordan, M., Christensen, U.R., Achauer, U., 2001. A mantle plume below the Eifel volcanic fields, Germany. Earth and Planetary Science Letters 186, 7-14.

Rizo, H., Andrault, D., Bennett, N., Humayun, M., Brandon, A., Vlastélic, I., Moine, B., Poirier, A., Bouhifd, M.A., Murphy, D., 2019. 182W evidence for core-mantle interaction in the source of mantle plumes. Geochem. Perspect. Lett 11, 6-11.

Rizo, H., Walker, R., Carlson, R., Touboul, M., Horan, M., Puchtel, I., Boyet, M., Rosing, M., 2016a. Early Earth differentiation investigated through 142Nd, 182W, and highly siderophile element abundances in samples from Isua, Greenland. Geochimica et Cosmochimica Acta 175, 319-336.

Rizo, H., Walker, R.J., Carlson, R.W., Horan, M.F., Mukhopadhyay, S., Manthos, V., Francis, D., Jackson, M.G., 2016b. Preservation of Earth-forming events in the tungsten isotopic composition of modern flood basalts. Science 352, 809-812.

Rohde, J., Hoernle, K., Hauff, F., Werner, R., O'Connor, J., Class, C., Garbe-Schönberg, D., Jokat, W., 2013. 70 Ma chemical zonation of the Tristan-Gough hotspot track. Geology 41, 335-338.

Rost, S., Garnero, E.J., Williams, Q., 2006. Fine-scale ultralow-velocity zone structure from high-frequency seismic array data. Journal of Geophysical Research: Solid Earth 111.

Sapienza, G.T., Griffin, W.L., O'Reilly, S.Y., Morten, L., 2007. Crustal zircons and mantle sulfides: Archean to Triassic events in the lithosphere beneath south-eastern Sicily. Lithos 96, 503–523.

Sarda, P., Moreira, M., Staudacher, T., Schilling, J.G. and Allègre, C.J., 2000. Rare gas systematics on the southernmost Mid-Atlantic Ridge: Constraints on the lower mantle and the Dupal source. *Journal of Geophysical Research: Solid Earth*, *105*(B3), pp.5973-5996.

Schilling, J.-G., 1967. Rare-earth fractionation and magmatic processes. Mantles of the Earth and terrestrial planets, 267-283.

Schilling, J.-G., Winchester, J.W., 1969. Rare earth contribution to the origin of Hawaiian lavas. Contributions to Mineralogy and Petrology 23, 27-37.

Schmidt, G., Snow, J., 2002. Os isotopes in mantle xenoliths from the Eifel volcanic field and the Vogelsberg (Germany): age constraints on the lithospheric mantle. Contributions to Mineralogy and Petrology 143, 694-705.

Schmincke, H.-U., 2007. The Quaternary volcanic fields of the east and west Eifel (Germany), Mantle plumes. Springer, pp. 241-322.

Schmincke, H.-U., Lorenz, V., Seck, H., 1983. The quaternary Eifel volcanic fields, Plateau uplift. Springer, pp. 139-151.

Schneider, K., Kirchenbaur, M., Fonseca, R., Kasper, H., Münker, C., Froitzheim, N., 2016. Role of crustal assimilation and basement compositions in the petrogenesis of differentiated intraplate volcanic rocks: a case study from the Siebengebirge Volcanic Field, Germany. Contributions to Mineralogy and Petrology 171, 1-30.

Schoenberg, R., Kamber, B.S., Collerson, K.D., Eugster, O., 2002. New W-isotope evidence for rapid terrestrial accretion and very early core formation. Geochimica et Cosmochimica Acta 66, 3151-3160.

Schuth, S., König, S., Münker, C., 2011. Subduction zone dynamics in the SW Pacific plate boundary region constrained from high-precision Pb isotope data. Earth and Planetary Science Letters 311, 328-338.

Schwindrofska, A., Hoernle, K., Hauff, F., van den Bogaard, P., Werner, R., Garbe-Schönberg, D., 2016. Origin of enriched components in the South Atlantic: Evidence from 40 Ma geochemical zonation of the Discovery Seamounts. Earth and Planetary Science Letters 441, 167-177.

Shaw, D.M., 1970. Trace element fractionation during anatexis. Geochimica et Cosmochimica Acta 34, 237-243.

Shirey, S.B., Walker, R.J., 1998. The Re-Os isotope system in cosmochemistry and high-temperature geochemistry. Annual Review of Earth and Planetary Sciences 26, 423-500.

Shi, J.H., Zeng, G., Chen, L.H., Hanyu, T., Wang, X.J., Zhong, Y., Xie, L.W. and Xie, W.L., 2022. An eclogitic component in the Pitcairn mantle plume: Evidence from olivine compositions and Fe isotopes of basalts. Geochimica et Cosmochimica Acta, 318, pp.415-427.

Spera, F.J., Bohrson, W.A., 2001. Energy-constrained open-system magmatic processes I: General model and energy-constrained assimilation and fractional crystallization (EC-AFC) formulation. Journal of Petrology 42, 999-1018.

Sprung, P., Schuth, S., Münker, C., Hoke, L., 2007. Intraplate volcanism in New Zealand: the role of fossil plume material and variable lithospheric properties. Contributions to Mineralogy and Petrology 153, 669-687.

Starkey, N.A., Stuart, F.M., Ellam, R.M., Fitton, J.G., Basu, S., Larsen, L.M., 2009. Helium isotopes in early Iceland plume picrites: Constraints on the composition of high 3He/4He mantle. Earth Planet. Sci. Lett. 277, 91–100. https://doi.org/10.1016/j.epsl.2008.10.007

Salters, V.J. and Stracke, A., 2004. Composition of the depleted mantle. Geochemistry, Geophysics, Geosystems, 5(5).

Stosch, H.-G., Lugmair, G., 1984. Evolution of the lower continental crust: granulite facies xenoliths from the Eifel, West Germany. Nature 311, 368-370.

Stosch, H.-G., Lugmair, G., 1986. Trace element and Sr and Nd isotope geochemistry of peridotite xenoliths from the Eifel (West Germany) and their bearing on the evolution of the subcontinental lithosphere. Earth and Planetary Science Letters 80, 281-298.

Stracke, A., Hofmann, A.W., Hart, S.R., 2005. FOZO, HIMU, and the rest of the mantle zoo. Geochemistry, geophysics, geosystems 6.

Stuart, F.M., Lass-Evans, S., Fitton, J.G., Ellam, R.M., 2003. High 3He/4He ratios in picritic basalts from Baffin Island and the role of a mixed reservoir in mantle plumes. Nature 424, 57–59. https://doi.org/10.1038/nature01711

Tackley, P.J., 2002. Strong heterogeneity caused by deep mantle layering. Geochemistry, Geophysics, Geosystems 3, 1-22.

Tappe, S., Budde, G., Stracke, A., Wilson, A., Kleine, T., 2020. The tungsten-182 record of kimberlites above the African superplume: Exploring links to the core-mantle boundary. Earth Planet. Sci. Lett. 547, 116473.

Tatsumoto, M., Hedge, C., Engel, A., 1965. Potassium, rubidium, strontium, thorium, uranium, and the ratio of strontium-87 to strontium-86 in oceanic tholeiitic basalt. Science 150, 886-888.

Thiemens, M.M., Sprung, P., Fonseca, R.O.C., Leitzke, F.P., Münker, C., 2019. Early Moon formation inferred from hafnium–tungsten systematics. Nat. Geosci. 12, 696–700.

Thirlwall, M., Upton, B., Jenkins, C., 1994. Interaction between continental lithosphere and the Iceland plume—Sr-Nd-Pb isotope geochemistry of Tertiary basalts, NE Greenland. Journal of Petrology 35, 839-879.

Todt, W., Lippolt, H., 1980. K-Ar age determinations on tertiary volcanic rocks: 5. Siebengebirge, Siebengebirge-Graben. Journal of Geophysics 48, 18-27.

Tommasini, S., Heumann, A., Avanzinelli, R., Francalanci, L., 2007. The fate of high-angle dipping slabs in the subduction factory: an integrated trace element and radiogenic isotope (U, Th, Sr, Nd, Pb) study of Stromboli volcano, Aeolian Arc, Italy. J.Petrol.48, 2407–2430.

Touboul, M., Puchtel, I.S., Walker, R.J., 2012. 182W evidence for long-term preservation of early mantle differentiation products. science 335, 1065-1069.

Torsvik, T.H., Steinberger, B., Ashwal, L.D., Doubrovine, P.V. and Trønnes, R.G., 2016. Earth evolution and dynamics—a tribute to Kevin Burke. Canadian Journal of Earth Sciences, 53(11), pp.1073-1087.

Trampert, J., Deschamps, F., Resovsky, J., Yuen, D., 2004. Probabilistic tomography maps chemical heterogeneities throughout the lower mantle. Science 306, 853-856.

Trua, T., Esperança, S., & Mazzuoli, R. (1998). The evolution of the lithospheric mantle along the N. African Plate: geochemical and isotopic evidence from the tholeiitic and alkaline volcanic rocks of the Hyblean plateau, Italy. Contributions to Mineralogy and Petrology, 131(4), 307-322.

Trua, T., Serri, G., Marani, M.P., 2003. Lateral flow of African mantle below the nearby Tyrrhenian plate: geochemical evidence. Terra Nov. 15, 433–440.

Tusch, J., Hoffmann, E., Hasenstab, E., Münker, C., Fischer-Gödde, M., Marien, C.S., 2021a. Long-term preservation of Hadean protocrust in Earth's mantle.

Tusch, J., Hoffmann, J.E., Hasenstab, E., Fischer-Gödde, M., Marien, C.S., Wilson, A.H., Münker, C., 2022. Long-term preservation of Hadean protocrust in Earth's mantle. Proceedings of the National Academy of Sciences 119, e2120241119.

Tusch, J., Münker, C., Hasenstab, E., Jansen, M., Marien, C.S., Kurzweil, F., Van Kranendonk, M.J., Smithies, H., Maier, W., Garbe-Schönberg, D., 2021b. Convective isolation of Hadean mantle reservoirs through Archean time. Proceedings of the National Academy of Sciences 118.

Tusch, J., Sprung, P., van de Löcht, J., Hoffmann, J., Boyd, A., Rosing, M., Münker, C., 2019. Uniform 182W isotope compositions in Eoarchean rocks from the Isua region, SW Greenland: The role of early silicate differentiation and missing late veneer. Geochimica et Cosmochimica Acta 257, 284-310.

Van Acken, D., Brandon, A.D., Humayun, M., 2011. High-precision osmium isotopes in enstatite and Rumuruti chondrites. Geochimica et Cosmochimica Acta 75, 4020-4036.

Van den Bogaard, P., 1995. 40Ar/39Ar ages of sanidine phenocrysts from Laacher See Tephra (12,900 yr BP): Chronostratigraphic and petrological significance. Earth and Planetary Science Letters 133, 163-174.

van den Bogaard, P., Hall, C., Schmincke, H.-U., York, D., 1989. Precise single-grain 40Ar/39 Ar dating of a cold to warm climate transition in Central Europe. Nature 342, 523-525.

Viereck, L., 1984. Geologische und petrologische Entwicklung des pleistozänen Vulkankomplexes Rieden, Ost-Eifel. Inst. für Geologie d. Ruhr-Univ.

Vockenhuber, C., Oberli, F., Bichler, M., Ahmad, I., Quitté, G., Meier, M., Halliday, A.N., Lee, D.-C., Kutschera, W., Steier, P., 2004. New half-life measurement of H f 182: Improved chronometer for the early solar system. Physical Review Letters 93, 172501.

Walker R. J. (2009) Highly siderophile elements in the Earth, Moon and Mars: Update and implications for planetary accretion and differentiation. Chemie der Erde - Geochemistry **69**, 101–125.

Weyer, S., Münker, C., Rehkämper, M., Mezger, K., 2002. Determination of ultra-low Nb, Ta, Zr and Hf concentrations and the chondritic Zr/Hf and Nb/Ta ratios by isotope dilution analyses with multiple collector ICP-MS. Chem. Geol. 187, 295–313.

White, W.M., 1985. Sources of oceanic basalts: Radiogenic isotopic evidence. Geology 13, 115-118.

White, W.M., 2014. Isotope geochemistry. John Wiley & Sons.

White, W.M., Hofmann, A.W., 1982. Sr and Nd isotope geochemistry of oceanic basalts and mantle evolution. Nature 296, 821-825.

Wicks, J., Jackson, J., Sturhahn, W., 2010. Very low sound velocities in iron-rich (Mg, Fe) O: Implications for the core-mantle boundary region. Geophysical Research Letters 37.

Willbold, M., Elliott, T., Moorbath, S., 2011. The tungsten isotopic composition of the Earth's mantle before the terminal bombardment. Nature 477, 195-198.

Willbold, M., Mojzsis, S., Chen, H.-W., Elliott, T., 2015. Tungsten isotope composition of the Acasta Gneiss Complex. Earth and Planetary Science Letters 419, 168-177.

Willhite, L. N., Jackson, M. G., Blichert-Toft, J., Bindeman, I., Kurz, M. D., Halldórsson, S. A., Harðardóttir S., Gazel E., Price A. A., Byerly B., Byerly, B. L. (2019). Hot and heterogenous high-3He/4He components: New constraints from proto-Iceland plume lavas from Baffin Island. Geochemistry, Geophysics, Geosystems, 20(12), 5939-5967.

Wilson, M., Downes, H., 1991. Tertiary—Quaternary extension-related alkaline magmatism in western and central Europe. Journal of Petrology 32, 811-849.

Wilson, M., Rosenbaum, J.M. and Dunworth, E.A., 1995. Melilitites: partial melts of the thermal boundary layer?. Contributions to Mineralogy and Petrology, 119(2), pp.181-196.

Witt-Eickschen, G., Kramm, U., 1998. Evidence for the multiple stage evolution of the subcontinental lithospheric mantle beneath the Eifel (Germany) from pyroxenite and composite pyroxenite/peridotite xenoliths. Contributions to Mineralogy and Petrology 131, 258-272.

Witt-Eickschen, G., Seck, H., Mezger, K., Eggins, S., Altherr, R., 2003. Lithospheric mantle evolution beneath the Eifel (Germany): constraints from Sr–Nd–Pb isotopes and trace element abundances in spinel peridotite and pyroxenite xenoliths. Journal of Petrology 44, 1077-1095.

Wörner, G., Staudigel, H., Zindler, A., 1985. Isotopic constraints on open system evolution of the Laacher See magma chamber (Eifel, West Germany). Earth and Planetary Science Letters 75, 37-49.

Wörner, G., Zindler, A., Staudigel, H., Schmincke, H.-U., 1986. Sr, Nd, and Pb isotope geochemistry of Tertiary and Quaternary alkaline volcanics from West Germany. Earth and Planetary Science Letters 79, 107-119.

Yuan, Q. and Li, M., 2022. Instability of the African large low-shear-wave-velocity province due to its low intrinsic density. Nature Geoscience, 15(4), pp.334-339.

Zhang, H., Shi, X., Li, C., Yan, Q., Yang, Y., Zhu, Z., Zhang, H., Wang, S., Guan, Y., Zhao, R., 2020. Petrology and geochemistry of South Mid-Atlantic Ridge (19° S) lava flows: Implications for magmatic processes and possible plume-ridge interactions. Geoscience Frontiers, 11(6), 1953-1973.

Zhou, H., Hoernle, K., Geldmacher, J., Hauff, F., Homrighausen, S., Garbe-Schönberg, D., Jung, S., 2020. Geochemistry of Etendeka magmatism: Spatial heterogeneity in the Tristan-Gough plume head. Earth and Planetary Science Letters 535, 116123.

Zindler, A., Hart, S., 1986. Chemical geodynamics. Annual review of earth and planetary sciences 14, 493-571

Zindler, A., Jagoutz, E., Goldstein, S., 1982. Nd, Sr and Pb isotopic systematics in a three-component mantle: a new perspective. Nature 298, 519-523.

1

Appendix AI

Sample	Previously Investigated in:
La Réunion (REU 1; 11; 13; 17; 18; 19; 20) (major- and trace elements, Nd and Hf isotope compositions and W, U, Th concentrations)	Kurzweil, F., Münker, C., Grupp, M., Braukmüller, N., Fechtner, L., Christian, M., Hohl, S. V, Schoenberg, R., 2019. The stable tungsten isotope composition of modern igneous reservoirs. Geochim. Cosmochim. Acta 251, 176–191.
Mt Etna (ET 1; 2; 3; 4) (major- and trace elements, W, U, Th, Nb, Ta concentrations)	Bragagni A., Mastroianni F., Münker C., Conticelli S., Avanzinelli R (2021). A carbon-rich lithospheric mantle as source for the large CO2 emission of Etna. Accepted for publication on Geology the 1st of November 2021, DOI: 10.1130/G49510.1
Hyblean Plateau IBL (1; 2)	Bragagni A., Mastroianni F., Avanzinelli R., Conticelli S., Münker M., 2019. Extreme HFSE Fractionation in Italian Magmas: Metasomatism vs. Different Mantle Domains. Goldschmidt Abstracts, 371
Siebengebirge (SG 19; 30) (major- and trace elements, Nd and Hf isotope compositions)	Kolb, M., Paulick, H., Kirchenbaur, M., & Münker, C. (2012). Petrogenesis of mafic to felsic lavas from the Oligocene Siebengebirge volcanic field (Germany): implications for the origin of intracontinental volcanism in Central Europe. Journal of Petrology, 53(11), 2349-2379.
Ascension Island (MAR 4) (major- and trace elements, Nd and Hf isotope compositions and W, U, Th, Nb, Ta concentrations)	König, S., Münker, C., Hohl, S., Paulick, H., Barth, A.R., Lagos, M., Pfänder, J., Büchl, A., 2011. The Earth's tungsten budget during mantle melting and crust formation. Geochim. Cosmochim. Acta 75, 2119–2136.
Mt. Vesuvio (VES 01; 07; 16; 95; 97) (major- and trace elements, Nd and Hf isotope compositions and W, U, Th concentrations)	Avanzinelli, R., Casalini, M., Elliott, T., Conticelli, S., 2018. Carbon fluxes from subducted carbonates revealed by uranium excess at Mount Vesuvius, Italy. Geology 46, 259–262. Bragagni A., Mastroianni F., Avanzinelli R., Conticelli S., Münker M., 2019. Extreme HFSE Fractionation in Italian Magmas: Metasomatism vs. Different Mantle Domains. Goldschmidt Abstracts, 371
Mt. Stromboli (STR 07L; 50) (major- and trace elements, Nd and Hf isotope compositions and W, U, Th, Nb, Zr, Ta concentrations)	Bragagni A., Mastroianni F., Avanzinelli R., Conticelli S., Münker M., 2019. Extreme HFSE Fractionation in Italian Magmas: Metasomatism vs. Different Mantle Domains. Goldschmidt Abstracts, 371 Tommasini, S., Heumann, A., Avanzinelli, R., Francalanci, L., 2007. The Fate of High-Angle Dipping Slabs in the Subduction Factory: an Integrated Trace Element and Radiogenic Isotope (U, Th, Sr, Nd, Pb) Study of Stromboli Volcano, Aeolian Arc, Italy. J. Petrol. 48, 2407–2430. https://doi.org/10.1093/petrology/egm066
Mt. Vulture (VLT 14; 49) (major- and trace elements, Nd and Hf isotope compositions and W, U, Th, Nb, Zr, Ta concentrations)	Bragagni A., Mastroianni F., Avanzinelli R., Conticelli S., Münker M., 2019. Extreme HFSE Fractionation in Italian Magmas: Metasomatism vs. Different Mantle Domains. Goldschmidt Abstracts, 371 Conticelli, S., Carlson, R.W., Widom, E., Serri, G., 2007. Chemical and isotopic composition (Os, Pb, Nd, and Sr) ofNeogene to Quaternary calc-alkalic, shoshonitic, and ultrapotassic mafic rocks from the Italian peninsula: Inferences on the nature of their mantle sources. Cenozoic volcanism Mediterr. area 418, 171. Avanzinelli, R., Elliott, T., Tommasini, S., Conticelli, S., 2008. Constraints on the genesis of potassium-rich Italian volcanic rocks from U/Th disequilibrium. J. Petrol. 49, 195–223.

Table 1. .

Sample	**REU 1**	**REU 11**	**REU 13**	**REU 17**	**REU 18**	**REU 19**	**REU 20**
Locaylity	Piton de la Fournaise	Piton de la Fournaise	Piton de la Fournaise	Piton de la Fournaise	Piton des Neiges	Piton des Neiges	Piton des Neiges
Rocktype	Basalt	Basalt	Basalt	Basalt	Basalt	Basalt	Basalt
Longitude	55°42'47.160"	55°43'06.301"	55°47'44.160"	55°27'06.361"	55°27'37.681"	55°26'49.441"	55°27'13.32"
Latitude	21°06'51.840"	21°13'50.941"	21°15'11.581"	21°19'47.398"	21°15'18.658"	21°11'57.5412"	21°13'16.561"
wt.%							
SiO_2	47.0	47.3	47.5	46.9	48.2	46.7	46.3
TiO_2	2.67	2.75	2.47	2.57	2.61	1.95	1.76
Al_2O_3	14.6	14.2	13.0	13.8	14.0	11.4	10.5
Fe_2O_3	12.3	12.1	12.2	12.9	12.0	12.3	12.5
MnO	0.164	0.166	0.164	0.172	0.169	0.171	0.169
MgO	8.35	7.57	9.70	9.85	7.51	14.3	17.0
CaO	8.76	11.6	10.0	9.02	11.28	9.28	8.21
Na_2O	3.09	2.60	2.43	2.83	2.48	1.97	1.77
K_2O	0.961	0.780	0.655	0.838	0.675	0.331	0.276
P_2O_5	0.419	0.317	0.293	0.344	0.300	0.222	0.195
L.O.I.	0.0	0.0	0.0	0.3	0.0	0.2	0.2
Total	98.6	99.5	98.7	99.4	99.2	99.0	99.1
Mg#	57.3	55.4	61.1	60.3	55.4	69.7	72.8

Table 2

Sample	**ET 1**	**ET 2**	**ET 3**	**ET 4**	**IBL 1**	**IBL 2**
Locaylity	Mt. Etna (Aci Castello)	Mt. Etna (Aci Castello)	Mt Etna (Valle di Bove)	Mt Etna (Valle di Bove)	Hyblean Plateau	Hyblean Plateau
Rocktype	Basalt	Basalt	Basalt	Basalt	Basalt	Basalt
Longitude						
Latitude						
wt.%						
SiO_2	44.9	49.9	50.2	48.7	44.1	42.2
TiO_2	1.81	1.86	1.67	1.66	2.67	2.05
Al_2O_3	9.99	15.1	17.5	17.5	13.8	12.0
Fe_2O_3	13.3	10.2	10.0	11.2	12.4	11.7
MnO	0.178	0.120	0.164	0.185	0.182	0.187
MgO	19.0	7.14	4.61	5.16	9.84	12.3
CaO	7.46	9.43	8.79	10.0	10.5	13.0
Na_2O	1.96	3.19	4.40	3.97	2.68	2.64
K_2O	0.625	0.175	2.10	1.60	1.42	0.625
P_2O_5	0.330	0.453	0.761	0.537	0.990	1.44
L.O.I.	0.0	2.7	0.0	-0.2	1.5	1.9
Total	99.8	100.4	100.4	100.4	100.3	100.4
Mg#	73.9	58.0	47.7	47.8	61.0	67.5

Table 2 continued

Sample	**Ei 2**	**Ei 4**	**Ei 9**	**Ei 10b**	**Ei 12**	**Ei 16b**	**Ei 22**
Locaylity	Eppelsberg	Herrchenberg	Bausenberg	Hannebacher Ley	Leitenberg	Rothenberg	Rüderbusch
Rocktype	Basanite	Melilitite	Basanite	Melilitite	Melilitite	Basanite	Basanite
Longitude	07°19'07.222"	07°15'40.355"	07°13'40.393"	07°08'11.764"	07°18'16.748"	07°13'43.120"	06° 37.716'
Latitude	50°24'01.711"	50°27'59.830"	50°28'12.973"	50°26'53.105"	50°28'28.030"	50°23'51.268"	50° 17.760'
wt.%							
SiO_2	42.5	38.9	43.0	40.0	39.3	43.8	41.5
TiO_2	2.79	3.13	2.69	2.15	2.65	2.64	2.42
Al_2O_3	13.6	13.5	13.5	14.9	12.8	13.8	11.0
Fe_2O_3	11.3	11.4	10.9	11.0	11.0	10.7	10.5
MnO	0.180	0.210	0.170	0.280	0.200	0.170	0.180
MgO	9.80	8.51	9.59	4.61	8.42	9.08	10.9
CaO	12.1	14.0	12.0	12.7	15.3	11.3	14.0
Na_2O	2.73	3.87	2.75	6.09	3.24	3.23	2.54
K_2O	3.32	3.83	3.12	4.24	2.77	3.35	3.13
P_2O_5	0.510	0.660	0.530	1.22	0.720	0.610	0.693
L.O.I.	0.1	0.8	0.0	0.9	2.3	-0.1	1.03
Total	99.0	98.8	98.2	98.1	98.7	98.5	97.8
Mg#	63.2	59.7	63.5	45.4	60.3	62.7	67.5

Table 2 continued

Sample	**Ei 25**	**Ei 27**	**Ei 29**	**Ei 32**	**SG 19**	**SG 30**
Locaylity	Rockeskyller Kopf	Sarresdorfer Lavastrom	Wartgensberg	Am Steinseiter	Pertersberg	Erpeler Ley
Rocktype	Basanite	Basanite	Basanite	Basanite	Basalt	Basanite
Longitude	06°40'35.568"	06°39'4.682"	06°55'55.005"	06°45'41.779"	07°12'21.554"	07°14'44.970"
Latitude	50°15'23.112"	50°13'20.931"	50°06'29.410"	50°13'5.152"	50°41'19.875"	50°34'57.187"
wt.%						
SiO_2	43.6	43.2	42.9	41.6	47.2	44.4
TiO_2	2.45	2.32	2.42	2.73	2.20	2.67
Al_2O_3	11.6	12.1	11.3	11.6	14.2	13.8
Fe_2O_3	10.3	11.3	11.9	11.2	11.3	11.0
MnO	0.169	0.187	0.170	0.175	0.190	0.190
MgO	10.0	11.5	13.8	9.77	9.06	10.3
CaO	12.8	12.6	11.1	14.4	9.97	10.3
Na_2O	2.13	3.38	3.01	2.68	3.62	3.83
K_2O	3.88	1.51	1.49	3.34	1.19	0.910
P_2O_5	0.740	0.865	0.839	0.654	0.458	0.530
L.O.I.	0.9	-0.2	-0.3	-0.5	0.420	1.22
Total	98.5	98.8	98.6	97.6	99.8	99.0
Mg#	65.8	66.8	69.7	63.3	nd	nd

Table 2 continued

Sample	**ZM 10**	**ZM 12**	**ZM 14**	**PAD 6**	**PAD 8**	**DUR 1**	**DUR 7**
Locaylity	Maar de Beaunit	Coulée de Chilhac	Puy des Grosmanaux	Padloping Island	Padloping Island	Durban Island	Durban Island
Rocktype	Basalt	Basalt	Basalt	Basalt	Basalt	Basalt	Basalt
Longitude	02°57'35.341"	03°26,163"	02°57'11.880"	62°27'00.000"	62°27'36.000"	62°15'00.000"	62°9'36.000"
Latitude	45°54'00.961"	45°09,317"	45°45'35.218"	67°10'12.000"	67°09'0.000"	67°04'48.000"	67°05'24.000"
wt.%							
SiO_2	47.7	44.7	46.1	47.7	46.7	49.1	47.4
TiO_2	2.26	2.50	2.51	0.863	0.812	1.09	0.925
Al_2O_3	15.6	13.9	15.8	12.2	11.1	14.7	13.0
Fe_2O_3	nd	10.2	nd	10.1	10.4	10.6	10.1
MnO	0.175	0.17	0.186	0.175	0.178	0.189	0.178
MgO	6.89	10.1	6.71	17.2	20.0	9.66	16.7
CaO	9.85	10.1	10.2	10.3	9.48	12.6	10.2
Na_2O	1.65	1.85	1.51	1.34	1.29	1.77	1.06
K_2O	3.43	3.25	3.44	0.036	0.045	0.096	0.413
P_2O_5	0.582	0.588	0.564	0.068	0.071	0.102	0.095
L.O.I.	< 0.1%	0.910	< 0.1%	nd	nd	nd	nd
Total	98.3	98.2	98.3	99.9	100	99.9	100
Mg#	92.2	nd	93.9	63.2	59.7	63.5	45.4

Table 2 continued
d

Sample	**MAR 4**	**ASI 3**	**ASD 16**	**VES 01**	**VES 07**	**VES 16**	**VES 95**	**VES 97**
Locaylity	Seamount "Proto-Ascension"	Ascension Island (Sub-Aerial)	Ascension Island (Sub-Marine-Section)	Mt. Vesuvio	Mt. Vesuvio	Mt. Vesuvio	Mt. Veusivo	Mt. Vesuvio
Rocktype	Basalt	Basalt	Basalt	Basalt	Basalt	Basalt	Basalt	Basalt
Longitude	07°52'02.424"	07°55'48.000"	07°58'58.011"					
Latitude	13°25'50.109"	14°22'12.000"	14°23'43.009"					
wt.%								
SiO_2	48.8	47.0	nd	47.7	47.4	47.9	48.9	48.9
TiO_2	1.66	3.51	2.35	1.03	0.98	1.01	1.07	1.00
Al_2O_3	16.0	14.9	13.9	17.2	17.6	16.9	16.4	13.8
Fe_2O_3	9.4	12.7	13.1	8.60	8.68	8.94	9.21	7.84
MnO	0.160	0.220	0.209	0.150	0.160	0.160	0.158	0.139
MgO	8.06	5.04	6.04	4.49	3.96	4.80	4.37	7.52
CaO	11.6	9.06	9.65	9.95	9.20	10.6	8.95	12.4
Na_2O	2.42	3.52	2.41	2.40	2.53	2.31	2.69	1.89
K_2O	0.390	1.16	0.788	7.39	7.64	6.64	7.55	5.72
P_2O_5	0.360	0.887	0.374	0.980	0.870	0.890	0.766	0.760
L.O.I.	nd	-0.8	nd	0.3	0.460	0.280	0.399	0.886
Total	98.9	97.9	48.8	98.3	99.5	100	98.3	101
Mg#	60.3	62.7	65.8	66.8	51.5	55.6	69.7	69.1

Table 2 continued

Sample	**PAN 5**	**STR 07L**	**STR 50**	**VLT 14**	**VLT 49**
Locaylity	Pantelleria	Mt. Stromboli	Mt. Stromboli	Mt. Vulture	Mt. Vulture
Rocktype	Basalt	Basalt	Basalt	Basalt	Basalt
Longitude					
Latitude					
wt.%					
SiO_2	45.5	50.3	52.6	39.8	45.6
TiO_2	3.48	0.941	0.900	2.39	1.41
Al_2O_3	15.0	17.5	18.0	14.5	16.7
Fe_2O_3	9.13	1.33	nd	4.56	5.13
MnO	0.180	0.158	nd	0.220	0.157
MgO	6.41	6.36	5.19	4.37	6.55
CaO	10.8	11.4	9.08	16.4	12.0
Na_2O	3.76	2.57	2.33	4.01	2.50
K_2O	1.36	2.15	3.68	4.87	4.28
P_2O_5	0.740	0.620	0.650	1.04	1.00
L.O.I.	0.4	0.6	0.9	2.0	1.4
Total	98.3	98.3	98.3	98.3	98.3
Mg#	63.3	93.9	63.3	92.2	93.9

Table 2 continued

Sample	**REU 1**	**REU 11**	**REU 13**	**REU 17**	**REU 18**	**REU 19**	**REU 20**
Rocktype	Basalt	Basalt	Basalt	Basalt	Basalt	Basalt	Basalt
(ppm)							
Sc	23.1	23.9	24.1	20.7	26.9	28.0	24.6
Cr	306	315	488	402	189	824	922
Ni	203	122	237	266	129	530	747
Cu	60.2	104	100	53.9	131	106	91.1
Zn	110	125	143	110	107	106	103
Rb	17.8	15.0	12.3	16.8	10.2	7.50	6.74
Sr	436	303	300	354	308	271	228
Y	28.6	22.6	24.2	28.2	25.0	21.3	19.7
Zr	262	182	180	209	192	142	128
Nb	30.4	25.3	21.1	24.4	20.6	14.4	13.0
Cs	0.169	0.280	0.241	0.280	0.189	0.136	0.191
Ba	208	159	127	169	137	89	81
La	28.3	20.9	18.4	22.4	18.5	12.9	11.6
Ce	61.5	46.9	42.3	49.9	43.5	30.7	27.0
Pr	8.14	6.34	5.82	6.80	6.10	4.29	3.79
Nd	33.9	27.1	25.5	29.3	27.1	19.2	16.8
Sm	7.17	6.05	5.86	6.58	6.25	4.53	4.03
Eu	2.33	2.00	1.98	2.19	2.08	1.56	1.39
Gd	6.93	6.10	6.05	6.69	6.39	4.74	4.27
Tb	1.06	0.950	0.944	1.04	1.00	0.755	0.696
Dy	5.81	5.31	5.30	5.82	5.63	4.27	3.95
Ho	1.09	0.990	0.994	1.10	1.07	0.815	0.754
Er	2.79	2.59	2.56	2.85	2.77	2.14	1.97
Tm	0.377	0.348	0.345	0.391	0.377	0.292	0.270
Yb	2.26	2.07	2.04	2.30	2.26	1.75	1.60
Lu	0.315	0.289	0.285	0.326	0.316	0.244	0.226
Hf	6.11	4.63	4.57	5.16	4.86	3.47	3.17
Ta	1.97	1.60	1.34	1.54	1.33	0.932	0.843
Pb	2.28	1.58	1.43	1.71	1.52	1.08	0.953
Th	3.52	2.56	2.16	2.66	2.10	1.44	1.33
U	0.837	0.625	0.546	0.640	0.487	0.370	0.344

Table 3

Sample	**ET 1**	**ET 2**	**ET 3**	**ET 4**	**IBL 1**	**IBL 2**
Rocktype	Basalt	Basalt	Basalt	Basalt	Basalt	Basalt
(ppm)						
Sc	29.1	25.1	22.1	27.5	27.9	28.8
Cr	366	190	48.9	30.7	414	265
Ni	193	142	28.3	23.5	273	209
Cu	86.8	87.4	163	129	75.7	61.8
Zn	93.2	99.4	105	107	91.8	137
Rb	1.56	1.30	43.6	34.5	8.67	27.9
Sr	596	592	1154	1195	1400	954
Y	23.5	22.8	30.3	27.9	33.6	31.5
Zr	130	142	266	226	220	292
Nb	39.5	37.7	76.2	58.0	90.2	77.3
Cs	0.038	0.050	0.506	0.744	0.397	0.417
Ba	206	127	882	691	661	485
La	36.8	32.4	89.9	65.1	99.9	59.6
Ce	72.5	62.3	164	124	191	120
Pr	8.38	7.18	17.9	13.9	21.3	14.0
Nd	33.7	29.4	66.9	53.4	79.5	56.3
Sm	6.70	6.16	11.3	9.55	13.1	10.5
Eu	2.19	2.09	3.09	2.77	3.86	3.21
Gd	6.22	5.91	9.10	7.99	11.0	9.12
Tb	0.873	0.848	1.17	1.04	1.38	1.23
Dy	4.71	4.61	5.90	5.43	6.86	6.37
Ho	0.845	0.829	1.06	0.983	1.20	1.12
Er	2.13	2.06	2.76	2.54	2.97	2.80
Tm	0.284	0.277	0.381	0.350	0.385	0.374
Yb	1.74	1.67	2.41	2.19	2.35	2.27
Lu	0.254	0.243	0.358	0.326	0.346	0.330
Hf	2.88	3.13	5.20	4.52	3.58	5.67
Ta	1.62	1.59	3.41	2.59	3.34	3.39
Pb	2.51	2.40	10.5	6.33	4.06	2.97
Th	4.05	4.02	14.7	9.23	8.99	6.09
U	1.07	1.16	3.59	2.49	2.35	1.73

Table 3 continued

Sample	**Ei 2**	**Ei 4**	**Ei 9**	**Ei 10b**	**Ei 12**	**Ei 16b**	**Ei 22**
Rocktype	Basanite	Basanite	Basanite	Melilitite	Melilitite	Basanite	Basanite
(ppm)							
Sc	35.3	27.8	39.0	11.9	32.7	35.3	32.5
Cr	228	126	236	10.5	97.7	235	455
Ni	142	63.6	130	20.5	63.6	126	176
Cu	76.1	70.7	84.7	77.3	72.9	88.2	109
Zn	84.9	94.6	92.8	134.1	99.2	94.7	77.2
Rb	98.5	97.6	83.7	103	72.0	94.0	104
Sr	839	1225	845	2149	1254	971	951
Y	22.3	26.7	23.3	41.7	27.6	24.7	20.3
Zr	248	286	290	388	322	323	271
Nb	75.9	141	74.7	264	143	87.0	100
Cs	0.868	0.567	0.796	1.476	0.595	0.896	0.964
Ba	1112	1363	1023	804	1078	1132	1208
La	59.8	91.9	57.1	181	91.0	70.3	77
Ce	118	177	115	327	178	135	149
Pr	nd	19.9	13.1	34.2	19.8	14.9	16.3
Nd	50.1	72.2	50.4	119	73.3	55.7	61
Sm	8.42	11.3	8.67	17.1	11.6	9.24	9.47
Eu	2.38	3.14	2.46	4.68	3.21	2.60	2.68
Gd	6.94	9.03	7.10	13.3	9.15	7.51	7.23
Tb	0.910	1.14	0.949	1.68	1.17	0.990	0.905
Dy	4.70	5.66	4.96	8.45	5.86	5.12	4.45
Ho	0.841	1.00	0.890	1.52	1.04	0.918	0.777
Er	2.14	2.54	2.22	3.90	2.58	2.32	1.93
Tm	0.282	0.326	0.295	0.522	0.342	0.315	0.256
Yb	1.77	2.05	1.84	3.27	2.11	1.97	1.57
Lu	0.249	0.283	0.263	0.459	0.302	0.285	0.234
Hf	5.74	5.82	6.54	6.23	6.62	6.99	6.08
Ta	4.32	7.09	4.40	12.0	7.23	4.95	5.14
Pb	4.31	5.61	4.76	1.81	3.15	5.68	6.75
Th	6.32	9.39	5.70	19.8	9.82	7.26	8.18
U	1.43	2.71	1.29	5.93	2.77	1.69	1.94

Table 3 continued

Sample	**Ei 25**	**Ei 27**	**Ei 29**	**Ei 32**	**SG 19**	**SG 30**
Rocktype	Basanite	Basanite	Basanite	Basanite	Basalt	Basanite
(ppm)						
Sc	32.6	25.7	26.1	37.0	25.0	32.0
Cr	368	417	527	293	243	264
Ni	149	227	315	115	157	196
Cu	107	64.5	72.7	123	68.1	51.2
Zn	78.3	94.3	92.6	81.1	119	113
Rb	123	49.4	38.5	97.8	35.1	49.1
Sr	896	1195	894	821	796	825
Y	20.9	29.5	24.6	20.8	25.8	26.2
Zr	291	227	213	238	275	224
Nb	91.9	98.0	75.6	93.0	63.2	76.2
Cs	1.22	0.915	0.606	1.02	0.390	0.860
Ba	1192	963	746	1078	793	644
La	77.6	93.5	73.3	58.8	49.0	54.8
Ce	147	165	132	122	90.0	105.0
Pr	16.2	17.2	13.8	14.1	10.3	12.2
Nd	60.8	63.9	52.6	55.3	39.2	46.6
Sm	9.52	10.9	9.35	9.29	7.60	8.80
Eu	2.68	3.29	2.86	2.66	2.35	2.65
Gd	7.31	9.18	7.99	7.26	6.74	7.50
Tb	0.928	1.22	1.06	0.929	0.980	1.05
Dy	4.60	6.25	5.40	4.62	5.34	5.57
Ho	0.799	1.10	0.938	0.793	0.970	0.990
Er	2.00	2.72	2.28	1.97	2.39	2.39
Tm	0.265	0.360	0.296	0.260	0.320	0.320
Yb	1.64	2.20	1.80	1.59	1.92	1.90
Lu	0.242	0.324	0.261	0.237	0.270	0.260
Hf	6.79	4.80	4.68	5.63	4.78	5.73
Ta	4.92	4.25	3.83	4.74	3.41	4.26
Pb	7.60	5.12	4.32	4.61	2.72	4.27
Th	8.93	9.73	8.10	6.38	5.33	6.95
U	1.89	3.54	207	1.70	1.41	1.80

Table 3 continued

Sample	**ZM 10**	**ZM 12**	**ZM 14**	**PAD 6**	**PAD 8**	**DUR 1**	**DUR 7**
Rocktype	Basalt	Basalt	Basalt	Basalt	Basalt	Basalt	Basalt
(ppm)							
Sc	78.8	13.3	24.9	40.4	35.1	45.3	35.8
Cr	215	273	123	1465	1984	420	1233
Ni	77.0	192	52.3	647	789	147	512
Cu	37.0	50.5	55.1	97.0	93.1	132	82.2
Zn	96.0	101	101	78.7	75.2	71.1	75.4
Rb	22.0	66.28	41.9	0.368	nd	0.673	32.6
Sr	722	780	763	97.0	88.0	121	225
Y	33.0	66.3	27.3	17.6	16.2	22.7	17.8
Zr	221	257	252	49.9	42.9	58.0	52.4
Nb	51.0	95.6	68.3	4.19	1.40	2.90	5.09
Cs	0.830	1.36	0.563	nd	nd	nd	nd
Ba	586	593	562	21.2	12.0	27.3	52.4
La	53.0	50.3	48.3	3.39	1.92	3.15	3.92
Ce	91.5	93.71	92.8	8.39	5.72	8.54	9.36
Pr	10.5	11.3	10.4	1.22	0.957	1.35	1.31
Nd	37.5	41.7	39.9	6.04	5.04	7.07	6.33
Sm	7.08	8.31	7.48	1.90	1.68	2.36	1.90
Eu	2.27	2.68	2.34	0.666	0.595	0.858	0.684
Gd	6.49	7.42	6.82	2.45	2.20	3.15	2.43
Tb	0.947	1.07	0.962	0.436	0.386	0.555	0.414
Dy	5.23	5.66	5.26	2.89	2.56	3.72	2.79
Ho	1.015	1.03	0.992	0.605	0.530	0.775	0.576
Er	2.68	2.62	2.58	1.79	1.57	2.30	1.68
Tm	0.391	0.366	0.355	0.279	0.246	0.359	0.264
Yb	2.38	2.18	2.26	1.70	1.49	2.18	1.59
Lu	0.357	0.316	0.334	0.262	0.227	0.332	0.241
Hf	4.82	5.42	4.86	1.50	1.18	1.83	1.46
Ta	3.30	5.18	3.82	0.253	0.284	0.204	0.362
Pb	4.30	3.06	3.15	nd	nd	nd	nd
Th	8.20	8.17	5.57	0.411	0.147	0.265	0.452
U	2.70	2.34	1.42	0.063	0.109	0.082	0.141

Table 3 continued

Sample	**MAR 4**	**ASI 3**	**ASD 16**	**VES 01**	**VES 07**	**VES 16**	**VES 95**	**VES 97**
Rocktype	Basalt	Basalt	Basalt	Basalt	Basalt	Basalt	Basalt	Basalt
(ppm)								
Sc	36.2	26.6	37.8	17.0	17.0	23.0	nd	nd
Cr	195	36.5	469	nd	20.0	30.0	48.0	218
Ni	nd	26.8	31.5	30.0	110	110	28.0	66.0
Cu	66.3	23.6	163	100	70.0	70.0	119	68.0
Zn	86.4	132	123	60.0	20.0	18.0	nd	nd
Rb	11.0	20.2	10.4	302	331	225	266	227
Sr	245	464	210	1037	1013	964	1050	694
Y	24.2	37.1	35.3	27.4	29.5	26.1	24.1	21.9
Zr	104	219	155	187	213	186	186	180
Nb	18.1	43.4	21.6	30.5	29.8	26.6	30.3	32.0
Cs	nd	0.076	0.427	18.5	23.0	13.0	13.0	12.2
Ba	116	298	149	2171	2107	2214	2630	1710
La	12.5	30.9	17.1	44.8	47.2	44.0	52.6	46.0
Ce	27.3	67.8	38.4	93.5	101	93.3	104	94
Pr	3.65	8.98	5.25	11.3	12.5	11.5	12.6	11.7
Nd	16.0	39.3	23.3	42.3	46.6	44.5	46.6	45.3
Sm	4.16	9.08	5.97	9.61	10.1	10.1	9.30	9.50
Eu	1.37	3.01	1.95	2.44	2.56	2.51	2.49	2.27
Gd	4.38	9.18	6.64	7.70	8.22	7.46	8.16	8.20
Tb	0.710	1.36	1.09	1.06	1.08	1.10	0.900	0.920
Dy	4.33	7.54	6.60	5.48	5.33	5.29	4.50	4.23
Ho	0.860	1.41	1.33	0.930	0.910	0.960	0.800	0.770
Er	2.32	3.59	3.56	2.47	2.47	2.54	2.29	2.20
Tm	0.330	0.485	0.515	0.351	0.345	0.358	0.290	0.250
Yb	2.13	3.01	3.33	2.24	2.08	2.24	2.20	1.90
Lu	0.320	0.429	0.482	0.311	0.320	0.328	0.311	0.260
Hf	2.80	5.24	4.09	4.64	5.20	4.67	4.63	4.83
Ta	1.02	2.50	1.24	1.45	1.46	1.28	1.43	1.23
Pb	0.86	2.66	1.27	21.00	30.0	27.0	nd	nd
Th	1.26	2.93	1.67	16.8	20.3	15.5	16.6	17.1
U	0.400	0.851	0.451	5.71	7.25	4.66	6.59	6.12

Table 3 continued

Sample	**PAN 5**	**STR 07L**	**STR 50**	**VLT 14**	**VLT 49**
Rocktype	Basalt	Basalt	Basalt	Basalt	Basalt
(ppm)					
Sc	24.4	29.0	24.9	nd	26.1
Cr	196	50.0	nd	11.5	42.0
Ni	80.0	40.0	30.2	19.0	27.0
Cu	68.0	100	nd	71.8	63.0
Zn	112	80.0	nd	160	78.0
Rb	24.1	70.0	127	94.5	142
Sr	648	704	865	2540	2660
Y	28.9	28.3	29.1	75.4	52.9
Zr	305	157	180	550	426
Nb	63.4	20.2	25.4	133	66.8
Cs	0.200	4.70	8.96	6.12	6.50
Ba	338	949	1780	2290	2740
La	60.8	48.0	55.8	213.3	208.0
Ce	118	95.5	108	412	397
Pr	14.5	10.8	14.7	47.4	46.0
Nd	54.1	42.7	58.7	170	163
Sm	10.5	8.42	11.6	33.7	29.1
Eu	3.07	2.33	2.81	7.63	6.52
Gd	9.84	7.28	10.9	24.8	24.3
Tb	1.18	1.05	1.30	3.61	2.56
Dy	6.11	5.58	6.23	15.4	11.6
Ho	1.12	0.980	1.08	2.40	1.88
Er	3.04	2.74	2.92	6.00	4.87
Tm	0.340	0.392	0.380	0.728	0.560
Yb	2.20	2.49	2.48	4.09	3.60
Lu	0.327	0.346	0.355	0.346	0.480
Hf	6.99	3.79	4.46	11.4	10.4
Ta	3.63	1.03	1.49	6.46	3.83
Pb	nd	18.0	27.1	34.1	46.6
Th	6.12	14.5	18.5	53.6	50.9
U	1.85	3.89	4.13	17.6	11.6

Table 3 continued

1

Sample	Rocktype	$^{176}Hf/^{177}Hf$	(±2σ)	εHf(0Ma)	$^{143}Nd/^{144}Nd$	(±2σ)	εNd(0Ma)
REU 1	Basalt	0.283041	±6	+9.0	0.512844	±15	4.2
REU 11	Basalt	0.283048	±5	+9.3	0.512854	±13	4.4
REU 13	Basalt	0.283049	±5	+9.0	0.512896	±15	4.4
REU 17	Basalt	0.283038	±5	+8.9	0.512853	±15	4.3
REU 18	Basalt	0.283044	±6	+9.1	0.512841	±15	4.1
REU 19	Basalt	0.283059	±10	+9.7	0.512850	±12	4.3
REU 20	Basalt	0.283047	±4	+9.3	0.512858	±14	4.5
ET 1	Basalt	0.283108	±14	+11.4	0.512988	±6	7.0
ET 2	Basalt	0.283099	±12	+11.1	0.513004	±5	7.3
ET 3	Basalt	0.283014	±17	+8.1	0.512882	±3	4.9
ET 4	Basalt	0.283025	±18	+8.5	0.512884	±7	5.0
IBL 1	Basalt	0.283067	±12	+10.0	nd	nd	nd
IBL 2	Basalt	0.283069	±8	+10.1	0.512991	±12	7.0
Ei 2	Basanite	0.282767	±4	-0.6	0.512671	±6	0.8
Ei 4	Basanite	0.282787	±5	+0.1	0.512692	±10	1.2
Ei 9	Basanite	0.282771	±5	-0.5	0.512692	±6	1.2
Ei 10b	Melilitite	0.282761	±5	-0.8	0.512705	±3	1.5
Ei 12	Melilitite	0.282773	±6	-0.4	0.512694	±9	1.2
Ei 16b	Basanite	0.282747	±7	-1.3	0.512669	±9	0.8
Ei 22	Basanite	0.282791	±6	0.7	0.512713	±6	1.5
Ei 25	Basanite	0.282681	±6	-3.7	0.512656	±8	0.5
Ei 27	Basanite	0.282897	±5	+4.0	0.512813	±7	3.6
Ei 29	Basanite	0.282892	±7	+3.8	0.512810	±6	3.5
Ei 32	Basanite	0.282845	±6	+2.1	0.512693	±6	1.2
SG 19	Basalt	0.282986	±6	+7.6	0.512862	7	+4.4
SG 30	Basanite	0.282955	±6	+6.5	0.512844	4	+4.0
ZM 10	Basalt	0.282989	±8	+7.2	0.512803	±12	3.4
ZM 12	Basalt	nd	nd	nd	nd	nd	nd
ZM 14	Basalt	0.283025	±9	+8.5	0.512830	±11	3.9
PAD 6	Basalt	0.283208	±7	+14.9	0.512951	±6	6.3
PAD 8	Basalt	0.283281	±6	+17.5	0.513114	±15	9.4
DUR 1	Basalt	0.283265	±6	+17.0	0.513065	±7	8.5
DUR 7	Basalt	0.283178	±5	+13.9	0.512919	±10	5.6
MAR 4	Basalt	0.283131	±5	+12.2	0.513094	±10	9.1
ASI 3	Basalt	0.283096	±10	+11.0	0.513021	±1	7.6
ASD 16	Basalt	0.283153	±5	+13.0	0.513037	±13	7.9
VES 01	Basalt	0.282771	±9	-0.5	0.512478	nd	-3.0
VES 07	Basalt	0.282781	±5	-0.1	0.512465	nd	-3.2
VES 16	Basalt	0.282787	±6	-0.1	0.512472	nd	-3.0
VES 95	Basalt	0.282782	±9	-0.1	0.512477	nd	-3.0
VES 97	Basalt	0.282779	±11	-0.2	0.512458	nd	-3.3
PAN 5	Basalt	0.283036	±7	+8.9	0.512953	nd	6.3
STR 07L	Basalt	0.282865	±12	+2.8	nd	nd	nd
STR 50	Basalt	0.282822	±15	+1.3	0.512474	nd	-3.0
VLT 14	Basalt	0.282757	±11	-1.0	0.512591	nd	-0.8
VLT 49	Basalt	0.282778	±3	-0.2	0.512672	nd	0.8

Table 4

Sample	**REU 1**	**REU 11**	**REU 13**	**REU 17**	**REU 18**	**REU 19**	**REU 20**
Location	**Piton de la Fournaise**	**Piton de la Fournaise**	**Piton de la Fournaise**	**Piton de la Fournaise**	**Piton des Neiges**	**Piton des Neiges**	**Piton des Neiges**
μ^{182}W (6/4) (± 95% CI)	-3.8 ± 3.8	-6.1 ± 4.2	-8.8 ± 4.1	-5.7 ± 2.4	-1.9 ± 4.5	-2.2 ± 4.1	+0.0 ± 6.3
μ^{183}W (6/4) (± 95% CI)	-1.9 ± 4.2	-0.9 ± 4.0	-1.2 ± 3.7	-3.0 ± 3.1	+1.5 ± 4.6	-1.7 ± 4.3	-3.5 ± 7.5
μ^{182}W (6/3) (± 95% CI)	-3.5 ± 2.9	-4.8 ± 2.8	-7.7 ± 2.3	-4.4 ± 2.0	-2.7 ± 3.1	-4.5 ± 2.7	+0.9 ± 4.2
μ^{184}W (6/3) (± 95% CI)	+1.3 ± 2.8	+0.6 ± 2.7	+0.8 ± 2.5	+2.0 ± 2.1	-1.0 ± 3.1	+1.2 ± 2.9	+2.3 ± 5.0
μ^{182}W Corr (6/3) (± 95% CI)	-5.3 ± 3.6	-5.4 ± 3.8	-8.0 ± 3.6	+2.0 ± 2.1	-2.3 ± 4.5	-5.5 ± 5.9	-3.6 ± 9.9
Sample Weight (g)	2.5	2.5	3.8	3.8	5.1	10.4	10.7
W (μg/g)	0.363	0.331	0.281	0.308	0.225	0.170	0.155
Th (μg/g)	2.56	2.57	2.11	2.65	2.01	1.36	1.30
U (μg/g)	0.860	0.650	0.540	0.650	0.490	0.371	0.363
W/Th	0.142	0.129	0.133	0.116	0.112	0.125	0.119
W/U	0.422	0.509	0.520	0.474	0.459	0.457	0.427
Ta (μg/g)	1.89	1.51	1.27	1.53	1.06	0.866	0.791
Zr (μg/g)	256	186	177	206	187	129	118
Nb (μg/g)	28.7	23.7	20.2	24.2	13.2	12.9	16.8

Table 5

Sample	**ET 1 (ave)**	**ET 1 (1)**	**ET 1(2)**	**ET 2**	**ET 3**	**ET 4**
Location	**Aci Castello**	**Aci Castello**	**Aci Castello**	**Aci Castello**	**Valle di Bove**	**Valle di Bove**
μ^{182}W (6/4) (± 95% CI)	**+1.4 ± 3.1**	+1.0 ± 3.7	+1.9 ± 2.6	+1.2 ± 4.2	+0.2 ± 3.0	+2.0 ± 4.7
μ^{183}W (6/4) (± 95% CI)		+5.3 ± 2.7	+2.2 ± 3.3	+1.7 ± 3.3	-3.0 ± 4.6	-2.7 ± 2.9
μ^{182}W (6/3) (± 95% CI)		-1.1 ± 3.5	+0.8 ± 3.0	-0.5 ± 3.5	+2.2 ± 4.9	+1.4 ± 2.5
μ^{184}W (6/3) (± 95% CI)		-3.5 ± 1.8	-1.5 ± 2.2	-1.1 ± 2.2	+2.0 ± 3.1	+1.8 ± 1.9
μ^{182}W Corr (6/3) (± 95% CI)		+1.0 ± 4.1	+2.2 ± 3.0	+0.8 ± 4.7	-2.5 ± 5.1	-1.8 ± 3.4
Sample Weight (g)		10.3	21.65	5.2	2.3	2.20
W (μg/g)	0.171			0.247	0.893	0.783
Th (μg/g)	4.13			4.13	14.68	9.59
U (μg/g)	1.14			1.24	3.85	2.67
W/Th	0.041			0.0598	0.0608	0.082
W/U	0.150			0.199	0.232	0.293
Ta (μg/g)	1.60			1.60	3.34	2.50
Zr (μg/g)	125			136	251	213
Nb (μg/g)	40.1			38.6	74.3	56.8

Table 5 continued

Sample	IBL 1 (ave)	IBL 1 (1)	IBL 1 (2)	IBL 2 (ave)	IBL 2 (1)	IBL 2 (2)
Location	**Hyblean Plateau**			**Hyblean Plateau**		
μ^{182}W (6/4) (± 95% CI)	**-2.1 ± 2.5**	-2.3 ± 2.6	-2.0 ± 2.5	**-2.5 ± 3.1**	-2.0 ± 3.2	-3.0 ± 3.1
μ^{183}W (6/4) (± 95% CI)		+2.2 ± 2.4	-2.3 ± 1.5		-0.4 ± 2.5	-3.4 ± 3.0
μ^{182}W (6/3) (± 95% CI)		+1.5 ± 1.6	-1.0 ± 1.1		-2.0 ± 2.2	-1.3 ± 1.6
μ^{184}W (6/3) (± 95% CI)		-1.5 ± 1.6	+1.5 ± 1.0		+0.3 ± 1.7	+2.3 ± 2.0
μ^{182}W Corr (6/3) (± 95% CI)		-3.5 ± 2.1	-1.6 ± 2.3		-2.7 ± 3.9	-3.7 ± 3.1
Sample Weight (g)		10.43	10.62		10.3	10.52
W (μg/g)	0.937			0.837		
Th (μg/g)	9.13			6.39		
U (μg/g)	2.55			1.69		
W/Th	0.103			0.131		
W/U	0.368			0.495		
Ta (μg/g)	nd			nd		
Zr (μg/g)	nd			nd		
Nb (μg/g)	nd			nd		

Table 5 continued

Sample	**Ei 2***	**Ei 4***	**Ei 9***	**Ei 10b***	**Ei 12***	**Ei 16b***	**Ei 22***	**Ei 25***
Location	**Eppelsberg**	**Herrchenberg**	**Bausenberg**	**Hannebacher Ley**	**Leitenberg**	**Rothenberg**	**Rüderbusch**	**Rockeskyller Kopf**
μ^{182}W (6/4) (± 95% CI)	-0.8 ± 2.6	2.8 ± 4.1	-0.4 ± 3.3	+1.2 ± 4.3	+3.9 ± 4.0	+1.9 ± 4.6	-0.2 ± 5.3	+1.8 ± 3.8
μ^{183}W (6/4) (± 95% CI)	-14.5 ± 2.5	-9.6 ± 3.5	-11.1 ± 3.7	-9.5 ± 2.9	-9.2 ± 5.2	-15.5 ± 3.3	-0.4 ± 4.1	+2.0 ± 5.5
μ^{182}W (6/3) (± 95% CI)	+8.9 ± 2.5	+10.1 ± 2.8	+14.0 ± 3.0	+8.7 ± 3.7	+10.3 ± 2.4	11.9 ± 3.4	-0.5 ± 4.0	+1.5 ± 5.7
μ^{184}W (6/3) (± 95% CI)	+9.6 ± 1.7	+6.4 ± 2.3	+7.4 ± 2.5	+6.3 ± 1.9	+6.1 ± 3.4	10.3 ± 2.2	+0.3 ± 2.7	-1.3 ± 3.7
μ^{182}W Corr (6/3) (± 95% CI)	-0.4 ± 2.9	+5.8 ± 3.9	-0.5 ± 3.6	+2.7 ± 5.1	+5.1 ± 7.1	+2.7 ± 4.9	-1.0 ± 6.1	+3.5 ± 5.6
Sample Weight (g)	2.1	2.1	2.1	2.1	2.1	2.1	2.1	2.0
W (μg/g)	1.12	1.23	0.893	0.601	0.727	1.197	0.675	1.196
Th (μg/g)	6.32	9.39	5.70	19.8	9.82	7.26	8.18	8.93
U (μg/g)	1.43	2.71	1.29	5.93	2.77	1.69	1.94	1.89
W/Th	0.177	0.131	0.157	0.0303	0.0740	0.165	0.0825	0.134
W/U	0.783	0.454	0.693	0.101	0.263	0.708	0.348	0.633
Ta (μg/g)	nd	nd	nd	nd	nd	nd	nd	nd
Zr (μg/g)	nd	nd	nd	nd	nd	nd	nd	nd
Nb (μg/g)	nd	nd	nd	nd	nd	nd	nd	nd

Table 5 continued

Sample	**Ei 27 (ave)***	**Ei 27 (1)**	**Ei 27 (2)***	**Ei 27 (3)**	**Ei 29***	**Ei 32***
Location	**Sarresdorf**	**Sarresdorf**	**Sarresdorf**	**Sarresdorf**	**Wartgensberg**	**Am Steinseiter**
μ^{182}W (6/4) (± 95% CI)	**-1.0 ± 4.2**	-3.4 ± 2.3	-2.9 ± 6.4	+3.1 ± 3.9	-0.5 ± 2.1	+0.4 ± 2.8
μ^{183}W (6/4) (± 95% CI)		+0.5 ± 1.7	+5.0 ± 8.9	+2.9 ± 4.9	+1.8 ± 1.5	-0.2 ± 2.2
μ^{182}W (6/3) (± 95% CI)		-3.3 ± 1.9	-7.1 ± 7.1	+1.2 ± 2.0	-1.2 ± 1.9	+0.8 ± 1.8
μ^{184}W (6/3) (± 95% CI)		-0.3 ± 1.1	-3.3 ± 5.9	-1.9 ± 3.3	+1.2 ± 1.0	+0.1 ± 1.5
μ^{182}W Corr (6/3) (± 95% CI)		-3.4 ± 3.2	-3.7 ± 5.7	+3.0 ± 6.2	+0.3 ± 2.7	+0.5 ± 2.9
Sample Weight (g)		2.1	1.2	1.4	2	2
W (μg/g)	0.870				1.23	1.07
Th (μg/g)	9.73				8.10	6.38
U (μg/g)	3.54				2.07	1.70
W/Th	0.0894				0.152	0.168
W/U	0.246				0.594	0.629
Ta (μg/g)	nd				nd	nd
Zr (μg/g)	nd				nd	nd
Nb (μg/g)	nd				nd	nd

Table 5 continued

Sample	ZM 10	ZM 12	ZM 14	SG 19	SG 30
Location	Maar de Beaunit	Coulée de Chilhac	Puy des Grosmanaux	Pertersberg	Erpeler Ley
μ^{182}W (6/4) (± 95% CI)	+0.0 ± 3.7	-1.3 ± 3.2	-4.4 ± 3.6	+0.1 ± 4.1	+1.1 ± 4.1
μ^{183}W (6/4) (± 95% CI)	+0.4 ± 3.5	+0.5 ± 2.5	-4.3 ± 4.6	+1.0 ± 3.9	+0.1 ± 4.3
μ^{182}W (6/3) (± 95% CI)	-0.9 ± 2.0	-1.2 ± 2.6	-2.1 ± 2.7	+1.4 ± 2.9	-2.5 ± 5.2
μ^{184}W (6/3) (± 95% CI)	-0.3 ± 2.4	-0.3 ± 1.7	+2.9 ± 3.1	-0.7 ± 2.6	-0.1 ± 2.9
μ^{182}W Corr (6/3) (± 95% CI)	-1.0 ± 3.6	-0.4 ± 3.6	-6.4 ± 5.2	+2.1 ± 3.8	-0.7 ± 2.8
Sample Weight (g)	5.8	2.1	5.7	2.2	2.1
W (μg/g)	1.506	1.66	0.798	1.11	1.02
Th (μg/g)	6.53	8.17	5.71	5.33	6.95
U (μg/g)	1.90	2.34	1.53	1.41	1.80
W/Th	0.231	0.203	0.140	0.208	0.147
W/U	0.793	0.709	0.521	0.786	0.568
Ta (μg/g)	28.3	nd	40.9	nd	nd
Zr (μg/g)	209	nd	219	nd	nd
Nb (μg/g)	56.5	nd	62.2	nd	nd

Table 5 continued

Sample	MAR 4	ASI 3	ASD 16	PAD 6	PAD 8	DUR 1	DUR 7
Location	"Proto-Ascension"	Sub-Aerial	Sub-Marine-Section	Padloping Island	Padloping Island	Durban Island	Durban Island
μ^{182}W (6/4) (± 95% CI)	+0.1 ± 4.7	-0.2 ± 3.5	+0.5 ± 1.8	-4.5 ± 8.7	+2.2 ± 6.3	+0.9 ± 2.0	+1.2 ± 6.8
μ^{183}W (6/4) (± 95% CI)	-2.0 ± 3.6	-3.6 ± 3.1	-0.7 ± 1.0	-15.8 ± 6.6	-2.1 ± 9.2	-0.6 ± 1.5	-6.2 ± 7.0
μ^{182}W (6/3) (± 95% CI)	+2.5 ± 4.3	+3.2 ± 3.1	+1.3 ± 1.4	+4.1 ± 9.3	+4.1 ± 7.0	+1.0 ± 1.8	+5.5 ± 2.5
μ^{184}W (6/3) (± 95% CI)	+1.3 ± 2.4	+2.4 ± 2.1	+0.5 ± 0.7	+10.5 ± 4.4	+1.4 ± 6.6	+0.4 ± 1.0	+4.1 ± 4.7
μ^{182}W Corr (6/3) (± 95% CI)	+0.8 ± 5.2	-0.2 ± 3.4	+1.7 ± 1.6	-6.8 ± 11.1	+1.0 ± 10.4	-0.6 ± 1.9	+3.2 ± 5.2
Sample Weight (g)	5.2	3.2	7.2	10.9	11.6	1.2	12.2
W (μg/g)	0.220	0.451	55.2	0.061	0.020	4.246	0.050
Th (μg/g)	1.26	2.89	1.55	0.383	0.165	0.258	0.415
U (μg/g)	0.400	0.663	0.537	0.0500	0.0400	0.0680	0.101
W/Th	0.175	0.156	35.6	0.159	0.121	16.5	0.120
W/U	0.550	0.680	103	1.220	0.498	62.4	0.495
Ta (μg/g)	nd	2.62	1.18	0.215	0.253	0.174	0.252
Zr (μg/g)	nd	215	166	45.9	39.3	56.1	50.5
Nb (μg/g)	nd	42.3	18.9	3.66	1.30	2.89	4.44

Table 5 continued

Sample	VES 01 (ave)	VES 01	VES 01 (2)	VES 07	VES 16	VES 95 (ave)	VES 95	VES 95 (2)	VES 97
Location		**Mt. Vesuvio**	**Mt. Veusivo**	**Mt. Veusivo**	**Mt. Veusivo**		**Mt. Veusivo**	**Mt. Veusivo**	**Mt. Veusivo**
μ^{182}W (6/4) (± 95% CI)	**-2.0 ± 2.5**	-1.3 ± 3.2	-2.8 ± 1.9	+0.2 ± 2.6	-3.1 ± 2.7	**-4.5 ± 2.9**	-5.3 ± 2.7	-3.8 ± 3.1	-1.6 ± 1.5
μ^{183}W (6/4) (± 95% CI)		+2.0 ± 1.9	-1.4 ± 2.3	+1.0 ± 1.8	-1.0 ± 2.6		-1.8 ± 2.4	-0.8 ± 2.3	+0.6 ± 2.0
μ^{182}W (6/3) (± 95% CI)		-3.2 ± 2.2	-2.0 ± 1.0	-1.4 ± 1.7	-2.6 ± 2.1		-3.6 ± 2.2	-2.3 ± 2.3	-2.3 ± 2.0
μ^{184}W (6/3) (± 95% CI)		-1.4 ± 1.2	+0.9 ± 1.6	-0.7 ± 1.2	+0.7 ± 1.8		+1.2 ± 1.6	+0.5 ± 1.5	-0.4 ± 1.4
μ^{182}W Corr (6/3) (± 95% CI)		-2.0 ± 2.9	-2.5 ± 2.6	-0.9 ± 2.6	-3.3 ± 2.8		-4.2 ± 2.8	-2.9 ± 3.2	-2.0 ± 2.2
Sample Weight (g)		1.2	1.6	1.5	1.8		1.1	1.4	1.1
W (μg/g)	4.11			6.12	4.62	6.77			4.70
Th (μg/g)	16.8			20.3	15.5	16.6			17.1
U (μg/g)	5.71			7.2	4.7	6.59			6.12
W/Th	0.245			0.301	0.298	0.408			0.274
W/U	0.720			0.844	0.991	1.027			0.768
Ta (μg/g)	nd			nd	nd	nd			nd
Zr (μg/g)	nd			nd	nd	nd			nd
Nb (μg/g)	nd			nd	nd	nd			nd

Table 5 continued

Sample	STR 07L	STR 50	VLT 14	VLT 49	PAN 5
Location	Mt. Stromboli	Mt. Stromboli	Mt. Vulture	Mt. Vulture	Pantelleria
μ^{182}W (6/4) (± 95% CI)	+0.1 ± 2.6	-2.2 ± 3.4	-1.5 ± 1.9	+0.4 ± 2.9	-1.4 ± 3.6
μ^{183}W (6/4) (± 95% CI)	-2.2 ± 2.4	-1.9 ± 2.6	+0.7 ± 1.3	+2.8 ± 2.3	+0.6 ± 2.9
μ^{182}W (6/3) (± 95% CI)	+1.1 ± 2.0	-2.4 ± 3.6	-2.0 ± 1.0	-0.7 ± 2.5	-2.7 ± 2.3
μ^{184}W (6/3) (± 95% CI)	+1.5 ± 1.6	+1.3 ± 1.7	-0.4 ± 0.9	-1.9 ± 1.6	-0.4 ± 1.9
μ^{182}W Corr (6/3) (± 95% CI)	-0.4 ± 3.0	-4.5 ± 3.1	-1.2 ± 1.7	+1.0 ± 3.0	-1.8 ± 3.9
Sample Weight (g)	2.1	1.1	1.1	1.1	3.1
W (μg/g)	1.87	1.45	3.41	2.38	0.816
Th (μg/g)	14.5	18.5	53.6	50.9	6.12
U (μg/g)	3.89	4.13	17.6	11.6	1.85
W/Th	0.129	0.078	0.0636	0.0468	0.133
W/U	0.481	0.351	0.194	0.205	0.441
Ta (μg/g)	1.03	1.49	6.46	3.83	3.63
Zr (μg/g)	157	180	550	426	305
Nb (μg/g)	20.2	25.4	133.5	66.80	63.4

Table 5 continued

Appendix AII

Sample	Previously Investigated in:
DSDP Leg 74 525 A 57 5W 141-148 (80060941)	Rohde, J., Hoernle, K., Hauff, F., Werner, R., O'Connor, J., Class, C., Garbe-Schönberg, D. and Jokat, W. (2013a) 70 Ma chemical zonation of the Tristan-Gough hotspot track. Geology 43, 335-338. Rohde, J.K., van den Bogaard, P., Hoernle, K., Hauff, F. and Werner, R. (2013b) Evidence for an age progression along the Tristan-Gough volcanic track from new 40Ar/39Ar ages on phenocryst phases. Tectonophysics 604, 60-71
DR90-6	Homrighausen, S., Hoernle, K., Geldmacher, J., Wartho, J.A., Hauff, F., Portnyagin, M., Werner, R., van den Bogaard, P. and Garbe-Schönberg, D. (2018)Unexpected HIMU-type late-stage volcanism on the Walvis Ridge. Earth Planet Sc Lett 492, 251-263
DR89-7	Homrighausen, S., Hoernle, K., Geldmacher, J., Wartho, J.A., Hauff, F., Portnyagin, M., Werner, R., van den Bogaard, P. and Garbe-Schönberg, D. (2018) Unexpected HIMU-type late-stage volcanism on the Walvis Ridge. Earth Planet Sc Lett 492, 251-264
MSM19/3 DR49-2	Schwindrofska, A., Hoernle, K., Hauff, F., van den Bogaard, P., Werner, R. and Garbe-Schönberg, D. (2016) Origin of enriched components in the South Atlantic: Evidence from 40 Ma geochemical zonation of the Discovery Seamounts. Earth Planet Sc Lett 441, 167-177
MSM19/3 DR53-1A	Schwindrofska, A., Hoernle, K., Hauff, F., van den Bogaard, P., Werner, R. and Garbe-Schönberg, D. (2016) Origin of enriched components in the South Atlantic: Evidence from 40 Ma geochemical zonation of the Discovery Seamounts. Earth Planet Sc Lett 441, 167-179
MSM19/3 DR7-1	Hoernle, K., Schwindrofska, A., Werner, R., van den Bogaard, P., Hauff, F., Uenzelmann-Neben, G. and Garbe-Schönberg, D. (2016)Tectonic dissection and displacement of parts of Shona hotspot volcano 3500 km along the Agulhas-Falkland Fracture Zone. Geology 44, 263-266.
NAM19	Zhou, H., Hoernle, K., Geldmacher, J., Hauff, F., Homrighausen, S., Garbe-Schönberg, D. and Jung, S. (2020) Geochemistry of Etendeka magmatism: Spatial heterogeneity in the Tristan-Gough plume head. Earth Planet Sc Lett 535, 116123.
NM3	Zhou, H., Hoernle, K., Geldmacher, J., Hauff, F., Homrighausen, S., Garbe-Schönberg, D. and Jung, S. (2020) Geochemistry of Etendeka magmatism: Spatial heterogeneity in the Tristan-Gough plume head. Earth Planet Sc Lett 535, 116123.
NAM61	Zhou et al. Submited
NM52	Zhou, H., Hoernle, K., Geldmacher, J., Hauff, F., Homrighausen, S., Garbe-Schönberg, D. and Jung, S. (2020) Geochemistry of Etendeka magmatism: Spatial heterogeneity in the Tristan-Gough plume head. Earth Planet Sc Lett 535, 116123.
NM53	Zhou, H., Hoernle, K., Geldmacher, J., Hauff, F., Homrighausen, S., Garbe-Schönberg, D. and Jung, S. (2020) Geochemistry of Etendeka magmatism: Spatial heterogeneity in the Tristan-Gough plume head. Earth Planet Sc Lett 535, 116123.
NM54	Zhou, H., Hoernle, K., Geldmacher, J., Hauff, F., Homrighausen, S., Garbe-Schönberg, D. and Jung, S. (2020) Geochemistry of Etendeka magmatism: Spatial heterogeneity in the Tristan-Gough plume head. Earth Planet Sc Lett 535, 116123.

Table 1

*Data gained in this study comprises ^{182}W isotope compositions and W, U, Th isotope concentrations. All other data has been previously published.

Sample ID	**DSDP Leg 74 525 A 57 5W 141-148 (80060941)**	**DR90-6**	**DR89-7**	**MSM19/3 DR49-2**	**MSM19/3 DR53-1A**	**MSM19/3 DR7-1**	**NAM19**	**NM3**	**NAM61**	**NM52**	**NM53**	**NM54**
Location	Walvis Ridge	Walvis Ridge	Walvis Ridge	Northern Discovery Seamounts	Southern Discovery Seamounts	Meteor - Shona track	Etendeka	Etendeka	Etendeka	Etendeka	Etendeka	Etendeka
Geochemical flavour	EM I Gough-type)	HIMU	HIMU	EM I (Gough-type)	EMI (Southern Discory-type)	EM I (Gough-type)	EM I	EM I	HIMU	EM I	EM I	EM I
wt.%												
SiO_2	50.5	47.3	48.0	46.4	49.8	48.9	47.9	48.7	41.7	44.9	44.5	46.4
TiO_2	2.51	2.80	4.08	2.51	2.24	4.00	2.54	2.61	3.64	0.39	0.41	0.75
Al_2O_3	14.7	14.4	17.2	16.8	16.1	7.86	9.53	10.1	12.4	11.4	12.8	12.7
Fe_2O_3	12.5	12.3	14.5	11.8	7.94	13.0	12.8	12.6	14.3	10.5	10.5	10.5
MnO	0.12	0.26	0.17	0.18	0.06	0.16	0.16	0.16	0.22	0.16	0.15	0.16
MgO	5.72	7.88	1.56	6.73	3.84	15.9	13.3	11.7	7.95	20.0	19.2	14.9
CaO	9.38	11.34	6.38	10.14	8.64	8.63	8.35	8.20	10.13	9.73	9.43	10.20
Na_2O	3.26	2.56	3.91	2.90	3.47	1.68	1.66	1.80	4.46	1.17	1.24	1.62
K_2O	1.05	0.83	2.75	0.611	2.64	0.70	1.02	1.05	2.07	0.18	0.20	0.43
P_2O_5	0.342	0.481	1.49	0.961	2.12	0.400	0.321	0.341	1.26	0.0400	0.0400	0.0800
L.O.I.	3.30	2.58	1.74	2.72	3.90	0.98	1.73	1.83	1.16	0.39	0.39	1.23
Total	100	99.9	100	99.1	96.8	100	97.7	97.2	98.1	98.5	98.5	97.5

Table 2

Sample ID	**DSDP Leg 74 525 A 57 5W 141-148 (80060941)**	**DR90-6**	**DR89-7**
Location	Walvis Ridge	Walvis Ridge	Walvis Ridge
(ppm)			
Sc	32.9	24.8	13.2
V	313	249	202
Cr	49	379	5
Co	34.3	47.4	22.1
Ni	26	185	6
Cu	55.7	85.8	5.2
Zn	99	112	77
Ga	22.0	21.9	30.6
Rb	13.48	14.72	31.20
Sr	396	552	819
Y	31.7	25.1	50.1
Zr	232	226	451
Nb	20.3	46.4	93.4
Cs	0.039	0.522	0.254
Ba	341	260	492
La	26.9	33.0	74.3
Ce	57.6	69.1	165.3
Pr	7.25	8.52	21.43
Nd	30.8	35.8	91.4
Sm	6.83	7.59	18.43
Eu	2.23	2.48	5.69
Gd	6.90	6.98	15.93
Tb	1.05	1.01	2.19
Dy	6.20	5.41	11.25
Ho	1.196	0.964	1.941
Er	3.13	2.36	4.64
Tm	0.437	0.309	0.577
Yb	2.77	1.84	3.38
Lu	0.410	0.263	0.466
Hf	5.30	5.06	10.18
Ta	1.13	2.90	5.82
W	0.223	0.441	1.213
Tl	0.054	0.021	0.048
Pb	1.74	1.88	2.54
Th	2.67	3.39	6.15
U	0.621	1.056	1.960

Table 3

Sample ID	**MSM19/3 DR49-2**	**MSM19/3 DR53-1A**	**MSM19/3 DR7-1**
Location	Northern Discovery Seamounts	Southern Discovery Seamounts	Meteor - Shona track
(ppm)			
Sc	21.6	13.2	25.5
V	215	154	266
Cr	315	58	877
Co	37.5	24.3	63.2
Ni	126	91	641
Cu	35.3	37.7	111.4
Zn	160	143	107
Ga	19.3	21.8	14.9
Rb	5.09	25.97	10.25
Sr	608	810	527
Y	21.9	30.9	31.3
Zr	207	363	340
Nb	24.2	24.1	15.5
Cs	0.0950	0.992	2.287
Ba	216	854	351
La	29.9	61.4	25.8
Ce	60.6	109.7	66.3
Pr	7.44	13.44	9.86
Nd	30.3	52.2	46.9
Sm	6.42	9.49	11.35
Eu	2.09	2.82	3.43
Gd	6.03	7.89	10.32
Tb	0.88	1.05	1.45
Dy	4.75	5.25	7.55
Ho	0.853	0.936	1.299
Er	2.09	2.31	3.08
Tm	0.277	0.297	0.391
Yb	1.67	1.79	2.31
Lu	0.234	0.258	0.307
Hf	4.80	8.00	8.50
Ta	1.39	1.32	0.98
W	0.246	0.307	0.260
Tl	0.0220	0.045	0.100
Pb	2.76	7.48	3.63
Th	2.93	6.36	2.10
U	0.737	1.216	0.514

Table 3 continued

Sample ID	**NAM19**	**NM3**	**NAM61**	**NM52**	**NM53**	**NM54**
Location	Etendeka	Etendeka	Etendeka	Etendeka	Etendeka	Etendeka
(ppm)						
Sc	25.6	29.2	18.40	33.4	30.0	36.5
V	257	295	215	192	193	277
Cr	725	965	199	2057	2074	1697
Co	65.9	68.7	41.4	86.3	87.6	72.3
Ni	514	340	141	907	902	594
Cu	120.8	119.5	35.7	64.7	71.5	95.2
Zn	107	117	151	65	67	75
Ga	18.5	19.4	25.9	10.9	11.6	14.5
Rb	18.89	19.65	44.5	8.10	8.89	18.20
Sr	505	544	1261	70	77	139
Y	27.0	26.2	47.4	12.0	13.0	18.4
Zr	214	242	514	28	32	66
Nb	19.5	17.3	133	2.1	2.3	3.9
Cs	0.828	0.824	1.2	0.510	0.600	2.350
Ba	366	368	847	37	44	98
La	27.4	24.6	95.7	2.4	2.8	6.3
Ce	59.2	55.6	186	5.4	6.0	14.1
Pr	7.65	7.32	22.7	0.75	0.83	1.94
Nd	32.9	32.3	89.9	3.6	3.8	8.7
Sm	7.29	7.22	17	1.11	1.20	2.35
Eu	2.36	2.30	5.09	0.40	0.44	0.76
Gd	6.82	6.65	14.4	1.50	1.64	2.75
Tb	0.99	0.95	1.93	0.28	0.31	0.47
Dy	5.43	5.19	9.76	1.94	2.08	3.05
Ho	0.976	0.929	1.69	0.420	0.450	0.640
Er	2.41	2.31	4.08	1.21	1.28	1.79
Tm	0.320	0.307	0.524	0.180	0.200	0.270
Yb	1.96	1.88	3.13	1.21	1.29	1.72
Lu	0.276	0.269	0.441	0.190	0.200	0.270
Hf	4.94	5.31	10.4	0.74	0.83	1.61
Ta	1.10	1.00	7.26	0.15	0.17	0.25
W	0.262	0.200	nd	nd	nd	nd
Tl	0.056	0.070	nd	0.050	0.060	0.100
Pb	3.72	4.28	6.65	1.08	1.29	2.44
Th	2.55	2.37	12.1	0.59	0.69	1.55
U	0.545	0.549	3.05	0.250	0.270	0.440

Table 3 continued

Sample ID	**DSDP Leg 74 525 A 57 5W 141-148 (80060941)**	**DR90-6**	**DR89-7**	**MSM19/3 DR49-2**	**MSM19/3 DR53-1A**	**MSM19/3 DR7-1**	**NAM19**	**NM3**	**NAM61**	**NM52**	**NM53**	**NM54**
Location	Walvis Ridge	Walvis Ridge	Walvis Ridge	Northern Discovery Seamounts	Southern Discovery Seamounts	Meteor - Shona track	Etendeka	Etendeka	Etendeka	Etendeka	Etendeka	Etendeka
$^{143}Nd/^{144}Nd$	0.512489	0.512864	0.512863	0.512435	0.512300	0.512593	0.512375	0.512365	0.512873	0.512633	0.512556	0.512499
(±2σ)	2.87E-06	3.46E-06	4.25E-06	2.43E-06	4.76E-06	3.98E-06	nd	nd	nd	nd	5.60E-06	nd
$^{86}Sr/^{87}Sr$	0.704841	0.702867	0.702995	0.705706	0.706362	0.704456	0.705124	0.705591	0.703257	0.708035	0.708856	0.709104
(±2σ)	5.00E-06	5.20E-06	4.33E-06	5.95E-06	5.55E-06	5.12E-06	nd	nd	nd	nd	4.44E-06	nd
$^{206}Pb/^{204}Pb$	17.7	20.6	20.9	18.3	17.8	17.2	17.4	17.7	20.5	19.7	19.7	19.3
(±2σ)	6.21E-04	1.10E-03	1.49E-03	7.36E-04	1.39E-03	8.14E-04	nd	nd	nd	nd	nd	nd
$^{207}Pb/^{204}Pb$	15.5	15.8	15.8	15.6	15.6	15.4	15.5	15.5	15.7	15.7	15.7	15.7
(±2σ)	7.30E-04	9.93E-04	1.13E-03	7.52E-04	1.35E-03	7.69E-04	nd	nd	nd	nd	nd	nd
$^{208}Pb/^{204}Pb$	38.2	39.9	40.2	38.8	38.5	37.7	38.0	38.2	40.2	39.0	39.0	39.2
(±2σ)	2.16E-03	2.73E-03	3.09E-03	2.34E-03	4.01E-03	2.17E-03	nd	nd	nd	nd	nd	nd
$^{176}Hf/^{177}Hf$	0.282747	nd	0.282836	0.282640	0.282517	0.282812	0.282639	0.282625	0.282901	nd	nd	nd
(±2σ)	nd	nd	4.96E-06	3.98E-06	5.30E-06	5.62E-06	nd	nd	nd	nd	nd	nd
Initial Isotope compositions												
$^{143}Nd/^{144}Nd\_IN$	0.512426	0.512791	0.512797	0.512416	0.512272	0.512522	0.512260	0.512249	0.512820	0.512470	0.512393	0.512358
$^{86}Sr/^{87}Sr\_IN$	0.704740	0.702772	0.702866	0.705698	0.706312	0.704396	0.704921	0.705395	0.703156	0.707410	0.708228	0.708393
$^{206}Pb/^{204}Pb\_IN$	17.4	20.1	20.2	18.2	17.8	17.1	17.2	17.5	20.2	19.4	19.4	19.1
$^{207}Pb/^{204}Pb\_IN$	15.5	15.7	15.7	15.6	15.6	15.3	15.5	15.5	15.7	15.7	15.7	15.7
$^{208}Pb/^{204}Pb\_IN$	37.8	39.4	39.5	38.7	38.4	37.6	37.7	38.0	39.8	38.7	38.8	38.9
$^{176}Hf/^{177}Hf\_IN$	0.28273	nd	0.28283	0.28264	0.28251	0.28280	0.28262	0.28261	0.28289	nd	nd	nd

Table 4

Sample	**DSDP Leg 74 525 A57 5W 141-148**	**DR 90-6**	**DR 89-7**	**MSM 19/3 DR 49-2**	**MSM 19/3 DR53-1A**
Location	Walvis Ridge	Walvis Ridge	Walvis Ridge	Discovery Smts. (N)	Discovery Smts. (S)
	EM I	HIMU	HIMU	EM I	EM I
μ^{182}W (6/4) (± 95% CI)	-1.4 ± 16.3	-5.6 ± 6.5	-4.8 ± 3.7	-0.4 ± 7.4	+3.2 ± 14.2
μ^{183}W (6/4) (± 95% CI)	-4.1 ± 6.0	-1.9 ± 2.5	-3.6 ± 3.6	+2.7 ± 5.6	+0.9 ± 6.4
μ^{182}W (6/3) (± 95% CI)	+2.5 ± 14.4	-3.6 ± 4.5	-3.5 ± 2.5	-0.1 ± 5.5	+0.3 ± 13.3
μ^{184}W (6/3) (± 95% CI)	+2.7 ± 4.0	+1.3 ± 1.7	+2.5 ± 2.4	-1.8 ± 3.7	-0.6 ± 4.3
μ^{182}W (6/3)corr (± 95% CI)	-1.3 ± 19.1	-4.2 ± 4.1	-6.8 ± 4.1	+1.3 ± 4.7	+1.4 ± 15.7
Sample Weight (g)	~5.7g	~4.8g	~3.6g	~4.1g	~2.1g
U (μg/g)	0.599	1.02	1.93	0.626	1.14
Th (μg/g)	2.67	2.87	6.16	2.70	6.0
W (μg/g)	0.208	0.412	1.11	0.156	0.154
W/Th	0.0778	0.144	0.180	0.0578	0.0254
U/W	0.347	0.403	0.576	0.249	0.135
$D^{Sr\text{-}Nd\text{-}Pb}$	0.87	0.74	0.75	0.91	1.06

Table 5

Sample	**MSM 19/3 DR 7-1**	**NAM 19**	**NM 3**	**NAM 61**	**MN 52**	**MN 53a**	**MN 54**
Location	Shona track	Etendeka	Etendeka	Etendeka	Etendeka	Etendeka	Etendeka
	EM I	EM I	EM I	HIMU	EM I	EM I	EM I
μ^{182}W (6/4) (± 95% CI)	-0.8 ± 2.4	-2.7 ± 2.3	-0.6 ± 2.9	-4.3 ± 4.0	+2.1 ± 3.6	+2.3 ± 4.6	+1.7 ± 3.1
μ^{183}W (6/4) (± 95% CI)	-5.2 ± 3.3	-2.3 ± 2.7	+0.6 ± 2.3	-0.4 ± 4.6	+3.3 ± 3.1	-1.9 ± 4.7	1.2 ± 2.6
μ^{182}W (6/3) (± 95% CI)	+3.7 ± 2.4	-1.0 ± 2.0	-0.6 ± 2.7	-1.3 ± 6.3	-1.1 ± 3.5	+2.2 ± 4.4	+1.5 ± 2.0
μ^{184}W (6/3) (± 95% CI)	+3.4 ± 2.2	+1.5 ± 2.0	-0.4 ± 1.5	+0.3 ± 3.1	-2.2 ± 2.1	+1.2 ± 3.2	-0.8 ± 1.7
μ^{182}W (6/3)corr (± 95% CI)	+0.0 ± 3.0	-3.1 ± 2.3	+0.1 ± 2.1	-2.0 ± 7.4	+0.8 ± 5.4	+0.4 ± 6.1	+2.3 ± 3.0
Sample Weight (g)	~24g	~24g	~20g	~3.1g	~26g	~20g	~20g
U (μg/g)	0.499	0.513	0.551	0.927	0.252	0.264	0.446
Th (μg/g)	2.02	2.28	2.29	7.21	0.592	0.629	1.51
W (μg/g)	0.423	0.229	0.225	0.464	0.123	0.132	0.185
W/Th	0.209	0.101	0.0985	0.0643	0.208	0.209	0.122
U/W	0.847	0.447	0.409	0.500	0.487	0.500	0.415
$D^{Sr\text{-}Nd\text{-}Pb}$	0.77	2.6	2.9	0.73	0.96	1.05	1.06

Table 5 continued

Appendix AIII

Sample Number	Ei 2	Ei 3	Ei 4
Locaylity	Eppelsberg	Eppelsberg	Herrchenberg
Classification (Le Maitre, 1984)	Basanite	Basanite	Foidite
Classification (Le Bas 1989)	Melanephelinite	Melanephelinite	Melilitite
Age (kyr)	223	223	452
Age Reference	Novell et al., (2006)	Novell et al., (2006)	Novell et al., (2006)
Longitude	E 07° 19'7.10"	E 07° 19'7.10"	E 07° 15'54.47"
Latitude	N 50° 24'23.05"	N 50° 24'23.05"	N 50° 28'39.88"
wt.%			
SiO_2	42.5	42.2	38.9
TiO_2	2.79	2.73	3.13
Al_2O_3	13.6	13.9	13.5
Fe_2O_3	11.4	11.5	11.4
MnO	0.180	0.190	0.210
MgO	9.80	8.39	8.51
CaO	12.1	12.0	14.0
Na_2O	2.73	3.58	3.87
K_2O	3.32	2.90	3.83
P_2O_5	0.510	0.610	0.660
L.O.I.	0.120	1.06	0.830
Total	99.0	99.1	98.8
Mg#	66.1	62.2	62.7

Table 1

Sample Number	**Ei 5**	**Ei 6**	**Ei 7**
Locaylity	Herrchenberg	Herrchenberg	Herrchenberg
Classification (Le Maitre, 1984)	Foidite	Foidite	Foidite
Classification (Le Bas 1989)	Melilitite	Melilitite	Melilitite
Age (kyr)	452	452	452
Age Reference	Novell et al., (2006)	Novell et al., (2006)	Novell et al., (2006)
Longitude	E 07° 15'54.47"	E 07° 15'54.47"	E 07° 15'54.47"
Latitude	N 50° 28'39.88"	N 50° 28'39.88"	N 50° 28'39.88"
wt.%			
SiO_2	38.7	38.8	38.3
TiO_2	3.09	3.11	3.04
Al_2O_3	13.5	13.5	13.4
Fe_2O_3	11.3	11.2	11.2
MnO	0.210	0.210	0.210
MgO	8.65	8.63	8.63
CaO	14.0	14.1	14.0
Na_2O	3.88	3.84	3.68
K_2O	3.87	3.76	4.00
P_2O_5	0.660	0.660	0.670
L.O.I.	1.20	1.08	1.85
Total	99.2	98.9	99.0
Mg#	63.2	63.4	63.5

Table 1 continued

Sample Number	**Ei 8**	**Ei 9**	**Ei 10a**
Locaylity	Upper-Mendig Flow	Bausenberg	Hannebacher Ley
Classification (Le Maitre, 1984)	Tephrite	Basanite	Foidite
Classification (Le Bas 1989)		Melanephelinite	Nephelinites
Age (kyr)	150	140	470
Age Reference	Novell et al., (2006)	Novell et al., (2006)	Novell et al., (2006)
Longitude	E 07° 17'19.43"	E 07° 13'15.81"	E 07° 7'29.23"
Latitude	N 50° 22'42.30"	N 50° 28'4.38"	N 50° 27'1.26"
wt.%			
SiO_2	47.3	43.0	40.8
TiO_2	2.06	2.69	2.22
Al_2O_3	16.5	13.5	14.9
Fe_2O_3	8.67	10.9	11.4
MnO	0.190	0.170	0.290
MgO	4.35	9.59	4.34
CaO	8.88	12.0	11.5
Na_2O	4.75	2.75	5.61
K_2O	4.52	3.12	3.75
P_2O_5	0.530	0.530	1.21
L.O.I.	0.69	< 0.1	2.32
Total	98.4	98.3	98.3
Mg#	53.1	66.6	46.2

Table 1 continued

Sample Number	**Ei 10b**	**Ei 11 a**	**Ei 12**
Locaylity	Hannebacher Ley	Schorberg	Leitenberg
Classification (Le Maitre, 1984)	Foidite	Basanite	Basanite
Classification (Le Bas 1989)	Nephelinites	Melanephelinite	Melilitite-Nephelinite
Age (kyr)	470	287	
Age Reference	Novell et al., (2006)	Novell et al., (2006)	Novell et al., (2006)
Longitude	E 07° 7'29.23"	E 07° 9'9.46"	E 07° 18'19.74''
Latitude	N 50° 27'1.26"	N 50° 25'47.16"	N 50° 28'32.40"
wt.%			
SiO_2	40.0	44.0	39.3
TiO_2	2.15	2.18	2.65
Al_2O_3	14.9	13.6	12.8
Fe_2O_3	11.0	10.2	11.0
MnO	0.280	0.180	0.200
MgO	4.61	9.50	8.42
CaO	12.7	11.6	15.3
Na_2O	6.09	3.15	3.24
K_2O	4.24	3.27	2.77
P_2O_5	1.22	0.530	0.720
L.O.I.	0.870	0.170	2.33
Total	98.1	98.4	98.7
Mg#	48.5	67.7	63.3

Table 1 continued

Sample Number	**Ei 13**	**Ei 14**	**Ei 15**
Locaylity	Hohe Buche	Plaidter Hummerich	Nettetal
Classification (Le Maitre, 1984)	Basanite	Basanite	Basanite
Classification (Le Bas 1989)	Melanephelinite	Melanephelinite	Melanephelinite
Age (kyr)	367	207	180
Age Reference	Novell et al., (2006)	Novell et al., (2006)	Novell et al., (2006)
Longitude	E 07° 20'1.38"	E 07° 22'1.74"	E 07° 17'19.60"
Latitude	N 50° 27'52.94"	N 50° 23'4.957"	N 50° 21'23.70"
wt.%			
SiO_2	42.7	43.8	43.7
TiO_2	2.76	2.63	2.58
Al_2O_3	13.2	14.1	14.5
Fe_2O_3	11.1	10.8	10.7
MnO	0.160	0.180	0.170
MgO	9.94	8.59	8.36
CaO	11.9	10.9	11.0
Na_2O	2.78	3.23	3.17
K_2O	2.87	3.33	3.39
P_2O_5	0.570	0.650	0.660
L.O.I.	0.0900	- 0.0800	0.120
Total	98.1	98.1	98.4
Mg#	66.8	64.2	63.6

Table 1 continued

Sample Number	**Ei 16b**	**Ei 17**	**Ei 18**
Locaylity	Rothenberg	Lower-Mendig Flow	Eppelsberg Coarse
Classification (Le Maitre, 1984)	Basanite	Basanite	Basanite
Classification (Le Bas 1989)	Melanephelinite	Melanephelinite	Melanephelinite
Age (kyr)	202	160	223
Age Reference	Novell et al., (2006)	Novell et al., (2006)	Novell et al., (2006)
Longitude	E 07° 24'59.59"	E 07° 17'30.00"	E 07° 19'7.10"
Latitude	N 50° 24'51.66"	N 50° 32'36.00"	N 50° 24'23.05"
wt.%			
SiO_2	43.8	44.3	42.8
TiO_2	2.64	2.53	2.74
Al_2O_3	13.8	15.3	14.2
Fe_2O_3	10.7	10.7	11.7
MnO	0.170	0.202	0.188
MgO	9.08	6.34	7.69
CaO	11.3	10.6	12.0
Na_2O	3.23	4.05	3.52
K_2O	3.35	3.65	3.11
P_2O_5	2.64	0.792	0.720
L.O.I.	- 0.140	0.395	0.388
Total	100.6	98.8	99.1
Mg#	65.6	57.2	59.7

Table 1 continued

Sample Number	**Ei 19**	**Ei 20**	**Ei 21**
Locaylity	Eppelsberg Dike	Lower-Mendig Flow	relict flow. Hill W' Jägerheim
Classification (Le Maitre, 1984)	Basanite	Basanite	Basanite
Classification (Le Bas 1989)	Melanephelinite	Melanephelinite	Melanephelinite
Age (kyr)	223		
Age Reference	Novell et al., (2006)		
Longitude	E 07° 19'7.10"	E 07° 16'36.21"	E 07° 17'42.0"
Latitude	N 50° 24'23.05"	N 50° 23'17.95"	N 50° 27'24.00"
wt.%			
SiO_2	42.9	44.4	44.2
TiO_2	2.46	2.54	2.65
Al_2O_3	14.4	15.3	14.5
Fe_2O_3	11.4	10.7	10.7
MnO	0.195	0.203	0.165
MgO	7.52	6.57	8.87
CaO	11.8	10.7	11.2
Na_2O	3.62	3.92	2.78
K_2O	3.12	3.68	3.24
P_2O_5	0.754	0.791	0.63
L.O.I.	1.14	0.124	0.42
Total	99.3	98.9	99.4
Mg#	59.7	58.1	65.1

Table 1 continued

Sample Number	**Ei 22a**	**Ei 23**	**Ei 24**
Locaylity	Rüderbusch	Steffelner Kopf	Goßberg
Classification (Le Mairte, 1984)	Basanite	Basanite	Basanite
Classification (Le Bas 1989)	Melanephelinite	Melanephelinite	Melanephelinite
Age (kyr)	941		153
Age Reference	Novell et al., (2006)		Novell et al., (2006)
Longitude	E 06° 37'42.96"	E 06° 33'27.96"	E 06° 42.'11.94"
Latitude	N 50° 17'42.96"	N 50° 16'59.22"	N 50° 16'25.07"
wt.%			
SiO_2	41.5	41.6	42.9
TiO_2	2.42	2.72	2.40
Al_2O_3	11.0	11.3	11.3
Fe_2O_3	10.5	11.0	9.86
MnO	0.180	0.177	0.156
MgO	10.9	10.2	11.1
CaO	14.0	13.8	13.4
Na_2O	2.54	2.71	2.68
K_2O	3.13	3.82	3.53
P_2O_5	0.693	0.708	0.603
L.O.I.	1.03	1.00	0.250
Total	97.9	99.0	98.1
Mg#	70.2	67.4	71.7

Table 1 continued

Sample Number	**Ei 25**	**Ei 26**	**Ei 27**
Locaylity	Rockeskyller Kopf	Kalem	Sarresdorf Lavaflow
Classification (Le Maitre, 1984)	Basanite	Basanite	Basanite
Classification (Le Bas 1989)	Melanephelinite	Melilitite-Nephelinite	Melanephelinite
Age (kyr)	629	540	320
Age Reference	Novell et al., (2006)	Novell et al., (2006)	Mertz et al., (2015)
Longitude	E 06° 40'36.72"	E 06° 37'51.06"	E 06° 39'4.43"
Latitude	N 50° 15'23.4"	N 50° 11'30.72"	N 50° 13'20.70"
wt.%			
SiO_2	43.6	39.3	43.2
TiO_2	2.45	2.86	2.32
Al_2O_3	11.6	11.8	12.1
Fe_2O_3	10.3	11.8	11.3
MnO	0.169	0.212	0.187
MgO	10.0	9.55	11.5
CaO	12.8	14.9	12.6
Na_2O	2.13	3.24	3.38
K_2O	3.88	2.66	1.51
P_2O_5	0.740	0.990	0.865
L.O.I.	0.850	0.980	1.00
Total	98.5	98.3	99.9
Mg#	68.6	64.5	69.7

Table 1 continued

Sample Number	**Ei 28**	**Ei 29**	**Ei 30**
Locaylity	Fächerhöhe	Wartgensberg	Mosenberg
Classification (Le Maitre, 1984)	Basanite	Basanite	Basanite
Classification (Le Bas 1989)	Melanephelinite	Melanephelinite	Melanephelinite
Age (kyr)	400	500	810
Age Reference	Mertz et al., (2015)	Mertz et al., (2015)	Novell et al., (2006)
Longitude	E 07° 1'13.32"	E 06° 55'54.95"	E 06° 46'36.36"
Latitude	N 50° 4'27.41"	N 50° 6'29.34"	N 50° 4'52.14"
wt.%			
SiO_2	42.6	42.9	41.6
TiO_2	2.30	2.42	2.64
Al_2O_3	11.6	11.3	12.1
Fe_2O_3	11.8	11.9	11.7
MnO	0.174	0.170	0.186
MgO	13.6	13.8	12.1
CaO	11.8	11.1	12.5
Na_2O	2.91	3.01	3.58
K_2O	1.47	1.49	2.02
P_2O_5	0.916	0.839	0.909
L.O.I.	1.00	1.00	1.00
Total	100.2	100.0	100.3
Mg#	72.2	72.2	69.8

Table 1 continued

Sample Number	**Ei 31**	**Ei 32**	**Ei 33**
Locaylity	Auf der Hardt	Am Steinseiter	Sulzbusch
Classification (Le Mairte, 1984)	Basanite	Basanite	Basanite
Classification (Le Bas 1989)	Melanephelinite	Melanephelinite	Melanephelinite
Age (kyr)	476	540	340
Age Reference	Novell et al., (2006)	Novell et al., (2006)	Novell et al., (2006)
Longitude	E 06° 52'5.99"	E 06° 45'41.76"	E 07° 16'44.1"
Latitude	N 50° 11'10.92"	N 50° 13'5.16"	N 50° 21'32.9"
wt.%			
SiO_2	42.1	41.6	44.1
TiO_2	2.46	2.73	2.15
Al_2O_3	11.8	11.6	14.1
Fe_2O_3	10.8	11.2	9.78
MnO	0.168	0.175	0.203
MgO	9.56	9.77	8.94
CaO	14.1	14.4	11.2
Na_2O	2.87	2.68	3.75
K_2O	3.11	3.34	3.37
P_2O_5	0.711	0.654	0.640
L.O.I.	0.280	1.00	0.450
Total	97.9	99.1	98.7
Mg#	66.5	66.3	67.3

Table 1 continued

Sample Number	**Ei 34**	**Ei 36**	**Ei 38**
Locaylity	Sulzbusch	An der Ahl	Etringer Bellerberg
Classification (Le Maitre, 1984)	Basanite	Basanite	Phono-Tephrite
Classification (Le Bas 1989)	Melanephelinite		
Age (kyr)	340	623	300
Age Reference	Novell et al., (2006)	Novell et al., (2006)	Novell et al., (2006)
Longitude	E 07° 16'44.1"	E 07° 11'21.1"	E 07° 13'25.7"
Latitude	N 50° 21'32.9"	N 50° 20'47.3"	N 50° 20'99.8"
wt.%			
SiO_2	44.1	44.5	50.2
TiO_2	2.15	1.87	1.78
Al_2O_3	14.2	16.6	16.6
Fe_2O_3	9.81	9.63	7.50
MnO	0.206	0.253	0.168
MgO	8.91	4.41	4.51
CaO	11.1	9.58	7.77
Na_2O	3.45	5.25	4.66
K_2O	3.15	4.65	4.22
P_2O_5	0.635	0.842	0.415
L.O.I.	1.10	0.360	0.650
Total	98.8	97.9	98.5
Mg#	67.1	50.7	57.4

Table 1 continued

Sample Number	**Ei 39**	**Ei 40**	**Ei 41**
Locaylity	Karmelenberg	Humersberg	Engelner Kopf
Classification (Le Maite, 1984)	Basanite	Basanite	Phonolithe
Classification (Le Bas 1989)	Melanephelinite	Melanephelinite	
Age (kyr)	200		320
Age Reference	Novell et al., (2006)		Novell et al., (2006)
Longitude	E 07° 25'34.3"	E 07° 8'34.1"	E 07° 8'32.5"
Latitude	N 50° 20'47.5"	N 50° 24'29.5"	N 50° 25'33.9"
wt.%			
SiO_2	44.6	44.4	50.4
TiO_2	2.54	2.15	0.399
Al_2O_3	14.4	15.0	21.3
Fe_2O_3	10.5	10.1	3.27
MnO	0.171	0.222	0.216
MgO	8.28	7.23	0.385
CaO	11.0	10.7	1.51
Na_2O	3.37	4.49	8.51
K_2O	3.47	3.60	8.87
P_2O_5	0.642	0.796	0.0690
L.O.I.	0.0400	0.960	1.26
Total	99.0	99.6	96.2
Mg#	63.9	61.7	20.9

Table 1 continued

Sample Number	**Ei 42**	**Ei 43**	**Ei 44**
Locaylity	Schellkopf	Meirother Kopf	Tiefenstein
Classification (Le Maite, 1984)	Phonolithe	Basanite	Basanite
Classification (Le Bas 1989)		Melanephelinite	Melanephelinite
Age (kyr)	380	420	
Age Reference	Novell et al., (2006)	Novell et al., (2006)	
Longitude	E 07° 9'54.5"	E 07° 11'12.0"	E 07° 11'18.1"
Latitude	N 50° 25'75.4"	N 50° 25'9.8"	N 50° 25'27.5
wt.%			
SiO_2	50.7	42.3	42.5
TiO_2	0.267	2.44	2.41
Al_2O_3	21.3	13.2	13.6
Fe_2O_3	2.65	10.3	10.1
MnO	0.219	0.180	0.182
MgO	0.121	10.5	9.40
CaO	1.67	12.5	12.5
Na_2O	8.07	3.35	3.23
K_2O	10.2	3.38	3.69
P_2O_5	0.0290	0.641	0.649
L.O.I.	1.60	0.120	0.550
Total	96.8	98.9	98.8
Mg#	9.31	69.5	67.6

Table 1 continued

Sample Number	**Ei 45**	**Ei 46**	**Ei 47**
Locaylity	Meirother Kopf	An der Hardt	Schorenberg
Classification (Le Maite, 1984)	Basanite	Phonolithe	Basanite
Classification (Le Bas 1989)	Melanephelinite		
Age (kyr)	420	289	287
Age Reference	Novell et al., (2006)	Novell et al., (2006)	Novell et al., (2006)
Longitude	E 07° 11'12.0"	E 7°10'19.3"	E 7°11'01.1"
Latitude	N 50° 25'9.8"	N 50°23'45.1"	N 50°23'39.4"
wt.%			
SiO_2	41.9	47.4	48.1
TiO_2	2.42	0.694	0.892
Al_2O_3	13.5	22.2	18.9
Fe_2O_3	10.3	4.26	5.18
MnO	0.185	0.192	0.200
MgO	9.44	0.533	1.05
CaO	12.5	2.78	5.99
Na_2O	3.37	7.76	5.83
K_2O	3.41	9.37	7.94
P_2O_5	0.654	0.0820	0.319
L.O.I.	0.770	2.33	3.46
Total	98.4	97.6	97.9
Mg#	67.4	21.9	31.2

Table 1 continued

Sample Number	**Ei 48**	**Ei 49a**	**Ei 49b**
Locaylity	Burgberg	Burg Olbrück	Burg Olbrück
Classification (Le Maite, 1984)	Phonolithe	Phonolithe	Phonolithe
Classification (Le Bas 1989)	Phonolithe	Phonolithe	Phonolithe
Age (kyr)	344	374	374
Age Reference	Novell et al., (2006)	Novell et al., (2006)	Novell et al., (2006)
Longitude	E 7°11'39.1"	E 7°09'57.2"	E 7°09'57.2"
Latitude	N 50°23'30.7"	N 50°26'53.2"	N 50°26'53.2"
wt.%			
SiO_2	52.1	52.8	52.5
TiO_2	0.212	0.275	0.262
Al_2O_3	21.4	21.8	21.6
Fe_2O_3	2.76	3.03	2.95
MnO	0.250	0.247	0.235
MgO	0.157	0.110	0.0910
CaO	1.63	0.722	1.49
Na_2O	7.98	7.95	8.01
K_2O	8.72	9.99	9.77
P_2O_5	0.0170	0.0310	0.0230
L.O.I.	3.91	1.60	1.86
Total	99.1	98.6	98.8
Mg#	11.3	7.54	6.48

Table 1 continued

Sample Number	**Ei 50**	**Ei 51**	**Ei 53**
Locaylity	Perler Kopf	Perler Kopf	Kempenich
Classification (Le Maite, 1984)	Foidite	Foidite	Phonolithe
Classification (Le Bas 1989)			
Age (kyr)	374	374	
Age Reference	Novell et al., (2006)	Novell et al., (2006)	
Longitude	E 7°08'32.1"	E 7°08'36.2"	E 7°07'23.5"
Latitude	N 50°27'11.3"	N 50°27'09.1"	N 50°25'22.3"
wt.%			
SiO_2	47.7	46.5	52.4
TiO_2	1.07	1.04	0.392
Al_2O_3	19.0	18.2	21.8
Fe_2O_3	6.83	6.57	3.37
MnO	0.309	0.315	0.228
MgO	1.38	1.29	0.289
CaO	6.39	7.78	1.06
Na_2O	6.71	7.12	7.54
K_2O	5.21	5.36	8.98
P_2O_5	0.497	0.453	0.0800
L.O.I.	3.35	3.62	2.59
Total	98.4	98.2	98.7
Mg#	31.2	30.6	16.2

Table 1 continued

Sample Number	**Ei 55**	**Ei 56**	**Ei 57**
Locaylity	Bräunig Vulkan	NE' Üdersdorf	Emmelberg
Classification (Le Maite, 1984)	Basanite	Basanite	Basanite
Classification (Le Bas 1989)	Melilitithe-Nephelinite	Melilitite-Nephelinite	Melanephelinite
Age (kyr)		510	500
Age Reference		Novell et al., (2006)	Mertz et al., (2015)
Longitude	E 07° 09'29.3"	E 06° 48'40.32"	E 06° 48'24.84"
Latitude	N 50° 24'02.0"	N 50° 9'28.68"	N 50° 8'57.72"
wt.%			
SiO_2	41.1	41.1	41.4
TiO_2	2.16	2.31	2.87
Al_2O_3	12.2	11.1	12.8
Fe_2O_3	10.9	10.7	10.4
MnO	0.200	0.200	0.210
MgO	12.2	11.2	10.8
CaO	13.8	15.7	13.1
Na_2O	3.32	3.21	4.46
K_2O	2.64	2.76	2.16
P_2O_5	0.730	0.757	0.758
L.O.I.	0.480	0.550	0.860
Total	99.7	99.6	99.8
Mg#	71.5	70.1	69.9

Table 1 continued

Sample Number	**Ei 58a**	**Ei 59**	**EI 60**
Locaylity	Leyendecker Quary	Wolfsschlucht	Alte Burg cone
Classification (Le Maite, 1984)	Basanite	Basanite	Basanite
Classification (Le Bas 1989)	Basanite	Melanephelinite	Melanephelinite
Age (kyr)	740	610	
Age Reference	Mertz et al., (2015)	Mertz et al., (2015)	
Longitude	E 06° 44'18.48"	E 06° 48'6.12"	E 07° 17'2.29"
Latitude	N 50° 6'3.71"	N 50° 4'29.34"	N 50° 24'33.44"
wt.%			
SiO_2	44.7	40.8	40.8
TiO_2	2.17	2.37	2.90
Al_2O_3	11.5	11.3	14.4
Fe_2O_3	10.6	12.0	11.6
MnO	0.180	0.200	0.200
MgO	14.1	14.5	7.18
CaO	10.6	12.7	12.1
Na_2O	2.99	3.28	3.26
K_2O	1.18	1.68	3.44
P_2O_5	0.764	0.892	0.629
L.O.I.	- 0.150	- 0.130	0.390
Total	98.6	99.5	96.9
Mg#	74.9	73.2	58.2

Table 1 continued

Sample Number	**EI 61**	**Ei 62**
Locaylity	Lorenzfelsen	Booser Maar
Classification (Le Maite, 1984)	Basanite	
Classification (Le Bas 1989)	Melanephelinite	
Age (kyr)		
Age Reference		
Longitude	E 07° 16'46.94"	E 07° 0'37.01"
Latitude	N 50° 25'22.05"	N 50° 18'54.60"
wt.%		
SiO_2	38.4	nd
TiO_2	3.24	nd
Al_2O_3	13.9	nd
Fe_2O_3	11.5	nd
MnO	0.201	nd
MgO	6.69	nd
CaO	12.6	nd
Na_2O	3.29	nd
K_2O	3.42	nd
P_2O_5	0.670	nd
L.O.I.	5.87	nd
Total	99.7	nd
Mg#	64.1	nd

Table 1 continued

Sample Number	**Ei 2**	**Ei 3**	**Ei 4**
Locaylity	Eppelsberg	Eppelsberg	Herrchenberg
(ppm)			
Sc	35.3	nd	27.8
Cr	228	nd	126
Ni	142	nd	63.6
Cu	76.1	nd	70.7
Zn	84.9	nd	94.6
Rb	98.5	nd	97.6
Sr	839	nd	1225
Y	22.3	nd	26.7
Zr	248	nd	286
Nb	75.9	nd	141
Cs	0.868	nd	0.567
Ba	1112	nd	1363
La	59.8	nd	91.9
Ce	118	nd	177
Pr	13.3	nd	19.9
Nd	50.1	nd	72.2
Sm	8.42	nd	11.3
Eu	2.38	nd	3.14
Gd	6.94	nd	9.03
Tb	0.910	nd	1.14
Dy	4.70	nd	5.66
Ho	0.841	nd	0.999
Er	2.14	nd	2.54
Tm	0.282	nd	0.326
Yb	1.77	nd	2.05
Lu	0.249	nd	0.283
Hf	5.74	nd	5.82
Ta	4.33	nd	7.09
Pb	4.31	nd	5.61
Th	6.32	nd	9.39
U	1.43	nd	2.71
(ppb)			
Re	0.707	nd	1.883
Os	0.037	nd	0.148
Ir	0.061	nd	0.035
Pt	0.797	nd	1.179

Table 2

Sample Number	**Ei 5**	**Ei 6**	**Ei 7**
Locaylity	Herrchenberg	Herrchenberg	Herrchenberg
(ppm)			
Sc	28.5	27.7	26.7
Cr	118	118	123
Ni	67.7	67.0	65.8
Cu	72.2	72.5	104
Zn	94.3	95.7	90.3
Rb	92.0	87.0	107
Sr	1142	1047	1277
Y	27.0	26.7	26.1
Zr	265	262	280
Nb	141	139	136
Cs	1.07	0.680	1.02
Ba	1304	1277	1342
La	90.3	84.5	89.7
Ce	185	173	173
Pr	19.2	18.8	19.4
Nd	69.6	68.0	70.8
Sm	11.0	10.8	11.1
Eu	3.12	3.07	3.08
Gd	8.62	8.50	8.85
Tb	1.10	1.08	1.12
Dy	5.56	5.49	5.55
Ho	1.01	0.990	0.982
Er	2.51	2.48	2.49
Tm	0.340	0.340	0.323
Yb	2.02	2.02	2.01
Lu	0.290	0.290	0.280
Hf	5.94	5.94	5.74
Ta	7.48	7.37	6.95
Pb	5.38	2.78	2.30
Th	9.43	9.38	9.22
U	2.73	2.73	2.65
(ppb)			
Re	nd	nd	nd
Os	nd	nd	nd
Ir	nd	nd	nd
Pt	nd	nd	nd

Table 2 continued

Sample Number	**Ei 8**	**Ei 9**	**Ei 10a**
Locaylity	Upper-Mendig Flow	Bausenberg	Hannebacher Ley
(ppm)			
Sc	17.0	39.0	12.2
Cr	27.3	236	8.97
Ni	29.8	130	18.0
Cu	29.4	84.7	64.7
Zn	98.3	92.8	152
Rb	131	83.7	120
Sr	1673	845	1473
Y	28.5	23.3	43.2
Zr	367	290	363
Nb	131	74.7	304
Cs	1.59	0.796	1.68
Ba	1702	1023	675
La	98.7	57.1	187
Ce	179	115	333
Pr	18.8	13.1	34.2
Nd	64.9	50.4	117
Sm	9.93	8.68	17.2
Eu	2.80	2.47	4.77
Gd	8.14	7.10	13.2
Tb	1.08	0.949	1.67
Dy	5.62	4.96	8.57
Ho	1.04	0.890	1.57
Er	2.77	2.22	4.05
Tm	0.379	0.295	0.560
Yb	2.44	1.84	3.39
Lu	0.353	0.263	0.480
Hf	7.01	6.54	6.44
Ta	6.52	4.40	13.4
Pb	10.3	4.76	10.5
Th	11.8	5.70	21.0
U	2.79	1.29	5.62
(ppb)			
Re	nd	0.491	nd
Os	nd	0.035	nd
Ir	nd	0.058	nd
Pt	nd	0.943	nd

Table 2 continued

Sample Number	**Ei 10b**	**Ei 11 a**	**Ei 12**
Locaylity	Hannebacher Ley	Schorberg	Leitenberg
(ppm)			
Sc	11.9	34.6	32.7
Cr	10.5	317	97.7
Ni	20.5	136	63.6
Cu	77.3	94.5	72.9
Zn	134	90.2	99.3
Rb	103	92.6	72.0
Sr	2149	1062	1254
Y	41.7	23.5	27.6
Zr	388	252	322
Nb	264	105	143
Cs	1.48	1.24	0.595
Ba	804	962	1078
La	181	71.9	91.0
Ce	327	137	178
Pr	34.2	14.7	19.8
Nd	119	54.4	73.3
Sm	17.1	8.84	11.6
Eu	4.68	2.45	3.21
Gd	13.3	7.19	9.15
Tb	1.68	0.943	1.17
Dy	8.45	4.86	5.86
Ho	1.52	0.875	1.04
Er	3.90	2.23	2.58
Tm	0.522	0.300	0.342
Yb	3.27	1.89	2.11
Lu	0.459	0.273	0.302
Hf	6.23	5.49	6.63
Ta	12.0	4.89	7.23
Pb	1.81	5.81	3.15
Th	19.8	8.22	9.82
U	5.93	2.55	2.77
(ppb)			
Re	nd	nd	0.067
Os	nd	nd	0.012
Ir	nd	nd	0.016
Pt	nd	nd	0.331

Table 2 continued

Sample Number	**Ei 13**	**Ei 14**	**Ei 15**
Locaylity	Hohe Buche	Plaidter Hummerich	Nettetal
(ppm)			
Sc	40.1	32.7	33.1
Cr	264	145	155
Ni	128	108	90.8
Cu	68.9	65.2	59.9
Zn	89.5	99.3	96.1
Rb	93.7	98.0	97.6
Sr	830	1003	974
Y	22.9	26.0	24.9
Zr	296	309	318
Nb	71.6	87.0	84.1
Cs	0.768	1.10	0.927
Ba	1063	1183	1125
La	60.7	69.6	71.8
Ce	122	135	139
Pr	13.8	15.2	15.3
Nd	52.6	57.0	56.9
Sm	8.90	9.61	9.34
Eu	2.49	2.70	2.62
Gd	7.19	7.84	7.55
Tb	0.946	1.04	0.994
Dy	4.88	5.40	5.13
Ho	0.867	0.971	0.923
Er	2.17	2.46	2.36
Tm	0.287	0.332	0.321
Yb	1.78	2.08	1.99
Lu	0.255	0.295	0.289
Hf	6.79	6.74	6.84
Ta	4.14	5.08	4.77
Pb	4.68	4.50	6.57
Th	5.95	7.31	7.35
U	1.36	1.67	1.37
(ppb)			
Re	nd	nd	nd
Os	nd	nd	nd
Ir	nd	nd	nd
Pt	nd	nd	nd

Table 2 continued

Sample Number	**Ei 16b**	**Ei 17**	**Ei 18**
Locaylity	Rothenberg	Lower-Mendig Flow	Eppelsberg Coarse
(ppm)			
Sc	35.3	23.5	29.8
Cr	235	60.1	87.9
Ni	126	53.4	67.0
Cu	88.2	41.8	56.9
Zn	94.7	113	104
Rb	94.0	96.9	77.4
Sr	971	1185	1066
Y	24.7	31.6	28.8
Zr	323	360	333
Nb	87.0	122	104
Cs	0.896	1.20	0.900
Ba	1132	1196	1018
La	70.3	88.2	74.7
Ce	136	177	154
Pr	14.9	19.3	17.1
Nd	55.7	70.3	63.6
Sm	9.24	11.5	10.6
Eu	2.60	3.30	3.10
Gd	7.51	9.20	8.60
Tb	0.990	1.20	1.10
Dy	5.12	6.30	5.90
Ho	0.918	1.20	1.10
Er	2.32	3.00	2.70
Tm	0.315	0.400	0.400
Yb	1.98	2.50	2.30
Lu	0.285	0.400	0.300
Hf	6.99	8.10	8.00
Ta	4.95	7.60	6.50
Pb	5.68	7.30	6.10
Th	7.26	10.1	8.20
U	1.69	2.30	1.90
(ppb)			
Re	0.82	nd	nd
Os	0.194	nd	nd
Ir	0.046	nd	nd
Pt	1.27	nd	nd

Table 2 continued

Sample Number	**Ei 19**	**Ei 20**	**Ei 21**
Locaylity	Eppelsberg Dike	Lower-Mendig Flow	relict flow, Hill W' Jägerheim
(ppm)			
Sc	26.8	23.5	32.3
Cr	120	61.3	130
Ni	83.0	55.5	88.5
Cu	56.8	42.1	58.6
Zn	109	114	87.7
Rb	106	95.4	91.0
Sr	1030	1173	858
Y	27.4	31.6	23.5
Zr	294	357	277
Nb	105	121	77.2
Cs	1.10	1.20	0.900
Ba	1033	1202	1196
La	74.5	85.4	58.4
Ce	151	173	120
Pr	16.6	19.0	13.4
Nd	60.6	69.3	49.8
Sm	9.90	11.4	8.50
Eu	2.90	3.30	2.50
Gd	8.00	9.10	6.90
Tb	1.00	1.20	0.900
Dy	5.50	6.30	4.80
Ho	1.00	1.20	0.900
Er	2.60	3.00	2.20
Tm	0.400	0.400	0.300
Yb	2.20	2.50	1.80
Lu	0.300	0.400	0.300
Hf	7.00	8.20	7.00
Ta	6.30	7.50	4.70
Pb	2.20	7.40	6.00
Th	8.90	10.1	6.40
U	2.00	2.30	1.40
(ppb)			
Re	nd	0.866	nd
Os	nd	0.012	nd
Ir	nd	0.013	nd
Pt	nd	0.056	nd

Table 2 continued

Sample Number	**Ei 22a**	**Ei 23**	**Ei 24**
Locaylity	Rüderbusch	Steffelner Kopf	Goßberg
(ppm)			
Sc	32.5	37.6	36.2
Cr	455	282	474
Ni	176	124	169
Cu	109	143	105
Zn	77.2	81.3	71.7
Rb	104	110	103
Sr	951	859	830
Y	20.3	19.8	18.6
Zr	271	260	216
Nb	100	86.1	88.3
Cs	0.964	1.02	0.982
Ba	1208	1215	1202
La	77.0	62.8	63.8
Ce	149	130	127
Pr	16.3	14.8	13.9
Nd	61.0	57.2	52.8
Sm	9.47	9.28	8.37
Eu	2.68	2.65	2.39
Gd	7.23	7.13	6.48
Tb	0.905	0.898	0.820
Dy	4.45	4.43	4.06
Ho	0.777	0.762	0.711
Er	1.93	1.88	1.78
Tm	0.256	0.245	0.238
Yb	1.57	1.50	1.46
Lu	0.234	0.219	0.217
Hf	6.08	6.13	4.93
Ta	5.14	4.89	4.50
Pb	6.75	5.82	4.89
Th	8.18	6.13	7.72
U	1.94	1.53	1.98
(ppb)			
Re	0.609	nd	nd
Os	0.023	nd	nd
Ir	0.01	nd	nd
Pt	1.828	nd	nd

Table 2 continued

Sample Number	**Ei 25**	**Ei 26**	**Ei 27**
Locaylity	Rockeskyller Kopf	Kalem	Sarresdorf Lavaflow
(ppm)			
Sc	32.6	34.5	25.7
Cr	368	189	417
Ni	149	88.0	227
Cu	107	129	64.5
Zn	78.3	94.6	94.3
Rb	123	80.1	49.4
Sr	896	910	1195
Y	20.9	27.2	29.5
Zr	291	315	227
Nb	91.9	131	98.0
Cs	1.22	1.13	0.915
Ba	1192	1142	963
La	77.6	92.4	93.5
Ce	147	179	165
Pr	16.2	20.3	17.2
Nd	60.8	78.0	63.9
Sm	9.52	12.6	10.9
Eu	2.68	3.56	3.29
Gd	7.31	9.69	9.18
Tb	0.928	1.22	1.22
Dy	4.60	6.01	6.25
Ho	0.799	1.04	1.10
Er	2.00	2.56	2.72
Tm	0.265	0.334	0.360
Yb	1.64	2.04	2.20
Lu	0.242	0.296	0.324
Hf	6.79	7.20	4.80
Ta	4.92	7.44	4.25
Pb	7.60	6.58	5.12
Th	8.93	9.12	9.73
U	1.89	2.42	3.54
(ppb)			
Re	nd	1.178	0.452
Os	nd	0.06	0.052
Ir	nd	0.008	0.039
Pt	nd	0.158	0.7

Table 2 continued

Sample Number	**Ei 28**	**Ei 29**	**Ei 30**
Locaylity	Fächerhöhe	Wartgensberg	Mosenberg
(ppm)			
Sc	29.2	26.1	27.4
Cr	536	527	402
Ni	286	315	221
Cu	72.6	72.7	62.8
Zn	88.1	92.6	94.9
Rb	41.5	38.5	61.3
Sr	941	894	1096
Y	25.1	24.6	29.0
Zr	212	213	259
Nb	75.8	75.6	113
Cs	0.754	0.606	0.955
Ba	770	746	1006
La	76.6	73.3	89.2
Ce	138	132	162
Pr	14.5	13.8	17.3
Nd	55.3	52.6	65.4
Sm	9.61	9.35	11.3
Eu	2.89	2.86	3.39
Gd	8.10	7.99	9.35
Tb	1.07	1.06	1.23
Dy	5.47	5.40	6.27
Ho	0.952	0.938	1.09
Er	2.35	2.28	2.69
Tm	0.308	0.296	0.352
Yb	1.87	1.80	2.15
Lu	0.275	0.261	0.312
Hf	4.60	4.68	5.37
Ta	3.90	3.83	5.58
Pb	4.11	4.32	4.69
Th	8.36	8.10	10.0
U	2.02	2.07	2.46
(ppb)			
Re	nd	0.23	nd
Os	nd	0.043	nd
Ir	nd	0.033	nd
Pt	nd	0.471	nd

Table 2 continued

Sample Number	**Ei 31**	**Ei 32**	**Ei 33**
Locaylity	Auf der Hardt	Am Steinseiter	Sulzbusch
(ppm)			
Sc	37.2	37.0	23.6
Cr	290	293	243
Ni	110	115	132
Cu	152	123	43.8
Zn	80.3	81.1	88.6
Rb	89.0	97.8	94.2
Sr	880	821	1365
Y	21.3	20.8	27.3
Zr	242	238	249
Nb	98.3	93.0	140
Cs	0.889	1.02	1.51
Ba	1032	1078	1082
La	71.8	58.8	116
Ce	140	122	202
Pr	15.8	14.1	21.2
Nd	60.2	55.3	74.0
Sm	9.67	9.29	11.0
Eu	2.72	2.66	3.11
Gd	7.42	7.26	8.86
Tb	0.945	0.929	1.14
Dy	4.68	4.62	5.84
Ho	0.814	0.793	1.06
Er	2.04	1.97	2.76
Tm	0.271	0.260	0.380
Yb	1.68	1.59	2.39
Lu	0.246	0.237	0.360
Hf	5.52	5.63	5.15
Ta	5.13	4.74	6.18
Pb	5.85	4.61	8.20
Th	7.81	6.38	12.4
U	2.07	1.70	2.95
(ppb)			
Re	nd	nd	nd
Os	nd	nd	nd
Ir	nd	nd	nd
Pt	nd	nd	nd

Table 2 continued

Sample Number	**Ei 34**	**Ei 36**	**Ei 38**
Locaylity	Sulzbusch	An der Ahl	Etringer Bellerberg
(ppm)			
Sc	23.3	9.24	18.3
Cr	247	40.4	60.1
Ni	134	23.2	41.9
Cu	45.8	29.0	33.9
Zn	94.8	113	88.4
Rb	96.5	111	133
Sr	1387	2227	1059
Y	27.0	36.4	25.3
Zr	245	312	363
Nb	138	207	99.8
Cs	1.52	2.07	2.28
Ba	1092	1006	1227
La	116	172	84.7
Ce	203	297	147
Pr	21.0	30.3	15.1
Nd	72.9	103	52.7
Sm	10.9	14.6	8.37
Eu	3.07	4.06	2.40
Gd	8.74	11.5	7.00
Tb	1.13	1.48	0.950
Dy	5.77	7.56	5.09
Ho	1.05	1.39	0.960
Er	2.74	3.69	2.60
Tm	0.380	0.520	0.390
Yb	2.37	3.23	2.54
Lu	0.360	0.470	0.390
Hf	5.07	5.77	6.91
Ta	6.10	8.75	4.47
Pb	7.65	13.0	10.4
Th	12.4	17.0	13.7
U	3.19	5.05	3.39
(ppb)			
Re	nd	nd	nd
Os	nd	nd	nd
Ir	nd	nd	nd
Pt	nd	nd	nd

Table 2 continued

Sample Number	**Ei 39**	**Ei 40**	**Ei 41**
Locaylity	Karmelenberg	Humersberg	Engelner Kopf
(ppm)			
Sc	27.9	17.7	1.02
Cr	125	141	12.7
Ni	82.8	88.1	1.44
Cu	55.2	61.5	5.16
Zn	86.6	101	86.0
Rb	91.2	101	120
Sr	941	1676	627
Y	24.8	30.9	17.5
Zr	306	273	519
Nb	84.7	153	314
Cs	1.05	1.78	3.11
Ba	1148	1241	796
La	72.3	128	45.8
Ce	139	228	75.8
Pr	15.7	24.0	9.29
Nd	58.5	84.3	30.3
Sm	9.76	12.6	4.63
Eu	2.86	3.54	1.41
Gd	8.08	10.1	3.77
Tb	1.06	1.30	0.570
Dy	5.45	6.57	3.38
Ho	0.980	1.20	0.690
Er	2.54	3.11	2.09
Tm	0.360	0.440	0.350
Yb	2.18	2.68	2.47
Lu	0.330	0.400	0.390
Hf	6.74	5.37	5.77
Ta	4.89	6.92	5.25
Pb	6.71	6.84	14.6
Th	9.17	12.9	22.5
U	2.09	3.54	5.01
(ppb)			
Re	nd	nd	nd
Os	nd	nd	nd
Ir	nd	nd	nd
Pt	nd	nd	nd

Table 2 continued

Sample Number	**Ei 42**	**Ei 43**	**Ei 44**
Locaylity	Schellkopf	Meirother Kopf	Tiefenstein
(ppm)			
Sc	0.670	29.9	31.0
Cr	8.17	241	221
Ni	0.450	114	97.9
Cu	4.11	64.0	69.5
Zn	90.6	79.2	88.0
Rb	185	91.4	94.7
Sr	676	1006	1059
Y	15.8	23.2	26.3
Zr	589	261	262
Nb	230	110	125
Cs	3.69	1.21	1.30
Ba	309	1107	1217
La	56.5	83.8	84.8
Ce	85.0	158	166
Pr	9.17	17.2	17.6
Nd	27.3	63.3	63.0
Sm	3.79	10.1	10.0
Eu	1.12	2.89	2.80
Gd	3.11	8.16	8.00
Tb	0.480	1.05	1.00
Dy	2.85	5.30	5.30
Ho	0.610	0.920	1.00
Er	1.87	2.39	2.50
Tm	0.320	0.330	0.300
Yb	2.28	2.03	2.00
Lu	0.370	0.310	0.300
Hf	6.87	5.78	6.20
Ta	4.12	5.84	6.70
Pb	21.5	6.79	5.00
Th	27.0	10.3	11.1
U	8.19	2.73	2.90
(ppb)			
Re	nd	nd	nd
Os	nd	nd	nd
Ir	nd	nd	nd
Pt	nd	nd	nd

Table 2 continued

Sample Number	**Ei 45**	**Ei 46**	**Ei 47**
Locaylity	Meirother Kopf	An der Hardt	Schorenberg
(ppm)			
Sc	29.6	2.46	4.00
Cr	221	1.41	5.37
Ni	99.8	3.32	3.34
Cu	69.6	4.82	8.99
Zn	81.1	110	113
Rb	94.7	150	136
Sr	1063	1460	1964
Y	24.8	19.7	28.0
Zr	268	359	347
Nb	119	187	211
Cs	1.29	2.17	2.45
Ba	1232	1796	1514
La	90.5	81.8	113
Ce	169	136	202
Pr	18.4	12.5	19.6
Nd	67.0	37.3	63.9
Sm	10.6	4.99	9.00
Eu	3.00	1.47	2.52
Gd	8.52	4.05	7.03
Tb	1.10	0.570	0.940
Dy	5.52	3.27	5.03
Ho	0.990	0.680	0.990
Er	2.53	2.00	2.74
Tm	0.350	0.310	0.410
Yb	2.17	2.06	2.61
Lu	0.330	0.310	0.380
Hf	5.86	4.87	5.24
Ta	6.06	5.06	6.81
Pb	5.15	14.8	13.8
Th	11.3	18.6	19.6
U	2.93	1.57	2.98
(ppb)			
Re	nd	nd	nd
Os	nd	nd	nd
Ir	nd	nd	nd
Pt	nd	nd	nd

Table 2 continued

Sample Number	**Ei 48**	**Ei 49a**	**Ei 49b**
Locaylity	Burgberg	Burg Olbrück	Burg Olbrück
(ppm)			
Sc	3.75	3.52	3.55
Cr	1.42	1.12	2.63
Ni	0.500	0.380	0.600
Cu	0.220	0.330	2.56
Zn	141	149	136
Rb	187	216	193
Sr	806	654	792
Y	15.3	20.0	21.7
Zr	657	599	607
Nb	216	251	253
Cs	4.24	3.97	3.83
Ba	226	355	280
La	80.4	71.2	70.1
Ce	128	119	119
Pr	10.4	10.6	10.4
Nd	27.5	29.8	29.1
Sm	3.16	3.95	3.92
Eu	0.880	1.16	1.15
Gd	2.57	3.35	3.33
Tb	0.360	0.520	0.520
Dy	2.15	3.21	3.27
Ho	0.470	0.710	0.730
Er	1.54	2.31	2.39
Tm	0.270	0.400	0.410
Yb	2.02	2.78	2.92
Lu	0.330	0.430	0.450
Hf	8.39	7.46	7.55
Ta	2.78	3.64	3.67
Pb	29.7	25.7	26.1
Th	32.6	31.7	32.9
U	7.97	6.57	9.59
(ppb)			
Re	nd	nd	nd
Os	nd	nd	nd
Ir	nd	nd	nd
Pt	nd	nd	nd

Table 2 continued

Sample Number	**Ei 50**	**Ei 51**	**Ei 53**
Locaylity	Perler Kopf	Perler Kopf	Kempenich
(ppm)			
Sc	5.38	5.10	3.10
Cr	4.67	4.00	3.00
Ni	2.66	2.20	1.40
Cu	8.15	7.20	2.10
Zn	172	186	121
Rb	114	89.9	161
Sr	1657	1954	781
Y	39.7	37.9	18.3
Zr	615	584	501
Nb	310	298	364
Cs	3.96	3.70	3.10
Ba	1329	1252	760
La	157	142	45.9
Ce	278	264	82.1
Pr	28.5	26.5	9.50
Nd	95.1	88.2	30.3
Sm	13.6	12.7	4.50
Eu	3.71	3.50	1.30
Gd	10.5	9.80	3.70
Tb	1.37	1.30	0.600
Dy	7.27	6.90	3.40
Ho	1.40	1.30	0.700
Er	3.84	3.60	2.10
Tm	0.570	0.500	0.400
Yb	3.61	3.50	2.40
Lu	0.530	0.500	0.400
Hf	8.59	8.20	5.90
Ta	10.6	10.1	9.20
Pb	27.0	25.5	16.8
Th	34.2	32.6	25.7
U	4.87	4.50	6.30
(ppb)			
Re	nd	nd	nd
Os	nd	nd	nd
Ir	nd	nd	nd
Pt	nd	nd	nd

Table 2 continued

Sample Number	**Ei 55**	**Ei 56**	**Ei 57**
Locaylity	Bräunig Vulkan	NE' Üdersdorf	Emmelberg
(ppm)			
Sc	32.4	34.9	29.3
Cr	434	449	389
Ni	222	159	152
Cu	51.0	105	33.5
Zn	97.5	101	105
Rb	73.6	82.5	72.6
Sr	1220	1025	1367
Y	26.2	22.4	30.3
Zr	245	232	296
Nb	115	102	151
Cs	1.00	0.700	1.10
Ba	882	1163	1454
La	87.6	75.8	97.2
Ce	175	158	186
Pr	18.2	16.8	18.7
Nd	64.9	61.3	66.8
Sm	10.2	9.70	11.2
Eu	2.90	2.80	3.30
Gd	8.10	7.50	9.30
Tb	1.00	0.900	1.20
Dy	5.30	4.70	6.20
Ho	1.00	0.800	1.10
Er	2.40	2.00	2.80
Tm	0.300	0.300	0.400
Yb	2.00	1.60	2.20
Lu	0.300	0.200	0.300
Hf	5.70	5.20	6.10
Ta	5.80	5.60	7.60
Pb	4.20	6.90	8.50
Th	9.10	9.40	14.9
U	2.60	2.50	5.30
(ppb)			
Re	nd	0.36	0.573
Os	nd	0.052	0.02
Ir	nd	0.238	0.03
Pt	nd	16.95	0.797

Table 2 continued

Sample Number	**Ei 58a**	**Ei 59**	**EI 60**
Locaylity	Leyendecker Quary	Wolfsschlucht	Alte Burg cone
(ppm)			
Sc	25.3	26.4	29.2
Cr	554	580	98.9
Ni	384	350	68.0
Cu	40.7	65.4	55.9
Zn	85.9	101	98.6
Rb	81.7	55.2	85.2
Sr	931	1100	943
Y	24.8	27.5	25.2
Zr	199	239	279
Nb	94.4	112	92.0
Cs	2.40	0.800	1.00
Ba	655	855	1074
La	75.2	81.0	63.8
Ce	150	160	135
Pr	15.3	16.3	14.4
Nd	55.6	59.8	53.4
Sm	9.50	10.3	8.90
Eu	2.70	3.10	2.60
Gd	7.90	8.70	7.30
Tb	1.00	1.10	1.00
Dy	5.10	5.70	5.10
Ho	0.900	1.00	0.900
Er	2.30	2.50	2.40
Tm	0.300	0.300	0.300
Yb	1.80	1.90	2.00
Lu	0.300	0.300	0.300
Hf	4.40	5.30	6.80
Ta	5.00	5.90	5.70
Pb	5.60	4.60	5.40
Th	10.4	10.9	7.80
U	2.40	2.70	1.90
(ppb)			
Re	nd	0.296	nd
Os	nd	0.051	nd
Ir	nd	0.125	nd
Pt	nd	1.489	nd

Table 2 continued

Sample Number	**EI 61**	**Ei 62**
Locaylity	Lorenzfelsen	Booser Maar
(ppm)		
Sc	29.8	28.3
Cr	21.4	
Ni	32.7	
Cu	92.6	57.3
Zn	95.5	101
Rb	84.5	46.4
Sr	1105	792
Y	28.5	26.4
Zr	305	225
Nb	108	79.3
Cs	1.10	0.663
Ba	965	683
La	71.7	55.0
Ce	153	103
Pr	16.5	11.7
Nd	61.7	44.9
Sm	10.5	8.70
Eu	3.10	2.71
Gd	8.60	7.71
Tb	1.10	1.060
Dy	5.80	5.50
Ho	1.10	0.981
Er	2.70	2.41
Tm	0.400	0.321
Yb	2.20	1.85
Lu	0.300	0.262
Hf	7.20	5.25
Ta	6.80	4.29
Pb	5.00	4.26
Th	8.10	6.80
U	1.80	1.70
(ppb)		
Re	nd	nd
Os	nd	nd
Ir	nd	nd
Pt	nd	nd

Table 2 continued

Sample Number	**Ei 2**	**Ei 3**	**Ei 4**
Locaylity	Eppelsberg	Eppelsberg	Herrchenberg
wt. %			
Quartz	0	0	0
Plagioclase (wt.%)	15.5	13.6	8.51
Orthoclase (wt.%)	0	0	0
Nepheline (Foid) (wt.%)	12.8	16.9	18.3
Leucite (Foid) (wt.%)	15.7	13.9	18.3
Kalsilite (wt.%)	0	0	0
Corundum (wt.%)	0	0	0
Diopside (CPx) (wt.%)	29.9	33.5	11.6
Hypersthene (OPx) (wt.%)	0	0	0
Wollastonite (wt.%)	0	0	0
Olivine (wt.%)	16.2	12.8	20.2
Larnite (wt.%)	1.62	0.8	13.7
Acmite (wt.%)	0	0	0
K2SiO3 (wt.%)	0	0	0
Na2SiO3 (wt.%)	0	0	0
Rutile (wt.%)	0	0	0
Ilmenite (wt.%)	5.41	5.36	6.13
Magnetite (wt.%)	1.68	1.71	1.71
Hematite (wt.%)	0	0	0
Apatite (wt.%)	1.2	1.46	1.58
Zircon (wt.%)	0	0	0
Perovskite (wt.%)	0	0	0
Chromite (wt.%)	0	0	0
Sphene (wt.%)	0	0	0
Pyrite (wt.%)	0	0	0
Halite (wt.%)	0	0	0
Fluorite (wt.%)	0	0	0
Anhydrite (wt.%)	0	0	0
Na2SO4 (wt.%)	0	0	0
Calcite (wt.%)	0	0	0
Na2CO3 (wt.%)	0	0	0
Total (wt.%)	100	100	100
Anorthite	15.5	13.6	8.51
Albite	0	0	0
Orthoclase	0	0	0
Diopside (CPx)	29.9	33.5	11.6
Hypersthene (OPx)	0	1	2
Olivine	16.2	12.8	20.2

Table 3

Sample Number	**Ei 5**	**Ei 6**	**Ei 7**
Locaylity	Herrchenberg	Herrchenberg	Herrchenberg
wt. %			
Quartz	0	0	0
Plagioclase (wt.%)	8.3	8.76	8.61
Orthoclase (wt.%)	0	0	0
Nepheline (Foid) (wt.%)	18.3	18.2	17.6
Leucite (Foid) (wt.%)	18.5	18	19.3
Kalsilite (wt.%)	0	0	0
Corundum (wt.%)	0	0	0
Diopside (CPx) (wt.%)	10.5	11.8	8.86
Hypersthene (OPx) (wt.%)	0	0	0
Wollastonite (wt.%)	0	0	0
Olivine (wt.%)	20.8	20.2	21.4
Larnite (wt.%)	14.2	13.7	15
Acmite (wt.%)	0	0	0
K2SiO3 (wt.%)	0	0	0
Na2SiO3 (wt.%)	0	0	0
Rutile (wt.%)	0	0	0
Ilmenite (wt.%)	6.06	6.1	6
Magnetite (wt.%)	1.7	1.68	1.68
Hematite (wt.%)	0	0	0
Apatite (wt.%)	1.58	1.58	1.62
Zircon (wt.%)	0	0	0
Perovskite (wt.%)	0	0	0
Chromite (wt.%)	0	0	0
Sphene (wt.%)	0	0	0
Pyrite (wt.%)	0	0	0
Halite (wt.%)	0	0	0
Fluorite (wt.%)	0	0	0
Anhydrite (wt.%)	0	0	0
Na2SO4 (wt.%)	0	0	0
Calcite (wt.%)	0	0	0
Na2CO3 (wt.%)	0	0	0
Total (wt.%)	100	100	100
Anorthite	8.3	8.76	8.61
Albite	0	0	0
Orthoclase	0	0	0
Diopside (CPx)	10.5	11.8	8.86
Hypersthene (OPx)	3	4	5
Olivine	20.8	20.2	21.4

Table 3 continued

Sample Number	**Ei 8**	**Ei 9**	**Ei 10a**
Locaylity	Upper-Mendig Flow	Bausenberg	Hannebacher Ley
wt. %			
Quartz	0	0	0
Plagioclase (wt.%)	13.4	15.7	4.62
Orthoclase (wt.%)	27.5	0.85	0
Nepheline (Foid) (wt.%)	21.1	13	27.1
Leucite (Foid) (wt.%)	0	14.2	18.3
Kalsilite (wt.%)	0	0	0
Corundum (wt.%)	0	0	0
Diopside (CPx) (wt.%)	25.6	33.9	30.2
Hypersthene (OPx) (wt.%)	0	0	0
Wollastonite (wt.%)	0	0	0
Olivine (wt.%)	5.88	14.2	7.33
Larnite (wt.%)	0	0	3.38
Acmite (wt.%)	0	0	0
K2SiO3 (wt.%)	0	0	0
Na2SiO3 (wt.%)	0	0	0
Rutile (wt.%)	0	0	0
Ilmenite (wt.%)	4.03	5.26	4.44
Magnetite (wt.%)	1.29	1.62	1.74
Hematite (wt.%)	0	0	0
Apatite (wt.%)	1.27	1.25	2.94
Zircon (wt.%)	0	0	0
Perovskite (wt.%)	0	0	0
Chromite (wt.%)	0	0	0
Sphene (wt.%)	0	0	0
Pyrite (wt.%)	0	0	0
Halite (wt.%)	0	0	0
Fluorite (wt.%)	0	0	0
Anhydrite (wt.%)	0	0	0
Na2SO4 (wt.%)	0	0	0
Calcite (wt.%)	0	0	0
Na2CO3 (wt.%)	0	0	0
Total (wt.%)	100	100	100
Anorthite	10.8	15.7	4.62
Albite	2.6	0	0
Orthoclase	27.5	0.85	0
Diopside (CPx)	25.6	33.9	30.2
Hypersthene (OPx)	0	0	0
Olivine	5.88	14.2	7.33

Table 3 continued

Sample Number **Locaylity**	**Ei 10b** Hannebacher Ley	**Ei 11 a** Schorberg	**Ei 12** Leitenberg
wt. %			
Quartz	0	0	0
Plagioclase (wt.%)	0.83	13.7	11.3
Orthoclase (wt.%)	0	4.72	0
Nepheline (Foid) (wt.%)	29	14.9	15.7
Leucite (Foid) (wt.%)	20.4	11.9	16
Kalsilite (wt.%)	0	0	0
Corundum (wt.%)	0	0	0
Diopside (CPx) (wt.%)	19.6	33.9	27.2
Hypersthene (OPx) (wt.%)	0	0	0
Wollastonite (wt.%)	0	0	0
Olivine (wt.%)	11.2	14	17.7
Larnite (wt.%)	10.1	0	4.35
Acmite (wt.%)	0	0	0
K2SiO3 (wt.%)	0	0	0
Na2SiO3 (wt.%)	0	0	0
Rutile (wt.%)	0	0	0
Ilmenite (wt.%)	4.24	4.25	4.73
Magnetite (wt.%)	1.65	1.52	1.52
Hematite (wt.%)	0	0	0
Apatite (wt.%)	2.94	1.25	1.53
Zircon (wt.%)	0	0	0
Perovskite (wt.%)	0	0	0
Chromite (wt.%)	0	0	0
Sphene (wt.%)	0	0	0
Pyrite (wt.%)	0	0	0
Halite (wt.%)	0	0	0
Fluorite (wt.%)	0	0	0
Anhydrite (wt.%)	0	0	0
Na2SO4 (wt.%)	0	0	0
Calcite (wt.%)	0	0	0
Na2CO3 (wt.%)	0	0	0
Total (wt.%)	100	100	100
Anorthite	0.83	13.7	11.3
Albite	0	0	0
Orthoclase	0	4.72	0
Diopside (CPx)	19.6	33.9	27.2
Hypersthene (OPx)	0	0	0
Olivine	11.2	14	17.7

Table 3 continued

Sample Number	**Ei 13**	**Ei 14**	**Ei 15**
Locaylity	Hohe Buche	Plaidter Hummerich	Nettetal
wt. %			
Quartz	0	0	0
Plagioclase (wt.%)	15.5	14.6	15.7
Orthoclase (wt.%)	2.17	11.6	10.5
Nepheline (Foid) (wt.%)	13.2	15.2	14.9
Leucite (Foid) (wt.%)	12	6.73	7.95
Kalsilite (wt.%)	0	0	0
Corundum (wt.%)	0	0	0
Diopside (CPx) (wt.%)	33.5	29.7	29.1
Hypersthene (OPx) (wt.%)	0	0	0
Wollastonite (wt.%)	0	0	0
Olivine (wt.%)	15.2	13.8	13.6
Larnite (wt.%)	0	0	0
Acmite (wt.%)	0	0	0
K2SiO3 (wt.%)	0	0	0
Na2SiO3 (wt.%)	0	0	0
Rutile (wt.%)	0	0	0
Ilmenite (wt.%)	5.41	5.13	5.03
Magnetite (wt.%)	1.65	1.61	1.59
Hematite (wt.%)	0	0	0
Apatite (wt.%)	1.37	1.55	1.58
Zircon (wt.%)	0	0	0
Perovskite (wt.%)	0	0	0
Chromite (wt.%)	0	0	0
Sphene (wt.%)	0	0	0
Pyrite (wt.%)	0	0	0
Halite (wt.%)	0	0	0
Fluorite (wt.%)	0	0	0
Anhydrite (wt.%)	0	0	0
Na2SO4 (wt.%)	0	0	0
Calcite (wt.%)	0	0	0
Na2CO3 (wt.%)	0	0	0
Total (wt.%)	100	100	100
Anorthite	15.5	14.6	15.7
Albite	0	0	0
Orthoclase	2.17	11.6	10.5
Diopside (CPx)	33.5	29.7	29.1
Hypersthene (OPx)	0	0	0
Olivine	15.2	13.8	13.6

Table 3 continued

Sample Number	**Ei 16b**	**Ei 17**	**Ei 18**
Locaylity	Rothenberg	Lower-Mendig Flow	Eppelsberg
wt. %			
Quartz	0	0	0
Plagioclase (wt.%)	16.4	13.1	14.1
Orthoclase (wt.%)	19.9	14.5	1.39
Nepheline (Foid) (wt.%)	13.2	19	16.6
Leucite (Foid) (wt.%)	0	5.93	13.7
Kalsilite (wt.%)	0	0	0
Corundum (wt.%)	0	0	0
Diopside (CPx) (wt.%)	20.7	29.2	34.3
Hypersthene (OPx) (wt.%)	0	0	0
Wollastonite (wt.%)	0	0	0
Olivine (wt.%)	17.1	9.76	11.2
Larnite (wt.%)	0	0	0
Acmite (wt.%)	0	0	0
K2SiO3 (wt.%)	0	0	0
Na2SiO3 (wt.%)	0	0	0
Rutile (wt.%)	0	0	0
Ilmenite (wt.%)	5.03	4.94	5.32
Magnetite (wt.%)	1.55	1.59	1.73
Hematite (wt.%)	0	0	0
Apatite (wt.%)	6.14	1.88	1.71
Zircon (wt.%)	0	0	0
Perovskite (wt.%)	0	0	0
Chromite (wt.%)	0	0	0
Sphene (wt.%)	0	0	0
Pyrite (wt.%)	0	0	0
Halite (wt.%)	0	0	0
Fluorite (wt.%)	0	0	0
Anhydrite (wt.%)	0	0	0
Na2SO4 (wt.%)	0	0	0
Calcite (wt.%)	0	0	0
Na2CO3 (wt.%)	0	0	0
Total (wt.%)	100	100	100
Anorthite	13.3	13.1	14.1
Albite	3.15	0	0
Orthoclase	19.9	14.5	1.39
Diopside (CPx)	20.7	29.2	34.3
Hypersthene (OPx)	0	0	0
Olivine	17.1	9.76	11.2

Table 3 continued

Sample Number	**Ei 19**	**Ei 20**	**Ei 21**
Locaylity	Eppelsberg (dike)	Lower-Mendig Flow	relict flow. Hill W' Jägerheim
wt. %			
Quartz	0	0	0
Plagioclase (wt.%)	14.3	13.7	17.9
Orthoclase (wt.%)	3.23	14.3	13.6
Nepheline (Foid) (wt.%)	17.1	18.4	13
Leucite (Foid) (wt.%)	12.3	6.25	4.69
Kalsilite (wt.%)	0	0	0
Corundum (wt.%)	0	0	0
Diopside (CPx) (wt.%)	33.3	28.7	28.1
Hypersthene (OPx) (wt.%)	0	0	0
Wollastonite (wt.%)	0	0	0
Olivine (wt.%)	11.4	10.3	14.6
Larnite (wt.%)	0	0	0
Acmite (wt.%)	0	0	0
K2SiO3 (wt.%)	0	0	0
Na2SiO3 (wt.%)	0	0	0
Rutile (wt.%)	0	0	0
Ilmenite (wt.%)	4.81	4.92	5.13
Magnetite (wt.%)	1.7	1.58	1.58
Hematite (wt.%)	0	0	0
Apatite (wt.%)	1.81	1.88	1.48
Zircon (wt.%)	0	0	0
Perovskite (wt.%)	0	0	0
Chromite (wt.%)	0	0	0
Sphene (wt.%)	0	0	0
Pyrite (wt.%)	0	0	0
Halite (wt.%)	0	0	0
Fluorite (wt.%)	0	0	0
Anhydrite (wt.%)	0	0	0
Na2SO4 (wt.%)	0	0	0
Calcite (wt.%)	0	0	0
Na2CO3 (wt.%)	0	0	0
Total (wt.%)	100	100	100
Anorthite	14.3	13.7	17.9
Albite	0	0	0
Orthoclase	3.23	14.3	13.6
Diopside (CPx)	33.3	28.7	28.1
Hypersthene (OPx)	0	0	0
Olivine	11.4	10.3	14.6

Table 3 continued

Sample Number	**Ei 22a**	**Ei 23**	**Ei 24**
Locaylity	Rüderbusch	Steffelner Kopf	Goßberg
wt. %			
Quartz	0	0	0
Plagioclase (wt.%)	9.77	7.63	8.65
Orthoclase (wt.%)	0	0	0
Nepheline (Foid) (wt.%)	12.2	12.8	12.7
Leucite (Foid) (wt.%)	15.1	18.3	16.9
Kalsilite (wt.%)	0	0	0
Corundum (wt.%)	0	0	0
Diopside (CPx) (wt.%)	30.7	27.6	33.2
Hypersthene (OPx) (wt.%)	0	0	0
Wollastonite (wt.%)	0	0	0
Olivine (wt.%)	18.1	17.7	16.6
Larnite (wt.%)	6.13	7.38	4.45
Acmite (wt.%)	0	0	0
K2SiO3 (wt.%)	0	0	0
Na2SiO3 (wt.%)	0	0	0
Rutile (wt.%)	0	0	0
Ilmenite (wt.%)	4.79	5.34	4.69
Magnetite (wt.%)	1.58	1.64	1.48
Hematite (wt.%)	0	0	0
Apatite (wt.%)	1.67	1.69	1.44
Zircon (wt.%)	0	0	0
Perovskite (wt.%)	0	0	0
Chromite (wt.%)	0	0	0
Sphene (wt.%)	0	0	0
Pyrite (wt.%)	0	0	0
Halite (wt.%)	0	0	0
Fluorite (wt.%)	0	0	0
Anhydrite (wt.%)	0	0	0
Na2SO4 (wt.%)	0	0	0
Calcite (wt.%)	0	0	0
Na2CO3 (wt.%)	0	0	0
Total (wt.%)	100	100	100
Anorthite	9.77	7.63	8.65
Albite	0	0	0
Orthoclase	0	0	0
Diopside (CPx)	30.7	27.6	33.2
Hypersthene (OPx)	0	0	0
Olivine	18.1	17.7	16.6

Table 3 continued

Sample Number **Locaylity**	**Ei 25** Rockeskyller Kopf	**Ei 26** Kalem	**Ei 27** Sarresdorf Lavaflow
wt. %			
Quartz	0	0	0
Plagioclase (wt.%)	11	10.2	13.7
Orthoclase (wt.%)	0	0	7.31
Nepheline (Foid) (wt.%)	10.1	15.5	15.8
Leucite (Foid) (wt.%)	18.6	12.8	1.4
Kalsilite (wt.%)	0	0	0
Corundum (wt.%)	0	0	0
Diopside (CPx) (wt.%)	38.3	22.9	35.8
Hypersthene (OPx) (wt.%)	0	0	0
Wollastonite (wt.%)	0	0	0
Olivine (wt.%)	13.3	19.1	17.8
Larnite (wt.%)	0.63	9.8	0
Acmite (wt.%)	0	0	0
K2SiO3 (wt.%)	0	0	0
Na2SiO3 (wt.%)	0	0	0
Rutile (wt.%)	0	0	0
Ilmenite (wt.%)	4.81	5.64	4.5
Magnetite (wt.%)	1.54	1.78	1.67
Hematite (wt.%)	0	0	0
Apatite (wt.%)	1.78	2.39	2.04
Zircon (wt.%)	0	0	0
Perovskite (wt.%)	0	0	0
Chromite (wt.%)	0	0	0
Sphene (wt.%)	0	0	0
Pyrite (wt.%)	0	0	0
Halite (wt.%)	0	0	0
Fluorite (wt.%)	0	0	0
Anhydrite (wt.%)	0	0	0
Na2SO4 (wt.%)	0	0	0
Calcite (wt.%)	0	0	0
Na2CO3 (wt.%)	0	0	0
Total (wt.%)	100	100	100
Anorthite	11	10.2	13.7
Albite	0	0	0
Orthoclase	0	0	7.31
Diopside (CPx)	38.3	22.9	35.8
Hypersthene (OPx)	0	0	0
Olivine	13.3	19.1	17.8

Table 3 continued

Sample Number	**Ei 28**	**Ei 29**	**Ei 30**
Locaylity	Fächerhöhe	Wartgensberg	Mosenberg
wt. %			
Quartz	0	0	0
Plagioclase (wt.%)	14.5	14.6	11.2
Orthoclase (wt.%)	6.82	8.98	0
Nepheline (Foid) (wt.%)	13.6	13.3	16.7
Leucite (Foid) (wt.%)	1.61	0	9.55
Kalsilite (wt.%)	0	0	0
Corundum (wt.%)	0	0	0
Diopside (CPx) (wt.%)	31.6	30.2	30.6
Hypersthene (OPx) (wt.%)	0	0	0
Wollastonite (wt.%)	0	0	0
Olivine (wt.%)	23.6	24.4	20.6
Larnite (wt.%)	0	0	2.44
Acmite (wt.%)	0	0	0
K2SiO3 (wt.%)	0	0	0
Na2SiO3 (wt.%)	0	0	0
Rutile (wt.%)	0	0	0
Ilmenite (wt.%)	4.44	4.71	5.09
Magnetite (wt.%)	1.74	1.77	1.73
Hematite (wt.%)	0	0	0
Apatite (wt.%)	2.15	1.99	2.15
Zircon (wt.%)	0	0	0
Perovskite (wt.%)	0	0	0
Chromite (wt.%)	0	0	0
Sphene (wt.%)	0	0	0
Pyrite (wt.%)	0	0	0
Halite (wt.%)	0	0	0
Fluorite (wt.%)	0	0	0
Anhydrite (wt.%)	0	0	0
Na2SO4 (wt.%)	0	0	0
Calcite (wt.%)	0	0	0
Na2CO3 (wt.%)	0	0	0
Total (wt.%)	100	100	100
Anorthite	14.5	13.2	11.2
Albite	0	1.41	0
Orthoclase	6.82	8.98	0
Diopside (CPx)	31.6	30.2	30.6
Hypersthene (OPx)	0	0	0
Olivine	23.6	24.4	20.6

Table 3 continued

Sample Number	**Ei 31**	**Ei 32**	**Ei 33**
Locaylity	Auf der Hardt	Am Steinseiter	Sulzbusch
wt. %			
Quartz	0	0	0
Plagioclase (wt.%)	10.5	10	12
Orthoclase (wt.%)	0	0	6.06
Nepheline (Foid) (wt.%)	13.6	12.7	17.7
Leucite (Foid) (wt.%)	14.9	15.9	11.3
Kalsilite (wt.%)	0	0	0
Corundum (wt.%)	0	0	0
Diopside (CPx) (wt.%)	33.1	29.1	32.9
Hypersthene (OPx) (wt.%)	0	0	0
Wollastonite (wt.%)	0	0	0
Olivine (wt.%)	14.8	16.6	12.9
Larnite (wt.%)	4.92	7.15	0
Acmite (wt.%)	0	0	0
K2SiO3 (wt.%)	0	0	0
Na2SiO3 (wt.%)	0	0	0
Rutile (wt.%)	0	0	0
Ilmenite (wt.%)	4.82	5.34	4.2
Magnetite (wt.%)	1.62	1.67	1.45
Hematite (wt.%)	0	0	0
Apatite (wt.%)	1.71	1.55	1.53
Zircon (wt.%)	0	0	0
Perovskite (wt.%)	0	0	0
Chromite (wt.%)	0	0	0
Sphene (wt.%)	0	0	0
Pyrite (wt.%)	0	0	0
Halite (wt.%)	0	0	0
Fluorite (wt.%)	0	0	0
Anhydrite (wt.%)	0	0	0
Na2SO4 (wt.%)	0	0	0
Calcite (wt.%)	0	0	0
Na2CO3 (wt.%)	0	0	0
Total (wt.%)	100	100	100
Anorthite	10.5	10	12
Albite	0	0	0
Orthoclase	0	0	6.06
Diopside (CPx)	33.1	29.1	32.9
Hypersthene (OPx)	0	0	0
Olivine	14.8	16.6	12.9

Table 3 continued

Sample Number	**Ei 34**	**Ei 36**	**Ei 38**
Locaylity	Sulzbusch	An der Ahl	Etringer Bellerberg
wt. %			
Quartz	0	0	0
Plagioclase (wt.%)	14.5	8.24	27.9
Orthoclase (wt.%)	11.2	10.5	25.7
Nepheline (Foid) (wt.%)	16.3	24.9	13.5
Leucite (Foid) (wt.%)	6.26	14.1	0
Kalsilite (wt.%)	0	0	0
Corundum (wt.%)	0	0	0
Diopside (CPx) (wt.%)	30.8	29.2	20.1
Hypersthene (OPx) (wt.%)	0	0	0
Wollastonite (wt.%)	0	0	0
Olivine (wt.%)	13.7	6.03	7.18
Larnite (wt.%)	0	0	0
Acmite (wt.%)	0	0	0
K2SiO3 (wt.%)	0	0	0
Na2SiO3 (wt.%)	0	0	0
Rutile (wt.%)	0	0	0
Ilmenite (wt.%)	4.22	3.67	3.48
Magnetite (wt.%)	1.46	1.45	1.12
Hematite (wt.%)	0	0	0
Apatite (wt.%)	1.53	2.02	1
Zircon (wt.%)	0	0	0
Perovskite (wt.%)	0	0	0
Chromite (wt.%)	0	0	0
Sphene (wt.%)	0	0	0
Pyrite (wt.%)	0	0	0
Halite (wt.%)	0	0	0
Fluorite (wt.%)	0	0	0
Anhydrite (wt.%)	0	0	0
Na2SO4 (wt.%)	0	0	0
Calcite (wt.%)	0	0	0
Na2CO3 (wt.%)	0	0	0
Total (wt.%)	100	100	100
Anorthite	14.5	8.24	12.3
Albite	0	0	15.7
Orthoclase	11.2	10.5	25.7
Diopside (CPx)	30.8	29.2	20.1
Hypersthene (OPx)	0	0	0
Olivine	13.7	6.03	7.18

Table 3 continued

Sample Number	**Ei 39**	**Ei 40**	**Ei 41**
Locaylity	Karmelenberg	Humersberg	Engelner Kopf
wt. %			
Quartz	0	0	0
Plagioclase (wt.%)	14.2	10.4	0
Orthoclase (wt.%)	12.9	9.48	42.2
Nepheline (Foid) (wt.%)	15.8	21	34.5
Leucite (Foid) (wt.%)	6.27	9.62	10.3
Kalsilite (wt.%)	0	0	0
Corundum (wt.%)	0	0	0
Diopside (CPx) (wt.%)	30.2	31.4	6.49
Hypersthene (OPx) (wt.%)	0	0	0
Wollastonite (wt.%)	0	0	0
Olivine (wt.%)	12.7	10.5	1.92
Larnite (wt.%)	0	0	0
Acmite (wt.%)	0	0	1.01
K2SiO3 (wt.%)	0	0	0
Na2SiO3 (wt.%)	0	0	2.63
Rutile (wt.%)	0	0	0
Ilmenite (wt.%)	4.92	4.18	0.8
Magnetite (wt.%)	1.55	1.49	0
Hematite (wt.%)	0	0	0
Apatite (wt.%)	1.51	1.88	0.16
Zircon (wt.%)	0	0	0
Perovskite (wt.%)	0	0	0
Chromite (wt.%)	0	0	0
Sphene (wt.%)	0	0	0
Pyrite (wt.%)	0	0	0
Halite (wt.%)	0	0	0
Fluorite (wt.%)	0	0	0
Anhydrite (wt.%)	0	0	0
Na2SO4 (wt.%)	0	0	0
Calcite (wt.%)	0	0	0
Na2CO3 (wt.%)	0	0	0
Total (wt.%)	100	100	100
Anorthite	14.2	10.4	0
Albite	0	0	0
Orthoclase	12.9	9.48	42.2
Diopside (CPx)	30.2	31.4	6.49
Hypersthene (OPx)	0	0	0
Olivine	12.7	10.5	1.92

Table 3 continued

Sample Number	**Ei 42**	**Ei 43**	**Ei 44**
Locaylity	Schellkopf	Meirother Kopf	Tiefenstein
wt. %			
Quartz	0	0	0
Plagioclase (wt.%)	0	11.3	12
Orthoclase (wt.%)	33.6	0	0
Nepheline (Foid) (wt.%)	30.1	15.7	15.2
Leucite (Foid) (wt.%)	23.4	16	17.6
Kalsilite (wt.%)	0	0	0
Corundum (wt.%)	0	0	0
Diopside (CPx) (wt.%)	7.52	27.2	28.4
Hypersthene (OPx) (wt.%)	0	0	0
Wollastonite (wt.%)	0	0	0
Olivine (wt.%)	0.37	17.7	15.3
Larnite (wt.%)	0	4.35	3.77
Acmite (wt.%)	0.81	0	0
K2SiO3 (wt.%)	0	0	0
Na2SiO3 (wt.%)	3.6	0	0
Rutile (wt.%)	0	0	0
Ilmenite (wt.%)	0.53	4.73	4.71
Magnetite (wt.%)	0	1.52	1.51
Hematite (wt.%)	0	0	0
Apatite (wt.%)	0.07	1.53	1.55
Zircon (wt.%)	0	0	0
Perovskite (wt.%)	0	0	0
Chromite (wt.%)	0	0	0
Sphene (wt.%)	0	0	0
Pyrite (wt.%)	0	0	0
Halite (wt.%)	0	0	0
Fluorite (wt.%)	0	0	0
Anhydrite (wt.%)	0	0	0
Na2SO4 (wt.%)	0	0	0
Calcite (wt.%)	0	0	0
Na2CO3 (wt.%)	0	0	0
Total (wt.%)	100	100	100
Anorthite	0	11.3	12
Albite	0	0	0
Orthoclase	33.6	0	0
Diopside (CPx)	7.52	27.2	28.4
Hypersthene (OPx)	0	0	0
Olivine	0.37	17.7	15.3

Table 3 continued

Sample Number	**Ei 45**	**Ei 46**	**Ei 47**
Locaylity	Meirother Kopf	An der Hardt	Schorenberg
wt. %			
Quartz	0	0	0
Plagioclase (wt.%)	12.1	0	2.07
Orthoclase (wt.%)	0	11.9	28.5
Nepheline (Foid) (wt.%)	16	35.4	28.5
Leucite (Foid) (wt.%)	16.3	36.4	16.8
Kalsilite (wt.%)	0	0	0
Corundum (wt.%)	0	0	0
Diopside (CPx) (wt.%)	27.7	12.1	18.4
Hypersthene (OPx) (wt.%)	0	0	0
Wollastonite (wt.%)	0	0	0
Olivine (wt.%)	16	0.76	0
Larnite (wt.%)	4.11	0	0
Acmite (wt.%)	0	1.3	0
K2SiO3 (wt.%)	0	0	0
Na2SiO3 (wt.%)	0	0.54	0
Rutile (wt.%)	0	0	0
Ilmenite (wt.%)	4.75	1.39	1.8
Magnetite (wt.%)	1.54	0	0.8
Hematite (wt.%)	0	0	0
Apatite (wt.%)	1.58	0.21	0.79
Zircon (wt.%)	0	0	0
Perovskite (wt.%)	0	0	0
Chromite (wt.%)	0	0	0
Sphene (wt.%)	0	0	0
Pyrite (wt.%)	0	0	0
Halite (wt.%)	0	0	0
Fluorite (wt.%)	0	0	0
Anhydrite (wt.%)	0	0	0
Na2SO4 (wt.%)	0	0	0
Calcite (wt.%)	0	0	0
Na2CO3 (wt.%)	0	0	0
Total (wt.%)	100	100	100
Anorthite	12.1	0	2.07
Albite	0	0	0
Orthoclase	0	11.9	28.5
Diopside (CPx)	27.7	12.1	18.4
Hypersthene (OPx)	0	0	0
Olivine	16	0.76	0

Table 3 continued

Sample Number	**Ei 48**	**Ei 49a**	**Ei 49b**
Locaylity	Burgberg	Burg Olbrück	Burg Olbrück
wt. %			
Quartz	0	0	0
Plagioclase (wt.%)	0	0	0
Orthoclase (wt.%)	54.1	50.7	45.7
Nepheline (Foid) (wt.%)	35.1	31.7	31.8
Leucite (Foid) (wt.%)	0.09	8.11	11
Kalsilite (wt.%)	0	0	0
Corundum (wt.%)	0	0	0
Diopside (CPx) (wt.%)	7.39	3.11	6.64
Hypersthene (OPx) (wt.%)	0	0	0
Wollastonite (wt.%)	0	0	0
Olivine (wt.%)	0.75	2.55	0.96
Larnite (wt.%)	0	0	0
Acmite (wt.%)	0.84	0.9	0.9
K2SiO3 (wt.%)	0	0	0
Na2SiO3 (wt.%)	1.25	2.34	2.43
Rutile (wt.%)	0	0	0
Ilmenite (wt.%)	0.42	0.53	0.51
Magnetite (wt.%)	0	0	0
Hematite (wt.%)	0	0	0
Apatite (wt.%)	0.05	0.07	0.05
Zircon (wt.%)	0	0	0
Perovskite (wt.%)	0	0	0
Chromite (wt.%)	0	0	0
Sphene (wt.%)	0	0	0
Pyrite (wt.%)	0	0	0
Halite (wt.%)	0	0	0
Fluorite (wt.%)	0	0	0
Anhydrite (wt.%)	0	0	0
Na2SO4 (wt.%)	0	0	0
Calcite (wt.%)	0	0	0
Na2CO3 (wt.%)	0	0	0
Total (wt.%)	100	100	100
Anorthite	0	0	0
Albite	0	0	0
Orthoclase	54.1	50.7	45.7
Diopside (CPx)	7.39	3.11	6.64
Hypersthene (OPx)	0	0	0
Olivine	0.75	2.55	0.96

Table 3 continued

Sample Number	**Ei 50**	**Ei 51**	**Ei 53**
Locaylity	Perler Kopf	Perler Kopf	Kempenich
wt. %			
Quartz	0	0	0
Plagioclase (wt.%)	11.2	0	0.85
Orthoclase (wt.%)	32.6	45.7	55.4
Nepheline (Foid) (wt.%)	30.1	31.8	34.7
Leucite (Foid) (wt.%)	0	11	0
Kalsilite (wt.%)	0	0	0
Corundum (wt.%)	0	0	0
Diopside (CPx) (wt.%)	19.9	6.64	4.35
Hypersthene (OPx) (wt.%)	0	0	0
Wollastonite (wt.%)	0	0	0
Olivine (wt.%)	1.79	0.96	2.65
Larnite (wt.%)	0	0	0
Acmite (wt.%)	0	0.9	1.01
K2SiO3 (wt.%)	0	0	0
Na2SiO3 (wt.%)	0	2.43	0.14
Rutile (wt.%)	0	0	0
Ilmenite (wt.%)	2.15	0.51	0.78
Magnetite (wt.%)	1.04	0	0
Hematite (wt.%)	0	0	0
Apatite (wt.%)	1.23	0.05	0.19
Zircon (wt.%)	0	0	0
Perovskite (wt.%)	0	0	0
Chromite (wt.%)	0	0	0
Sphene (wt.%)	0	0	0
Pyrite (wt.%)	0	0	0
Halite (wt.%)	0	0	0
Fluorite (wt.%)	0	0	0
Anhydrite (wt.%)	0	0	0
Na2SO4 (wt.%)	0	0	0
Calcite (wt.%)	0	0	0
Na2CO3 (wt.%)	0	0	0
Total (wt.%)	100	100	100
Anorthite	6.73	0	0
Albite	4.48	0	0.85
Orthoclase	32.6	45.7	55.4
Diopside (CPx)	19.9	6.64	4.35
Hypersthene (OPx)	0	0	0
Olivine	1.79	0.96	2.65

Table 3 continued

Sample Number	**Ei 55**	**Ei 56**	**Ei 57**
Locaylity	Bräunig Vulkan	NE' Üdersdorf	Emmelberg
wt. %			
Quartz	0	0	0
Plagioclase (wt.%)	10.7	7.75	8.63
Orthoclase (wt.%)	0	0	0
Nepheline (Foid) (wt.%)	15.5	15	20.9
Leucite (Foid) (wt.%)	12.5	13	10.2
Kalsilite (wt.%)	0	0	0
Corundum (wt.%)	0	0	0
Diopside (CPx) (wt.%)	21.9	24.6	29
Hypersthene (OPx) (wt.%)	0	0	0
Wollastonite (wt.%)	0	0	0
Olivine (wt.%)	23.7	20.6	17.4
Larnite (wt.%)	8.3	11.2	5.08
Acmite (wt.%)	0	0	0
K2SiO3 (wt.%)	0	0	0
Na2SiO3 (wt.%)	0	0	0
Rutile (wt.%)	0	0	0
Ilmenite (wt.%)	4.18	4.46	5.56
Magnetite (wt.%)	1.61	1.58	1.55
Hematite (wt.%)	0	0	0
Apatite (wt.%)	1.71	1.78	1.78
Zircon (wt.%)	0	0	0
Perovskite (wt.%)	0	0	0
Chromite (wt.%)	0	0	0
Sphene (wt.%)	0	0	0
Pyrite (wt.%)	0	0	0
Halite (wt.%)	0	0	0
Fluorite (wt.%)	0	0	0
Anhydrite (wt.%)	0	0	0
Na2SO4 (wt.%)	0	0	0
Calcite (wt.%)	0	0	0
Na2CO3 (wt.%)	0	0	0
Total (wt.%)	100	100	100
Anorthite	10.7	7.75	8.63
Albite	0	0	0
Orthoclase	0	0	0
Diopside (CPx)	21.9	24.6	29
Hypersthene (OPx)	0	0	0
Olivine	23.7	20.6	17.4

Table 3 continued

Sample Number	**Ei 58a**	**Ei 59**	**EI 60**
Locaylity	Leyendecker Quary	Wolfsschlucht	Alte Burg cone
wt. %			
Quartz	0	0	0
Plagioclase (wt.%)	24	11.2	15.2
Orthoclase (wt.%)	7.15	0	0
Nepheline (Foid) (wt.%)	8.98	15.3	15.7
Leucite (Foid) (wt.%)	0	7.92	16.7
Kalsilite (wt.%)	0	0	0
Corundum (wt.%)	0	0	0
Diopside (CPx) (wt.%)	27.4	24.9	27.3
Hypersthene (OPx) (wt.%)	0	0	0
Wollastonite (wt.%)	0	0	0
Olivine (wt.%)	24.9	27.5	13
Larnite (wt.%)	0	4.81	3.08
Acmite (wt.%)	0	0	0
K2SiO3 (wt.%)	0	0	0
Na2SiO3 (wt.%)	0	0	0
Rutile (wt.%)	0	0	0
Ilmenite (wt.%)	4.22	4.58	5.77
Magnetite (wt.%)	1.57	1.75	1.75
Hematite (wt.%)	0	0	0
Apatite (wt.%)	1.81	2.11	1.53
Zircon (wt.%)	0	0	0
Perovskite (wt.%)	0	0	0
Chromite (wt.%)	0	0	0
Sphene (wt.%)	0	0	0
Pyrite (wt.%)	0	0	0
Halite (wt.%)	0	0	0
Fluorite (wt.%)	0	0	0
Anhydrite (wt.%)	0	0	0
Na2SO4 (wt.%)	0	0	0
Calcite (wt.%)	0	0	0
Na2CO3 (wt.%)	0	0	0
Total (wt.%)	100	100	100
Anorthite	14.6	11.2	15.2
Albite	9.32	0	0
Orthoclase	7.15	0	0
Diopside (CPx)	27.4	24.9	27.3
Hypersthene (OPx)	0	0	0
Olivine	24.9	27.5	13

Table 3 continued

Sample Number	**EI 61**	**Ei 62**
Locaylity	Lorenzfelsen	
wt. %		
Quartz	0	nd
Plagioclase (wt.%)	17.4	nd
Orthoclase (wt.%)	5.79	nd
Nepheline (Foid) (wt.%)	14.1	nd
Leucite (Foid) (wt.%)	5.98	nd
Kalsilite (wt.%)	0	nd
Corundum (wt.%)	0	nd
Diopside (CPx) (wt.%)	32.1	nd
Hypersthene (OPx) (wt.%)	0	nd
Wollastonite (wt.%)	0	nd
Olivine (wt.%)	16.1	nd
Larnite (wt.%)	0	nd
Acmite (wt.%)	0	nd
K2SiO3 (wt.%)	0	nd
Na2SiO3 (wt.%)	0	nd
Rutile (wt.%)	0	nd
Ilmenite (wt.%)	5.22	nd
Magnetite (wt.%)	1.8	nd
Hematite (wt.%)	0	nd
Apatite (wt.%)	1.48	nd
Zircon (wt.%)	0	nd
Perovskite (wt.%)	0	nd
Chromite (wt.%)	0	nd
Sphene (wt.%)	0	nd
Pyrite (wt.%)	0	nd
Halite (wt.%)	0	nd
Fluorite (wt.%)	0	nd
Anhydrite (wt.%)	0	nd
Na2SO4 (wt.%)	0	nd
Calcite (wt.%)	0	nd
Na2CO3 (wt.%)	0	nd
Total (wt.%)	100	nd
Anorthite	17.4	nd
Albite	0	nd
Orthoclase	5.79	nd
Diopside (CPx)	32.1	nd
Hypersthene (OPx)	0	nd
Olivine	16.1	nd

Table 3 continued

Sample Number	**Ei 2**	**Ei 3**	**Ei 4**
Locaylity	Eppelsberg	Eppelsberg	Herrchenberg
$^{86}Sr/^{87}Sr$	0.704559	nd	0.704567
(±2σ)	±13	nd	±11
$^{143}Nd/^{144}Nd$	0.512671	nd	0.512692
(±2σ)	±6	nd	±10
eNd	0.6	nd	1.1
$^{206}Pb/^{204}Pb$ 2rsd (ppm)	19.1	nd	19.3
$^{207}Pb/^{204}Pb$ 2rsd (ppm)	15.7	nd	15.7
$^{208}Pb/^{204}Pb$ 2rsd (ppm)	39.3	nd	39.5
D7/4	8.95	nd	7.56
D8/4	58.1	nd	54.6
$^{176}Hf/^{177}Hf$	0.282767	nd	0.282787
(±2σ)	±4	nd	±5
eHf	-0.1	nd	0.6
$^{187}Os/^{188}Os$	0.2027	nd	0.3308
(±2σ)	0.0031	nd	0.0062
Re/Os	19.11	nd	12.72
$^{187}Re/^{188}Os$	91.9	nd	62.2
(±2σ)	2.76		1.87
$^{187}Os/^{188}Os$ (i)	0.2019	nd	0.3303
γOs	59.6	nd	160

Table 4

Sample Number	**Ei 5**	**Ei 6**	**Ei 7**
Locaylity	Herrchenberg	Herrchenberg	Herrchenberg
$^{86}Sr/^{87}Sr$	0.704436	0.704455	0.704648
(±2σ)	±9	±10	±17
$^{143}Nd/^{144}Nd$	0.512696	0.512697	0.512689
(±2σ)	±6	±8	±6
eNd	1.1	1.1	1.0
$^{206}Pb/^{204}Pb$ 2rsd (ppm)	nd	nd	19.3
$^{207}Pb/^{204}Pb$ 2rsd (ppm)	nd	nd	15.7
$^{208}Pb/^{204}Pb$ 2rsd (ppm)	nd	nd	39.5
D7/4	nd	nd	9.15
D8/4	nd	nd	56.8
$^{176}Hf/^{177}Hf$	0.282781	0.282788	0.282791
(±2σ)	±5	±5	±5
eHf	0.4	0.7	0.7
$^{187}Os/^{188}Os$	nd	nd	nd
(±2σ)	nd	nd	nd
Re/Os	nd	nd	nd
$^{187}Re/^{188}Os$ (±2σ)	nd	nd	nd
$^{187}Os/^{188}Os$ (i)	nd	nd	nd
γOs	nd	nd	nd

Table 4 continued

Sample Number	**Ei 8**	**Ei 9**	**Ei 10a**
Locaylity	Upper-Mendig Flow	Bausenberg	Hannebacher Ley
$^{86}Sr/^{87}Sr$	0.704635	0.704885	0.704445
(±2σ)	±10	±9	±12
$^{143}Nd/^{144}Nd$	0.512688	0.512692	0.512696
(±2σ)	±10	±6	±9
eNd	1.0	1.1	1.1
$^{206}Pb/^{204}Pb$ 2rsd (ppm)	nd	18.9	nd
$^{207}Pb/^{204}Pb$ 2rsd (ppm)	nd	15.6	nd
$^{208}Pb/^{204}Pb$ 2rsd (ppm)	nd	39.1	nd
D7/4	nd	9.54	nd
D8/4	nd	63.4	nd
$^{176}Hf/^{177}Hf$	0.282803	0.282771	0.282763
(±2σ)	±5	±5	±5
eHf	1.2	0.0	-0.3
$^{187}Os/^{188}Os$	nd	0.2606	nd
(±2σ)	nd	0.0017	nd
Re/Os	nd	14.03	nd
$^{187}Re/^{188}Os$	nd	68.0	nd
(±2σ)		2.04	
$^{187}Os/^{188}Os$ (i)	nd	0.2600	nd
γOs	nd	105	nd

Table 4 continued

Sample Number	**Ei 10b**	**Ei 11 a**	**Ei 12**
Locaylity	Hannebacher Ley	Schorberg	Leitenberg
$^{86}Sr/^{87}Sr$	0.704749	0.704785	0.704497
(±2σ)	±9	±8	±9
$^{143}Nd/^{144}Nd$	0.512705	0.51267	0.512694
(±2σ)	±3	±8	±9
eNd	1.3	0.6	1.1
$^{206}Pb/^{204}Pb$ 2rsd (ppm)	19.3	19	19.3
$^{207}Pb/^{204}Pb$ 2rsd (ppm)	15.7	15.7	15.7
$^{208}Pb/^{204}Pb$ 2rsd (ppm)	39.5	39.2	39.5
D7/4	8.39	10.5	7.68
D8/4	55	57.8	54.5
$^{176}Hf/^{177}Hf$	0.282761	0.28277	0.282773
(±2σ)	±5	±6	±6
eHf	-0.3	0.0	0.1
$^{187}Os/^{188}Os$	nd	nd	0.6986
(±2σ)	nd	nd	0.0044
Re/Os	nd	nd	5.58
$^{187}Re/^{188}Os$ (±2σ)	nd	nd	28.6 0.859
$^{187}Os/^{188}Os$ (i)	nd	nd	0.6984
γOs	nd	nd	450

Table 4 continued

Sample Number	**Ei 13**	**Ei 14**	**Ei 15**
Locaylity	Hohe Buche	Plaidter Hummerich	Nettetal
$^{86}Sr/^{87}Sr$	0.704631	0.704766	0.70463
(±2σ)	±8	±7	±13
$^{143}Nd/^{144}Nd$	0.512722	0.512675	0.512666
(±2σ)	±9	±6	±7
eNd	1.6	0.7	0.5
$^{206}Pb/^{204}Pb$	19	19	18.9
2rsd (ppm)			±194
$^{207}Pb/^{204}Pb$	15.6	15.7	15.6
2rsd (ppm)			±236
$^{208}Pb/^{204}Pb$	39.3	39.2	39.1
2rsd (ppm)			±319
D7/4	10.4	10.9	10.2
D8/4	73.4	64.7	69.7
$^{176}Hf/^{177}Hf$	0.282795	0.28278	0.282751
(±2σ)	±7	±5	±7
eHf	0.9	0.4	-0.7
$^{187}Os/^{188}Os$	nd	nd	nd
(±2σ)	nd	nd	nd
Re/Os	nd	nd	nd
$^{187}Re/^{188}Os$	nd	nd	nd
(±2σ)			
$^{187}Os/^{188}Os$ (i)	nd	nd	nd
γOs	nd	nd	nd

Table 4 continued

Sample Number	**Ei 16b**	**Ei 17**	**Ei 18**
Locaylity	Rothenberg	Lower-Mendig Flow	Eppelsberg (coarse)
$^{86}Sr/^{87}Sr$	0.704689	nd	0.704854
(±2σ)	±9	nd	±9
$^{143}Nd/^{144}Nd$	0.512669	nd	0.512689
(±2σ)	±9	nd	±7
eNd	0.6	nd	1.0
$^{206}Pb/^{204}Pb$	19	nd	18.9
2rsd (ppm)			±194
$^{207}Pb/^{204}Pb$	15.6	nd	15.6
2rsd (ppm)			±236
$^{208}Pb/^{204}Pb$	39.2	nd	39.2
2rsd (ppm)			±319
D7/4	10.1	nd	9.15
D8/4	64.4	nd	66.8
$^{176}Hf/^{177}Hf$	0.282747		0.282763
(±2σ)	±7		±4
eHf	-0.8		-0.2
$^{187}Os/^{188}Os$	0.5000	nd	nd
(±2σ)	0.0018	nd	nd
Re/Os	4.23	nd	nd
$^{187}Re/^{188}Os$	21.1	nd	nd
(±2σ)	91.9		
$^{187}Os/^{188}Os$ (i)	0.6340	nd	nd
γOs	294	nd	nd

Table 4 continued

Sample Number	**Ei 19**	**Ei 20**	**Ei 21**
Locaylity	Eppelsberg (dike)	Lower-Mendig Flow	relict flow. Hill W' Jägerheim
$^{86}Sr/^{87}Sr$	nd	0.704554	0.704607
(±2σ)	nd	±10	±9
$^{143}Nd/^{144}Nd$	nd	0.512695	0.512642
(±2σ)	nd	±7	±7
eNd	nd	1.1	0.1
$^{206}Pb/^{204}Pb$	nd	19	18.6
2rsd (ppm)		±194	±194
$^{207}Pb/^{204}Pb$	nd	15.6	15.6
2rsd (ppm)		±236	±236
$^{208}Pb/^{204}Pb$	nd	39.2	38.9
2rsd (ppm)		±319	±319
D7/4	nd	8.63	11
D8/4	nd	60.9	77
$^{176}Hf/^{177}Hf$		0.282789	0.282711
(±2σ)		±5	±4
eHf		0.7	-2.1
$^{187}Os/^{188}Os$	nd	0.4150	nd
(±2σ)	nd	0.02	nd
Re/Os	nd	72.17	nd
$^{187}Re/^{188}Os$	nd	357	nd
(±2σ)		10.7	
$^{187}Os/^{188}Os$ (i)	nd	0.4120	nd
γOs	nd	227	nd

Table 4 continued

Sample Number	**Ei 22a**	**Ei 23**	**Ei 24**
Locaylity	Rüderbusch	Steffelner Kopf	Goßberg
$^{86}Sr/^{87}Sr$	0.704385	0.704649	0.704385
(±2σ)	±11	±13	±12
$^{143}Nd/^{144}Nd$	0.512713	0.512688	0.512681
(±2σ)	±6	±6	±5
eNd	1.5	1.0	0.8
$^{206}Pb/^{204}Pb$	19.4	19	19.4
2rsd (ppm)	±87	±87	±87
$^{207}Pb/^{204}Pb$	15.7	15.7	15.7
2rsd (ppm)	±86	±86	±86
$^{208}Pb/^{204}Pb$	39.7	39.3	39.6
2rsd (ppm)	±106	±106	±106
D7/4	6.83	9.71	6.84
D8/4	59.1	68.6	51.1
$^{176}Hf/^{177}Hf$	0.282791	0.282763	0.282763
(±2σ)	±6	±6	±6
eHf	0.7	-0.2	-0.2
$^{187}Os/^{188}Os$	0.1403	nd	nd
(±2σ)	0.0016	nd	nd
Re/Os	26.48	nd	nd
$^{187}Re/^{188}Os$	126	nd	nd
(±2σ)	3.77		
$^{187}Os/^{188}Os$ (i)	0.1392	nd	nd
γOs	10.5	nd	nd

Table 4 continued

Sample Number	**Ei 25**	**Ei 26**	**Ei 27**
Locaylity	Rockeskyller Kopf	Kalem	Sarresdorf Lavaflow
$^{86}Sr/^{87}Sr$	0.70478	0.704326	0.70395
(±2σ)	±13	±17	±15
$^{143}Nd/^{144}Nd$	0.512656	0.512745	0.512813
(±2σ)	±8	±10	±7
eNd	0.4	2.1	3.4
$^{206}Pb/^{204}Pb$	19.1	19.6	19.4
2rsd (ppm)	±194	±87	±87
$^{207}Pb/^{204}Pb$	15.7	15.7	15.6
2rsd (ppm)	±236	±86	±86
$^{208}Pb/^{204}Pb$	39.4	39.7	39.3
2rsd (ppm)	±319	±106	±106
D7/4	9.55	4.52	3.44
D8/4	64.8	37.1	18.9
$^{176}Hf/^{177}Hf$	0.282681	0.282879	0.282897
(±2σ)	±6	±7	±5
eHf	-3.2	3.9	4.5
$^{187}Os/^{188}Os$	nd	0.1388	0.2965
(±2σ)	nd	0.0084	0.0024
Re/Os	nd	19.63	8.69
$^{187}Re/^{188}Os$	nd	331	51.2
(±2σ)		9.92	1.37
$^{187}Os/^{188}Os$ (i)	nd	0.1360	0.2961
γOs	nd	9.29	133

Table 4 continued

Sample Number	**Ei 28**	**Ei 29**	**Ei 30**
Locaylity	Fächerhöhe	Wartgensberg	Mosenberg
$^{86}Sr/^{87}Sr$	0.704457	0.703897	0.703916
(±2σ)	±19	±16	±12
$^{143}Nd/^{144}Nd$	0.512811	0.51281	0.5128
(±2σ)	±7	±6	±5
eNd	3.4	3.4	3.2
$^{206}Pb/^{204}Pb$	19.5	19.4	19.4
2rsd (ppm)	±87	±87	±194
$^{207}Pb/^{204}Pb$	15.6	15.6	15.6
2rsd (ppm)	±86	±86	±236
$^{208}Pb/^{204}Pb$	39.3	39.3	39.4
2rsd (ppm)	±106	±106	±319
D7/4	2.63	2.94	3.63
D8/4	18.4	19	22.4
$^{176}Hf/^{177}Hf$	0.282935	0.282892	0.282909
(±2σ)	±6	±7	±6
eHf	5.8	4.3	4.9
$^{187}Os/^{188}Os$	nd	0.3159	nd
(±2σ)	nd	0.0034	nd
Re/Os	nd	5.35	nd
$^{187}Re/^{188}Os$	nd	18.71	nd
(±2σ)		0.516	
$^{187}Os/^{188}Os$ (i)	nd	0.3157	nd
γOs	nd	149	nd

Table 4 continued

Sample Number	**Ei 31**	**Ei 32**	**Ei 33**
Locaylity	Auf der Hardt	Am Steinseiter	Sulzbusch
$^{86}Sr/^{87}Sr$	0.704457	0.70458	0.704678
(±2σ)	±13	±14	±8
$^{143}Nd/^{144}Nd$	0.512676	0.512693	0.512681
(±2σ)	±6	±6	±6
eNd	0.7	1.1	0.8
$^{206}Pb/^{204}Pb$	19.6	19.7	19.1
2rsd (ppm)	±87	±87	±194
$^{207}Pb/^{204}Pb$	15.7	15.7	15.7
2rsd (ppm)	±86	±86	±236
$^{208}Pb/^{204}Pb$	39.7	39.8	39.2
2rsd (ppm)	±106	±106	±319
D7/4	5.66	4.47	9.32
D8/4	45.6	31.3	50.8
$^{176}Hf/^{177}Hf$	0.28283	0.282845	0.282738
(±2σ)	±7	±6	±10
eHf	2.1	2.7	-1.1
$^{187}Os/^{188}Os$	nd	nd	nd
(±2σ)	nd	nd	nd
Re/Os	nd	nd	nd
$^{187}Re/^{188}Os$	nd	nd	nd
(±2σ)			
$^{187}Os/^{188}Os$ (i)	nd	nd	nd
γOs	nd	nd	nd

Table 4 continued

Sample Number	**Ei 34**	**Ei 36**	**Ei 38**
Locaylity	Sulzbusch	An der Ahl	Etringer Bellerberg
$^{86}Sr/^{87}Sr$	0.704823	0.704767	0.705288
(±2σ)	±7	±6	±7
$^{143}Nd/^{144}Nd$	0.512678	0.512673	0.512626
(±2σ)	±8	±7	±7
eNd	0.8	0.7	-0.2
$^{206}Pb/^{204}Pb$ 2rsd (ppm)	nd	nd	nd
$^{207}Pb/^{204}Pb$ 2rsd (ppm)	nd	nd	nd
$^{208}Pb/^{204}Pb$ 2rsd (ppm)	nd	nd	nd
D7/4	nd	nd	nd
D8/4	nd	nd	nd
$^{176}Hf/^{177}Hf$	0.282724	0.282732	0.282762
(±2σ)	±10	±13	±11
eHf	-1.6	-1.3	-0.3
$^{187}Os/^{188}Os$	nd	nd	nd
(±2σ)	nd	nd	nd
Re/Os	nd	nd	nd
$^{187}Re/^{188}Os$ (±2σ)	nd	nd	nd
$^{187}Os/^{188}Os$ (i)	nd	nd	nd
γOs	nd	nd	nd

Table 4 continued

Sample Number	**Ei 39**	**Ei 40**	**Ei 41**
Locaylity	Karmelenberg	Humersberg	Engelner Kopf
$^{86}Sr/^{87}Sr$	0.704919	0.704811	0.704515
(±2σ)	±9	±10	±11
$^{143}Nd/^{144}Nd$	0.512673	0.512665	0.512684
(±2σ)	±7	±8	±6
eNd	0.7	0.5	0.9
$^{206}Pb/^{204}Pb$	19	nd	nd
2rsd (ppm)	±194		
$^{207}Pb/^{204}Pb$	15.6	nd	nd
2rsd (ppm)	±236		
$^{208}Pb/^{204}Pb$	39.3	nd	nd
2rsd (ppm)	±319		
D7/4	4.94	nd	nd
D8/4	70.2	nd	nd
$^{176}Hf/^{177}Hf$	0.282775	0.282732	0.28275
(±2σ)	±14	±16	±22
eHf	0.2	-1.3	-0.7
$^{187}Os/^{188}Os$	nd	nd	nd
(±2σ)	nd	nd	nd
Re/Os	nd	nd	nd
$^{187}Re/^{188}Os$	nd	nd	nd
(±2σ)			
$^{187}Os/^{188}Os$ (i)	nd	nd	nd
γOs	nd	nd	nd

Table 4 continued

Sample Number	**Ei 42**	**Ei 43**	**Ei 44**
Locaylity	Schellkopf	Meirother Kopf	Tiefenstein
$^{86}Sr/^{87}Sr$	0.704488	0.704622	0.704653
(±2σ)	±10	±7	±8
$^{143}Nd/^{144}Nd$	0.512688	0.512697	0.512716
(±2σ)	±7	±7	±23
eNd	1.0	1.2	1.5
$^{206}Pb/^{204}Pb$	nd	19	nd
2rsd (ppm)		±194	
$^{207}Pb/^{204}Pb$	nd	15.6	nd
2rsd (ppm)		±236	
$^{208}Pb/^{204}Pb$	nd	39.3	nd
2rsd (ppm)		±319	
D7/4	nd	9.61	nd
D8/4	nd	62.9	nd
$^{176}Hf/^{177}Hf$	0.282767	0.282757	0.282747
(±2σ)	±12	±11	±4
eHf	-0.1	-0.5	-0.8
$^{187}Os/^{188}Os$	nd	nd	nd
(±2σ)	nd	nd	nd
Re/Os	nd	nd	nd
$^{187}Re/^{188}Os$	nd	nd	nd
(±2σ)			
$^{187}Os/^{188}Os$ (i)	nd	nd	nd
γOs	nd	nd	nd

Table 4 continued

Sample Number	**Ei 45**	**Ei 46**	**Ei 47**
Locaylity	Meirother Kopf	An der Hardt	Schorenberg
$^{86}Sr/^{87}Sr$	0.704789	0.704488	0.704639
(±2σ)	±10	±10	±9
$^{143}Nd/^{144}Nd$	0.512681	0.512708	0.51268
(±2σ)	±7	±25	±7
eNd	0.8	1.4	0.8
$^{206}Pb/^{204}Pb$ 2rsd (ppm)	nd	nd	nd
$^{207}Pb/^{204}Pb$ 2rsd (ppm)	nd	nd	nd
$^{208}Pb/^{204}Pb$ 2rsd (ppm)	nd	nd	nd
D7/4	nd	nd	nd
D8/4	nd	nd	nd
$^{176}Hf/^{177}Hf$	0.282751	0.282767	0.282712
(±2σ)	±17	±6	±6
eHf	-0.7	-0.1	-2.1
$^{187}Os/^{188}Os$	nd	nd	nd
(±2σ)	nd	nd	nd
Re/Os	nd	nd	nd
$^{187}Re/^{188}Os$ (±2σ)	nd	nd	nd
$^{187}Os/^{188}Os$ (i)	nd	nd	nd
γOs	nd	nd	nd

Table 4 continued

Sample Number	**Ei 48**	**Ei 49a**	**Ei 49b**
Locaylity	Burgberg	Burg Olbrück	Burg Olbrück
$^{86}Sr/^{87}Sr$	0.70446	0.704501	0.704528
(±2σ)	±10	±10	±11
$^{143}Nd/^{144}Nd$	0.512658	0.512697	0.512712
(±2σ)	±0	±7	±18
eNd	0.4	1.2	1.4
$^{206}Pb/^{204}Pb$ 2rsd (ppm)	nd	nd	nd
$^{207}Pb/^{204}Pb$ 2rsd (ppm)	nd	nd	nd
$^{208}Pb/^{204}Pb$ 2rsd (ppm)	nd	nd	nd
D7/4	nd	nd	nd
D8/4	nd	nd	nd
$^{176}Hf/^{177}Hf$	0.282757	0.282769	0.282753
(±2σ)	±6	±5	±7
eHf	-0.5	0.0	-0.6
$^{187}Os/^{188}Os$	nd	nd	nd
(±2σ)	nd	nd	nd
Re/Os	nd	nd	nd
$^{187}Re/^{188}Os$ (±2σ)	nd	nd	nd
$^{187}Os/^{188}Os$ (i)	nd	nd	nd
γOs	nd	nd	nd

Table 4 continued

Sample Number	**Ei 50**	**Ei 51**	**Ei 53**
Locaylity	Perler Kopf	Perler Kopf	Kempenich
$^{86}Sr/^{87}Sr$	0.704718	0.704715	0.704529
(±2σ)	±8	±11	±10
$^{143}Nd/^{144}Nd$	0.512722	0.512677	0.512683
(±2σ)	±0	±6	±7
eNd	1.6	0.8	0.9
$^{206}Pb/^{204}Pb$ 2rsd (ppm)	nd	nd	nd
$^{207}Pb/^{204}Pb$ 2rsd (ppm)	nd	nd	nd
$^{208}Pb/^{204}Pb$ 2rsd (ppm)	nd	nd	nd
D7/4	nd	nd	nd
D8/4	nd	nd	nd
$^{176}Hf/^{177}Hf$	0.282749	0.282763	0.282753
(±2σ)	±4	±6	±6
eHf	-0.7	-0.3	-0.6
$^{187}Os/^{188}Os$	nd	nd	nd
(±2σ)	nd	nd	nd
Re/Os	nd	nd	nd
$^{187}Re/^{188}Os$ (±2σ)	nd	nd	nd
$^{187}Os/^{188}Os$ (i)	nd	nd	nd
γOs	nd	nd	nd

Table 4 continued

Sample Number	**Ei 55**	**Ei 56**	**Ei 57**
Locaylity	Bräunig Vulkan	NE' Üdersdorf	Emmelberg
$^{86}Sr/^{87}Sr$	0.704419	0.704249	0.703872
(±2σ)	±10	±13	±10
$^{143}Nd/^{144}Nd$	0.512716	0.512724	0.512824
(±2σ)	±8	±7	±7
eNd	1.5	1.7	3.6
$^{206}Pb/^{204}Pb$	19.2	19.6	19.5
2rsd (ppm)	±194	±194	±194
$^{207}Pb/^{204}Pb$	15.6	15.7	15.6
2rsd (ppm)	±236	±236	±236
$^{208}Pb/^{204}Pb$	39.3	39.7	39.4
2rsd (ppm)	±319	±319	±319
D7/4	7.58	5.23	3.64
D8/4	51.7	42.2	26.3
$^{176}Hf/^{177}Hf$	0.282794	0.28284	0.282886
(±2σ)	±6	±6	±7
eHf	0.8	2.5	4.1
$^{187}Os/^{188}Os$	nd	0.2963	0.3689
(±2σ)	nd	0.81	0.0034
Re/Os	nd	6.92	28.65
$^{187}Re/^{188}Os$	nd	33.7	141
(±2σ)		0.0890	0.368
$^{187}Os/^{188}Os$ (i)	nd	0.2960	0.3677
γOs	nd	133	190

Table 4 continued

Sample Number	**Ei 58a**	**Ei 59**	**EI 60**
Locaylity	Leyendecker Quary	Wolfsschlucht	Alte Burg cone
$^{86}Sr/^{87}Sr$	0.705409	0.703856	0.704538
(±2σ)	±8	±9	±9
$^{143}Nd/^{144}Nd$	0.512739	0.512822	0.512731
(±2σ)	±7	±8	±49
eNd	2.0	3.6	1.8
$^{206}Pb/^{204}Pb$	19.4	19.4	19
2rsd (ppm)	±194	±194	±194
$^{207}Pb/^{204}Pb$	15.6	15.6	15.6
2rsd (ppm)	±236	±236	±236
$^{208}Pb/^{204}Pb$	39.3	39.3	39.2
2rsd (ppm)	±319	±319	±319
D7/4	4.63	3.16	8.84
D8/4	28.7	21.4	62.6
$^{176}Hf/^{177}Hf$	0.282796	0.282907	0.282785
(±2σ)	±6	±5	±6
eHf	0.9	4.9	0.5
$^{187}Os/^{188}Os$	nd	0.4906	nd
(±2σ)	nd	0.0018	nd
Re/Os	nd	5.80	nd
$^{187}Re/^{188}Os$	nd	29.0	nd
(±2σ)		0.490	
$^{187}Os/^{188}Os$ (i)	nd	0.4904	nd
γOs	nd	286	nd

Table 4 continued

Sample Number	**EI 61**	**Ei 62**
Locaylity	Lorenzfelsen	Booser Maar
$^{86}Sr/^{87}Sr$	0.704451	0.703782
(±2σ)	±10	±12
$^{143}Nd/^{144}Nd$	0.512691	0.512826
(±2σ)	±23	±32
eNd	1.0	3.7
$^{206}Pb/^{204}Pb$	19.2	19.2
2rsd (ppm)	±194	±194
$^{207}Pb/^{204}Pb$	15.6	15.631
2rsd (ppm)	±236	±236
$^{208}Pb/^{204}Pb$	39.4	39.128
2rsd (ppm)	±319	±319
D7/4	6.77	5.77
D8/4	54.2	27.7
$^{176}Hf/^{177}Hf$	0.282835	
(±2σ)	±5	
eHf	2.3	
$^{187}Os/^{188}Os$	nd	nd
(±2σ)	nd	nd
Re/Os	nd	nd
$^{187}Re/^{188}Os$	nd	nd
(±2σ)		
$^{187}Os/^{188}Os$ (i)	nd	nd
γOs	nd	nd

Table 4 continued

Sample Number	**Ei 2**	**Ei 3**	**Ei 4**	**Ei 5**	**Ei 6**	**Ei 7**
Locaylity	Eppelsberg	Eppelsberg	Herrchenberg	Herrchenberg	Herrchenberg	Herrchenberg
Nb/Ta	17.6	nd	20.0	18.9	18.8	19.5
Lu/Hf	0.0434	nd	0.0486	0.0488	0.0488	0.0488
Ce/Pb	27.4	nd	31.5	34.3	62.2	75.4
Nb/U	53.1	nd	52.2	51.6	50.7	51.3
Zr/Hf	43.2	nd	49.1	44.6	44.1	48.8
KN/KN*	1.20	nd	0.737	0.737	0.736	0.723
$(Dy/Yb)_N$	1.75	nd	1.78	2.75	2.72	2.76
$(La/Yb)_N$	23.7	nd	1.82	1.82	1.79	1.82
			31.3	31.3	29.2	31.2
CaO/TiO_2	4.32	4.40	4.46	4.53	4.52	4.62
CaO/Al_2O_3	0.880	0.87	1.03	1.04	1.04	1.05

Table 5

Sample Number	**Ei 8**	**Ei 9**	**Ei 10a**	**Ei 10b**	**Ei 11 a**	**Ei 12**
Locaylity	Upper-Mendig Flow	Bausenberg	Hannebacher Ley	Hannebacher Ley	Schorberg	Leitenberg
Nb/Ta	20.1	17.0	22.7	21.9	21.4	19.8
Lu/Hf	0.0504	0.0402	0.0745	0.0737	0.0497	0.0456
Ce/Pb	17.3	24.2	31.7	180.9	23.6	56.5
Nb/U	47.1	58.0	54.0	44.4	41.1	51.7
Zr/Hf	52.4	44.4	56.4	62.2	46.0	48.7
KN/KN*	0.900	1.21	0.506	0.574	0.761	0.538
$(Dy/Yb)_N$	1.52	1.78	1.67	1.71	1.70	1.83
$(La/Yb)_N$	28.3	21.7	38.5	38.7	26.5	30.2
CaO/TiO_2	4.31	4.48	5.19	5.90	5.30	5.76
CaO/Al_2O_3	0.540	0.870	0.770	0.850	0.850	1.19

Table 5 continued

Sample Number	**Ei 13**	**Ei 14**	**Ei 15**	**Ei 16b**	**Ei 17**	**Ei 18**
Locaylity	Hohe Buche	Plaidter Hummerich	Nettetal	Rothenberg	Lower-Mendig Flow	Eppelsberg (coarse)
Nb/Ta	17.3	17.1	17.6	17.6	16.1	16.0
Lu/Hf	0.0376	0.0438	0.0423	0.0408	0.0494	0.0375
Ce/Pb	26.0	30.1	21.1	23.8	24.2	25.2
Nb/U	52.8	52.1	61.4	51.5	53.1	54.9
Zr/Hf	43.6	45.8	46.5	46.2	44.4	41.7
KN/KN*	1.11	1.05	1.20	1.02	0.826	0.835
$(Dy/Yb)_N$	1.81	1.72	1.70	1.71	1.66	1.69
$(La/Yb)_N$	23.9	23.4	25.3	24.9	24.7	22.7
CaO/TiO_2	4.33	4.16	4.28	4.30	4.21	4.39
CaO/Al_2O_3	0.900	0.770	0.760	0.820	0.700	0.840

Table 5 continued

Sample Number	**Ei 19**	**Ei 20**	**Ei 21**	**Ei 22a**	**Ei 23**	**Ei 24**
Locaylity	Eppelsberg (dike)	Lower-Mendig Flow	relict flow. Hill W' Jägerheim	Rüderbusch	Steffelner Kopf	Goßberg
Nb/Ta	16.6	16.2	16.4	19.5	17.6	19.6
Lu/Hf	0.0429	0.0488	0.0429	0.0385	0.0357	0.0440
Ce/Pb	68.6	23.4	20.0	22.1	22.3	26.0
Nb/U	52.3	52.7	55.1	51.5	56.3	44.6
Zr/Hf	42.0	43.6	39.6	44.6	42.4	43.8
KN/KN*	0.819	0.832	1.17	0.866	1.27	1.02
$(Dy/Yb)_N$	1.65	1.66	1.76	1.87	1.95	1.83
$(La/Yb)_N$	23.7	23.9	22.7	34.3	29.3	30.5
CaO/TiO_2	4.80	4.21	4.23	5.79	5.06	5.57
CaO/Al_2O_3	0.820	0.700	0.770	1.28	1.22	1.19

Table 5 continued

Sample Number	**Ei 25**	**Ei 26**	**Ei 27**	**Ei 28**	**Ei 29**	**Ei 30**
Locaylity	Rockeskyller Kopf	Kalem	Sarresdorf Lavaflow	Fächerhöhe	Wartgensberg	Mosenberg
Nb/Ta	18.7	17.6	23.1	19.4	19.7	20.3
Lu/Hf	0.0356	0.0411	0.0675	0.0598	0.0558	0.0581
Ce/Pb	19.3	27.2	32.2	33.6	30.6	34.5
Nb/U	48.6	54.1	27.7	37.5	36.5	45.9
Zr/Hf	42.9	43.8	47.3	46.1	45.5	48.2
KN/KN*	1.12	0.572	0.306	0.446	0.448	0.454
$(Dy/Yb)_N$	1.85	1.94	1.87	1.93	1.98	1.92
$(La/Yb)_N$	33.1	31.7	29.7	28.6	28.5	29.0
CaO/TiO_2	5.22	5.20	5.43	5.16	4.59	4.74
CaO/Al_2O_3	1.10	1.27	1.04	1.02	0.98	1.03

Table 5 continued

Sample Number	**Ei 31**	**Ei 32**	**Ei 33**	**Ei 34**	**Ei 36**	**Ei 38**
Locaylity	Auf der Hardt	Am Steinseiter	Sulzbusch	Sulzbusch	An der Ahl	Etringer Bellerberg
Nb/Ta	19.2	19.6	22.6	22.6	23.6	22.3
Lu/Hf	0.0446	0.0421	0.0699	0.0710	0.0815	0.0564
Ce/Pb	23.9	26.5	24.7	26.5	22.9	14.1
Nb/U	47.5	54.7	47.3	43.3	41.0	29.4
Zr/Hf	43.8	42.3	48.4	48.4	54.1	52.6
KN/KN*	0.830	1.01	0.630	0.572	0.606	0.874
$(Dy/Yb)_N$	1.84	1.92	1.61	1.61	1.54	1.32
$(La/Yb)_N$	29.9	25.8	34.1	34.2	37.2	23.3
CaO/TiO_2	5.72	5.27	5.20	5.18	5.14	4.37
CaO/Al_2O_3	1.19	1.25	0.790	0.780	0.580	0.470

Table 5 continued

Sample Number	**Ei 39**	**Ei 40**	**Ei 41**	**Ei 42**	**Ei 43**	**Ei 44**
Locaylity	Karmelenberg	Humersberg	Engelner Kopf	Schellkopf	Meirother Kopf	Tiefenstein
Nb/Ta	17.3	22.1	59.7	55.8	18.9	18.7
Lu/Hf	0.0490	0.0745	0.0676	0.0539	0.0536	0.0484
Ce/Pb	20.8	33.3	5.19	3.95	23.2	33.2
Nb/U	40.5	43.2	62.6	28.1	40.4	43.1
Zr/Hf	45.3	50.8	90.0	85.8	45.2	42.3
KN/KN*	0.982	0.584	0.880	0.918	0.735	0.734
$(Dy/Yb)_N$	1.65	1.62	0.902	0.824	1.72	1.75
$(La/Yb)_N$	23.2	33.4	13.0	17.3	28.9	29.6
CaO/TiO_2	4.33	4.98	3.78	6.24	5.12	5.21
CaO/Al_2O_3	0.760	0.710	0.0700	0.0800	0.940	0.920

Table 5 continued

Sample Number	**Ei 45**	**Ei 46**	**Ei 47**	**Ei 48**	**Ei 49a**	**Ei 49b**
Locaylity	Meirother Kopf	An der Hardt	Schorenberg	Burgberg	Burg Olbrück	Burg Olbrück
Nb/Ta	19.6	37.0	30.9	77.6	68.8	68.9
Lu/Hf	0.0563	0.0637	0.0725	0.0393	0.0576	0.0596
Ce/Pb	32.7	9.16	14.7	4.30	4.63	4.58
Nb/U	40.6	119.1	70.6	27.1	38.1	26.4
Zr/Hf	45.7	73.7	66.3	78.3	80.3	80.5
KN/KN*	0.697	2.14	1.25	0.823	0.947	0.764
$(Dy/Yb)_N$	1.68	0.702	1.27	0.702	0.761	0.739
$(La/Yb)_N$	29.1	27.8	30.2	27.8	17.9	16.8
CaO/TiO_2	5.19	4.01	6.72	7.69	2.63	5.67
CaO/Al_2O_3	0.930	0.130	0.320	0.0800	0.0300	0.0700

Table 5 continued

Sample Number	**Ei 50**	**Ei 51**	**Ei 53**	**Ei 55**	**Ei 56**	**Ei 57**
Locaylity	Perler Kopf	Perler Kopf	Kempenich	Bräunig Vulkan	NE' Üdersdorf	Emmelberg
Nb/Ta	29.3	29.5	39.6	19.8	18.2	19.9
Lu/Hf	0.0617	0.0610	0.0678	0.0526	0.0385	0.0492
Ce/Pb	10.3	10.4	4.89	41.8	22.9	21.9
Nb/U	63.6	66.2	57.8	44.1	40.8	28.5
Zr/Hf	71.7	71.2	85.0	43.0	44.6	48.5
KN/KN*	0.644	0.725	0.727	0.575	0.748	0.287
$(Dy/Yb)_N$	1.33	1.30	0.934	1.75	1.94	1.86
$(La/Yb)_N$	30.3	28.4	13.4	30.6	33.1	30.9
CaO/TiO_2	6.00	7.49	2.69	6.36	6.83	4.55
CaO/Al_2O_3	0.340	0.430	0.0500	1.13	1.42	1.02

Table 5 continued

Sample Number	**Ei 58a**	**Ei 59**	**EI 60**	**EI 61**	**Ei 62**
Locaylity	Leyendecker Quary	Wolfsschlucht	Alte Burg cone	Lorenzfelsen	Booser Maar
Nb/Ta	18.9	19.0	16.1	15.9	18.4
Lu/Hf	0.0682	0.0566	0.0441	0.0417	0.0495
Ce/Pb	26.7	34.7	24.9	30.5	24.2
Nb/U	39.3	41.6	48.4	60.0	46.6
Zr/Hf	45.1	45.0	41.0	42.3	42.9
KN/KN*	0.296	0.362	1.00	0.973	
$(Dy/Yb)_N$	1.87	1.98	1.68	1.74	1.67
$(La/Yb)_N$	29.2	29.8	22.3	22.8	28.5
CaO/TiO_2	4.91	5.33	4.18	3.89	nd
CaO/Al_2O_3	0.930	1.12	0.840	0.890	nd

Table 5 continued

First, I would like to express my gratitude to my supervisor Carsten Münker who has brought me into the field of geochemistry. I am more than thankful for the opportunity of doing my Bachelor-, Master- and now my Ph.D. Thesis with you. During the last years, your door has always been open for me and my questions – no matter if it was regarding research or life in general. I can´t thank you enough for that. I am also thankful for all the amazing field trips, social events and conferences that I was able to attend.

More than special thanks go out to Jonas Tusch. Nothing would have been possible without you. From the beginning of my studies, you have given me opportunities – like my first job as being a tutor – and became one of the most important friends in my life. I am more than grateful for everything you have taught me, all the help you provided and the uncountable hours we have shared in the lab, on the Neptune or reading my manuscripts.

I thank Chris Marien for being a mentor during my studies and teaching me the fundamentals of how to be a geochemist. We have shared some of my very first moments in the lab and on the machines – you have levelled my way. Special thanks go out to Eric Hasenstab who is an amazing geochemist, co-worker and friend. We have spend numerous hours of laughing, discussing, crafting Ph.D.-hats or crushing rocks on amazing field trips. Florian Kurzweil is thanked for being a mentor and friend during all my studies and for being a more than perfect office and coffee mate. Your comments greatly improved my thesis and my manuscripts. I would like to express further gratitude to Frank Wombacher for his support in the lab and on the machines – you have kept it all running, no matter what. Mario Fischer-Gödde is thanked for all the discussions, his help on the machines and all the cigarettes we shared around the world – times and conversations I will never forget. Benedikt Ritter is thanked for the most amazing field trip to India and for providing his assistance during my studies, for reading my manuscripts and for being a great mentor on my way. Andreas Vogt and Jochen Scheld are thanked for all their help in the Blackbox and their assistance during my projects – without you this building would not work. Josua Pakulla is thanked for his help in the lab and preparing samples – and of course, for being a great student that I gladly supervised.

I would further like to thank Christiane Schnabel, Ramon Reifenröther, Alessandro Bragagni. Maxwell Thiemens, Carina Gerritzen, Ninja Braukmüller, Jens Barosch, Laura Müller, Daniela Hülle, Almut Katzemich, Markus Pfeifer, Bo-Magnus Elfers, Tibor Dunai, Reiner Kleinschrodt, Sandro Jahn, Tomasz Goral and many many others – I am thankful our ways have crossed and I surely hope they will do it again.

I cannot finish this chapter without thanking my wife and – until now he is still in Moms belly – my son Mats. Maike, you are the love of my life, you will be an amazing mother and I am thankful for you sharing all the good and the tough times with me.

Further, without my Parents Hans-Peter and Meta Jansen, nothing would have been possible. I am more than grateful for all your support during the last 31 years of my life.

My parents in law – Uwe and Astrid Dürscheid are thanked for providing their support and always being around when needed.

Lukas & Johanna, Family Ehlke – I am grateful to have you as friends – especially during the final moments of my study, you have been an amazing help.

Financial support for this thesis has been provided by the European Comission through ERC grant 669666.

Erklärung

Chapter I baut auf meiner Masterarbeit “High precision W-isotope measurements on modern oceanic island and intraplate basalts” auf. Im Rahmen dieser Masterarbeit wurden an 19 Proben aus der Eifel, von La Réunion und Ascension Island ^{182}W Isotopenmessungen durchgeführt. Da diese Daten jedoch zum Teil von zu großen Messfehlern behaftet war, wurden analytische Protokolle überarbeitet und der Datensatz durch neue Lokationen ergänzt. In die Publikation, die Chapter I darstellt, sind auch die Daten aus meiner Masterarbeit eingeflossen. Deshalb werden in dieser Dissertation sowohl der Datensatz der Masterarbeit als auch die hier gewonnenen Daten in ihrer Gesamtheit vorgestellt und neu interpretiert.

Chapter III baut auf den Bachelorarbeiten von Vera Schmitt „Geochemische Untersuchungen von mafischen Quartären Vulkaniten der Westeifel“, Robin Tordy „Geochemische und petrologische Untersuchungen von quartären Melilitithen und Basaniten der Osteifel“ und meiner eigenen „Geochemisch-petrologische Untersuchungen an Vulkaniten aus der Frühphase des Osteifel-Vulkanismus“ auf. Die in diesen Arbeiten präsentieren Daten werden durch einen großen Datensatz neuer Proben und umfassende Neumessungen ergänzt und zum ersten mal in Ihrer Gesamtheit vorgestellt und interpretiert.

Ich versichere, dass ich die von mir vorgelegte Dissertation selbständig angefertigt, die benutzten Quellen und Hilfsmittel vollständig angegeben und die Stellen der Arbeit - einschließlich Tabellen, Karten und Abbildungen -, die anderen Werken im Wortlaut oder dem Sinn nach entnommen sind, in jedem Einzelfall als Entlehnung kenntlich gemacht habe; dass diese Dissertation noch keiner anderen Fakultät oder Universität zur Prüfung vorgelegen hat; dass sie − abgesehen von unten angegebenen Teilpublikationen − noch nicht veröffentlicht worden ist, sowie, dass ich eine solche Veröffentlichung vor Abschluss des Promotionsverfahrens nicht vornehmen werde. Die Bestimmungen der Promotionsordnung sind mir bekannt. Die von mir vorgelegte Dissertation ist von Prof. Dr. Carsten Münker betreut worden.

Nachfolgend genannte Teilpublikationen liegen vor:

Chapter I, Appendix A1

Jansen, M.W., Tusch, J., Münker, C., Bragagni, A., Avanzinelli, R., Mastroianni, F., Stuart, F.M., Kurzweil, F., 2022. Upper mantle control on the W isotope record of shallow level plume and intraplate volcanic settings. Earth and Planetary Science Letters 585, 117507.

Datum: 05.09.2022 Unterschrift: